On the use of metamodeling for modeling and analysis of the radar response of forests

Panagiotis Piteros

▶ To cite this version:

HAL Id: tel-01332615

https://theses.hal.science/tel-01332615

Submitted on 16 Jun 2016

Thèse de Doctorat

de

l'Université PARIS-SACLAY

préparée à

CentraleSupélec

ÉCOLE DOCTORALE N° : 575
Physique et Ingénierie : Électrons, Photons, Sciences du vivant (EOBE)

Spécialité de doctorat : Génie Électrique

Par

Παναγιώτης Σωτ. Πιτερός
(Panagiotis Sot. PITEROS)

De l'utilisation de la méta-modélisation pour la modélisation et l'analyse de la réponse radar des forêts

Thèse présentée et soutenue à Gif-sur-Yvette, le 15 avril 2016 :

Composition du Jury :

M. Monod H.	Directeur de Recherche, INRA	President du jury
M. Iooss B.	Ingénieur Chercheur Senior, EDF	Rapporteur
M. Lautru D.	Professeur, Université de Nanterre	Rapporteur
M. Lambert M.	Chargé de Recherche, CNRS	Directeur de thèse
M. Guinvarc'h R.	Professeur Adjoint, CentraleSupélec	Encadrant et Invité
Mme Thirion-Lefèvre L.	Professeur Adjoint, CentraleSupélec	Encadrante et Invitée

PhD Dissertation

OF

PARIS-SACLAY University

PREPARED AT

CentraleSupélec

DOCTORAL SCHOOL N°: 575
Electrical, Optical, Bio-physics and Engineering

PhD in Electrical Engineering

By

Παναγιώτης Σωτ. Πιτερός
(Panagiotis Sot. PITEROS)

On the use of metamodeling for modeling and analysis of the radar response of forests

PhD defended at Gif-sur-Yvette, the 15$^{\text{th}}$ of April 2016:

Composition of the jury:

M. Monod H.	Directeur de Recherche, INRA	President of the jury
M. Iooss B.	Ingénieur Chercheur Senior, EDF	Reviewer
M. Lautru D.	Professeur, Université de Nanterre	Reviewer
M. Lambert M.	Chargé de Recherche, CNRS	Thesis advisor
M. Guinvarc'h R.	Professeur Adjoint, CentraleSupélec	Co-supervisor and invited
Mme Thirion-Lefèvre L.	Professeur Adjoint, CentraleSupélec	Co-supervisor and invited

Acknowledgments

...Ἄλλα ζητεί ἡ ψυχη σου, γι᾿ ἄλλα κλαίει·
τὸν ἔπαινο του Δήμου καί τῶν Σοφιστῶν,
τὰ δύσκολα καὶ τ᾿ ἀνεκτιμητα Εὖγε·
τὴν Ἀγορά, τὸ Θέατρο, καί τούς Στεφάνους.
Αὐτά ποῦ θὰ στὰ δώσει ὁ Ἀρταξέρξης,
αὐτα ποῦ θὰ τὰ βρεῖς στὴ σατραπεία·
καὶ τί ζωὴ χωρὶς αὐτά θὰ κάμεις.

Contents

Summary in English

Introduction

Forest structure measurements are widely needed nowadays for both civil and military applications, such as the estimation of the biomass and the detection of hidden targets in forest environment. Radar remote sensing techniques show very promising performances at both regional and global scales. They provide temporal flexibility and more dynamic forest representations, complementing the ground-based measurements. Radars are able to operate under any weather conditions and emit electromagnetic waves which interact with elements having dimensions of the same magnitude as the wavelengths. In particular, if low frequency microwave radiation is selected ($\leq 2\,\text{GHz}$), the waves are able to penetrate within the forest and be scattered by large elements such as the branches and the trunks. If the microwaves have high frequencies, only the tree crowns contribute in the scattering events. Therefore, radars can support a thorough forest investigation by examining all layers and providing sometimes data well correlated with certain forest parameters.

Nevertheless, the acquisition of the forest radar signature is quite a challenging task. Forests constitute complex media with diverse contributions to the wave backscattering, depending on the radar configuration and on the physical characteristics of the scatterers. As a consequence, in order to characterize a forest, to identify its signature and to detect a hidden target within it, a thorough understanding of the forest scattering is essential. The difficulties of this task are the lack of an one-to-one correspondence between the forest parameters and the radar data and the fact that forest radar observations rarely take into account the effect of the environment in real-time. In this work, the use of statistical methods from Sensitivity Analysis and Metamodeling are used on an electromagnetic scattering numerical model, in order to suggest an innovative way to design radar campaigns over forests. A way which includes the organization and analysis of the already obtained data to extract information on the scene, which will be subsequently used in the design of the new signal to be emitted.

Radar and simulation studies of forested areas

Radar is believed to be the most appropriate tool for remote sensing observations of forested areas. It can "see" through conditions such as haze, fog, rain and snow and there is no limitation on where it can be located; on an airplane, a satellite, a ship, or placed on the ground. After the introduction of the Synthetic Aperture Radar (SAR) principle especially, which improved the azimuth resolution, more detailed observations like the ones necessary for the vegetation investigation were possible. During the interactions of the radar EM waves with the scatterers, there are three wave properties of interest. The intensity and the phase of the emitted wave and

its polarization state. These properties and their variations are directly related to the scatterer's characteristics, i.e. the range, the shape, the size, the orientation and the permittivity. Therefore, information on these characteristics can be extracted from the received radar signal. The main quantity describing how a radar target or surface feature scatters EM energy, is the scattering matrix. In our work, since forest are complex media and distributed targets, we also studied the backscattering coefficients in all polarizations and used the Pauli decomposition of the scattering matrix, to extract additional information on the scattering mechanisms. In particular, under the Forward Scattering Alignment (FSA) convention adopted by our numerical model, the three Pauli vector components correspond to the double bounces, the single bounces and the volume scattering respectively.

To carry out our simulation studies, a scattering model applied to the electromagnetic study of the forest backscattering called COSMO, was used. COSMO is a coherent and descriptive model. Coherent since it calculates the complex responses providing information on both the amplitude and the phase of the received signal and descriptive because it is based on the generation of the trees and the forest. COSMO operates in the frequency domain and provides both the scattering matrix and the polarization signature. Its results are extensively validated at P- and L-band, for the temperate (maritime pine trees) forests we considered and for polarimetric purposes. For our experiments, the generated simulation scenes were based on a 2-layer discrete model, containing only trunks and primary branches. The data used to estimate and predict the dimensions and the distributions of the forest elements were derived from allometric equations. The ground was assumed plane and the permittivities were derived from widely validated empirical models. The quantities we selected to study were the received electric fields under all polarizations, the backscattering coefficients and the Pauli vector components. These were subsequently analyzed to obtain the forest signature and each forest element's effect.

Sensitivity analysis of COSMO

The statistical methods of Sensitivity Analysis (SA) for numerical models are widely used in the domain of Design of Experiments. They can facilitate the identification of the factors which affect significantly the model overall and each one of its outputs and detect possible non-linear effects and interactions between the inputs. The knowledge obtained from the SA can be subsequently used for model analysis and reconsideration. In radar forest studies, empirical sensitivity analyses are sometimes performed over real data. Nonetheless, since sensitivity analyses of real data are based on the sparse datasets available and cannot be performed for numerous different scenarios, they are far from being thorough and complete. It is exactly where the statistical SA methods applied on numerical models can complement these studies and open the ground for a better understanding of the forest response. We applied these methods on COSMO to identify its most important parameters, in order to study and analyze the parameters effects in a next step. It was the first time, to the best of our knowledge, that such a mathematical technique was applied to radar studies of forests. Our SA study of COSMO aspired to provide new information on the dependence of the different COSMO outputs on the input factors. It aimed also to assist in designing an innovative way to perform radar campaigns based on these information and utilizing the cognitive radar principle in an upcoming step.

A qualitative SA method called the Elementary Effects (EE) method (or the Morris screening method), was preferred. This method can determine model inputs that have effects which can be

considered as negligible, or linear and additive, or non-linear and involved in interactions with other factors. It uses only a few model runs, calculates a number of incremental ratios, the EE, for each input variable and studies their distributions. The information on the inputs effects are extracted from the statistical measures of these distributions, the mean μ of the EE, their standard deviation σ and the mean μ^* of their absolute values. In COSMO we examined different cases concerning fully or quasi-periodical forests, having trunks only or trunks and branches. A wide domain was investigated for each of the inputs under consideration. By performing this SA on COSMO, we succeeded in assessing the importance of its main input factors, by their effects on the several different outputs. The frequency and the incidence angle of the emitted signal were identified as the most important COSMO parameters overall, as seen for example in Fig. 1 for a forest of trunks only. They were followed by the age of the forest and the permittivity of the vegetation, as the most important forest characteristics. On the contrary, the radar height, the temperature and the ground synthesis parameters showed negligible effects and can in most of the experiments be set at constant values to lighten COSMO, without largely affecting its performances. The case of the phase difference where the positioning parameters were of considerable importance was highlighted also. In addition, we discovered the fact that the angle can sometimes be the most important factor of the model, showing highly non-linear behavior and interactions with the frequency mostly - maybe due to the Brewster angle effect. These new information on COSMO and forest radar studies that the SA came with, needed to be further verified. In saying so, distinct COSMO simulation studies for each important factor were performed subsequently, in order to confirm its importance and examine the extent of the effect.
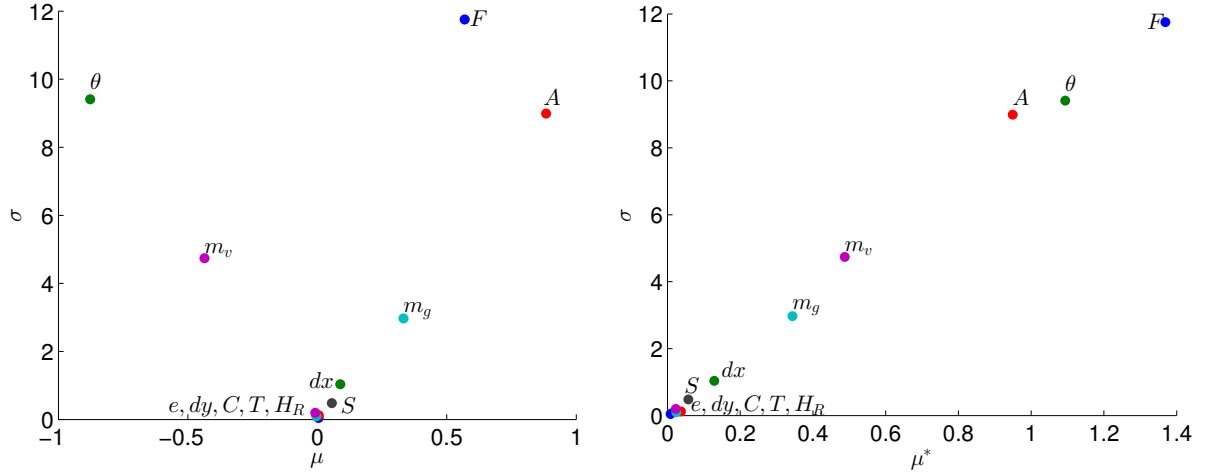
Figure 1 − The aggregate screening results for all normalized outputs considered at the whole COSMO frequency band [0.35, 2 GHz] and angles from 5° to 85° in the $\mu\sigma$-plane (left) and the $\mu^*\sigma$-plane (right). A periodical forest of trunks only was examined. High μ and/or μ^* show high overall importance and high σ shows strong non-linear effects. The frequency F and the angle of incidence θ are the most important parameters, followed by the age A and the permittivity m_v of the forest.

Analysis of the forest backscattering with COSMO

One of the objectives of this work was to organize the radar simulation datasets, analyze them with respect to the scene changes and thus extract complementary information during radar

observations of forests. The purpose of the analysis was not to fully exploit COSMO and go deeply into the physics of the forest scattering, but rather to justify and study the results of the SA and identify the exact effect of each parameter and forest element. In saying so, firstly to examine the influence on the output of the most important parameters (frequency, angle, age and vegetation humidity) variations, the effects of the branches as well as that of the target existence. The analyses were performed in both frequency and time domains - the latter for the first time in radar studies of forests. The physical interpretation of the parameters effects was assessed, whenever possible, in terms of the scattering mechanisms or the geometry of the scene. In addition, appropriate radar configurations for an easier identification of the discovered effects were suggested, based on the analysis results. The present analysis would be complemented later on by checking the applicability and the utility of the metamodel in the first step, while using the configurations suggested here. So that the use of the metamodel would provide a fast and real-time analysis to be carried out during our future adaptive radar observations.

The analyses done on the COSMO results, concerned the backscattering coefficients and the components of the Pauli feature vector in frequency domain and the amplitude of the received signal in time domain. In the frequency domain, the certain effects of the four important parameters were identified. To wit, the way the quantities were affected by the change of the input values and the behavior of the distinct scattering mechanisms. Also, the way the branches, the target and the forest arrangement respond within the whole frequency spectrum was discovered. In Fig. 2 for instance, we can see that the branches contribute mostly for frequencies higher than $1\,\mathrm{GHz}$ to the co-polarizations and for all frequencies to the cross-polarization. The time signal analysis resulted in the extraction of supplementary information on the forest geometrical structure. As seen for example in Fig. 3, the number of the signal peaks, the duration of the pulse and the peaks mutual distance correspond to the number of the tree lines in site dimension, the length of the scene and the distance between the tree lines respectively. The discovery of the certain effects which could be undoubtedly assigned to their corresponding sources, led us to "define" some matchings between them which could be subsequently used in the planning of more focused radar campaigns. Specific frequencies or polarizations could be favored in each observation, with respect to the effect under study. Last but not least, the Brewster angle effect in COSMO simulations was also examined. The cases where it can be significant, causing a big difference between the HH and VV backscattering, were highlighted.

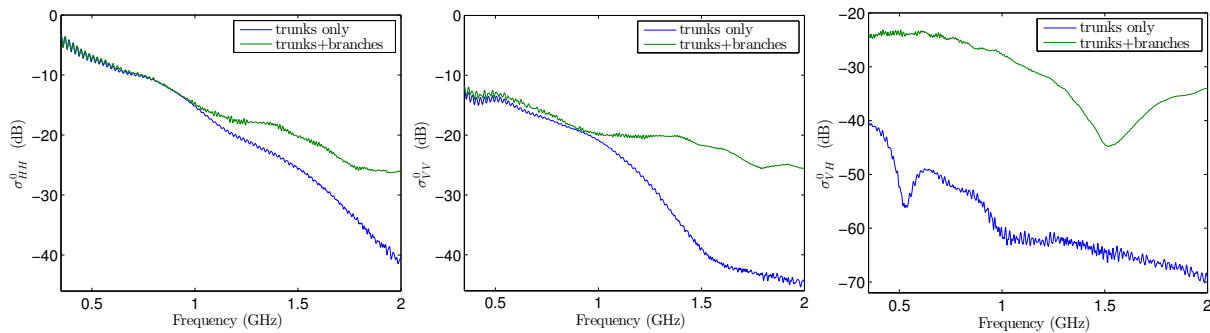*Figure 2 – The backscattering coefficients of the received signal in HH polarization (left), in VV (middle) and in VH (right) for the cases of a forest with trunks only and the same trunks with branches added. The branches contribute to the co-polarized signal after $1\,\mathrm{GHz}$ and to the cross-polarized one within the whole spectrum. The incidence angle of the emitted wave was $40°$.*
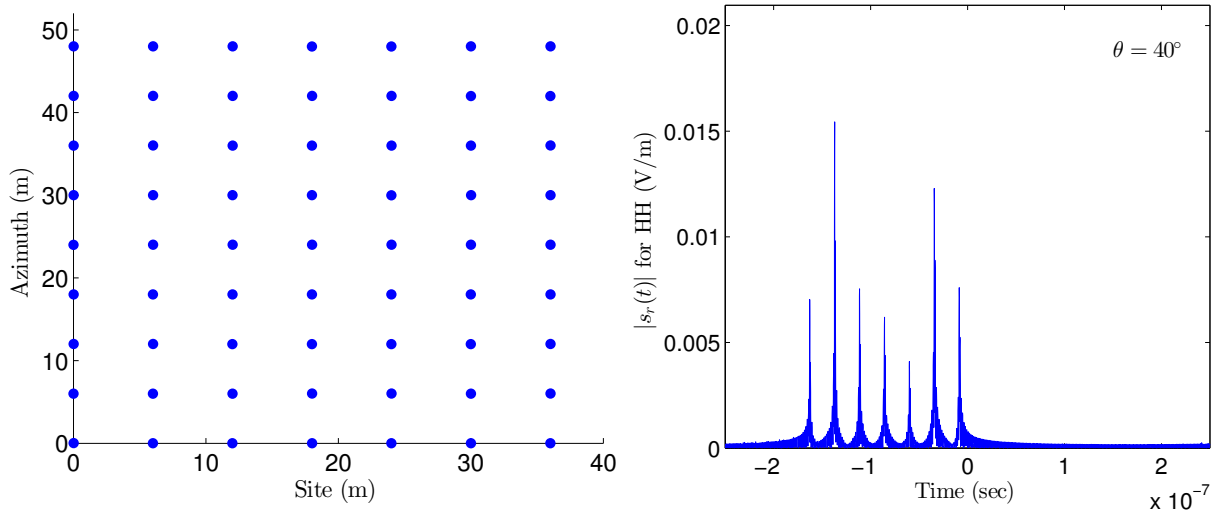
Figure 3 – The amplitude of the received time signal from a fully periodical forest in HH had seven peaks (right), corresponding to the trunk lines along the site dimension of the forest arrangement (left). The length of the whole pulse is proportional to the site dimension of the scene and the space between the peaks to the distance between the tree lines.

Surrogate modeling and approximation of COSMO

The second statistical method selected for our radar simulation studies is Surrogate Modeling (or Metamodeling). The SA statistical method applied on COSMO, provided valuable information on the model factors importances. These information were subsequently verified, in order to discover the exact parameters and forest elements effects, attribute their physical interpretations and recommend the optimal configurations for their identification during radar studies. The latter aims to be integrated in the radar observation practice at an upcoming step, in order to supplement it. Unfortunately, the necessary fast real-time analysis of the radar data is almost impossible, even when using numerical codes like COSMO. It is the use of a metamodel that can help us surpass this difficulty. A model like this, can approximate the numerical code values in very low computational time, based on a few simulation results only. Therefore it could substitute COSMO in the design of an adaptive, in real-time, radar observation strategy for forests. In addition, the metamodel operating frame could serve in designing an innovative adaptive strategy for future radar observations.

Among the various metamodeling techniques in practice today, the kriging interpolation method was selected to be applied to the COSMO approximation. This method, apart from the real values prediction with few simulation points, it provides also a measure of the prediction's uncertainty. This uncertainty can be subsequently used to construct more efficient adaptive metamodels. In our studies we constructed a metamodel like this, which was sequentially reducing the prediction uncertainty, each time we were adding a new point to the input sample. In approximating COSMO, we applied the metamodel to the backscattering coefficients and the Pauli vector components only. The metamodel succeeded in predicting the outputs corresponding to the cases studied during the analysis of the previous chapter, with few simulations and very low uncertainty. As seen for example in Fig. 4 and 5, the main variations of the VV backscattering coefficient were well approximated and the point where the change of the dominant scattering mechanism takes place, was detected with a very high accuracy. Therefore, the possibility to

detect the effects of the important inputs and the forest elements on the outputs was verified.
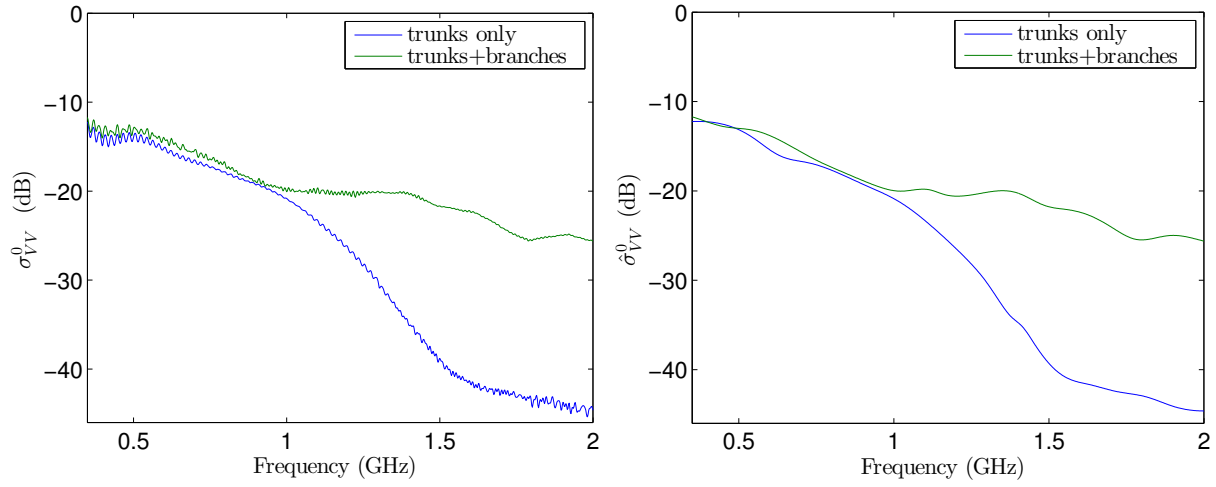
Figure 4 – The backscattering coefficients in VV for the two forest arrangements having trunks only and trunks with 10 branches each (left) and their kriging predictions based on 20 adaptively chosen frequency points (right). The metamodel can provide a satisfactory approximation showing the overall behavior of the σ_{VV}^0 values and the branches effect on it after $1\,\mathrm{GHz}$, in less than $1/40$ of the time required for the full simulation.
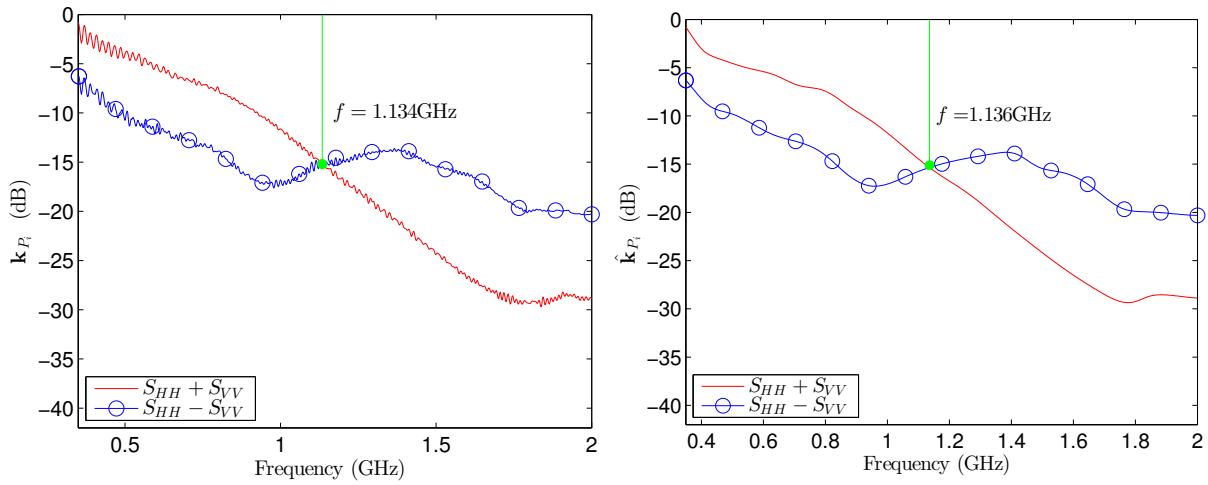
Figure 5 – The single and double bounces as represented by the first two Pauli components values (left) and their kriging predictions based on 20 adaptively chosen simulation points (right). The metamodel approximation provides the overall behavior of the two first Pauli vector components and also the frequency where the dominant scattering mechanism changes from double to single bounces, with a certain but very small error.

Cognitive radar principle in forest investigation

The cognitive radar is an innovative type of radar, envisaged by S. Haykin in 2006. Its main principle is that a radar system has to adjust the emitted signal, with respect to the environment. In saying so, each new signal to be emitted will be dependent on the previous radar returns

and the results from their analyses. So far, no system like this has been materialized, due to several technical limitations. In our work, we aspired to incorporate the cognitive radar principle in a radar observation strategy, conceived using COSMO as the simulator, the two statistical methods applied to it and the knowledge acquired in the previous chapters. The analogies between the metamodel and the cognitive radar general principles, led us to fit the cognitive radar idea to the global metamodel operating frame. The metamodel also assisted in accelerating the analysis done on the radar responses, as it was proven capable of identifying fast some of the scene characteristic effects. The results from the analysis chapter and the suggested radar configurations served the processing of the received signal and the extraction of the scene information, before designing the new signal to be emitted. The outcome was a new adaptive-cognitive strategy for radar simulation studies, which could adjust the signal with respect to the illuminated scene, in very low computational time. This proposed strategy, could hopefully open the ground for reconsidering and improve the way radar observations are carried out nowadays and to lead to an integrated realization of a cognitive radar.

The general flowchart of our proposed strategy based on COSMO simulations, can be seen in Fig. 6. After the initial observation, we quickly approximate the forest response with the metamodel and then proceed to the analysis step. There, intermediate objectives of the study can be put, with respect to the conclusions already extracted. The corresponding radar configurations are then selected and a new signal is designed and emitted, in order to update our knowledge on the scene. As soon as our objective is achieved, the whole loop closes or the observations continue until enough frequencies are emitted to construct the time signal. The strategy described above was successfully applied to four different examples, corresponding to the forest effects already studied in the analysis chapter. An example of the application of this strategy can be seen in Fig. 7 and 8. In the first figure the initial predictions of the backscattering coefficients and the Pauli vector components are presented, which indicated the existence of branches. By adaptively choosing new frequencies to be emitted along the narrowed frequency interval $[0.8, 1.3\,\mathrm{GHz}]$, we arrived at a final prediction for the Pauli vector components which provided the frequency where the change of the dominant scattering mechanism took place with an accuracy of 99.82%. The time needed to complete this adaptive investigation was less than $1/50$ of the computational time required for the whole investigation done in the analysis chapter.
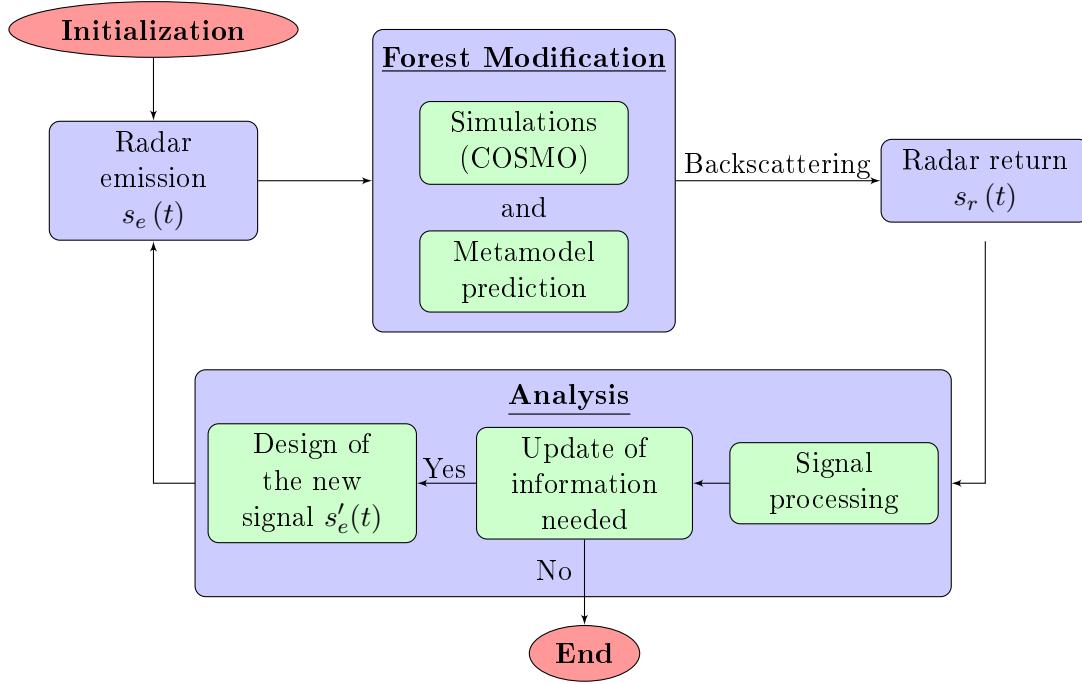
Figure 6 – The general flowchart representing the proposed adaptive-cognitive strategy, based on the meta-model operating frame.
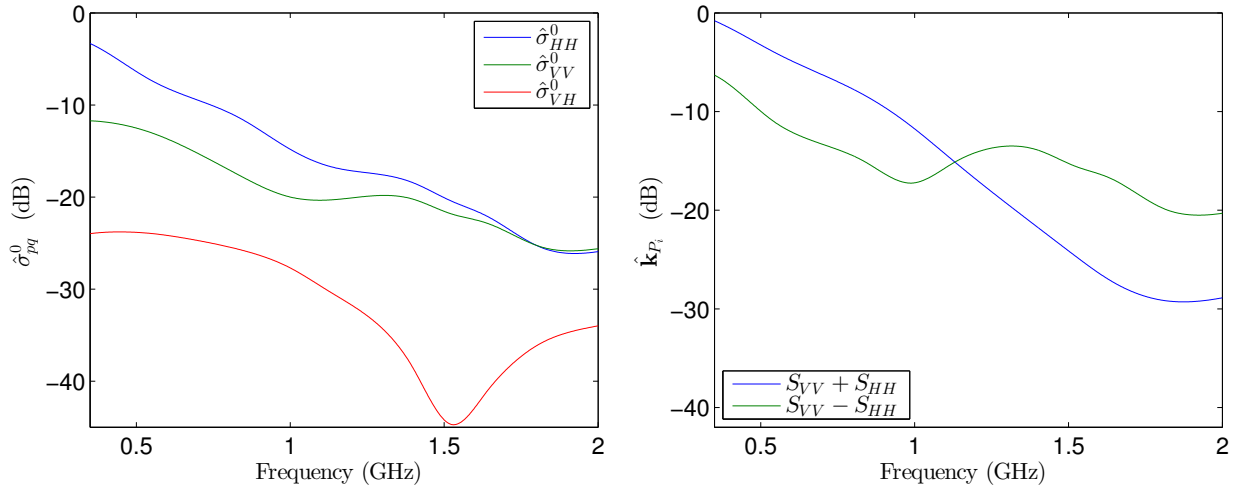
Figure 7 – The initial metamodel predictions for the backscattering coefficients (left) and the two first Pauli vector components (right). The change of the dominant scattering mechanism observed in the right plot, is a sign of the branches existence.
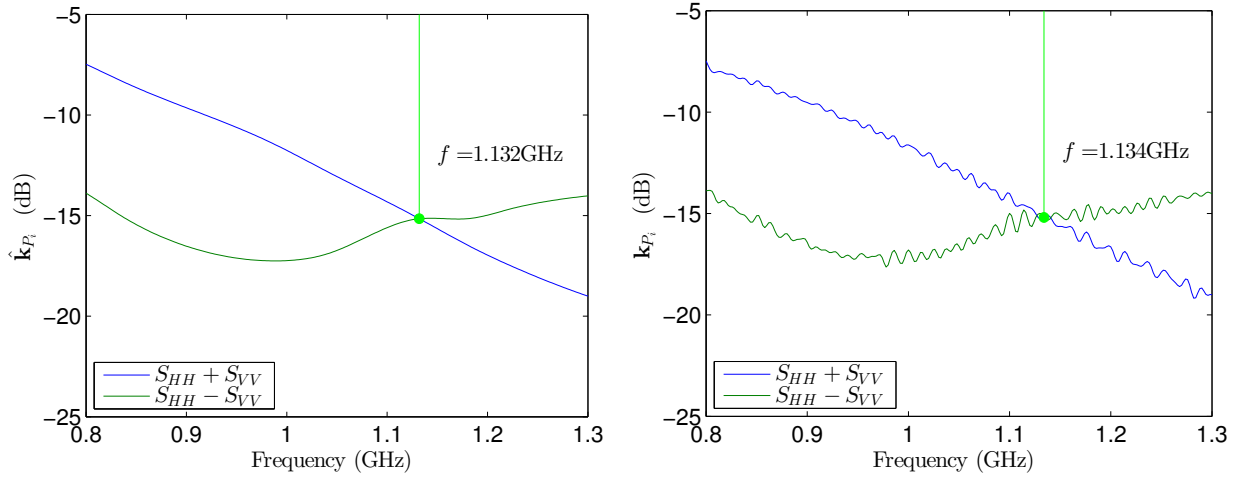
Figure 8 – The predicted values for the double and single bounces within the narrowed $0.8 - 1.3$ GHz frequency interval (left) and the corresponding real values (right). The point where the change of the dominant mechanism happens is predicted with an accuracy of about 99.8%, even if just 8 simulation results were used.

Résumé en français

Introduction

Des mesures de la structure d'une forêt sont largement nécessaires aujourd'hui pour des applications civiles et militaires, comme l'estimation de la biomasse et la détection de cibles cachées dans l'environnement forestier. Les techniques de la télédétection par radar montrent des performances très prometteuses à petite et grande échelle. Elles offrent une flexibilité temporelle et des représentations de la forêt plus dynamiques, en complément des mesures au sol. Les radars sont capables de fonctionner dans toutes les conditions météorologiques et d'émettre des ondes électromagnétiques qui interagissent avec des éléments ayant des dimensions du même ordre de grandeur que les longueurs des ondes. En particulier, si des basses fréquences sont sélectionnées ($\leq 2\,\mathrm{GHz}$), les ondes sont capables de pénétrer dans la forêt et d'être dispersées par les grands éléments tels que les branches et les troncs. Si les ondes ont des fréquences plus hautes, seules les couronnes des arbres contribuent à la diffusion. Par conséquent, les radars peuvent permettre une exploration approfondie de la forêt, en examinant toutes les couches et en fournissant parfois des données bien corrélées avec certains paramètres de la forêt.

Néanmoins, l'acquisition de la signature radar de la forêt est un travail très difficile. Les forêts constituent des milieux complexes avec des contributions diverses à la rétrodiffusion des ondes, en fonction de la configuration du radar et des caractéristiques physiques des diffuseurs. En conséquence, afin de caractériser une forêt, d'identifier sa signature radar et de détecter une cible qui y serait cachée, une compréhension approfondie de la dispersion des forêts est essentielle. Les difficultés de cette tâche sont l'absence d'une correspondance claire entre les paramètres de la forêt et les données radar ainsi que le fait que les observations radar des forêts prennent rarement en compte l'effet de l'environnement en temps réel. Dans ce travail, une combinaison de méthodes statistiques de l'analyse de sensibilité et de métamodélisation est appliquée sur un modèle numérique de diffusion électromagnétique, afin de proposer une façon innovante de concevoir des campagnes radar des forêts. Cette méthode inclut l'organisation et l'analyse des données déjà obtenues pour extraire des informations sur la scène, puis leurs utilisations pour la conception du nouveau signal à émettre.

Études de zones forestières par radar et simulations

Le radar est considéré comme l'outil le plus approprié pour les observations de télédétection des zones forestières. Il peut « voir » à travers des conditions telles que la brume, le brouillard, la pluie et la neige et il n'y a pas de limitation sur l'endroit où il peut être situé : sur un avion, un satellite, un bateau, ou placé au sol. En particulier, après l'introduction du principe de radar à synthèse d'ouverture (SAR), qui a amélioré la résolution en azimut, des observations

plus détaillées comme celles nécessaires à la caractérisation de la végétation, étaient possibles. Concernant les interactions des ondes électromagnétiques radar avec les diffuseurs, il y a trois propriétés d'intérêt d'une onde : son intensité, sa phase et son état de polarisation. Ces propriétés ainsi que leurs variations sont directement liées à la dispersion caractéristique, c'est à dire la distance, la forme, la taille, l'orientation et la permittivité du ou des diffuseurs. Par conséquent, des informations sur ces caractéristiques peuvent être extraites à partir du signal radar reçu. La quantité principale décrivant la façon dont une cible radar ou une surface diffuse l'énergie électromagnétique est la matrice de diffusion. Dans notre travail, comme les forêts sont des milieux complexes et des cibles distribuées, nous avons également étudié les coefficients de rétrodiffusion dans toutes les polarisations et utilisé la décomposition de Pauli de la matrice de diffusion, pour extraire des informations supplémentaires sur les mécanismes de la diffusion. En particulier, en vertu de la convention de l'alignement « dans le sens de l'onde » sélectionnée pour notre modèle numérique, les trois composantes du vecteur de Pauli correspondent aux double rebonds, aux simple rebonds et aux interactions de volume.

Pour réaliser nos études de simulation, un modèle cohérent et descriptif de dispersion appliquée à l'étude électromagnétique de la rétrodiffusion de forêt appelée COSMO, a été utilisé. Cohérent car il calcule les réponses complexes fournissant alors des informations sur l'amplitude et la phase du signal reçu et descriptif, car il est basé sur la génération des arbres et de la forêt à partir d'un ensemble de paramètres géométriques et électromagnétiques bien identifié. COSMO fonctionne dans le domaine fréquentiel et fournit à la fois la matrice de diffusion et la signature de polarisation. Ses résultats sont largement validés aux bandes P et L pour les forêts tempérées (pins maritimes) que nous avons considérées. Pour nos expériences, les scènes de simulation générées étaient basées sur un modèle discret à deux couches, ne contenant que des troncs et des branches primaires. Les données utilisées pour estimer et prévoir les dimensions et les distributions des éléments forestiers ont été obtenus à partir d'équations allométriques. Le sol était supposé plan et les permittivités constantes dans chaque scène et dérivées de modèles empiriques largement validés. Les quantités que nous avons sélectionnées pour notre étude étaient les champs électriques reçus sous toutes les polarisations, les coefficients de rétrodiffusion et les composantes du vecteur de Pauli. Celles-ci ont ensuite été exploitées pour obtenir la signature de la forêt et de l'effet de chaque élément de la forêt.

Analyse de sensibilité de COSMO

Les méthodes statistiques de l'Analyse de Sensibilité (AS) pour les modèles numériques sont largement utilisés dans le domaine des plan d'expériences. Elles peuvent faciliter l'identification des facteurs qui affectent de manière significative le modèle en general et chacune de ses sorties et détecter les effets non linéaires possibles et les interactions entre les entrées. Les connaissances acquises à partir de l'AS peuvent être ensuite utilisées pour l'analyse du modèle. Dans les études radar des forêts des analyses de sensibilité empiriques sont parfois effectuées sur des données réelles. Néanmoins, comme ces analyses s'appuient sur un ensemble de données disponibles réduits elles sont loin d'être exhaustives et complètes. C'est pourquoi les méthodes statistiques de l'AS appliquées sur les modèles numériques peuvent compléter ces études et ouvrir la voie à une meilleure compréhension de la réponse radar de la forêt. Nous avons appliqué ces méthodes sur COSMO pour identifier les paramètres les plus importants, afin d'étudier et d'analyser les effets des paramètres dans une étape ultérieure. Ce fut la première fois, pour autant que nous sachions, qu'une telle technique mathématique a été appliquée aux études radar des forêts.

Notre étude de l'AS appliquée à COSMO aspire à fournir de nouvelles informations sur la dépendance des différentes sorties de COSMO aux facteurs d'entrée. Elle vise également à aider à la conception innovante des campagnes de radar grace à l'utilisation du principe du radar cognitif.

Une méthode qualitative de l'AS intitulée la méthode des Effets Élémentaires (EE) (ou la méthode de criblage de Morris), a été choisie. Elle permet de déterminer les entrées du modèle qui ont des effets considérés comme négligeables, ou linéaire et additif, ou non-linéaire et impliqués dans les interactions avec d'autres facteurs. Elle utilise seulement quelques simulations du modèle, calcule un certain nombre de ratios incrémentaux les EE, pour chaque variable d'entrée et étudie leurs distributions. Les informations sur les effets des entrées sont extraites des mesures statistiques de ces distributions, la moyenne des EE, leur écart-type et la moyenne de leurs valeurs absolues. Avec COSMO, nous avons examiné différents cas de forêts périodiques ou quasi-périodiques, ayant des troncs seuls ou des troncs et des branches. Dans cette étude un large domaine a été étudié pour chacun des paramètres d'entrée. En effectuant cette AS de COSMO, nous avons réussi à évaluer l'importance des principaux facteurs d'entrée par leurs effets sur plusieurs sorties différentes. La fréquence et l'angle d'incidence du signal émis ont été identifiés comme les paramètres les plus importants de COSMO en général, comme on le voit par exemple dans la Fig. 9 pour une forêt de troncs seulement. Ils sont suivis par l'âge de la forêt et la permittivité de la végétation, comme les caractéristiques les plus importantes de la forêt. Au contraire, la hauteur du radar, la température et les paramètres de synthèse de sol ont montré des effets négligeables et peuvent dans la plupart des expériences être fixés à des valeurs constantes afin d'alléger COSMO sans en affecter significativement ses performances. Le cas de la différence de phases où les paramètres de positionnement avaient une importance considérable, a été soulignée également. En outre, nous avons découvert le fait que l'angle peut parfois être le facteur le plus important du modèle, montrant un comportement fortement non linéaire et les interactions avec la fréquence la plupart du temps – en raison de l'effet de l'angle de Brewster peut-être. Ces nouvelles informations sur COSMO et les études radar des forêts apportées de l'AS, doivent être vérifiées. À cette fin des simulations de COSMO distinctes pour chaque facteur important ont été effectuées afin de confirmer leur importance et vérifier l'ampleur de l'effet sur la sortie.

L'analyse de la rétrodiffusion de la forêt avec COSMO

Un des objectifs de ce travail était d'organiser les données de simulation de radar, les analyser par rapport aux changements de la scène et ainsi extraire des informations complémentaires au cours des observations radar des forêts. Le but de l'analyse était de ne pas exploiter pleinement COSMO et aller profondément dans la physique de la dispersion de la forêt, mais plutôt de justifier et d'étudier les résultats de l'AS et d'identifier l'effet exact de chaque paramètre et chaque élément de la forêt. En disant cela, tout d'abord d'examiner l'influence sur la sortie des paramètres les plus importants (la fréquence, l'angle, l'âge et l'humidité de la végétation) les variations, les effets des branches, ainsi que celui de l'existence de la cible. Les analyses ont été effectuées à la fois dans le domaine fréquentiel et le domaine temporel –celui-ci pour la première fois dans les études de COSMO. L'interprétation physique des effets des paramètres a été évaluée, chaque fois que possible, en termes de mécanismes de la diffusion ou de géométrie de la scène. En outre, des configurations de radar appropriées pour une identification plus facile des effets découverts ont été proposés à partir des résultats d'analyse. La présente analyse devra être complétée en vérifiant l'applicabilité et l'utilité du métamodèle développé lors de la première étape, tout
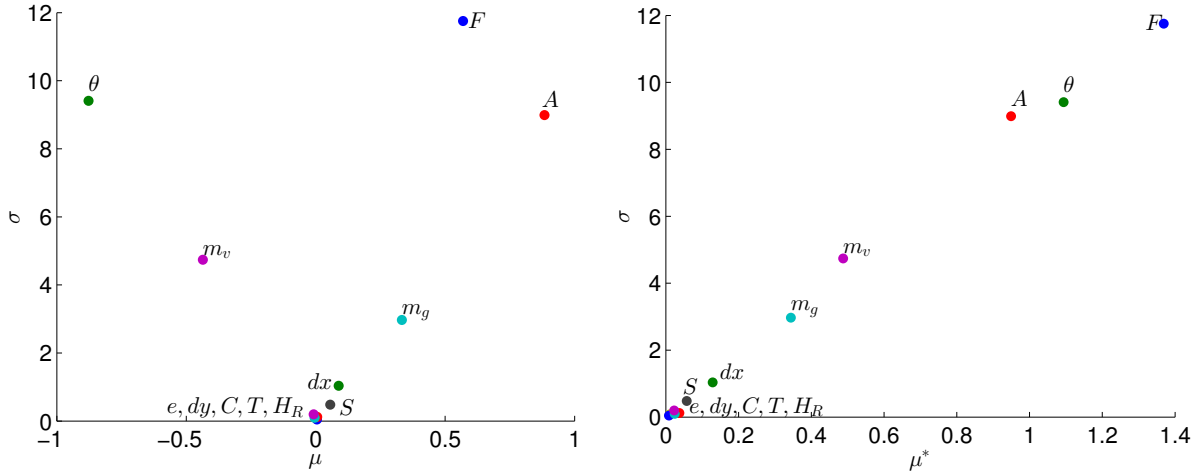
FIGURE *9 – Les résultats agrégés du criblage pour toutes les sorties normalisées examinées à l'ensemble de la bande de fréquence COSMO* [0.35, 2 GHz] *et les angles de 5° à 85° dans le plan $\mu\sigma$ (gauche) et dans le plan $\mu^*\sigma$ (droit). Une forêt périodique ne contenant que des troncs a été examinée. Des valeurs élevées pour μ et/ou μ^* montrent une importance globale élevée et pour σ montrent des effets non linéaires forts. La fréquence F et l'angle d'incidence θ sont les paramètres les plus importants du modèle, suivis par l'âge A et la permittivité m_v de la forêt.*

en utilisant les configurations proposées ici. L'utilisation du métamodèle devrait alors permettre de fournir une analyse en temps réel réalisable au cours de futures observations radar adaptatives.

Les analyses effectuées sur les résultats de COSMO concernent les coefficients de rétrodiffusion et les composantes du vecteur de Pauli dans le domaine fréquentiel et l'amplitude du signal reçu dans le domaine temporel. Dans le domaine fréquentiel, les effets de certains de ces quatre paramètres importants ont été identifiés. À savoir, la façon dont les quantités sont affectées par les changements des valeurs d'entrée et le comportement des mécanismes de diffusion distincts. En outre, la façon dont les branches, la cible et l'arrangement de la forêt réagissent sur tout le spectre de fréquences a été étudié. Fig. 10 par exemple, nous pouvons voir que les branches contribuent aux co-polarisations surtout pour les fréquences supérieures à 1 GHz et pour toutes les fréquences à la polarisation croisée. L'analyse du signal temporel a donné lieu à l'extraction d'informations supplémentaires sur la structure géométrique de la forêt. Comme on le voit par exemple Fig. 11, le nombre de pics du signal, la durée de l'impulsion et les distances entre pics correspondent respectivement au nombre de lignes d'arbres en portée, à la longueur de la scène et à la distance entre les lignes d'arbres. L'identification de certains effets qui peuvent être, sans aucun doute, attribuée à leurs sources correspondantes, nous a conduit à « définir » des couplages entre eux qui pourraient être utilisées par la suite dans la planification des campagnes de radar plus ciblées. Des fréquences ou des polarisations spécifiques pourraient être favorisées dans chaque observation, en fonction de l'effet à étudier. Dernier point, mais pas le moindre, l'effet de l'angle de Brewster dans les simulations COSMO a également été examinée. Les cas où il peut être important (identifiés par une grande différence entre la rétrodiffusion en HH et en VV) ont été mis en évidence.
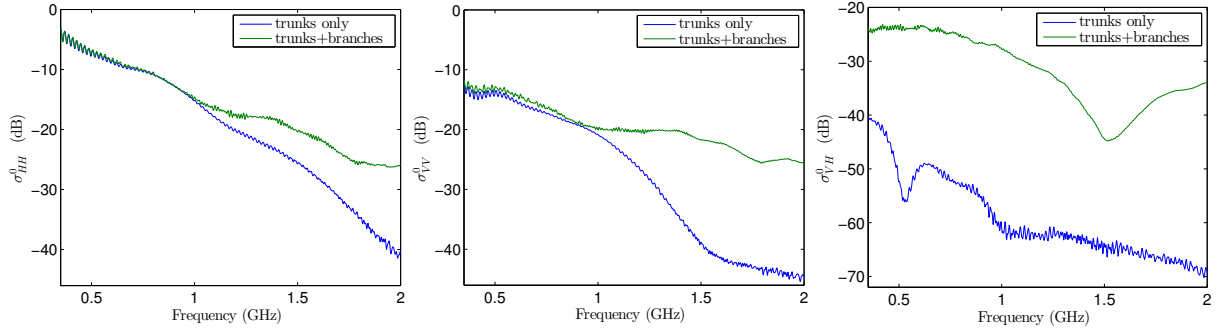
FIGURE 10 – *Les coefficients de rétrodiffusion du signal reçu en polarisation HH (à gauche), en VV (au milieu) et en VH (à droite) pour les cas d'une forêt avec des troncs seulement et les mêmes troncs avec des branches ajoutées. Les branches contribuent au signal copolaire après 1 GHz et en VH sur l'ensemble du spectre. L'angle d'incidence de l'onde émise était 40°.*
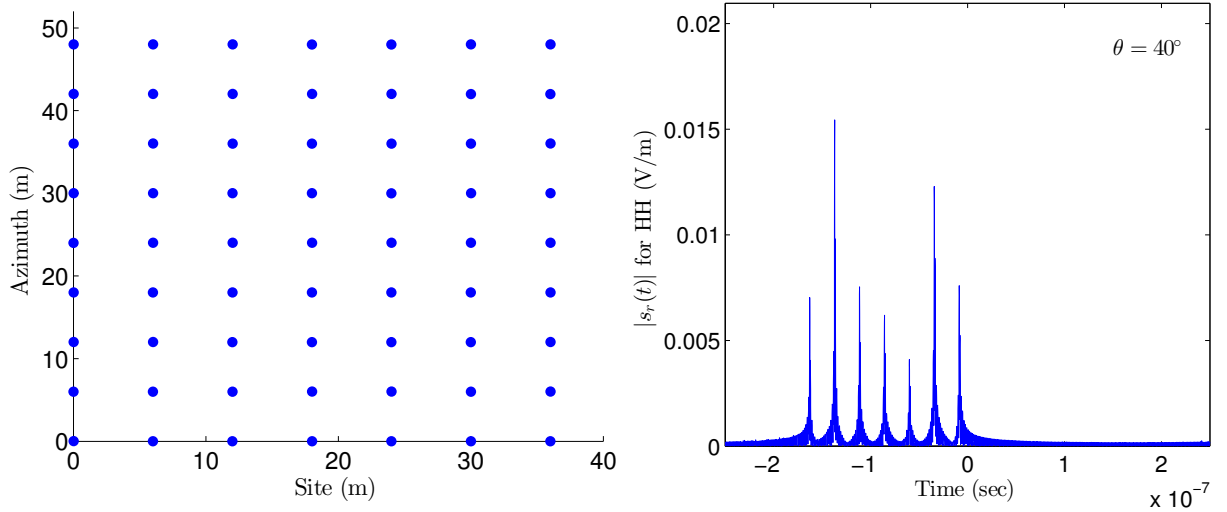

FIGURE 11 – *L'amplitude du signal temporel reçu d'une forêt périodique en HH a sept pics (à droite), correspondant aux lignes d'arbre de l'arrangement de la forêt en portée (à gauche). La longueur de l'ensemble de l'impulsion correspond à la taille de la scène et la distance entre les pics à la distance entre les lignes d'arbre.*

La modélisation de substitution et l'approximation de COSMO

La deuxième méthode statistique choisie pour nos études de simulation de radar est la Modélisation de Substitution (ou Métamodélisation). La méthode statistique de l'AS appliquée sur COSMO, a fourni des informations précieuses sur les importances des facteurs du modèle. Ces informations ont été vérifiées par la suite, afin de découvrir les effets des paramètres et des éléments forestiers, attribuer leurs interprétations physiques et de recommander les configurations optimales pour leur identification au cours des études radar. L'analyse rapide de données radar en temps réel est presque impossible, même en utilisant des codes numériques comme COSMO. En revanche l'utilisation d'un métamodèle qui peut nous aider à surpasser cette difficulté. Un tel modèle approché permet d'obtenir des résultats à un très faible coût de temps de calcul à partir de quelques résultats de simulation numérique exacte seulement. Par conséquent, il peut remplacer COSMO dans la conception d'une stratégie d'observation radar adaptative et temps réel des forêts De plus, le cadre de fonctionnement du métamodèle pourrait

servir dans la conception d'une stratégie adaptative innovante pour les futures observations radar.

Parmi les différentes techniques de métamodélisation, la méthode d'interpolation krigeage a été sélectionnée pour être appliquée à l'approximation de COSMO. Cette méthode, en dehors de la prédiction de valeurs réelles avec quelques points de simulation, fournit également une mesure de l'incertitude de la prédiction. Cette incertitude peut ensuite être utilisée pour construire des métamodèles adaptatifs plus efficaces. Dans nos études, un tel métamodèle est proposé, il est construit de manière manière séquentielle de façon à réduire l'incertitude de prédiction chaque fois qu'un nouveau point est ajouté aux échantillons d'entrée. En rapprochant COSMO, nous avons appliqué le métamodèle aux coefficients de rétrodiffusion et les composantes du vecteur de Pauli seulement. Le métamodèle a réussi à prédire, à partir de quelques simulations COSMO et avec une très faible incertitude, les sorties correspondantes aux cas étudiés lors de l'analyse du chapitre précédent Comme on le voit par exemple Fig. 12 et 13, les principales variations du coefficient de rétrodiffusion VV sont bien approximées et le point où le changement de mécanisme de diffusion dominant a lieu est détecté avec une bonne précision. Par conséquent, la possibilité de détecter les effets des paramètres importants et les éléments de la forêt sur les sorties a été vérifiée.
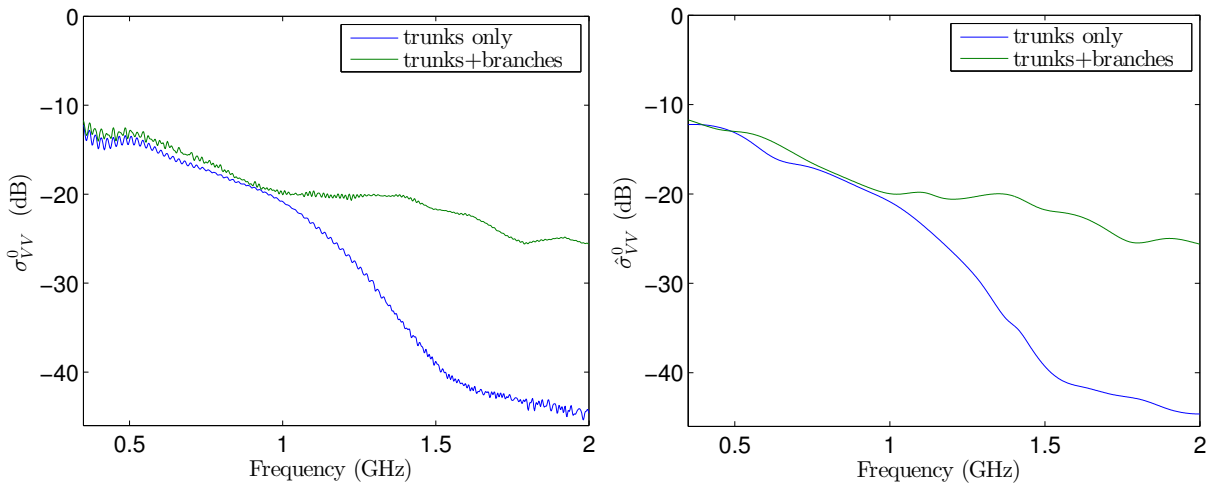

FIGURE 12 – *Les coefficients de rétrodiffusion en VV pour les deux arrangements forestiers ayant des troncs seulement et les troncs avec 10 branches chacune (à gauche) et leurs prévisions de krigeage basé sur 20 points de fréquence choisis d'une façon adaptative (à droite). Le métamodèle peut fournir une approximation satisfaisante montrant le comportement global des valeurs σ_{VV}^0 et l'effet des branches après $1\,\mathrm{GHz}$, en moins de $1/40$ du temps requis pour la simulation complète.*

Le principe du radar cognitif dans l'étude des forêts

Le radar cognitif est un type innovant de radar, envisagé par S. Haykin en 2006. Son principe essentiel est qu'un système radar doit ajuster le signal émis à son environnement. En disant cela, chaque nouveau signal à émettre dépendra des échos radar précédents et des résultats de leurs analyses. Jusqu'à présent, aucun système de ce genre n'a été réalisé, en raison de plusieurs limitations techniques. Dans notre travail, nous aspirions à intégrer le principe du radar cognitif dans une stratégie d'observation radar en utilisant COSMO comme simulateur, les deux méthodes statistiques appliquées et les connaissances acquises dans les chapitres précédents.
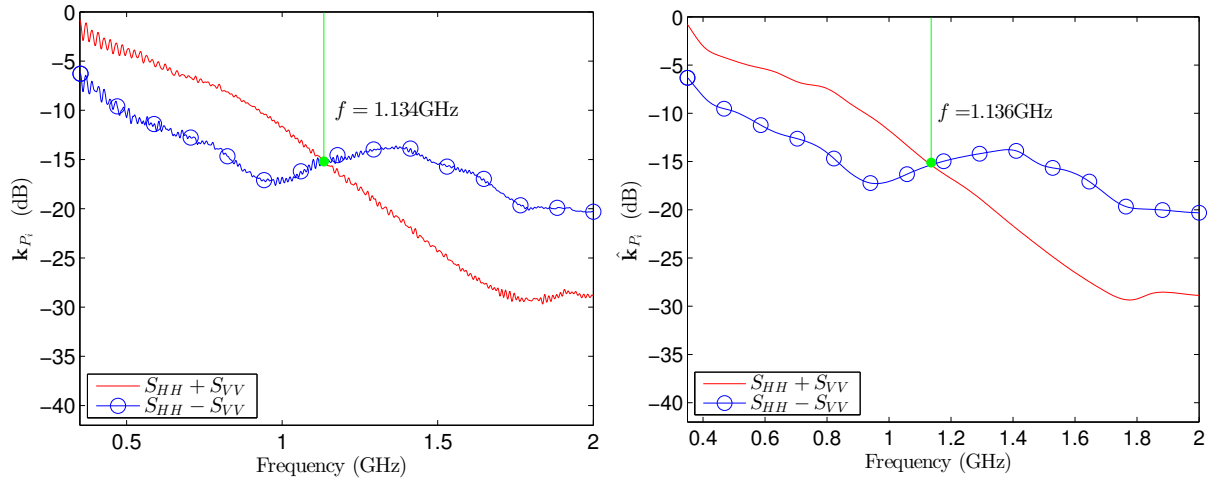
FIGURE *13 – Les rebonds simples et doubles, représentés par les deux premières valeurs de composants du vecteur de Pauli (à gauche) et leurs prévisions de krigeage basées sur 20 points de simulation choisis d'une façon adaptative (à droite). L'approximation de métamodèle fournit le comportement global des deux premières composantes du vecteur Pauli et également la fréquence à laquelle le mécanisme de diffusion dominant change du double rebonds au rebonds simples, avec une certaine mais petite erreur.*

L'analogie entre les principes généraux du métamodèle et ceux du radar cognitif nous ont amenés à adapter l'idée de radar cognitif sur le cadre de fonctionnement de métamodèle. Ce dernier a également contribué à l'accélération de l'analyse effectuée sur les réponses de radar, comme il a été prouvé par sa capacité à identifier rapidement une partie des effets caractéristiques de la scène. Les résultats du chapitre de l'analyse et les configurations radar proposées ont servi le traitement du signal reçu et l'extraction de l'information de la scène, avant de concevoir le nouveau signal à émettre. Le résultat a été une nouvelle stratégie adaptative-cognitive pour les études de simulation radar, ce qui pourrait permettre de définir le signal radar par rapport la scène étudiée en un très faible temps de calcul. La stratégie proposée pourrait préparer, espérons-le, le terrain pour réexaminer et améliorer la façon dont les observations radar sont réalisées aujourd'hui et conduire à la réalisation intégrée d'un radar cognitif.

L'organigramme général de notre stratégie proposée sur la base de simulations de COSMO, est présenté Fig. 14. Après l'observation initiale,la réponse de la forêt est rapidement approchée via le métamodèle, puis nous passons à l'étape d'analyse. Là, les objectifs intermédiaires de l'étude peuvent être définis en fonction des conclusions déjà extraites. Les configurations radar correspondantes sont alors sélectionnées et un nouveau signal est conçu et émis, afin de mettre à jour nos connaissances sur la scène. Une fois l'objectif atteint soit le processus stoppe soit les observations continuent jusqu'à ce que suffisamment de fréquences soient émises pour construire le signal en temps. La stratégie décrite ci-dessus a été appliquée avec succès à quatre exemples différents, correspondant aux effets de la forêt déjà étudiés dans le chapitre de l'analyse. Un exemple de l'application de cette stratégie est présenté Figs. 15 et 16. Dans la première figure, les prévisions initiales des coefficients de rétrodiffusion et les composantes du vecteur de Pauli sont présentées, ce qui indique l'existence de branches. En choisissant de manière adaptative des nouvelles fréquences à émettre dans l'intervalle $[0.8, 1.3\,\mathrm{GHz}]$, nous sommes arrivés à une prédiction finale pour les composantes du vecteur de Pauli qui a fourni la fréquence à laquelle le changement du mécanisme de diffusion dominant a eu lieu avec une précision de $99.82\,\%$. Le

temps nécessaire pour achever cette estimation adaptative était inférieure à 1/50 du temps de calcul nécessaire pour l'ensemble de l'estimation effectuée dans le chapitre de l'analyse.
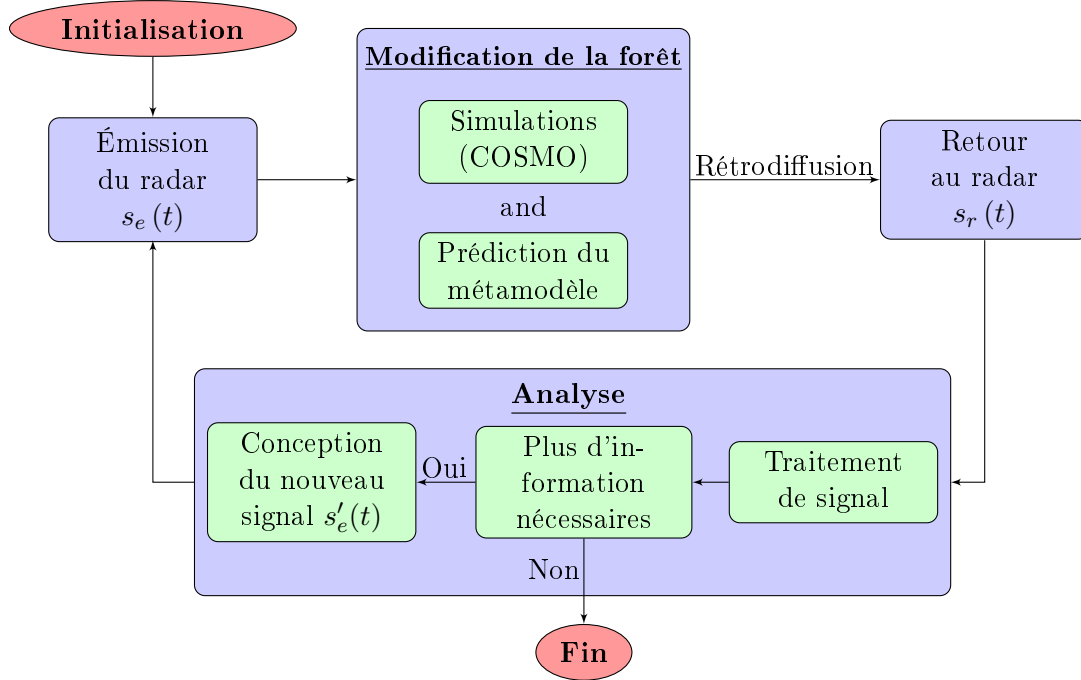

FIGURE 14 – *L'organigramme représentant une réalisation du radar cognitif, basé sur la boucle fermée du métamodèle.*
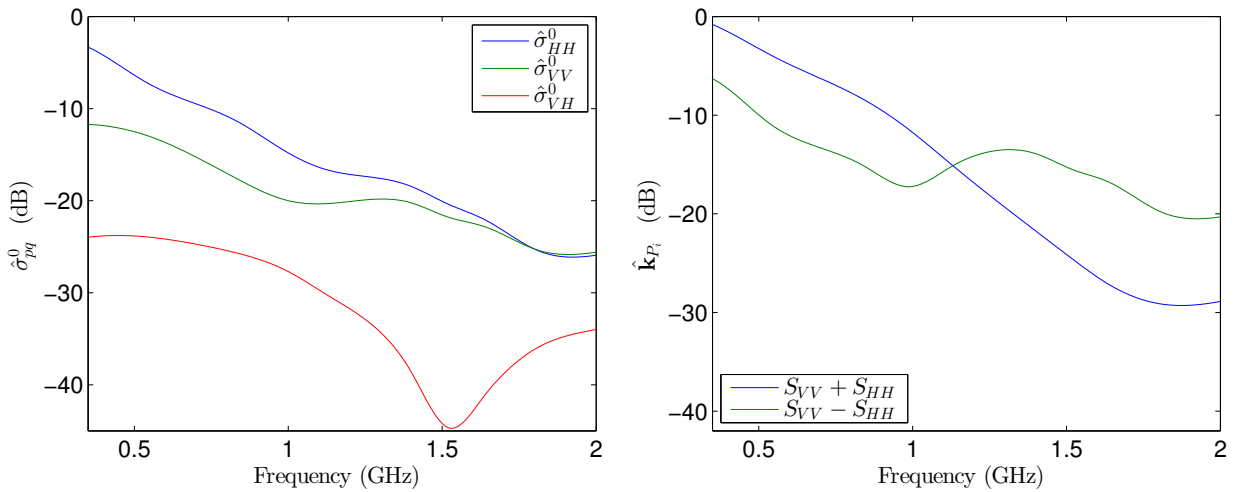

FIGURE 15 – *Les prédictions de métamodèle initiales pour les coefficients de rétrodiffusion (à gauche) et les deux premières composantes du vecteur de Pauli (à droite). Le changement du mécanisme de diffusion dominant observé dans le graphique de droite est un signe de l'existence de branches.*
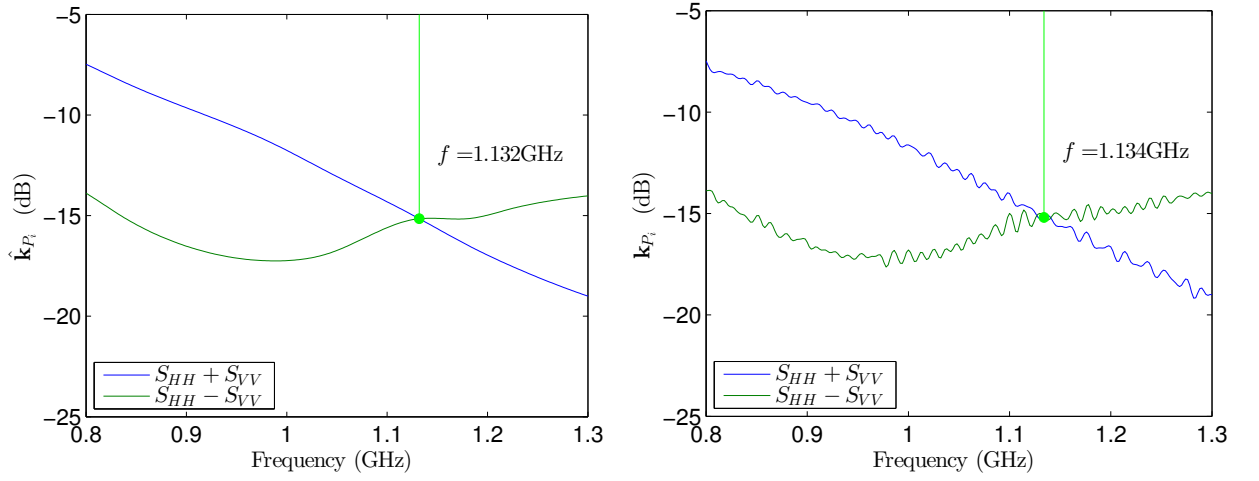
FIGURE 16 – *Les valeurs prévues pour les rebonds doubles et simples dans l'intervalle de fréquence* $0.8 - 1.3\,\mathrm{GHz}$ *(à gauche) et les valeurs réelles correspondantes (à droite). Le point où le changement du mécanisme dominant arrive est prédit avec une précision d'environ* $99.8\,\%$*, même si seulement 8 résultats de simulation ont été utilisés.*

List of Figures

List of Tables

Introduction

Timely and accurate measurements of forest structure are increasingly needed across large areas of scientific - and not only - interest. They can support a variety of activities either civil such as the estimation of the forest canopy height and the above ground biomass, or military such as the detection of targets in forest concealment. In particular, the biomass observation is a key parameter in forestry and ecology nowadays, as it can help quantifying the carbon emissions resulting from deforestation and land-use changes. However, ground-based forest inventories[1] - the most direct way to obtain information on forests - are limited in their spatial extent, expensive and difficult to perform. Fortunately, remote-sensing-based techniques for obtaining comprehensive measurements of forest structure, showed very promising performances at both regional and global scales. In addition, their temporal flexibility allows the planning and the accomplishment of several observations to examine the natural and human-induced changes, thus providing a more dynamic forest representation which was not feasible before. It is currently widely believed that remote sensing is the most practical tool for detailed studies of forested areas [Behan and Woodhouse, 1999].

Several types of remote sensing data, including aerial photography, radar and laser data have been used over forests to detect, identify, classify, evaluate and measure various forest cover types and their changes [Stellingwerf and Hussin, 1997]. The different remote sensing techniques can be used depending on the level of detail required and the extent of the area under study. As far as large areas are concerned for example, satellite imagery has been shown effective for forest classification and consequently mapping [Stellingwerf and Hussin, 1997]. Optical remote sensing was until recently the most commonly applied method. Its most recent implementation, the laser sensor system called Lidar (light detection and ranging), can even measure the tree height, and in some cases detect different types of vegetation, i.e. trees, grass, shrubs and herbacies plants and delineate them [Jakubowski et al., 2013]. However, optical remote sensing has some important limitations starting with the inability to penetrate clouds and rain. In addition, they can acquire only foliar biomass information [Ferrazzoli and Guerriero, 1995] and they are not always capable of differentiating between various forest cover types of interest [Stellingwerf and Hussin, 1997]. On the other hand, radar sensors are able to operate under any weather conditions, and their waves can penetrate into the lower forest layers, thus providing supplementary information.

Since 1990 and the comprehensive work of Ulaby and Elachi (see [Ulaby and Elachi, 1990]), radar remote sensing became from a promising tool for earth observation, a widely applied technique supporting international global campaigns like the upcoming BIOMASS mission (see

---

[1]Destructive measurements performed on location by forestry scientists. A detailed protocol for this type of measurements can be found in [Porté et al., 2000].

[Le Toan et al., 2011]). Due to their nature, electromagnetic waves can interact with elements having dimensions of the same magnitude as their wavelengths. In particular, when microwaves (frequencies from $300\,\mathrm{MHz}$ and higher) are emitted, the wavelegths $\lambda \leq 1\,\mathrm{m}$ are of the same order as the forest elements' dimensions. If low frequency is selected, i.e. less than $2\,\mathrm{GHz}$, the waves are able to penetrate within the forest and be scattered by large elements such as branches and trunks, which constitute the major part of the biomass [Le Toan et al., 1992]. If the radiations have a frequency over $2\,\mathrm{GHz}$, no penetration occurs and only the top part of the tree crowns plays a role in the scattering events. Therefore, radar remote sensing can facilitate a thorough investigation of a forest by examining all of its layers and in several cases it provides data showing good correlation with certain forest parameters [Le Toan et al., 1992]. The forest signature acquired during radar observations, can be subsequently used for both the military and civil applications desired: detection of targets concealed by forest, or forest biomass estimation. So, the interest of radar investigations to study the forest, is well established.

Nevertheless, the acquisition of the forest signature is quite a challenging task. Forests constistute complex media, including several different types of scatterers of various dimensions and orientations. This results in diverse contributions to the wave backscattering, depending on the radar configuration and the physical characteristics of the scatterers. Previous studies have shown that these contributions can result in a significant alteration of the emitted waveform, as roughly depicted in Fig. 1. The emitted signal $s_e(t)$ is highly perturbed by the forest, resulting in the transmitted signal $s_t(t)$. In a typical monostatic configuration in addition, the signal received by the radar will be altered a second time on its way back through the forest again. As a consequence, in order to characterize a forest, to identify its signature and to discover a hidden target within it, a thorough understanding of this modification is essential. However, since forest are complex media, there is rarely a one-to-one correspondence between their parameters and the data obtained by the radar [Bucci and Isernia, 1997]. For this reason, the radar observation campaigns have to be carefully designed and conducted.
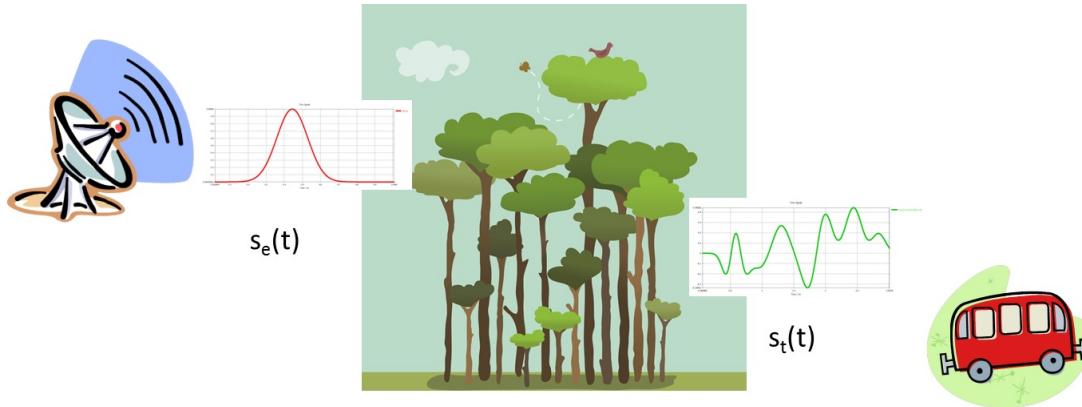
Figure 1 − A radar emits the signal $s_e(t)$ which the forest strongly modifies to $s_t(t)$, before it reaches the target. A thorough understanding of the forest modification is essential, to identify the waveform of the transmitted signal $s_t(t)$ and then extract information from its response.

Radar scientists, in order to deal with the complicated problem of identifying the forest modification of the signal and each element's behavior, perform several investigations of the same scene. These investigations are conducted under different radar configurations (frequency, angle

and polarization), at different times and often under unalike weather conditions. This leads to quite different datasets difficult to be analyzed and compared, as e.g. studies on the angle effect show (see [Mladenova et al., 2013]). In addition, there exist constraints which obstruct an optimal design of the radar forest campaigns. On the one hand, technical issues as the critical antenna size of the radar, the disturbing ionospheric effects, the unauthorized low frequencies for earth observation [Dechambre et al., 2003] and the extremely high cost of radar campaigns. On the other hand, forest radar observations almost never take into account the effect of the environment in real-time and in addition they provide a huge amount of data whose interpretation is rarely simple [Woodhouse, 2005]. Moreover, this interpretaton apart from difficult can be sometimes even misleading, as shown in [Brigui, 2010] regarding the construction of a SAR image. It is thus more than obvious that, in order to identify the way forests modify the incident electromagnetic waves before arriving back to the receiver or reaching a hidden target (see Fig. 1), more sophisticated and innovative strategies have to be developed. Strategies based on comprehensive studies of the different forest elements behavior, when illuminated by microwaves and which could take into account the information of the scene under study, acquired in real-time.

In the present dissertation, a sequential and adaptive way to study a forest using radar techniques to better characterize it, is proposed. This method is based on the use of COSMO, a numerical model for forest backscattering (see [Thirion et al., 2006]), and mathematical tools extensively employed in the Design of Experiments. The numerical model on the one hand, aims to substitute the real radar experiments, by providing simulation data for a multitude of scenarios - combinations of factor values - even for cases not observed in nature. The use of the mathematical tools on the other hand, intends to both assist in organizing and analyzing the vast amount of simulation data obtained and to accelarate and facilitate the model operation, via a surrogate model. Furthermore, the sequential design of the surrogate model could serve as a frame for incorporating the similarly operating cognitive radar principle, in our adaptive strategy. This principle addresses the idea that the waveform emitted from a radar at time $t + 1$ will be dependent on the radar returns at times $t, t - 1, \ldots$ and on the analysis that has been done on these returns [Haykin, 2006].

Since radar campaigns are usually designed without taking into account the effect of the environment under study, a certain waveform is generated and emitted corresponding to the technical requirements and a predefined objective. During the observation, several pulses are sent towards the scene, all of the same initial configuration. The response and the knowledge extracted from it are not involved in the emission procedure. What Haykin suggested, was to realize a radar which could be able to analyze the received signal and send the feedback to the transmitter. This idea has not been yet applied, to the best of our knowledge, to any radar studies. In this work, we combined the cognitive radar idea with the similar one of the sequential statistical procedures, i.e. the observations are analyzed before the next input combination is selected [Kleijnen, 2008], to design and attempt an elementary cognitive radar observation strategy. In doing so, we aspire both to open the ground for reconsidering the way radar observations are performed and to introduce mathematical tools which would organize these observations and facilitate the analysis of their results, while keeping the physics of the phenomenon.

This dissertation begins in Chapter 1 with the presentation of the state of art of forest radar measurements, in both real life experiments and in model simulations. The most common ways the forests are modeled and generated in simulation experiments are presented, together with the specifications for the ground characteristics and the dielectric constants of the elements. The chapter closes with the presentation of COSMO, the numerical model which will be employed in the simulations studies throughout this work.

Continuing in Chapter 2, the Sensitivity Analysis methods for assessing sensitivity to a model's input factors are reviewed. In particular, the qualitative Screening method which will be applied to our numerical model, is thoroughly analyzed and tested on an appropriate function. Next, the method is applied for a first time to COSMO, in order to examine the sensitivity of the outputs on most of the model numerical inputs, for certain scenarios. The most important model factors are thus identified and the knowledge obtained on the model, can be subsequently exploited and used in the upcoming chapters.

Sensitivity Analysis came up with some additional information concerning COSMO and the forest radar signature. So in Chapter 3, in order to verify these information, a detailed analysis is carried out on several forest scenes. The effects of the most important radar parameters and the various forest components on the outputs are examined, by trying different input combinations. In addition, their physical interpretation is provided, whenever possible, and configurations that could favor the investigation of each effect are proposed. During the aforementioned analyses, the Brewster angle effect on the backscattering appeared as a significant one and so it is examined separately at the end of this chapter.

Chapter 4 introduces the second statistical method to be used, Surrogate Modeling. Surrogate modeling is a way to construct models of other models, which are in a next step used to analyze, approximate and redesign the original models. The kriging method qualified for the treatment of our problem, is described in details and validated on the approximation of two toy functions. Then its applicability to the COSMO analysis conducted in Chapter 3, is examined. Where the metamodel can be used in substituting COSMO, to accelerate this analysis, and where it cannot. The last part of the chapter includes a discussion about the drawbacks of this prediction method and the limitations of its capabilities.

The main matter of this work closes in Chapter 5. This chapter addresses the attempt to integrate the cognitive radar principle in the design of an innovative sequential radar observation strategy. This attempt was achieved using the mathematical techniques and their results already introduced in the previous chapters. In particular, the surrogate model from which it borrows the operating frame and the analysis conclusions. The latter are used to identify and interpret the obtained information in real-time and to select the appropriate configuration for our purposes. Our sequential strategy is presented in details before being applied to four different examples, concerning different objectives of a forest investigation.

The last chapter of the dissertation is just concluding the main points treatised and provides a list of perspectives for future work. By reviewing the different steps of the project together, as a whole, the main ideas and the interconnections are highlighted. The constraints and deficiencies of our method are also mentioned, since they suggest - together with the intuition acquired on the subject - the list of the possible short and long-term perspectives.

1

Radar and simulation studies of forested areas

Contents

1.1 Introduction

The objective of this first chapter of the dissertation is not to go deeply into the way radar observation and simulation investigations are conducted, but rather to recall the key elements. So that an appropriate background is constructed, to better understand the rest of this work. For more details, the interested reader is invited to refer to the books from the general literature on radar systems, like [Skolnik, 1980] and [Peebles, 1998]. Radar polarimetry and its main tools are explained. Then, the most common ways forested areas can be modeled for microwave simulation practice, are reviewed. How to describe the vegetation and the ground and also how to evaluate the corresponding permittivities. Finally, our numerical model for the simulation studies of forest, COSMO, is described in details. In saying so, the way it generates the medium, the assumptions made and the way calculations of the forest backscattering are performed.

The chapter closes with the presentation of both unprocessed and processed simulation results, coming from a simple COSMO experiment.

1.2 Basics of radar remote sensing

Let us start by defining *Remote Sensing*, which "is the science and art of obtaining information about an object, area, or phenomenon through the analysis of data acquired by a device that is not in contact with the object, area, or phenomenon under investigation" [Lillesand et al., 2004]. It can be performed by using optical, radar or acoustic sensors - which make use of electromagnetic (EM) waves the first two and acoustic waves the latter - depending on the desired applications. For the investigation of forested areas, which is the subject of our work, optical and radar remote sensing are employed. In what follows, we are going to focus only on radar techniques which provide some key advantages explained below.

Radar technology, which was mainly introduced during the World War II for military target detection, is nowadays widely used in vegetation observations. The latter applications emerged in the last quarter of the 20th century and mostly because of the significant progress carried out in radar techniques. In particular, detailed land observations resulted from the development of the Synthetic Aperture Radar (SAR) technology and the polarimetric radars, which will be presented later on. These radar systems, when operating at low frequencies from $350 - 2000\,\text{MHz}$, represent a promising tool for earth observation [Ulaby and Elachi, 1990]. Nevertheless, despite the big steps forward already accomplished in the field, there are still problems to be solved as the critical antenna size of the radar, the disturbing ionospheric effects and also the unauthorized low frequencies for earth observation [Dechambre et al., 2003]. In addition, SAR instruments are particularly heavy, power consuming and data prolific and also, as we will see later on, the interpretation of their data is rarely simple [Woodhouse, 2005].

The term *Radar*, which stands for Radio Detection And Ranging, refers to an electronic device employed for the detection and location of objects usually called *targets*. This device is designed to receive and analyze EM waves reflected from these potential targets, in order to determine their existence and exact position (range). A radar can act as an active system, which means that it does not require any external illumination and it can be engineered to "see" through conditions impervious to optical sensors, such as darkness, haze, fog, rain and snow. In addition, there is almost no limitation on where it can be located, as it can be mounted on an airplane, a satellite, a ship and of course placed on the ground. Last but not least, is the fact that it can monitor repeatedly large areas over a period of time, giving better resolutions than the optical instruments. Radar seems therefore to be the most appropriate tool for remote sensing applications, to study the responses of objects of interest and acquire information on their characteristics.

There exist various types of radars with respect to their characteristics, but two main classifications stand for all of them. The first distinguishes the *active* radars which radiate their own signal to be reflected on the target, from the *passive* ones which act only as receivers of reflected waves. The second classification concerns the positioning of the transmitting and receiving antennas. If the same antenna is occupied for both transmission and reception the radar is called *monostatic*, while it is called *bistatic* if two distinct antennas are needed, one for
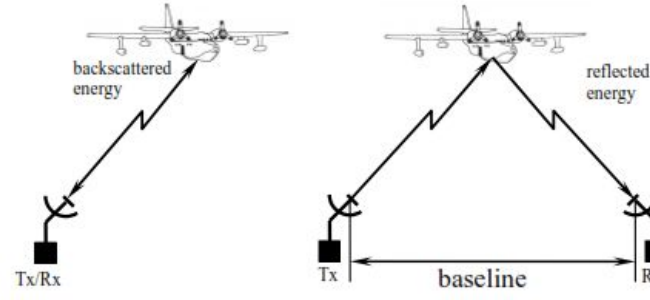
Figure 1.1 − A monostatic radar, where just one antenna is used for both transmitting (Tx) and receiving (Rx) (left) and a bistatic radar with two distinct antennas (right).

the transmission and the other for the reception of the EM waves (see Fig. 1.1). From now on, we suppose that the radar under consideration is an active and monostatic one, emitting in the P and L low frequency bands (see Table 1.1). The frequencies of these bands, as already mentioned in the Introduction of the dissertation, are widely employed in radar forest observations.

Radar band	Frequency (GHz)	Wavelength in free space (cm)
P-band[2]	0.3 - 1	100 - 30
L-band	1 - 2	30 - 15
S-band	2 - 4	15 - 7.5
C-band	4 - 8	7.5 - 3.8
X-band	8 - 12	3.8 - 2.5
Ku-band	12 - 18	2.5 - 1.7
K-band	18 - 27	1.7 - 1.1
Ka-band	27 - 40	1.1 - 0.75
V-band	40 - 75	0.75 - 0.4
W-band	75 - 110	0.4 - 0.27
mm-band	110 - 300	0.27 - 0.1

Table 1.1 − The standard Frequency Letter-Band Nomenclature for EM radiation, used for radar applications.

1.2.1   The SAR principle

The radar platform moves along the azimuth direction, with the antenna generally focused on a direction orthogonal to the azimuth: range (or slant-range). If the direction of observation is along the platform nadir (i.e. straight below the platform), the system is defined as boresight. On the other hand, when the direction is inclined with an angle θ (θ is called look angle) from the zenith, as seen in Fig. 1.2, it is defined as side-looking (for airborne radars it is called side looking airborne radar or SLAR). A side-looking solution is conventionally to be preferred to

---

[2]This band is known as the Ultra High Frequency (UHF) band in the IEEE standard letter designation. The letter P stands for *Previous*, since early British radars were using this band.

boresight, for the rejection of range ambiguities. The first simple radar systems were called Real Aperture Radars (RAR) and they were usually sending a pulse of a temporal length τ and a frequency bandwidth BW. A major disadvantage of these radars, was the poor resolution in both the range and azimuth directions. In this basic arrangement, the resolution in range δ_r is proportional to the length of the pulse or inversely proportional to the bandwidth:

$$\delta_r = \frac{c\tau}{2} = \frac{c}{2BW} \tag{1.1}$$

where c is the speed of light in vacuum. Two scatterers can be separated if their distance is bigger than half the duration of the pulse, otherwise the two pulses will overlap each other. In order to achieve a better range resolution and distinguish nearby targets, the bandwidth must increase, leading to very short effective pulses. This problem was solved with the introduction of a frequency modulation which increases the bandwidth, resulting thus in a higher resolution, without decreasing the pulse duration. The pulse obtained like this is called a *chirp* [Curlander and McDonough, 1991].
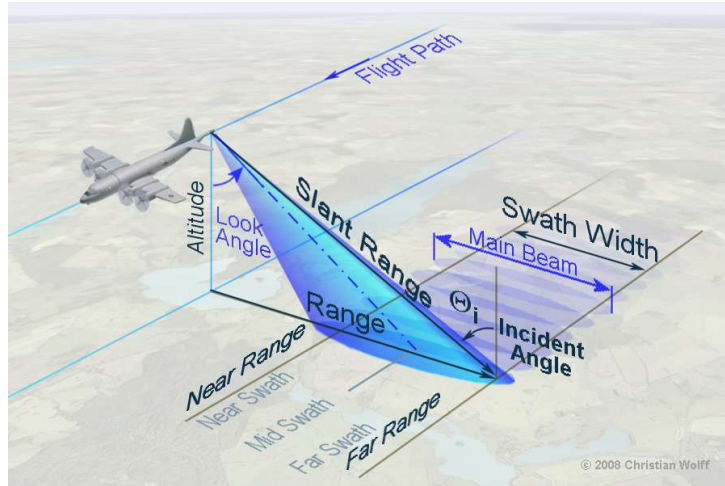
Figure 1.2 – The geometry concerning the SLAR radar observations. Image taken from: http://www.radartutorial.eu/20.airborne/ab06.en.html

Concerning the azimuth resolution now, all the points illuminated by the beam-width are collected together, hence they are inseparable. So the azimuth resolution δ_a is dependent on the beam-width (or aperture) d_a of the antenna:

$$\delta_a = \frac{\lambda}{d_a} \cdot r \tag{1.2}$$

where λ is the wavelength and r the range. When these radars are mounted to airborne or spaceborne platforms, with a range varying from a few kilometers up to $500\,\text{km}$, they show very poor azimuth resolution, as the antenna size also cannot exceed a few meters. It was the introduction of the *Synthetic Aperture Radar* (SAR) principle that improved the azimuth resolution [Skolnik, 1980], allowing more detailed observations like the ones necessary for the vegetation investigation. The basic idea of SAR is that a point on the ground is illuminated by the antenna not just with one single pulse, but with a sequence of pulses (see Fig. 1.3). If all the acquisitions for the same point are collected, it will be similar to having performed a

single acquisition with an antenna array with length equal to the whole footprint. Thus, the azimuth resolution becomes invariant under the range changes and proportional to the antenna length $\delta_a = d_a/2$. Conversely to (1.2), the resolution improves when the effective dimension of the antenna is reduced. This seems to contradict common sense, since a smaller antenna has a larger beam width (hence a larger footprint). In actual fact, when the aperture decreases, the footprint increases and with it the synthetic length of the antenna (see Fig. 1.3). As a consequence, the array becomes larger and the final beam-width sharper.
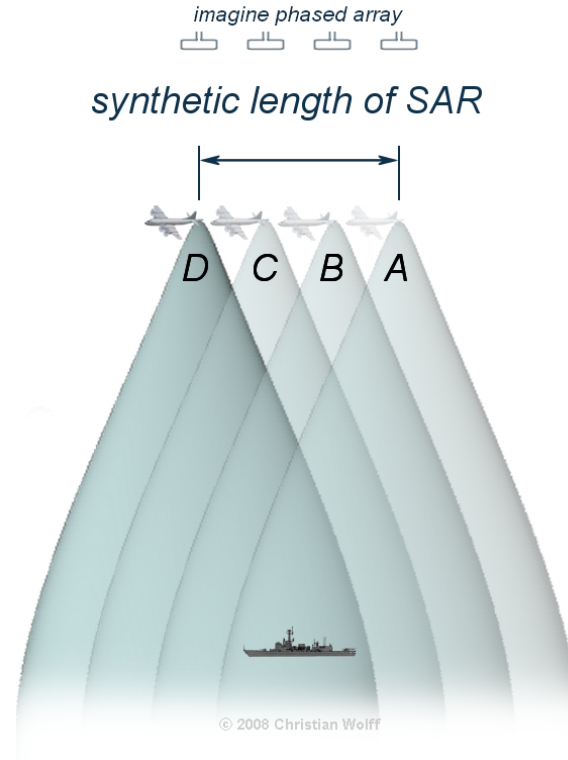
Figure 1.3 − The SAR principle: the radar emits a sequence of pulses to illuminate the scene and combine these acquisitions to reconstruct the signal, which would have been obtained by a several times longer antenna. The SAR works similarly to a phased array, but instead of the several antenna elements of a phased array, SAR uses only one antenna in time-multiplex. The different geometric positions of the antenna elements are resulting from the move of the platform where the antenna is mounted. Image taken from: http://www.radartutorial.eu/20.airborne/pic/sar_principle.print.png

1.2.2   Polarimetric SAR radars

Apart from the intensity and the phase of the emitted field, the alignment of the electric field in the perpendicular plane to the propagation direction, the so-called polarization state of the wave, can be changed also during the interactions with the scatterers. In the forest case the types of interactions are the scattering through the forest and the reflection on the ground. The polarization information thus contained in the backscattered wave, is directly related to the scatterer's geometrical structure i.e. shape, size orientation and to the geophysical properties like the dielectric constant. These information can be valuable in estimating the forest ecological characteristic and also in detecting potential man-made hidden targets, due to the contrast

between the forest and the target scattering. However, as already mentioned, the link between the measured polarimetric data and their interpretation is not obvious, because it depends on the tree species, structure, acquisition configuration, etc. As the structure information is very important, any additional information can be useful to learn the characteristics of clutter, and the foliage scattering that affects the signal propagation. For this to be accomplished, numerous observations under different conditions, concerning both the radar configuration (e.g. different angles) and the forest parameters (e.g. with or without branches, different humidity values) are necessary. Nevertheless, till nowadays radar technology does not support these requirements, either because of the cost of radar campaigns or because of technical limitations. And it is exactly this gap that numerical models can fill and help as extending our knowledge on forests.

Despite the fact that the frequency modulation and the SAR principle solved the problem of the poor resolution of primary radars, reliable vegetation observations could not have been possible before the appearance of the polarimetric radars. Traditional radars were transmitting and receiving signals with the same polarization[3] states i.e. the same alignments of the electric field in the perpendicular plane to the direction of the wave propagation. The main disadvantage of this kind of radars is that they cannot facilitate the determination of the complete vector nature of the scattered signal. If the scattered signal is depolarized because of multiple or anisotropic scattering, there is a loss of information regarding the target. In certain cases when the two polarizations states are orthogonal, the target can even be completely missed by the radar. On the other hand, polarimetric radars can transmit and receive signals with two orthogonal polarization states. Thus, it offers the possibility to determine and/or distinguish different types of targets, as for instance different structures in an environment (vegetation, constructions, etc). The most common polarization basis consists of the horizontal linear (H) and the vertical linear (V) polarizations depicted in Fig. 1.4. Orthogonal circular polarizations are also in use e.g. in weather radars, but we are only interested in linear ones. Whatever polarization a signal has, it can be decomposed into two different signals using the polarization states of the selected basis.

The polarization state of these incident electromagnetic waves can be changed as they pass through the medium between the radar and the target, as well as when they strike the target. This may cause the scattered waves to have completely different polarization state than that of the incident ones. Then a polarimetric radar can measure four different signals, the co-polarized HH and VV and the cross-polarized HV and VH, where the first letter refers to the polarization of the received wave and the second to that of the transmitted one. Note that there are single polarized radars, capable to treat just one of the above-mentioned signals each time, dual polarized that can treat two of them and fully polarized radars that can deal with all these four signals. The latter ones are the most useful as the measurement of all co-polarized and cross polarized signals facilitates the complete characterization of the scatterer, since any change in the polarization state depends upon the characteristic features of the scene under study. A radar receiving and processing the scattered waves can determine object features such as the size, the shape and the dielectric properties, by comparing the properties of the received waves with these of the emitted ones[4]. The primary description of how a radar target or surface feature scatters EM energy is given by the *scattering matrix*, which in full polarimetry takes the form:

---

[3]Polarization is a property of transverse waves and it describes in which way the oscillations are taking place. For EM waves in particular, it traces the path of the tip of the electric field vector.

[4]This is the object of the so-called *Radar Polarimetry*.
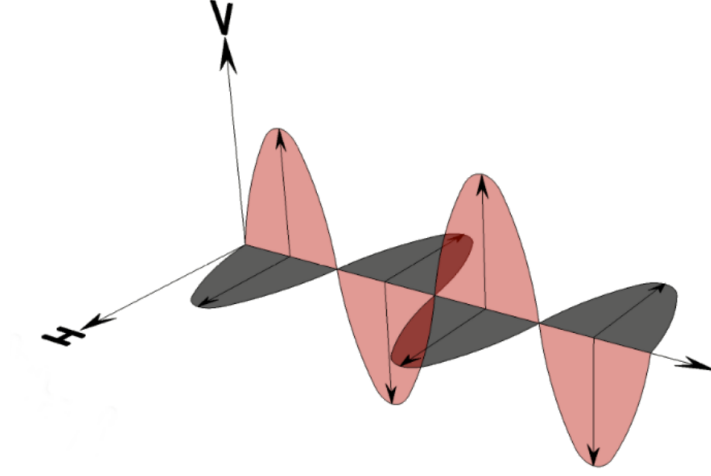
Figure 1.4 − The oscillation of the electric field vector in horizontal linear and vertical linear polarizations. These two polarizations form a basis and thus, all possible signal polarizations can be expressed by these two.

$$[\boldsymbol{S}] = \begin{pmatrix} S_{HH} & S_{HV} \\ S_{VH} & S_{VV} \end{pmatrix} \tag{1.3}$$

The elements of $[\boldsymbol{S}]$ are the four complex amplitudes $S_{pq} = |S_{pq}|e^{i\phi_{pq}}$. Apart from these amplitudes, the relative phases $\phi_{pq} - \phi_{mn}$ are also of interest in polarimetry. The scattering matrix describes the transformation of the two-dimensional incident plane wave vector $\mathbf{E}^i$ into the scattered one $\mathbf{E}^s$, performed by the scatterer and in the far field approximation is given by the equation:

$$\mathbf{E}^s = \frac{e^{-ik_0 r}}{r} [\boldsymbol{S}] \, \mathbf{E}^i \Leftrightarrow \begin{pmatrix} E_v^s \\ E_h^s \end{pmatrix} = \frac{e^{-ik_0 r}}{r} \begin{pmatrix} S_{HH} & S_{HV} \\ S_{VH} & S_{VV} \end{pmatrix} \begin{pmatrix} E_v^i \\ E_h^i \end{pmatrix} \tag{1.4}$$

where r is the distance between the target and the radar (range) and $k_0 = 2\pi/\lambda$ the wavenumber of the incident wave. For $[\boldsymbol{S}]$ to be measured, the radar has to transmit in both H and V polarizations and also receive in both of them (fully polarimetric systems are needed)[5]. Having measured this matrix, the strength and polarization of the scattered wave for an arbitrary polarization of the incident wave can be reconstructed as a linear combination of the elements of $[\boldsymbol{S}]$. In the monostatic case which is preassumed, the reciprocity stands in most conditions encountered in Earth observations and $S_{VH} = S_{HV}$, so the scattering matrix in (1.3) becomes complex symmetric and there are only three components of interest for the measurements, which can be represented by the *target vector*:

$$\mathbf{k} = \begin{pmatrix} S_{HH} \\ S_{VH} \\ S_{VV} \end{pmatrix} \tag{1.5}$$

---

[5]The circular polarization can be used instead, since the scattering matrix is independent of the basis used for its derivation.

For a more accurate estimate, it is often assumed that $S_{VH} = 1/2\,(S_{VH} + S_{HV})$, to reduce the effect of the noise. The three quantities of the target vector provide in addition the total power backscattered by the target, which in the case of a polarimetric radar it is called *Span* and is given by:

$$Span = |S_{HH}|^2 + |S_{VV}|^2 + 2|S_{VH}|^2 \tag{1.6}$$

If only the energy scattered from the target at range r and arriving to the radar is considered, the *Radar Cross Section (RCS)* is calculated, which for a point target is given by:

$$\sigma_{pq} = \lim_{r \to \infty} 4\pi r^2 \frac{|\mathbf{E}_p^s|^2}{|\mathbf{E}_q^i|^2} \tag{1.7}$$

The RCS characterises the backscattering property of the illuminated target and it depends on its size, shape and orientation as well as on the wavelength and the polarization of the incident signal. For the case of a distributed target, the *(normalized) backscattering coefficient* σ_{pq}^0 is calculated instead, which is actually the RCS normalized by the area A of the target:

$$\sigma_{pq}^0 = \lim_{r \to \infty} \frac{4\pi r^2}{A} \frac{|\mathbf{E}_p^s|^2}{|\mathbf{E}_q^i|^2} \tag{1.8}$$

The target vector is more convenient to use in place of the scattering matrix in the monostatic cases, but it is not always the most efficient way to deal with the polarimetric data. For example, if a point-like scatterer is observed, $[\mathbf{S}]$ can fully describe it, but in cases of distributed scatterers (as forests) it fails. In these cases, decomposition techniques are employed in order to express the scattering matrix as a combination of the scattering responses of simpler objects. That way, additional physical information of the target can be extracted from the radar measurements. A commonly used decomposition method, is the so-called *Pauli decomposition*. It uses the Pauli basis $\{[\sigma_0], [\sigma_1], [\sigma_2], [\sigma_3]\}$ given by the four following 2×2 matrices [Lee and Pottier, 2009]:

$$[\sigma_0] \equiv I_2 = \frac{1}{\sqrt{2}} \begin{pmatrix} 1 & 0 \\ 0 & 1 \end{pmatrix}, \ [\sigma_1] = \frac{1}{\sqrt{2}} \begin{pmatrix} 1 & 0 \\ 0 & -1 \end{pmatrix}, \ [\sigma_2] = \frac{1}{\sqrt{2}} \begin{pmatrix} 0 & 1 \\ 1 & 0 \end{pmatrix}, \ [\sigma_3] = \frac{1}{\sqrt{2}} \begin{pmatrix} 0 & -i \\ i & 0 \end{pmatrix} \tag{1.9}$$

If the reciprocity is assumed, this basis can be reduced to the form $\{[\sigma_0], [\sigma_1], [\sigma_2]\}$ and $[\mathbf{S}]$ can be written as:

$$[\mathbf{S}] = \begin{pmatrix} S_{HH} & S_{HV} \\ S_{VH} & S_{VV} \end{pmatrix} = a[\sigma_0] + b[\sigma_1] + c[\sigma_2] \tag{1.10}$$

where a, b, c are:

$$a = \frac{S_{HH} + S_{VV}}{\sqrt{2}}, \quad b = \frac{S_{HH} - S_{VV}}{\sqrt{2}}, \quad c = \frac{2S_{VH}}{\sqrt{2}} = \sqrt{2}S_{VH} \tag{1.11}$$

After the Pauli decomposition, the three quantities of interest given in (1.11), can be presented in a vector form which is called the *Pauli feature vector*:

$$\mathbf{k}_P = \frac{1}{\sqrt{2}} \begin{pmatrix} S_{HH} + S_{VV} \\ S_{HH} - S_{VV} \\ 2S_{VH} \end{pmatrix} \tag{1.12}$$

The components of this vector have a physical interpretation as they are linked to the different scattering mechanisms of the wave scattering. If the Forward Scattering Alignment (FSA) convention is assumed, which claims that the z-axis of the coordinate system describing the wave

propagation is always defined by the direction of the wave propagation[6], the first element of the Pauli vector corresponds to the "even" bounce backscattering. An example of such a scattering is the one from a dihedral corner reflector. In our case, $S_{HH} + S_{VV}$ will correspond to the double bounces mechanism. The second component refers to the "odd" bounce scattering, like scattering from a plane surface or a trihedral corner reflector and in our case it stands for the single bounces mechanism. The last Pauli vector element corresponds to the so-called volume scattering, scattering caused by the break of the symmetry. For more information on the physical interpetation of the Pauli vector, the interested reader can refer to [Papathanassiou, 1999] or [Lee and Pottier, 2009].

All the abovementioned expressions refer to the fully polarimetric operational mode. Nevertheless, to simplify the technology demanded and reduce the data volume, dual polarimetry is often prefered in practice. The dual polarimetric systems operate in $HH - VV$, $HH - HV$ or $HV - VV$ modes. In these cases, the scattering matrix and the Pauli vector given in Eq. 1.3 and 1.12 are taking a reduced form. For instance, if $HH - VV$ is employed which can be an alternative to fully polarimetric SAR (see [Ji and Wu, 2015]), we have:

$$[\boldsymbol{S}] = \begin{pmatrix} S_{HH} & 0 \\ 0 & S_{VV} \end{pmatrix}, \quad \mathbf{k}_P = \frac{1}{\sqrt{2}} \begin{pmatrix} S_{HH} + S_{VV} \\ S_{HH} - S_{VV} \end{pmatrix}$$

For both full and dual polarimetry, other polarimetric and interferometric tools and decomposition techniques exist also, such as for example the *Coherency Matrix* and the *H-a decomposition*. These methods are commonly used depending on the purpose of the study, but they are beyond the scope of this dissertation. More information on radar polarimetry can be found in [Cloude, 2009] and [Lee and Pottier, 2009].

1.3 A review of forest modeling for microwave studies

As presented in the previous section, radar forest investigations constitute a well established domain, with a variety of tools designed with respect to the objectives. However, radar campaigns have the disadvantage of being very costly and in addition it is almost impossible to be performed under the same conditions. This is the reason why the explosive growth of the computer technology during the last 20-30 years, resulted in a trend of substituting in several cases the real radar experiments with simulated ones. The latter are based on a model representation of the physical phenomenon with its existing factors and mechanisms. In the case of simulations of the land and vegetation backscattering, the mathematical formulation of the wave propagation and scattering and a detailed representation of the scene are necessary. In particular, when forests are considered, since they constitute very complex media consisting of various types of elements such as trunks, branches, needles and leaves, a detailed description of their constituents concerning the positions and geometric characteristics is imperative. These parts are of different orders of magnitude and orientations and so they contribute differently to the overall tree emissivity and wave extinction. Therefore, a radar simulation model has to take into account these structural characteristics, while respecting the ground truth data and the necessity for a reasonable computational load. There are still no generic and optimal ways to model a microwave forest

---

[6]For more information on the FSA and BSA conventions and how to go from one convention to the other see [Ulaby and Elachi, 1990] or [Lee and Pottier, 2009]

investigation. Different types of microwave models exist that are currently employed with respect to the objective and the real data available. They are differentiated in the way the forests are generated and the ground and dielectric constants are described. The most important and commonly used models among them, will be presented in the following paragraphs.

1.3.1 The discrete models

The most common models used to generate a forest for simulation studies in the microwave region are the so-called *discrete models*. The overall philosophy of these models is to provide a tool to simulate the electromagnetic interactions (emission, attenuation, scattering, etc.) occurring in the soil-vegetation system, through a detailed representation of the system elements. These interactions are modeled depending on the geometric and dielectric properties of the soil and the canopy constituents [Saleh et al., 2005].

Multilayer models

There are various types of discrete models with the most widespread to be the *multilayer model*. In this model, the forest is described as a superposition of continuous layers embedded with scatterers, which are subsequently represented by canonical geometric shapes[7]. Finite length dielectric cylinders are used for trunks, branches, twigs and needles, and elliptical disks or ellipsoids for the leaves. With this representation, both the canopy emission (passive case), and the backscatter (active case) can be covered. Following, the geometric properties of the scatterers are estimated from *allometric equations*, which provide the forest geometric description (FGD). These equations are relationships derived from forestry scientists using ground truth data[8] and they are commonly used to estimate and predict the amounts and the distributions of foliage or crown wood in trees ([Porté et al., 2000]). The crowns of the trees can also be described through simplified geometrical shapes such as spherical, ellipsoidal, or conical, depending on the tree species [Castel et al., 2001]. If coherent backscattering models (which provide estimates for both the amplitude and the phase) are considered, the orientation and the density of the various components have to be incorporated in the model - which is generally difficult to accomplish. Although the discrete approach is a very simplified description of the actual structure of the forest canopy, a good agreement has been obtained between simulations and remote sensing observations, especially when considering low frequency radiation, which penetrates the canopy and interacts with the big tree elements [Woodhouse, 2005]. It is also, due to its simplicity and flexibility, the most widely validated method (see for instance [Ferrazzoli et al., 2002] and [Thirion et al., 2006]). On the other hand, the main disadvantages of this method are the rough description of the canopy and the poor portability of most classical forest characterizations. Every new model requires its own adapted *in situ* measurements.

Vectorization and fractal based models

Two more recent approaches in discrete forest modeling, in order to reduce the effort required in collecting and analysing the real forest data, is the use of vectorization and the mathematical

---

[7]The representation of the forest parts by canonical shapes is adopted because the analytical computation of their electromagnetic backscatter is possible.

[8]The ground truth data are obtained during destructive sampling measurements performed on location by forestry scientists. A detailed protocol for this type of measurements can be found in [Porté et al., 2000].

fractal models. The vectorization method is a fine 3-D-tree architecture reconstruction. The goal of the method is to reconstruct a statistically accurate 3-D representation of canopy components, by means of judicious subsampling [Fournier et al., 1997]. Rather detailed ground measurements, concerning the dimensions and the spatial organization of trunks, different types of branches and leaves, are necessary. Then, the reconstruction of the trunks and primary branches (branches inserted directly to the trunk) takes place by incorporating these data and simulating data corresponding to the nonsampled segments, using some self-similarity principles. The new branches are simulated as a scaled replicate of the primary ones of the same trunk section, thus resulting in a final 3-D modeled distribution of the basic components. An example of using this method for constructing jack pine trees can be found in [Fournier et al., 1997].

The mathematical models on the other hand, are used in the computer graphics domain, where algorithms based on fractals and Lindenmayer systems (L-systems) already exist (see [Prusinkiewicz and Lindenmayer, 1990]). In these techniques, trees are viewed as recursive structures, where the development begins with a single stem that carries later buds, which in turns give rise to new branches. When the generation of the fractal tree is completed, the tree geometry is modeled using generalized cylinders, as seen in Fig. 1.5. If needed, organs such as leaves, flowers and small branches can be added to the tree. These methods have the ability to generate a wide variety of trees and shrubs [Runions et al., 2007]. For example, Lin and Sarabandi in [Lin and Sarabandi, 1999] applied L-systems with data from ground truth measurements incorporated in their model, to generate a forest of maple trees with branching structure. They treated the trees as clusters of scatterers composed of canonical shapes (cylinders and disks), in order to feed their coherent scattering model. These approaches are promising and interesting from an algorithmic as well as a graphic point of view. However, the disadvantage of these methods is their lack of physics as well as their low current outspread and thus their limited domain of validity, since there are not many studies using these models and compared with real data.

Architectural plant models (AMAP)

Another category of discrete forest models are the architectural plant models (AMAP[9]). These models were introduced to cover the limitations of the previous ones, which are either restricted to a single species and age, or are unable to describe the tree taking into account its growth process. AMAP models, which rely on both qualitative and quantitative architectural plant growth description, can provide realistic 3-D computing plants as seen in Fig. 1.6. The connection between tree architecture and growth process has been developed relatively recently, especially with the qualitative concept of *architectural model*. More recently, the AMAP models focus on the development of a quantitative approach of modeling and simulating plant architecture. This approach integrates previous botanists and computer scientists results and combines them with measurements on real plants, in order to deduce the parameters of their growth process. A basic approach of the AMAP tree development is based on three main steps [Castel et al., 2001]: 1) architectural analysis; 2) growth and branching processes modeling; and 3) simulation.

---

[9]AMAP is an abbreviation coming from the *Atelier de Modélisation de l'Architecture des Plantes* which in english can be translated as Architectural Plant Model.
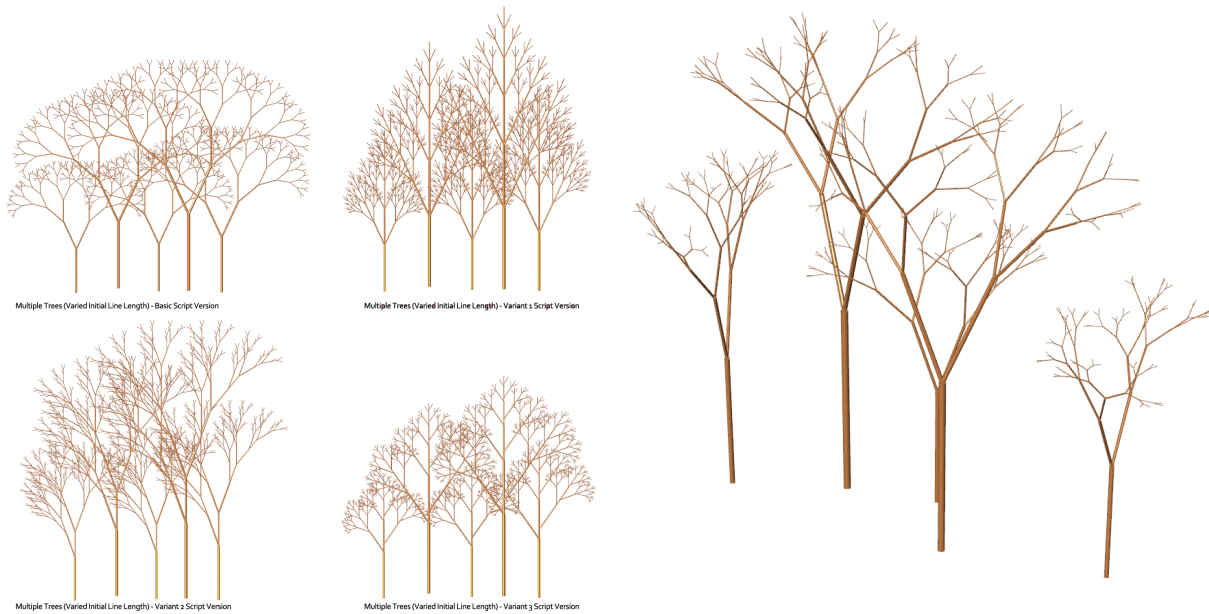
Figure 1.5 – Different types of trees generated using the L-Systems fractal algorithms (left) and a 3-D arrangement of them (right). Image taken from: https://generativelandscapes.wordpress.com/2014/10/07/fractal-trees-basic-l-system-example-9-4/
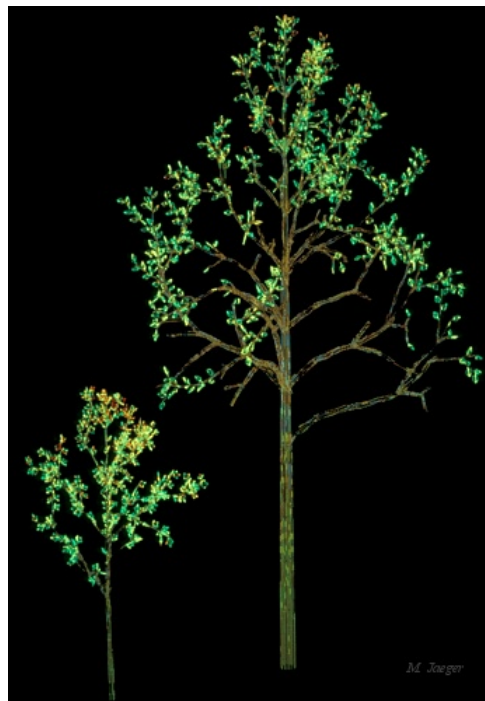
Figure 1.6 – Two growth steps of a poplar tree built with the use of AMAP. Image taken from: http://pma.cirad.fr/MJ_PICS/SelectedPics/Amap_Oldies_WF/slides/Poplars_Lines.html

1.3.2 Alternative models - Random volume over ground (RVoG)

Apart from the discrete forest models, there exist alternative types of models also. One of the most widespread ones, is the analytical model called *Random Volume over Ground* (RVoG). This is a simple model that do not consider and construct each scattering element separately. In the most basic case, the forested area is modeled as a set of possible overlapping volume vegetation layers, above an impenetrable ground. The most common RVoG models comprise two or three levels as for example in [López-Martínez et al., 2011] and [Cloude and Papathanassiou, 1998] respectively. If two layers are assumed, the first one corresponds to the vegetation layer, with a height h_v with respect to the ground height z_0 (see Fig. 1.7). This layer represents the volume scattering contibution of the forest canopy and it is assumed as a homogeneous volume of randomly oriented scatterers. The second and lowest layer, refer to the ground response and describes the backscattering of the wave by scatterers located at the ground level and by the ground-tree double-bounce interactions. Further simplification hypotheses can also be made for these models, as for instance to consider the concentration of the scatterers along the vertical direction as constant and/or to assume an isotropic distribution for the randomly oriented scatterers [Arnaubec et al., 2014]. These models serve as a good starting point for considering some radar investigation and inversion problems, but they do not account for the different scattering mechanisms and the contribution of each type of the tree elements as the discrete models do.
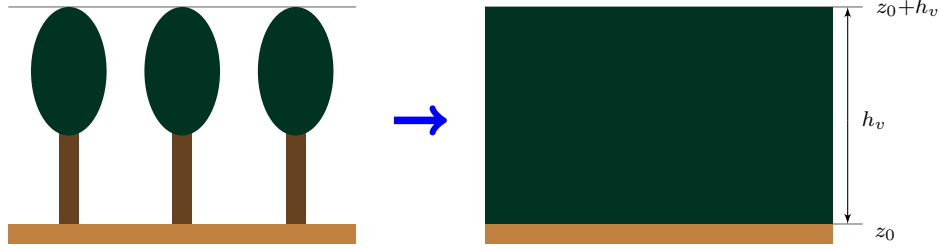
Figure 1.7 – A two-level Random Volume over Ground (RVoG) analytical forest model. The vegetation layer corresponds to the above ground tree elements, i.e. trunks and canopies with their individual scatterers and extends in a height of h_v above the ground. The second layer corresponds to the ground which is found at a reference height z_0.

1.3.3 Forest under study

As seen in the previous paragraphs, the architectural plant models and the fractal based ones seem able to provide the most sophisticated and realistic forest models up to now. However, their limited use and validation in the microwave simulation experiments domain and our lack of access to them, prevented us from using these models in the present work. A discrete model, already accessible to us, based on a forest geometric description was adopted, despite its more rough forest description. This kind of models, has been already proven suitable for low frequency studies in P- and L-bands (see for example [Thirion, 2003] and [Thirion et al., 2006]). In these frequency bands, where $\lambda \geq 15\,\text{cm}$, the electromagnetic field is weakly scattered by small branches and leaves. Trunks and primary branches - to wit, branches inserted directly in the trunk - contribute most to the tree emission and wave extinction at these frequensies. It is

due to the fact that the wavelength is of an order of magnitude comparable to these elements' dimensions [Woodhouse, 2005]. So despite the sometimes strong attenuation that needles or leaves can cause due to their large number [Chauhan et al., 1991], we are not going to consider them at all. As if the measurements were done in winter, when almost no leafage exist on the trees. Thus, a 2-layer discrete model considering only trunks and primary branches will be addressed in our simulations to follow. This representation is similar to the one successfully used and validated in [Thirion et al., 2006], where the numerical model to be used in this dissertation was introduced.

The ground truth data used to generate the forest during the simulations, come from the Les Landes forest located in southwest France (44 42 N, 0 46 W). This forest consists of maritime pine trees (*Pinus Pinaster Aït)* as seen Fig. 1.8, a native species to the western and south-western Mediterranean region. For this forest, several ground truth and radar campaigns have been performed, as for instance the PYLA 2001 experiment (see [Dechambre et al., 2003]) and extended datasets exist. The data used to estimate and predict the dimensions of the elements and the distributions of crown wood in the trees, are based on allometric equations taken from [Saleh et al., 2005]. In these equations the tree age was used as input information to simulate the forest geometric characteristics. The quantities estimated were the diameters and the heights concerning only the trunks and the primary branches. The trunk *diameter at breast height* (dbh), defined as the diameter at 1.30 m, was given by:

$$\hat{dbh} = 0.169 \cdot \log\left(age\right) - 0.257 \quad [\text{m}] \tag{1.13}$$

The trunks total height was derived from the dbh by:

$$\hat{H} = 56.618 \cdot \hat{dbh} + 0.646 \quad [\text{m}] \tag{1.14}$$

The height C of the naked trunks (bottom layer) when branches existed was obtained by:

$$\hat{C} = \left(\hat{H} - 1.30\right) \cdot \exp\left(\frac{-\left(p_1 + \frac{p_2}{age}\right) \cdot \hat{dbh}}{\hat{H} - 1.30}\right) \quad [\text{m}] \tag{1.15}$$

where $p_1 = 12.43$, $p_2 = 347.96$. The "hat" (^) over the symbols above, denotes the mean of each quantity taken from a population of even-aged trees.

As far as the branches were concerned, when existing, they were uniformly distributed around the trunks in the upper layer of the forest. Their dimensions, as sampled in [Saleh et al., 2005] from three different stands 5, 26 and 32 years old, were corresponding to certain distribution functions. To simplify our studies and focus on the branches effect on the signal when necessary, we chose to make all branches of coeval forests equal. Their radii and lengths selected were the mean ones for each age, resulting from an interpolation of the values given in [Saleh et al., 2005], in order to cover all ages to be examined.

1.3.4 Permittivity and ground description

Last but not least in forest modeling, is the modeling of the ground and the permittivities of the scatterers. During low frequency radar observations, penetration of the wave to the lower forest levels takes place. Subsequently, there are wave reflections from the ground and double

Figure 1.8 − A picture of the maritime pine forest at Les Landes. This coniferous species gives medium-sized long and thin trees, with needles as leaves, which can be found in the western Mediterranean. Image taken from: http://a402.idata.over-blog.com/3/69/76/43/Quizz/Juin-2011/Foret-des-landes---pin-maritime---Mimizan.jpg

bounce scattering between the ground and the vegetation. It is thus of high importance to interpret well the ground surface and consider both the soil and the vegetation permittivities. For the permittivities especially, which describe the reflectivity of the illuminated materials, extra attention has to be paid since they have a strong impact on the forest emissivity and backscattering, e.g. the wetter the soil, the higher the permittivity and the scattering [Woodhouse, 2005]. Moreover, the permittivity governs certain important phenomena such as for instance the Brewster's angle effect, addressed later in section 3.4. In most of the previously mentioned models for forest studies, the ground is considered as an arbitrary horizontal or tilted plane with a given dielectric constant and surface roughness. The roughness of a random ground can be described by two parameters, the Root Mean Square (RMS) height s and the correlation length l. The RMS height describes the vertical surface roughness, while l is the distance where the spatial correlation function decays by $1/e \approx 37\%$ [10]. In our case, a plane rough surface was selected to model the ground, with its s and l parameter values given during the presentation of the simulation results later on.

As far as the permittivity of the ground is concerned, it depends on the soil's textural composition (sand, silt and clay fractions[11]), the bulk density (the weight of the dried soil divided

---

[10]For more details about the ground description in models serving radar simulation studies see https://earth.esa.int/documents/653194/656796/Description_Of_Natural_Surfaces.pdf

[11]Sand, from fine to coarse, includes particles with diameters in the range between 0.02 and 2.0 mm, silt includes particles with diameters in the $0.002 − 0.06$ mm range, and clay includes particles with diameters smaller than 0.002 mm [Daniels, D.J and Institution of Electrical Engineers, 2004].

by its volume), the gravimetric (or volumetric) moisture content of the soil, the dielectric constant of the water, the physical temperature and of course the frequency of the emitted signal. The permittivity model adopted for this study is the one also used and validated in the forest backscattering studies in [Thirion et al., 2006]. The analytical expression of this model is given by [Peplinski et al., 1995b] and [Peplinski et al., 1995a]:

$$\varepsilon_g = \left[1 + \frac{\rho_b}{\rho_s} \left(\varepsilon_s^a - 1 \right) + m_{vol}^{\beta'} \varepsilon_{fw}^{'\alpha} - m_{vol} \right]^{1/\alpha} - i \left(m_{vol}^{\beta''} \varepsilon_{fw}^{''\alpha} \right)^{1/\alpha} \tag{1.16}$$

where ρ_b is the bulk density, ρ_s and ε_s are the specific density and relative permittivity of the solid soil particles, m_{vol} the volumetric moisture content related with the gravimetric one m_{grav} by the expression $m_{vol} = \rho_b m_{grav}$, ε_{fw}' the real part and ε_{fw}'' the opposite imaginary part[12] of the relative permittivity of the free water, $\alpha = 0.65$ a constant and β', β'' are soil-type dependent constants determined by the sand S and clay C content in % by the equations:

$$\beta' = 1.2748 - 0.519S - 0.152C, \qquad \beta'' = 1.33797 - 0.603S - 0.166C \tag{1.17}$$

In Fig. 1.9, we can see the variation of the permittivity values with respect to f and m_{grav} given a temperature $T = 10°C$, $S = 20\%$ of sand percentage, $C = 50\%$ of clay percentage and a bulk density of $\rho_b = 1.1$, corresponding to a clayey type of ground. The jump observed for both the real and the imaginary part at $1.3\,\text{GHz}$ is due to the different empirically derived models for the effective conductivity for frequencies lower and higher than $1.3\,\text{GHz}$ (see [Peplinski et al., 1995b] for more information). The real part of the dielectric constant increases sharply with the humidity and declines slightly with the frequency, whereas the imaginary part increases in general with both parameters, apart from the aforementioned jump.

In order to have an idea of how the soil permittivity varies, we will now give some reference permittivity values. For the fresh water $\varepsilon' = 81$, for the air $\varepsilon' = 1$ and for a dry sandy soil $\varepsilon' \in [4, 10]$ at $f = 100\,\text{MHz}$ [Daniels, D.J and Institution of Electrical Engineers, 2004]. The water content has the biggest influence on the dielectric properties of soil, as for example the ε' of saturated soil[13] approaches that of the liquid water (~ 80) $at \gtrsim 1\,\text{GHz}$ [Woodhouse, 2005]

On the other hand, the permittivity of the vegetation depends mainly upon the gravimetric moisture content m^{grav} of the vegetation and the emitted frequency f in GHz via the permittivities of the free and bounded water and is estimated by [Ulaby and El-Rayes, 1987]:

$$\varepsilon_v = \varepsilon_r + u_{fw}\varepsilon_f + u_b\varepsilon_b \tag{1.18}$$

where ε_r is a non-dispersive residual component, u_{fw} the volume fraction of free water, ε_f is the permittivity of the free water, u_b the volume fraction of the bulk vegetation-bound water mixture and ε_b the permittivity of this mixture. The temperature as well as the salinity of the free water are affecting also the permittivity values, but much less with respect to m_{grav} and f. More information on the estimation of these quantities can be found in [Ulaby and El-Rayes, 1987]. In Fig. 1.10, we can see the variation of the permittivity values with respect to f and m_{vol} given a temperature $T = 10°C$ and a percentage of salinity less than $10\%_0$. As the vegetation gets

---

[12]A complex relative permittivity ε is usually expressed as $\varepsilon = \varepsilon' - i\varepsilon''$ and it is the opposite imaginary part $-\varepsilon''$ variations that are being treated and presented.

[13]Saturated is called the soil for which the entire profile is saturated with water [Patel et al., 2008]. All pores between the saturated soil particles are temporarily or permanently filled with water.
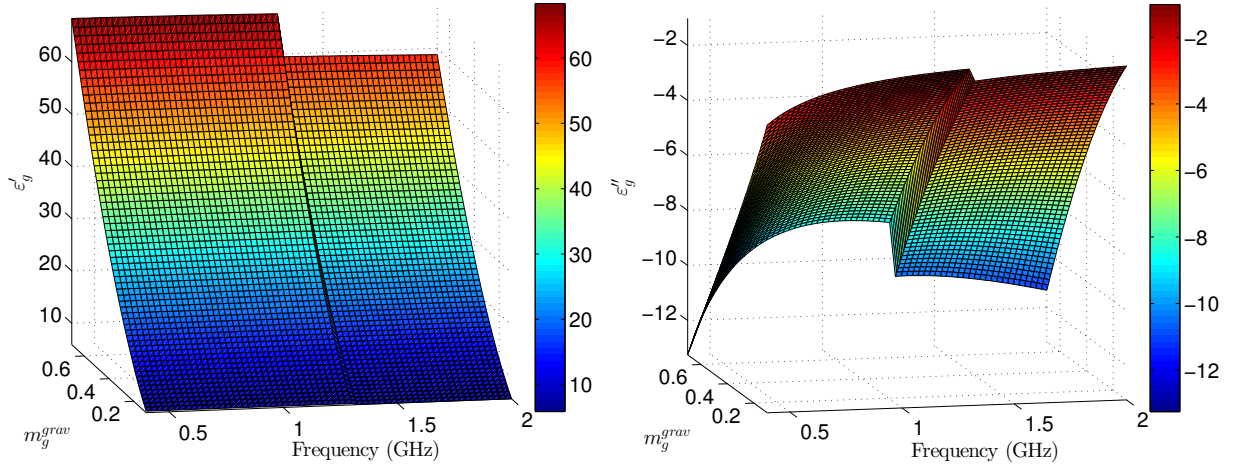
Figure 1.9 – The surface plots of the ground's relative permittivity real part values $\left(\varepsilon_g'\right)$ (left) and the imaginary part values $\left(-\varepsilon_g''\right)$ (right), with respect to the frequency and the gravimetric moisture content m_g^{grav}. The ambient temperature was $T = 10°C$, the sand content of the ground 20%, the clay content 50% and the bulk density $\rho_b = 1.1$.

wetter the real part of the permittivity rises, while a raise in frequency makes it to decrease. The imaginary part on the other hand, as for the case of the ground, it increases with both parameters.
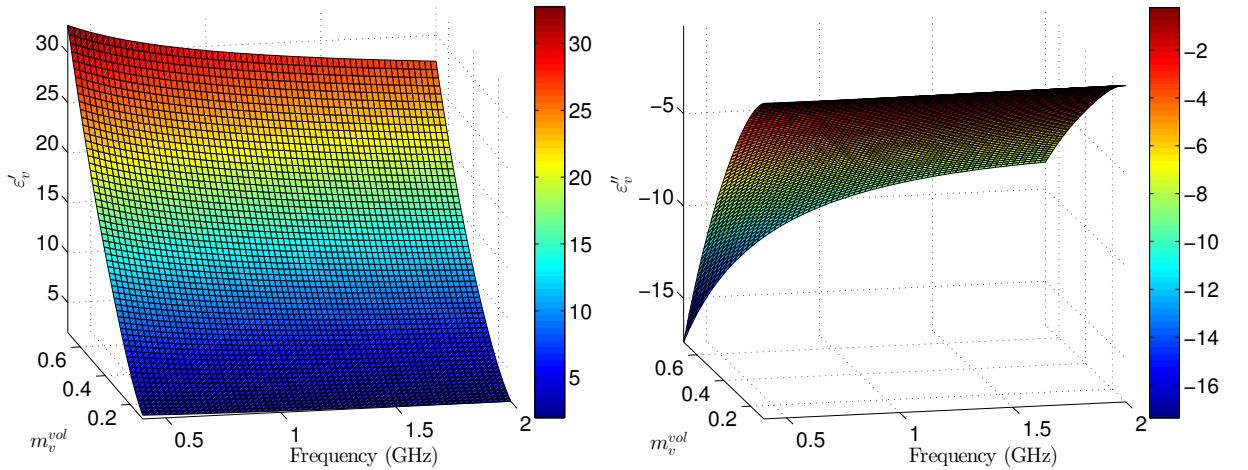
Figure 1.10 – The surface plots of the vegetation's relative permittivity real part values (ε_v') (left) and the imaginary part values $(-\varepsilon_v'')$ (right), with respect to the frequency and the volumetric moisture content. The ambient temperature was $T = 10°C$.

1.4 An example of a forward model: COSMO

As presented in the previous paragraphs, radar remote sensing is a powerfull tool for investigating forests and vegetation in general. Nevertheless, radar technology, as every evolving technology, has still many limitations in its applications, such as the unauthorized low frequencies for earth observation [Dechambre et al., 2003] or the fact that SAR instruments are particularly heavy and power consuming [Woodhouse, 2005]. For some of these limitations we are obliged to wait radar scientists to construct more sophisticated hardware to extend them, whilst other constraints can be surpassed by using techniques from other domains. One of these domains is Numerical Modeling, which can provide us codes that can simulate a wide range of radar observations in computer experiments. What these codes can provide to the earth studies practice is the low cost of the simulation experiments, the possibility to consider numerous scenarios and the opportunity to extend the radar capabilities and implement innovative strategies.

In the particular case of forested areas, one simulates the behavior of the environment either to predict the level of the radar response in amplitude and/or in phase, or to discriminate the relevant scattering mechanisms. The use of scattering models aims at a better understanding of the electromagnetic interactions. Improving our knowledge over the forest scattering can assist in the design of upcoming radar campaigns, as well as in facilitating the retrieval studies of the forest parameters. However, extended validation of the model results with respect to real data are mandatory, in order to properly utilize the model. An ideal modeling tool must have been tested for different radar configurations (incidence angles, frequencies and polarizations), for different purposes (radiometry, polarimetry, interferometry) and must have been applied to various types of forested areas. A model like this, introduced in 2006 by Thirion et al. (see [Thirion et al., 2006]), is available in our laboratory. It is the so-called *COherent Scattering Model* (COSMO) and it will be presented in details in the upcoming paragraphs, before applied to our work in the following chapters.

1.4.1 General presentation of COSMO

COSMO is a descriptive coherent scattering model, applied to the electromagnetic study of the backscattering by forested areas. Descriptive because it is based on the generation of the trees and the forest, in opposition to the analytical models such as the RVoG (see Paragraph 1.3.2). Analytical models consider forests as homogeneous media and they cannot facilitate low frequency and low vegetation density scenarios. On the other hand, the descriptive models generate the trees as groups of canonical elements, with dimensions derived by allometric equations. COSMO is also a coherent model, which means that it calculates the complex response providing information on both the amplitude and the phase of the received signal. Therefore, the construction of the Stokes matrix and the polarization signature retrieval from its results, are both possible.

Since COSMO is a descriptive model, the scene under study i.e. a virtual forest of a given arrangement - periodical or random - has first to be generated. This forest is subsequently treated as a multilayer medium, in order to suit to the format of the available ground truth data. Then the illumination of the forest by EM waves under a certain configuration is simulated, while considering the contributions of all scatterers, namely the ground, the trunks, the branches and the leaves, if existing. In that way, we can also study how these scatterers interact with each

other. COSMO operates in the Frequency Domain (FD) and sends a monochromatic wave for each frequency selected. COSMO performs all calculations using the FSA convention and it is able to produce outputs that can be treated with the same polarimetric and interferometric tools as those applied to real Synthetic Aperture Radar (SAR) images (see [Thirion et al., 2006]). Therefore, these outputs can be directly compared and validated with respect to real data. Up to now, extended validations at P- and L-bands, for both temperate (maritime pine trees) and tropical (mangrove) forests and for all purposes as radiometry, interferometry, and polarimetry have been performed (see [Thirion et al., 2006]).

1.4.2   Generation of the medium

As a descriptive model COSMO, starts by constructing the scene of the simulation experiment. A whole forest is generated within the range and azimuth dimensions given, having either a random or a periodical positioning for the trunks. Random forests have a structure similar to the natural ones, while periodical forests refer mostly to artificial ones (see Fig. 1.11). Trees are described as groups of canonical elements - cylinders and ellipsoids - corresponding to the trunks, the branches and the leaves, that are distributed in several layers. In our case two layers are concerned, where the bottom one contains the naked trunks and the top one the crowns (see Fig. 1.12). The geometrical characteristics of the forest elements, i.e. height and radius, are obtained by the allometric equations (1.13)-(1.15). The modeling of the shape of the crown can be also described, and it can be a sphere, an ellipsoid or a cone, depending on the type of forest we want to study. As far as the permittivities of the vegetation and the ground are concerned, they are supposed to be constant inside the trees and along the ground respectively. Finally, the ground is assumed to be a flat surface having a roughness with a given RMS height and correlation length. Once the forested area is generated, the scene is divided into cells along azimuth, distance and z- axes forming a 3-D grid consisting of voxels (volume pixels).
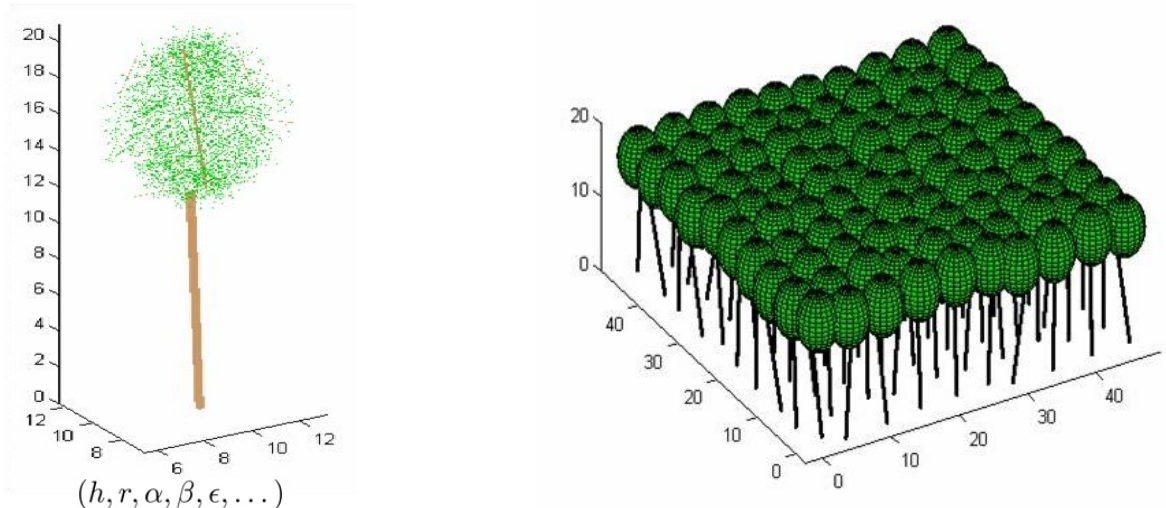
Figure 1.11 − Modeling the forest: generation of a tree (left) and of a whole forest where trees are regularly positioned (right). For the building of a tree several parameters are taken into account such as the height h, the trunk radius r, the eulerian angles α, β, the permittivity ε etc.
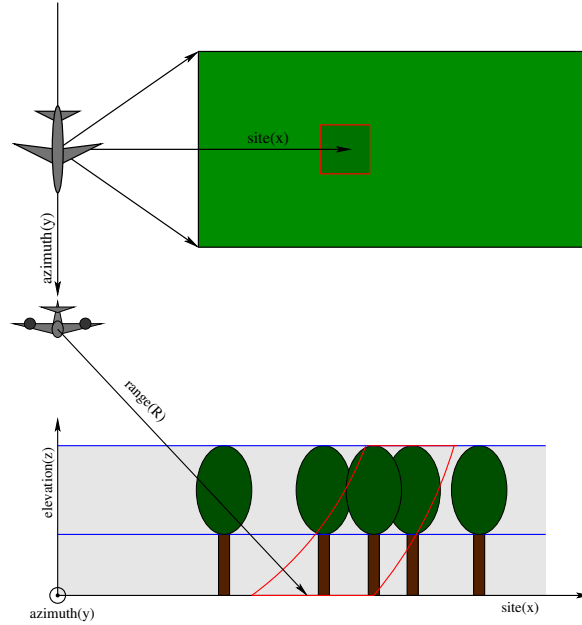
Figure 1.12 – Radar configuration: above view (top) and side view with the separation of the scene into layers (bottom). The intersection of a layer and a pixel, bounded with the red line, is a cell of the scene.

1.4.3   Evaluation of the forest backscattering

Since a whole forest is generated, as previously described, the contributions of all scatterers (trunks, branches and leaves) and their interactions can be considered for the calculations. That way, the computational load of the simulations will be very heavy. In order to reduce it, some hypotheses are necessary. Firstly, only the main scattering mechanisms are taken into account. In saying so, as depicted in Fig. 1.13, the direct backscattering where the EM wave hit the particle under the direction of incidence $\hat{i}$ and is scattered back under the direction $\hat{s}$ and the double bounces which refer to the ground-scatterer (gs), scatterer-ground (sg) and ground-scatterer-ground mechanisms. In addition, scatterers are assumed to be independent, therefore no mutual interactions are considered. Concerning the cylindrical elements, if they have small radii r compared to their semi-heights h and $k_0 h >> \lambda$, where k_0 is the wavenumber and λ the wavelength, the Infinite Cylinder Approximation is used (see [Thirion, 2003]). If not, the Physical Optics Approximation is used instead. The coherent scattered fields are then computed by considering each of the voxels of the scene as an ensemble of scatterers, with their specific positions, orientations and sizes. The attenuation and phase shift within the forest are taken into account to compute the field scattered by each individual particle. Finally, the scattered field for each pixel of given azimuth and distance, is the coherent sum of the contributions of all the scatterers embedded in the voxels having the same location in azimuth and distance. The way COSMO separates the scene in cells and voxels and calculates the outputs, is designed so that the latter suit the format of the available ground truth data.

All the contributions of the different mechanisms and the different types of scatterers together with the attenuation for each voxel, are available in the outputs of COSMO and they can help us understand how the total response is built. For the previous studies ([Thirion et al., 2006])
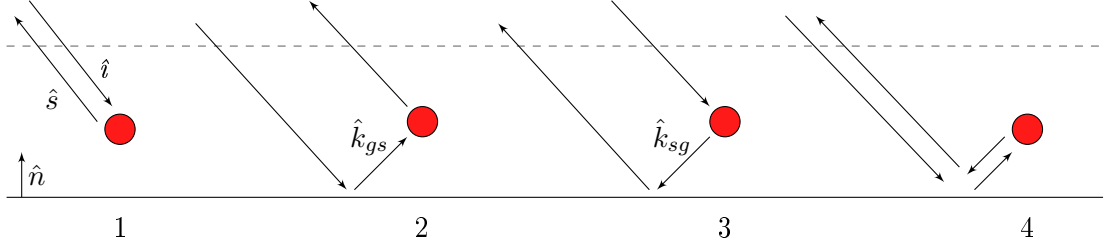
Figure 1.13 − The scattering mechanisms taken into account in COSMO evaluations of the backscattered field: 1: direct scattering, 2: ground-scatterer contribution, 3: scatterer-ground contribution and 4: ground-scatterer-ground contribution.

and for this one, the focus was mostly put on the outputs concerning the received electric field and the backscattering coefficients. In the latest COSMO versions, access to other kind of data like the attenuation and the interferometric heights is also possible. However, for our purpose we will not deal with these two recent contributions. We remind that the backscattering coefficient for an emitted signal with q polarization and scattered in p polarization as defined in Eq. (1.8) is:

$$\sigma_{pq}^0 = \lim_{r \to \infty} \left(\frac{4\pi r^2}{A} \frac{\left\langle |\mathbf{E}_p^s|^2 \right\rangle}{|\mathbf{E}_q^i|^2} \right)$$

and to be evaluated in dB we use the common logarithm:

$$\sigma_{pq}^0 = \lim_{r \to \infty} \left(10 \log_{10} \left(\frac{4\pi r^2}{A} \frac{\left\langle |\mathbf{E}_p^s|^2 \right\rangle}{|\mathbf{E}_q^i|^2} \right) \right) \tag{1.19}$$

Whenever Pauli decomposition was utilized to extract information about the scattering mechanisms, the spatially averaged Pauli vector components were calculated, normalized by the area A:

$$\frac{4\pi}{A} \left\langle (S_{HH} + S_{VV})^2 \right\rangle, \quad \frac{4\pi}{A} \left\langle (S_{HH} - S_{VV})^2 \right\rangle, \quad \frac{4\pi}{A} \left\langle (2S_{VH})^2 \right\rangle \tag{1.20}$$

and evaluated in dB $(10 \log_{10} (\cdot))$. The area normalization was done so that these quantities could be comparable between scenes of different sizes. From now on, the symbols $S_{HH} + S_{VV}$, $S_{HH} - S_{VV}$, $2S_{VH}$ and $\mathbf{k}_{P_i}$ concerning the Pauli vector components, will refer to these quantities in Eq. 1.20.

1.4.4 Presentation of the outputs

In this section we will present the data obtained after running COSMO under a certain forest and radar configuration. The scene under study was a 30 years old maritime pine forest, distributed semi-periodically within a scene of $40\,\mathrm{m} \times 50\,\mathrm{m}$. There were 56 totally vertical trees generated, having a $6\,\mathrm{m}$ mutual distance between them in both directions. The distribution was semi-periodical since a maximum displacement of $2\,\mathrm{m}$ from the exact periodical positions was allowed, as depicted in Fig. 1.14. Only trunks were considered and their dimensions were derived from the tree age, using the allometric equations already presented in Paragraph 1.3.3. The trunks dimensions together with the other parameters of the scene and the radar are given in Table 1.2.
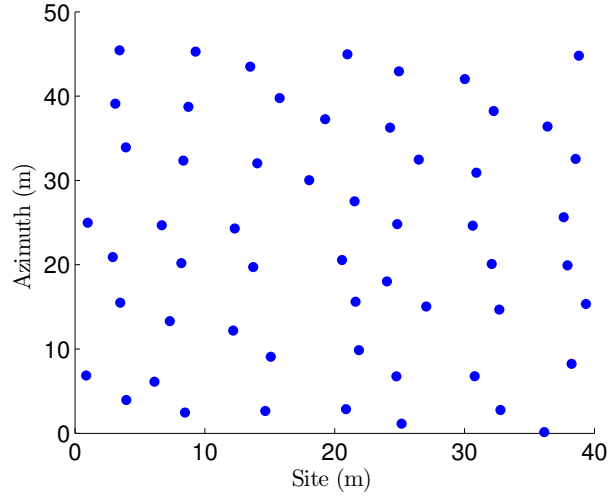
Figure 1.14 – The semi-periodical positioning of the trunks in the scene under study.   56 trees were generated, having trunks only, a mutual distance of 6 m and a maximum displacement from the exact periodical position of 2 m.

The scene was illuminated by a wave emitted by a radar found in a height of 3.6 km and the angle of incidence was 50°. Since COSMO operates in frequency domain and sends monochromatic waves, 826 different frequency values were selected, forming a rectangular pulse ranging from 350 MHz to 2 GHz (wavelengths from 86 cm to 15 cm) and having a frequency step $df = 2$ MHz. The large bandwidth, comparable to that of the ultra wideband radars, led to a high range resolution $\delta_r \approx 10$ cm. The advantages of a fine resolution like this, will become obvious when the signal will be analyzed in the time domain later on. The unprocessed COSMO results as obtained in frequency domain, are presented in Fig. 1.15 and 1.16. In the first figure, the amplitude of the received electric signal in HH and VH polarizations are presented. The results are highly oscillating, since no average or smoothing filter is applied yet. The huge difference observed between the order of the HH and the VH amplitudes, is due to the high symmetry of the scene. Only vertical trunks exist, so the co-polarizations are favored in general.

The last figure of the chapter, Fig. 1.17, presents some processed COSMO outputs. In the left plot we can see the three backscattering coefficients and in the right one the components of the Pauli feature vector. The former correspond to the smoothened, via the logarithm, amplitude values, while the latter correspond to the main scattering mechanisms, namely the double bounces, the single bounces and the volume scattering. The similar way of evaluating the σ_{VH}^0 and the $2S_{VH}$ quantities (see Section 1.4.3), makes the second one redundant in most of the following applications. The majority of the conclusions concerning the volume scattering can be also derived by the study of the σ_{VH}^0 values.

1.5   Conclusions

In this first chapter of the thesis, we provided the necessary radar background for this dissertation. We started by presenting the basics of radar polarimetry with the focus on the quantities and the methods employed in the upcoming chapters. Since our purpose was neither a full physical analysis of the forest scattering phenomenon nor the exploitation of the COSMO numerical

Parameters	Values
Trunk height	18.6 m
Trunk radius	15.9 cm
Temperature	15 °C
Gravimetric humidity of the ground	40%
Sand content	50%
Clay content	30%
Silt content	20%
$\mathrm{Re}\,(\varepsilon_g)$	$[33.6, 38.5]$
$\mathrm{Im}\,(\varepsilon_g)$	$[-5.8, -2.5]$
Volumetric / gravimetric humidity of the vegetation	40% / 35.7%
$\mathrm{Re}\,(\varepsilon_v)$	$[9.9, 13.1]$
$\mathrm{Im}\,(\varepsilon_v)$	$[-5.9, -3.3]$
RMS height of ground roughness	5 cm
Correlation length of ground roughness	1 m

Table 1.2 – The ground and vegetation parameters of the COSMO simulation.
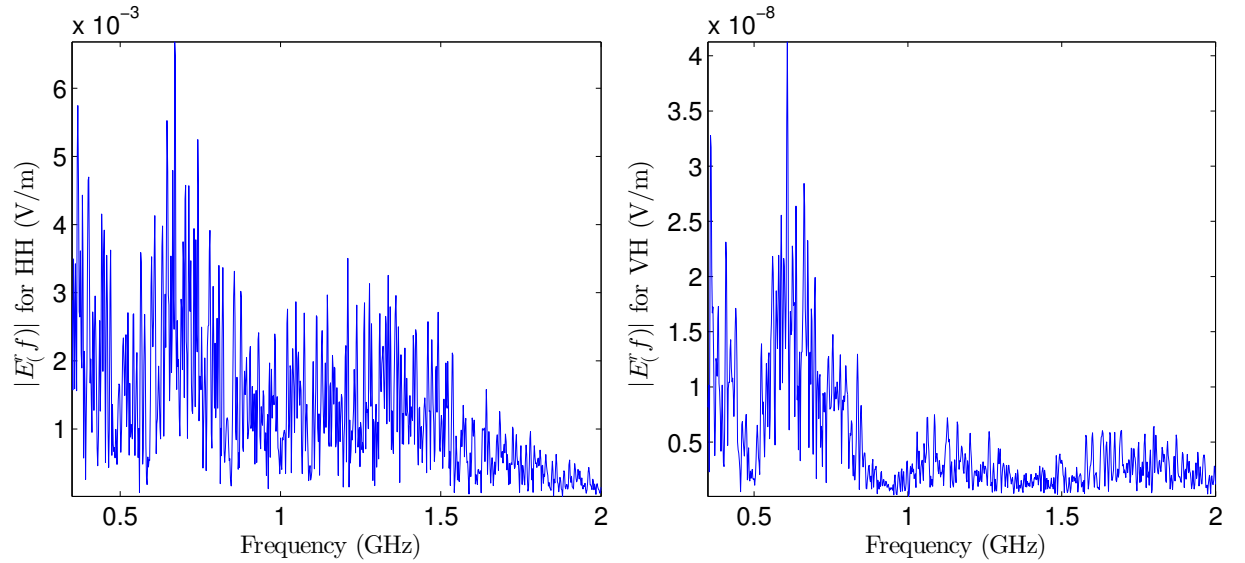
Figure 1.15 – The amplitude of the received electric field with respect to the frequency in HH polarization (left) and in VH (right). The angle of incidence was 50°. The values presented here are the unprocessed values obtained by COSMO. No average or smoothing filter was performed. The huge difference between the two amplitudes' values is due to the symmetry of the scene, as just the vertical trunks exist in it.

model, we selected a few tools, such as the Stokes matrix, the backscattering coefficients and the Pauli vector, upon which we applied our mathematical methods. It is obvious that other choices of tools were possible which could provide new directions in this study and complement the results obtained. Next, the various ways a forest can be modeled for microwave studies were explained. The AMAP, the vectorization and the fractal based models, the RVoG and the 2-
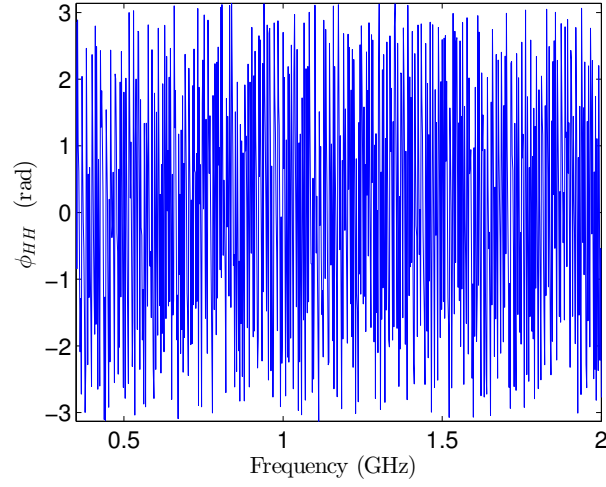
Figure 1.16 − The phase of the received signal with respect to the frequency in HH polarization and under an angle of incidence of 50°. *No average filter is performed and so the phase values are highly oscillating.*
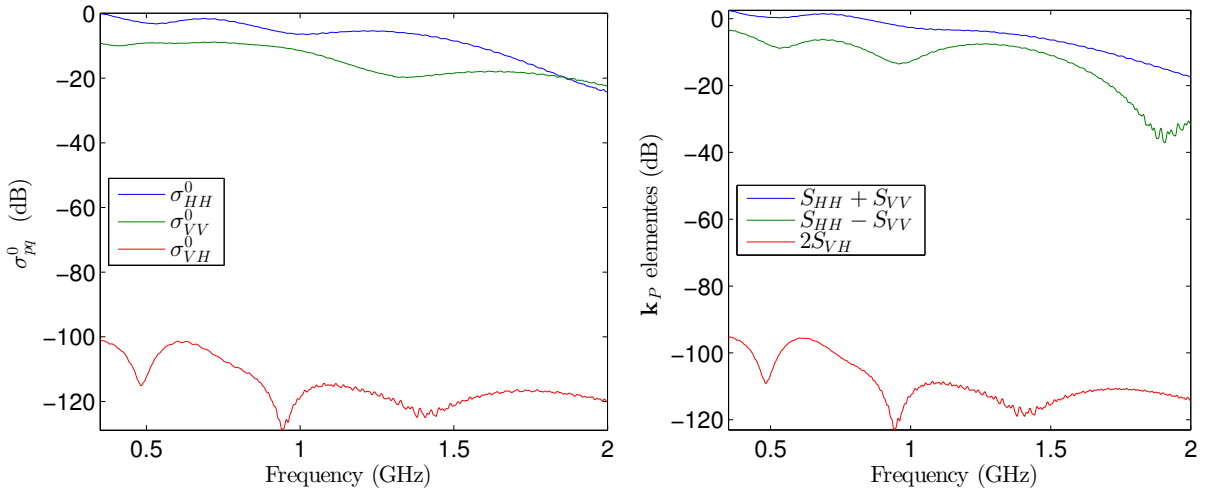
Figure 1.17 − The backscattering coefficients for all polarizations (left) and the Pauli feature vector elements (right), with respect to the emitted frequency. Trunks only were considered and a 50° *angle of incidence was chosen. The similar way of evaluating the* σ^0_{VH} *and the* $2S_{VH}$ *values is reflected in the corresponding curves.*

layer discrete model we finally adopted, were all presented. The description of the specific forest under study, the way its elements dimensions are calculated via allometric equations and the permittivity values are derived, followed. All these were necessary to understand how the forest was going to be generated, during our numerical simulation studies. The chapter continued with the presentation of our descriptive microwave model COSMO. Its general characteristics, the way it realizes the forest and the radar configuration and the evaluation of its outputs, concerning the forest backscattering, were discussed. The chapter closed with the presentation of the COSMO results acquired from a simulation example.

2

Sensitivity analysis of COSMO

Contents

2.1 Introduction

In this chapter, the statistical methods employed in Sensitivity Analysis (SA) of numerical models will be presented. These methods are widely used in Design and Analysis of Simulation Experiments (DASE), in order to understand the overall behavior of a model [Saltelli et al., 2004]. They can facilitate the identification of the factors which affect significantly the model overall and each one of its outputs. Moreover, they can detect possible non-linear effects and interactions between the inputs. The knowledge obtained from the SA can be subsequently used for model analysis and reconsideration. In our work however, a different and more integrated approach was attempted. This approach involved a unified strategy which started from the SA of the numerical model, to identify its most important parameters, and continued with the study and the analysis of these parameters effects at a next step. In doing so, we wanted to organize our radar simulation datasets, study them with respect to the scene changes and extract complementary information on radar observations of forests.

In radar forest studies, empirical sensitivity analyses are sometimes performed over real data. In [Huang et al., 2015] for instance, they are conducted to investigate the influence of the incidence angle and ground moisture on SAR backscatter. The results aimed to be used for checking the feasibility and applicability of normalized backscatter data. Nonetheless, since sensitivity analyses of real data are based on the sparse datasets available and cannot be performed for numerous different scenarios, they are far from being thorough and complete. It is exactly where the statistical SA methods applied on numerical models can complement these studies and open the ground for a better understanding of the forest response. The present SA study of COSMO, aspired to provide new information on the dependance of the different COSMO outputs to the input factors. It aimed also to assist in designing an innovative way to perform radar campaigns based on these information and utilizing the cognitive radar principle in an upcoming step. After presenting the aims of the COSMO SA, we will now proceed in a fast review of the SA methods and in a thorough presentation of the particular method selected for our purpose. The interested reader can find more information in the relevant bibliography, e.g. in [Saltelli et al., 2004] and [Saltelli et al., 2008].

2.2 Definitions and Methods of Sensitivity Analysis

Sensitivity Analysis can be defined as "*The study of how the uncertainty in the output of a model (numerical or otherwise) can be apportioned to different sources of uncertainty in the model input*" [Saltelli et al., 2004]. It is of prior importance in the modeling procedure, because it can provide objective criteria of judgement for different phases of the model-building process such as model identification and discrimination, model calibration and model corroboration [Saltelli et al., 2000]. SA can also reveal overparameterization by detecting parameters or parameter combinations to which the outputs are insensitive. Another reason why SA is essential in modeling, is the need to infer uncertainty in the model's predictions from the uncertainties in its parameters, forcing and boundary conditions. SA in addition can be used to check the extent of nonlinearity, helping assess the credibility of model results, indicating what extra data are needed to repair model deficiencies and seeing how much aggregation can be employed [Norton, 2009]. For our purposes we will discriminate the SA methods, based on the type of their results and their computational load, in two main categories (see [Campolongo et al., 2011]):

(i) the Screening methods that provide qualitative sensitivity measures, i.e. they rank the input factors in order of importance, but they do not quantify how much a given factor is more important than another and

(ii) the Quantitative methods, that estimate which percentage of the output variance each factor is responsible for, due to its first order component and/or its interactions with the other factors.

The methods of the first category share the philosophy of Max Morris (see [Morris, 1991]) who wanted to determine model inputs that have effects which can be considered as:

(i) negligible

(ii) linear and additive

(iii) non-linear or involved in interactions with other factors.

Morris' goal was to identify the subset of non-important factors in a model with just a few model runs. So the Screening methods seem more appropriate for large models but they do not quantify how much a given factor affects the output, or how much more important it is than another factor. On the other hand, the Quantitative measures give a comprehensive SA of the model, but in the price of a high number of model evaluations. For complicated models, where the number of involved factors is large and/or the model is time consuming, the estimation of quantitative sensitivity measures could be unfeasible and Screening methods are preferable [Campolongo et al., 2011]. As far as COSMO is concerned, we have seen that it has several numerical input parameters resulting in long simulations. For example, to simulate 1000 frequency points, for the case of a 100×100 m periodical forest consisted of vertical trunks and 10 equal branches per trunk, at least 40 hours are needed. In that case, global sensitivity methods are regarded as unaffordable. They require numerous simulations to obtain the full sensitivity measures, and also a different SA study for every qualitative input (e.g. polarization). Screening methods seem more plausible as they provide prioritization of the inputs concerning their importance, which definitely corresponds to our main objective. The most common ones are the Morris Elementary Effects method (see [Morris, 1991]) and the Sequential Bifurcation (see [Kleijnen, 2008]). For our purpose, the first method which is the most popular will be used, because of the separate investigation of each factor and the visualization of the results it provides.

2.3 The Morris Elementary Effects method

The *Elementary Effects* (EE) method originates from Morris' work in 1991 (see [Morris, 1991]) and it was implemented by Campolongo et al. in 2007 (see [Campolongo et al., 2007] and [Campolongo and Cariboni, 2007]). It is based on calculating a number of incremental ratios, the EEs, for each input variable in several random points within the input space [14]. The EE of the input factor x_i for a given point of the input space $\mathbf{x}$, is defined as follows:

$$EE_i\left(\mathbf{x}\right) = \frac{f\left(\mathbf{x} + \mathbf{e}_i \Delta\right) - f\left(\mathbf{x}\right)}{\Delta}$$

where $\mathbf{x} = \left(x_1, x_2, \ldots, x_n\right)^T$ is any selected vector in the sample space, $\mathbf{x} + \mathbf{e}_i \Delta$ is the transformed vector which has also to be in the sample space for every index $i = 1, 2, \ldots, n$, $\mathbf{e}_i = \left(0, 0, \ldots, 1, \ldots, 0\right)^T$ are the standard basis vectors of the euclidean space $\mathbb{R}^n$, f is the forward (I/O) function and Δ is the step by which we move each factor. To calculate the EEs, sampling several different points $\mathbf{x}$ in the input space is needed. For each of these points the I/O function both for $\mathbf{x}$ and $\mathbf{x} + \mathbf{e}_i \Delta$ needs to be evaluated.

2.3.1 Constructing the EEs sample space

If r random points are simply chosen for the computation of the EEs, the computational cost will be $2rn$ model runs. In order to reduce this cost, Morris proposed a different sampling where he used each simulation in computing more than one EEs [Morris, 1991]. He considered trajectories of $n+1$ points, each one starting from a random point and moving a different factor

---

[14]Each input factor is being scaled, so that the input sample space for the EE is included in the unit hypercube $[0, 1]^n$, where n is the dimension of the model's parameter space. Later the factors are transformed again to be distributed in their original intervals before evaluating the I/O function values.

at a time by $\pm\Delta$ on a p-level discrete grid of the input space, till all factors are moved. Every point on a trajectory therefore differed from the previous or the next one by Δ, in only one component. The result was a set of points $\mathbf{x}$, designed in a way that each evaluation of the forward function will participate in the calculation of two EEs.

For the j-th trajectory generated with the Morris method, the EEs were represented as $EE_{i,j}$, where i indicated the corresponding model factor. The trajectories were first constructed within the unit hypercube $[0,1]^n$, where the Δ step could only take values in $\{1/(p-1),\ldots,1-1/(p-1)\}$. p was the number of levels in which the unit hypercube have been separated in order to be "discretized" it by constructing a n-dimensional p-level grid as an experimental area (see Fig. 2.1). The x_i inputs were not regarded as continuous in this method, they could only take the values $1/(p-1), 2/(p-1), \ldots, 1$, which are always found on the p-level grid of the unit hypercube. As suggested in [Morris, 1991], an even p (e.g. $p = 4$) and Δ a multiple of $1/(p-1)$ are better to be chosen. After constructing the trajectories, the unit hypercube was expanded to the original input space before the calculation of the EEs.
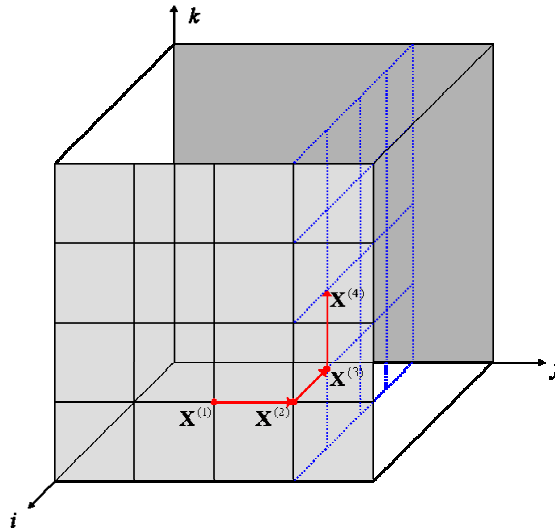
Figure 2.1 – An example of a trajectory in a 3-D input factor space with $p = 5$. One step is done each time, in a different direction, but always on a vertex of the grid. All the points of each trajectory rest in the same voxel.

A main drawback of the Morris trajectory plan was that the number r of the trajectories generated and used for the calculation of the the EEs was small and the only prerequisite was that the initial points should be randomly selected. However, this plan did not not guarantee that the points used for the EEs represent effectively the input space. Campolongo et al. suggested in 2007 a way to spread better the trajectories in the input space by introducing a trajectory distance (see [Campolongo et al., 2007]). A large number of trajectories is generated, their mutual distances are calculated and the r most distant ones are qualified for the EEs calculation. This plan was far too heavy from a computational point of view for our purpose, so in our work a different alternative was prefered. A *maximin Latin Hypercube Sampling (LHS)* (see [Santner et al., 2003]) was chosen for the initial trajectory points, so that these points were as representative as possible of the input space. After this selection, a p-level grid was introduced

around each of the initial points and each trajectory was constructed on its corresponding grid, by moving each factor by Δ at a time (see Fig. 2.2). The trajectories constructed that way were sufficiently spread and thus representing the whole input space, making the results trustworthy enough, as we will see in the next section.
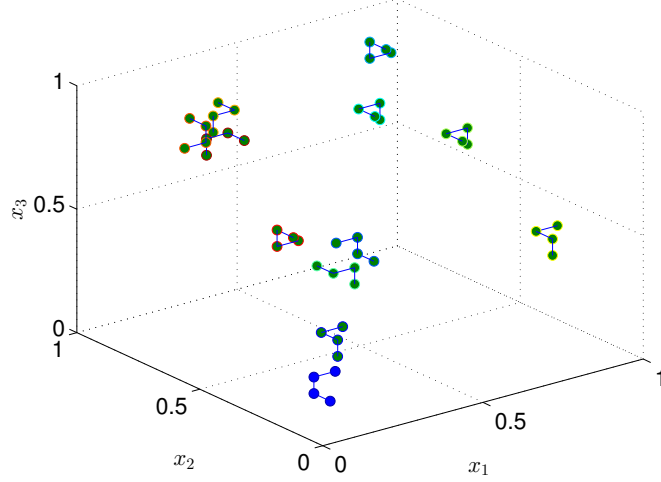
Figure 2.2 – An example of our proposed set of Morris trajectories in the 3-D unit hypercube, based on a LHS for the initial points and on a distinct grid around each point.

2.3.2   Statistical measures of the EEs

After realizing the trajectory construction, the EEs are evaluated and their finite distributions for each input are obtained. For the i-th input, the EEs values distribution is denoted by $\mathfrak{F}_i$, i.e. $EE_{i,r}(\mathbf{x}) \sim \mathfrak{F}_i$. Morris studied only the central tendency and the spread of these distributions. Nevertheless, in order to obtain better results, Campolongo et al. proposed in [Campolongo et al., 2007] the additional study of the mean of the EEs absolute values distribution, i.e. $|EE_{i,r}(\mathbf{x})| \sim \mathfrak{G}_i$. That way, the cancellation of EEs having both positive and negative signs during the calculation of the distribution's mean value, a common error of the Morris method, can be avoided. Finally, the three measures under consideration in this enhanced EEs method are the following:

- μ - the mean of $\mathfrak{F}_i$, which assesses the overall influence of the factor on the output:

$$\mu_i = \frac{\sum_{j=1}^{r} EE_{i,j}}{r}$$

- σ - the standard deviation of $\mathfrak{F}_i$, which estimates the ensemble of the factor's higher order effects, i.e. non-linear and/or due to interactions with other factors:

$$\sigma_i = \sqrt{\frac{\sum_{j=1}^{r}\left(EE_{i,j} - \mu_i\right)^2}{r}}$$

- and μ^* - the mean of $\mathfrak{G}_i$, which implements μ in detecting factors with EEs of both signs (non-monotonic):

$$\mu_i^* = \frac{\sum_{j=1}^{r} |EE_{i,j}|}{r}$$

.

Despite the local nature of the EEs, by averaging them the method can be regarded as a global one. It can be also linked theoretically to the global but expensive variance based measures like the Total Sensitivity Index, by expressing μ^* in terms of conditional variances [Campolongo et al., 2005].

2.3.3   Interpretation of the statistical measures

Taking a closer look on the distribution moments considered, we can attribute an intuitive explanation to their meanings. The first moment μ is the mean of the EEs distribution. This measure shows the overall importance of a factor, since a high mean implies high EEs values, i.e. big difference for the I/O function between two adjacent trajectory points. However, if the I/O function takes non-monotonic values and the EEs have both signs, μ alone can be misleading. It is exactly where μ^*, concerning the absolute values of the EEs, can complement our knowledge over a factor. The meaning of μ^* is exactly the same as that of μ, apart from the fact that it is stronger as a measure and more reliable. On the other hand, the standard deviation σ of the EEs can demonstrate the way the EEs values are distributed around the mean μ. The higher σ is, the further from the mean the EEs values are distributed. In so saying, the location of the points used for the evaluation of the EEs is important either because of the non-linear effect of the factor to the I/O function, or because of the interaction of this factor with the others.

If two of the EEs statistical measures are combined, extra information on the sensitivity of the model can be extracted. Morris in [Morris, 1991] recommended considering at the same time the values of μ and σ. He even adopted a graphical representation in the $\mu\sigma$-plane, which allowed the interpretation of the results by taking into account both sensitivity measures. If both μ and σ of an input factor x_i have large or small values, then x_i is a very important factor or non-significant respectively. High μ and high σ show a factor with large EEs values which are widely distributed from the mean and thus sensitive to the input combinations changes, i.e. non-linear and/or with interactions with other factors. If now μ is small while σ has a considerable value, then the factor probably has EEs of different signs which cancel each other and its overall importance is not reflected with μ. It is where μ^* can supplement our knowledge on the factor by showing the mean value of its EEs absolute values, to identify if the factor is finally important or not.

When μ and μ^* are combined, information on the signs of the effects that the factor has on the output, is provided. If for example μ is low while μ^* is high, it means that the factor examined has effects of different signs depending on the point of the space at which the effect is computed [Campolongo and Cariboni, 2007]. If μ and μ^* are both high, then the sign of the effect is almost always the same, i.e. the output function is monotonic with respect to that factor. When μ^* is combined with σ, linear and non-linear effects can be identified. If both μ^* and σ are low the factor show negligible effects, if μ^* is high while σ is low the factor is important but its strong effect on the output is close to linear. If both μ^* and σ have high values, the factor

shows non-linear effects and/or interaction effects with the other inputs. In Table 2.1, the effects that an input parameter can have on the forward function with respect to the EEs statistical measures, are gathered and roughly presented. Concerning the EEs statistical measures' results, in what follows both representation in the $\mu\sigma$- and $\mu^*\sigma$-planes will be adopted. In Fig. 2.3, the different steps of our screening method are depicted.

Values of statistical moments	Effect of the factor
High $\mu \Rightarrow$ high μ^*	High overall importance of the factor
High σ	High non-linear and/or interaction effects
Low μ and high μ^*	Non-monotonic effects, EEs of both signs
High μ^* and low σ	Strong linear effects, weak interactions
High μ^* and high σ	Strong effects including interactions and non-linearities

Table 2.1 − The different values and combinations of values for the statistical moments of the EEs and their corresponding effects on the I/O function.
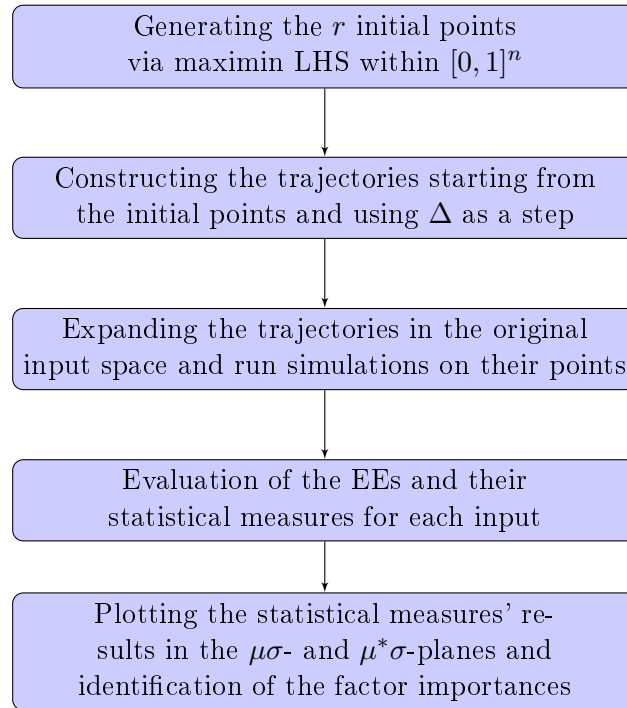
Figure 2.3 − The flowchart representing the step of the screening SA procedure.

2.4   Test with a toy function

After presenting the selected screening method, we will test it on a toy function to demonstrate its performance. The g-function introduced by Sobol' will be used for this test. This is a fairly complex function, which is commonly used as a toy function for SA. It can be defined for as many input variables necessary and for n dimensions it is given by the following formula:

$$g\left(\mathbf{x}\right) = \prod_{i=1}^{n} g_i\left(x_i\right) \tag{2.1}$$

where:

$$g_i\left(x_i\right) = \frac{|4x_i - 2| + a_i}{1 + a_i} \tag{2.2}$$

with $\mathbf{x} = (x_1, \ldots, x_n)^T \in [0,1]^n$ and $a_i \in [0, \infty)$ for all $i = 1, \ldots, n$. Using (2.2) and the fact that $0 \le x_i \le 1$ we can determine the range of variation of each $g_i\left(x_i\right)$, which depends on its corresponding a_i value:

$$1 - \frac{1}{1 + a_i} \le g_i\left(x_i\right) \le 1 + \frac{1}{1 + a_i} \tag{2.3}$$

It is obvious that the higher the a_i is, the less important the x_i is for the g-function [Campolongo and Cariboni, 2007]. Whilst for a small a_i value, the range of the corresponding $g_i\left(x_i\right)$ is wider, resulting in large EEs values and a strong effect on the g-function. For the test case presented here we considered $n = 6$ inputs and the corresponding a_i values used together with the ranges of variation for the $g_i\left(x_1\right)$ are given in Table 2.2. The levels of the discretization of the input space were $p = 20$, in order to have a finer study of that space, similar to the one performed on COSMO later on, and $\Delta = 1/\left[2(p-1)\right] \approx 0.0263$. There were 50 trajectories of $n + 1 = 7$ points generated and the whole simulation time was 0.2 s, using a common laptop. The results obtained by the SA of the g-function are presented in Fig. 2.4.

Factor	a_i	Range of $g_i\left(x_i\right)$
x_1	0.0001	$[0.0001, 1.9999]$
x_2	0.01	$[0.0099, 1.9901]$
x_3	1	$[0.5, 1.5]$
x_4	5	$[0.8333, 1.1667]$
x_5	40	$[0.9756, 1.0244]$
x_6	100	$[0.9901, 1.0099]$

Table 2.2 − The values of the a_i parameters and the corresponding $g_i\left(x_i\right)$ ranges of the 6-dimensional g-function. The larger the a_i, the narrower the domain of its $g_i\left(x_i\right)$ is and thus the less important the factor is for the function.

As expected, the first 2 variables x_1, x_2, having the smallest a_i values and thus the widest ranges of variation for the corresponding g_i's, are the most important factors of the function[15]. This is demonstrated by the high μ^* values, implying high EEs values and the high σ values implying strong interactions with the other factors and non-linear behavior. The x_3, x_4 are following, showing effects of medium and relatively minor importance. The last two variables have effects with almost zero values for all 3 moments of interest, being thus characterized as negligible for the model. It is also obvious from the differences between the μ and μ^* values, that all the factors produce EEs of both positive and negative signs, according to their overall importance, something expected because of the non-monotonic nature of the g-function. It can

---

[15]Since the Screening methods are not as detailed as the quantitative ones, variables that are of similar importance on the model's output are often grouped together. They are definitely separated from the other variables, but their position within their "group" don't always reflect their exact importance, as it happens in this example.
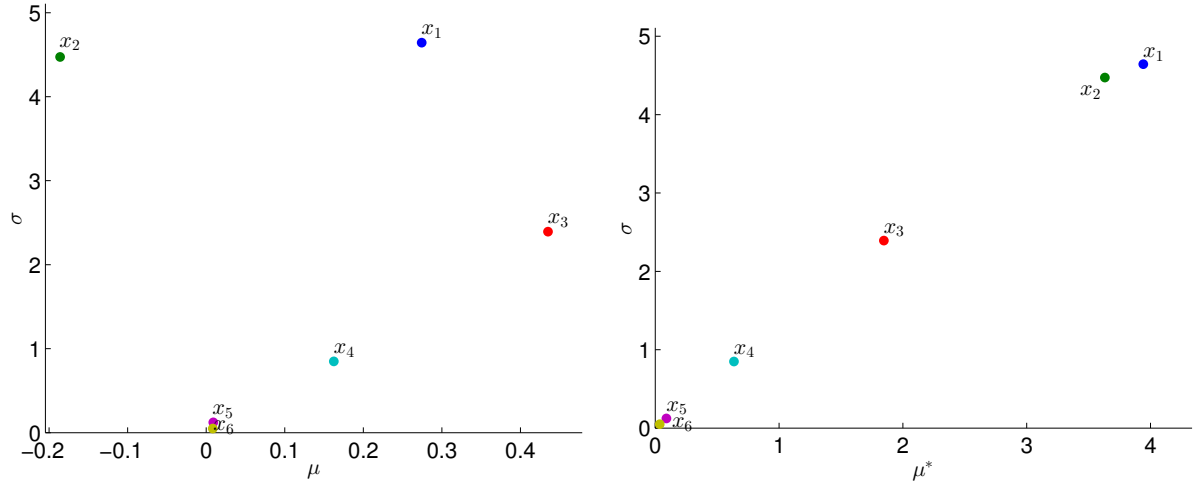
Figure 2.4 – The statistical measures of the EEs for the 6-D g-function in the $\mu\sigma$-plane (left) and in the $\mu^*\sigma$-plane (right).

be therefore concluded that this enhanced Morris method, despite the fact that it does not exploit the function under study, provides accurate and detailed enough results about the nature and the sensitivity of this function. So, we can proceed in applying this method to COSMO and examine the sensitivity with respect to a certain number of its input factors.

2.5   Application: Screening of COSMO

COSMO is able to generate many different forest arrangements and simulate their investigation under several radar configurations. It employs up to 40 numerical and non-numerical inputs. Because of the purpose of our study and in order to reduce the computational cost, which can be relatively high even for a rough screening study, we imposed some limitations. Firstly, only periodical or semi-periodical forests were examined, so that the tree positioning effect was highlighted. Random arrangements were not investigated, since they are represented only by the tree density parameter, which can be examined in the fully or semi-periodical cases also. Secondly, as already mentioned trunks and primary branches were only considered in this project and so the parameters concerning twigs, leaves and the tree crown were ignored. The non-numerical parameters could not be treated obviously. Finally, 12 factors concerning the radar configuration and the forest characteristics were qualified for the screening and they are listed, together with their corresponding symbols, in Table 2.3.

During the SA of COSMO several cases were considered, but only four, having the most representative results, will be presented here. These ones refered to a forest of trunks only and the same forest with 25 equal primary branches per trunk, illuminated under incidence angles within the $[20°, 70°]$ and the $[5°, 85°]$ ranges. The number of primary branches chosen was much higher than the average number observed in ground truth experiments of this type of forests, as seen in [Saleh et al., 2005]. This choice was done on purpose, so that the branches dimensions' effects could be more obvious during the SA investigation. Fourteen different COSMO outputs were investigated and they are presented in Table 2.4. These miscellaneous outputs correspond to the different observables treated during radar forest investigations, for certain potential

Physical quantity	Symbol
Signal frequency	F
Angle of incidence	θ
Moisture of the ground in %	m_g
Moisture of the vegetation in %	m_v
Forest age	A
Ambient temperature	T
Sand content of the ground in %	S
Clay content of the ground in %	C
Radar height	H_R
Distance in range dimension	dx
Distance in azimuth dimension	dy
Maximum displacement of trunks from periodical position	e

Table 2.3 – The 12 physical magnitudes considered for the screening of COSMO and their corresponding symbols. They were parameters concerning the radar configuration and the forest geometrical and ecological characteristics.

objectives. Each output was examined separately, but also grouped with other similar ones, like e.g. all the backscattering coefficients together, and even all outputs as a whole. Whenever all inputs were considered, the backscattering coefficients were not included, since their sensitivities are directly connected with these of the amplitudes of the received signal (see Eq. 1.8). The screening study of the groups was performed by examining the aggregate effect of each input to all the group outputs. However, when the grouped outputs were of different nature and thus magnitude, a normalization by the absolute value of their means before calculating the EEs was necessary so that all the EEs would be comparable. Every time a separate SA was performed for each output, or the outputs were of the same nature and magnitude, e.g. the phases, the values were not normalized. By running these different SA for COSMO, we aimed to identify the sensitivity of each output, as well as the overall sensitivity of the model.

As far as the EE method parameters are concerned now, $p = 20$ was the number of the inputs space levels and $\Delta = 1/\left[2(p-1)\right] \approx 0.0263$ the step in the unit hypercube. The p parameter was selected even, as recommended in [Campolongo and Cariboni, 2007], and big enough to discretize finely the input space. This fine discretization was proven indispensable to obtain trustworthy results. Since some input factors like the frequency have extended domains, separating the $[350\,\mathrm{MHz}, 2\,\mathrm{GHz}]$ interval into just 4 levels could be misleading. For the step Δ, in order to have an idea about the real step of each factor, it has to be multiplied by the range (maximum-minimum value) of each factor's domain. For the angle for example, considering the $[20°, 70°]$ domain, the real step was $\Delta_\theta = \Delta \cdot (70° - 20°) = 1.3°$. After providing the details of our Screening study of COSMO, the presentation of the results for each case separately follows.

2.5.1 Study of a forest of trunks - Radar angles

In this first SA test for COSMO we investigated extended ranges for all 12 factors varying, for the case of a forest of trunks only. There were actually 13 factors varying, in the other cases

Physical quantity	Symbol
Amplitude of the p-received q-emitted signal	$\|E^r_{pq}\|$
Backscattering coefficient of the p-received q-emitted signal	σ^0_{pq}
$HH - VV$ backscatter difference	$\sigma^0_{HH} - \sigma^0_{VV}$
Absolute phase of the p-received q-emitted signal	ϕ_{pq}
$HH - VV$ phase difference	$\phi_{HH} - \phi_{VV}$
First Pauli vector component	$S_{HH} + S_{VV}$
Second Pauli vector component	$S_{HH} - S_{VV}$
Third Pauli vector component	$2S_{VH}$

Table 2.4 – The different COSMO outputs examined during the screening and their corresponding symbols.

also, since the ground consists of sand, clay and slit, which all three have a fixed sum of 100%. So, whenever the sand and the clay contents were varying, the slit content was varying also. The ranges of variation for the 12 factors examined are presented in Table 2.5. For the sand and clay values, their sums were always less than 95% so that even a small percentage of slit could be present in the ground content. We did not examined thoroughly all possible cases for the synthesis of the ground, since its influence did not appear important for the model's outputs, as we will see in the following plots.

Variable	Domain
Frequency (F)	$[350, 2000]$ (MHz)
Angle of incidence (θ)	$[20°, 70°]$
Moisture of the ground (m_g)	$[10, 70]\,\%$
Moisture of the vegetation (m_v)	$[10, 70]\,\%$
Age (A)	$[10, 50]$ y.o.
Temperature (T)	$[0, 35]$ (°C)
Sand content (S)	$[10, 80]\,\%$
Clay content (C)	$[10, 80]\,\%$
Radar height (H_R)	$[200, 5000]$ (m)
Distance in range (dx)	$[3, 15]$ (m)
Distance in azimuth (dy)	$[3, 15]$ (m)
Displacement (e)	$[0.01, 5]$ (m)

Table 2.5 – Ranges of the inputs considered for the general Screening SA of COSMO.

Let us proceed now to the presentation and annotation of this SA results, depicted in the plots of Fig. 2.5. The first remark which can be done is that the frequency is the model's most important parameter, with respect to all three statistical measures, followed by the forest age. It is also obvious that the frequency has non-monotonic effects, since μ and μ^* values differ significantly, while the age shows definite linear effects. These behaviors can be attributed to the cylinder backscattering on the one hand and to the increasing backscattering of the trunks as the age and subsequently their dimensions are augmenting. Continuing, the gravimetric

humidity of the vegetation and the angle of incidence have average effects on the model and the humidity of the ground and the displacement e minor effects. Apart from the moisture of the ground which affects directly the permittivity and so the ground reflectivity, the other inputs show non-monotonic effects. The angle and the vegetation humidity show also a medium non-linearity due to several phenomena as the cylinder effect and the variation in the VV backscattering, with respect to the vegetation permittivity (probably because of the Brewster angle effect, see Section 3.4). The rest of the parameters can be considered as negligible, since they show EEs values very close to 0. If we focus on the SA of the separate outputs, the three amplitudes of the backscattered field as well as the backscattering coefficients in all polarizations show very similar results between them, as expected, and also with the aggregate ones as seen in Fig. 2.6. On the contrary, a very different relation between the phase difference $\phi_{HH} - \phi_{VV}$ and the inputs is depicted in Fig. 2.7. Concerning this output, all the parameters affecting the range, especially the height of the radar, the displacement and the distance along the site dimension were the most important factors, together with the incidence angle and the frequency.
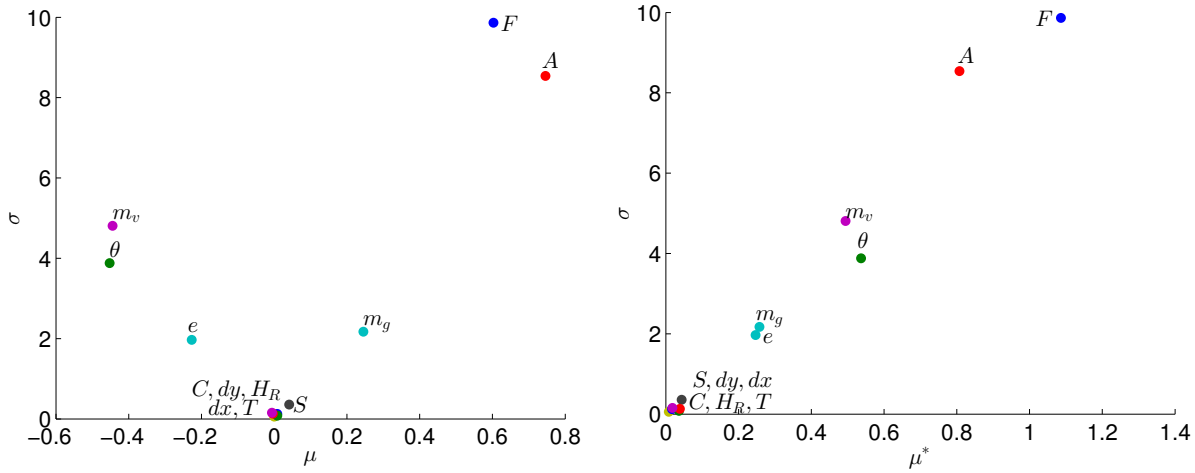
Figure 2.5 − The aggregate screening results for all normalized outputs considered at the whole COSMO frequency band and angles from $20°$ *to* $70°$ *in the* $\mu\sigma$*-plane (left) and the* $\mu^*\sigma$*-plane (right). A forest of trunks only was examined. The frequency, the age, the vegetation moisture and the incidence angle are the most important parameters overall.*

2.5.2   Study of a forest of trunks - All angles

In this second screening test all parameters were varying as in the first case, apart from the angle of incidence. In the previous analysis we focused on angles mostly used in radar campaigns, while in this one we extended the angle range to $[5°, 85°]$. The aggregate results for all outputs are shown in Fig. 2.8. An obvious change with respect to the previous case, is that the incidence angle is now the second most important parameter showing high non-linear effects too. This difference could be attributed to a fast decay of the backscattering observed for angles bigger than $70°$ and certain low frequencies and to the Brewster angle effect. As we will see in details in section 3.4, when just trunks are present, a big drop of the backscattered energy because of this effect is taking place for certain low frequencies mainly and under an angle of incidence around $15° - 20°$. These effects seem to affect significantly the frequency also, as it is still
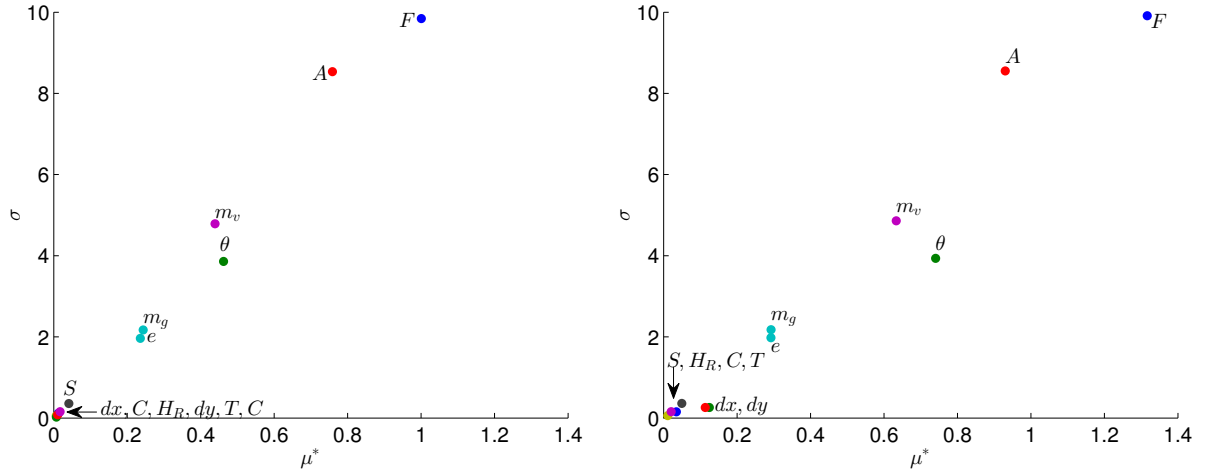
Figure 2.6 – The screening results for μ^*, σ of the received signal's amplitudes (left) and the backscattering coefficients (right) in all polarizations, considered at the whole COSMO frequency band and angles from $20°$ to $70°$. A forest of trunks only was examined. As expected, similar results are appearing in both plots due to the way the backscattering coefficients are calculated. These results are also similar to the ones of Fig. 2.5.
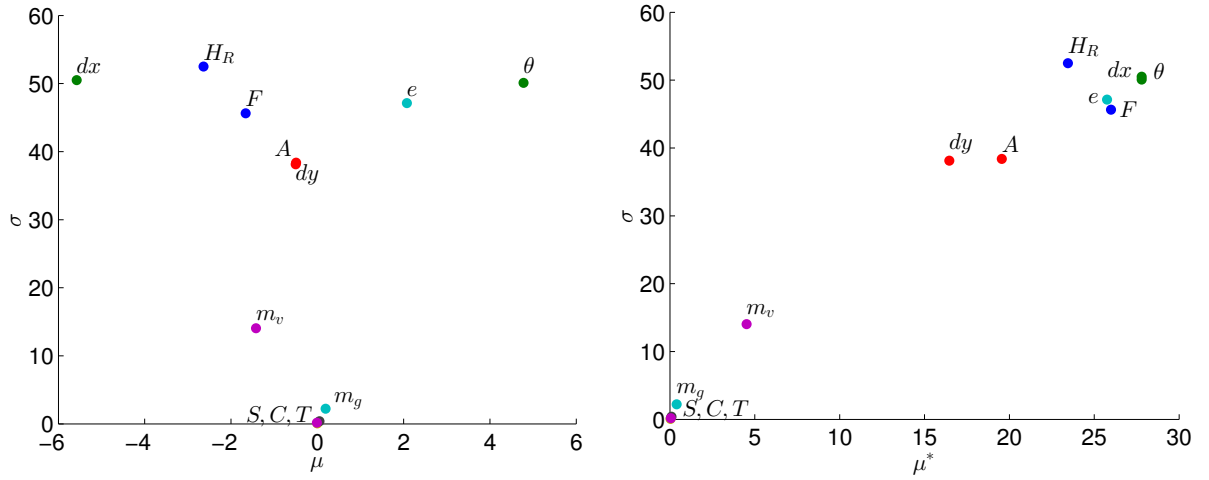
Figure 2.7 – The screening results for the phase difference $\phi_{HH} - \phi_{VV}$ considered at the whole COSMO frequency band and angles from $20°$ to $70°$. A forest of trunks only was examined. As expected, parameters affecting the range are among the most important ones.

the most important parameter, but with stronger influence than in the previous case. This stronger influence could be attributed mostly to the described mutual interactions with the angle.

Another important remark for this case is that while the humidity of the vegetation show the same more or less behavior in both cases, the ground moisture has a much stronger effect in the present case. This can be due to the fact that under large incident angles the double bounce scattering mechanisms, where the ground interferes, dominate the backscatter. About the separate outputs, the σ_{pq}^0 show the same dependence on the inputs as the aggregated outputs, while the phase difference is again highly affected by the positioning parameters. What is also
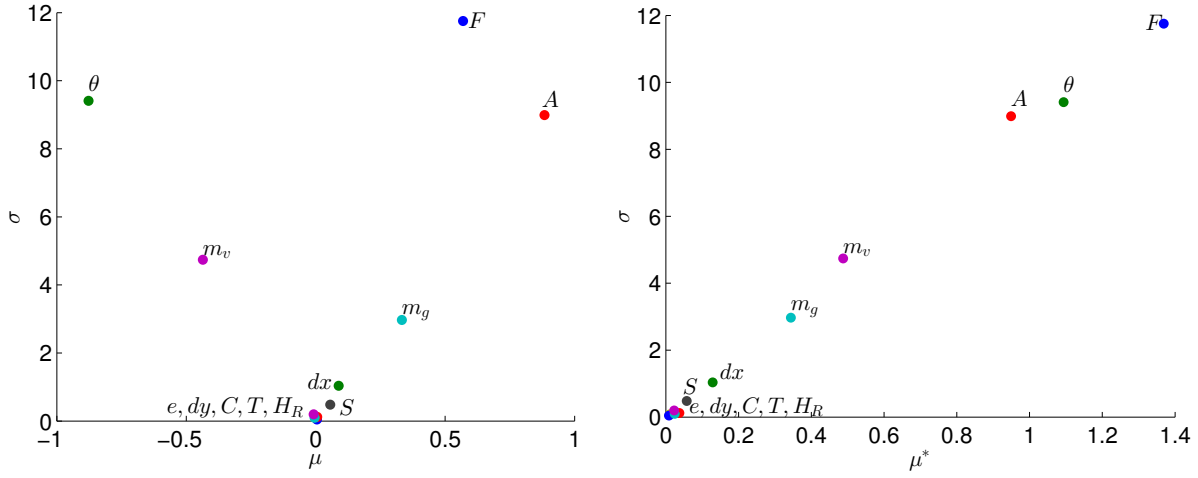
Figure 2.8 – The aggregate screening results for all normalized outputs considered at the whole COSMO frequency band and angles from 5° to 85° in the $\mu\sigma$-plane (left) and the $\mu^*\sigma$-plane (right). A forest of trunks only was examined. When expanding the angle domain of study, the angle becomes the second most important parameter behind the frequency only.

evident is the existence of interactions of the angle with the F, dx, e parameters and the two humidities. These interactions are reflected on the increased σ values of these factors compared to the ones corresponding to the radar angles, as seen in the right plots of Fig. 2.9 and 2.7.
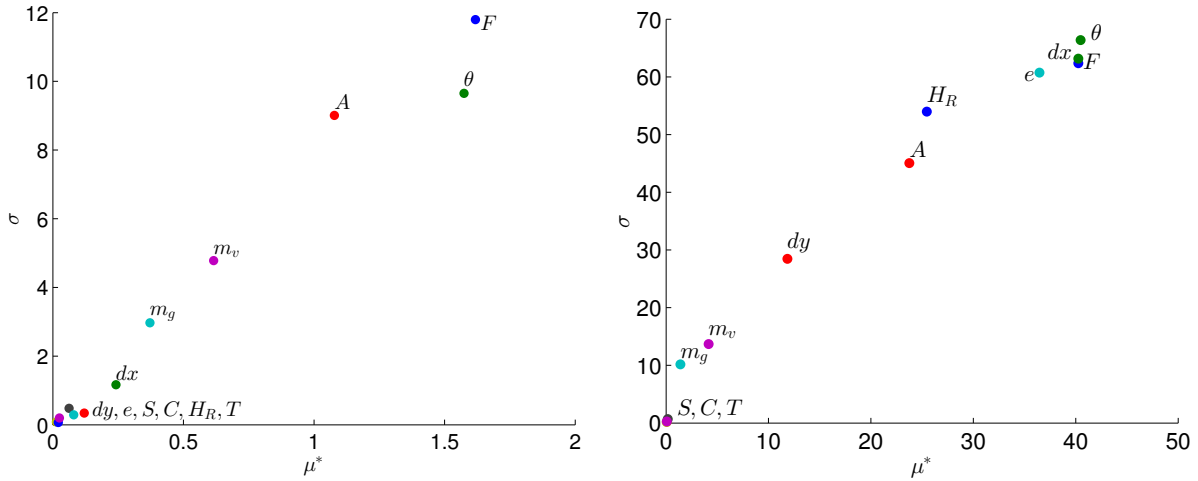
Figure 2.9 – The screening results for μ^*, σ of the backscattering coefficients in all polarizations (left) and of the phase difference $\phi_{HH} - \phi_{VV}$ (right), considered at the whole COSMO frequency band and angles from 5° to 85°. A forest of trunks only was examined. The angle θ is the most important factor for the phase difference and the second most important for the σ_{pq}^0.

2.5.3   Study of a forest of trunks and branches - Radar angles

After studying the simple case of a forest of trunks, let us now examine the effect of the branches addition to the model behavior. The same forest arrangements with the trunks

only cases were studied, where each trunk had now twenty five primary branches uniformly distributed around it. The number of the primary branches was selected bigger than in reality, in order to make the branches effect more obvious. The branches dimensions, same for all branches of the scene, were the average values derived from the age as explained in Paragraph 1.3.3. This means that all coeval forests had the same dimensions for their trunks and their branches. As far as the rest of the parameters were concerned, the same values and angle domains were investigated as in the cases of trunks only. When the angles commonly used by radars were considered, the screening aggregate results for all outputs can be seen in Fig. 2.10.
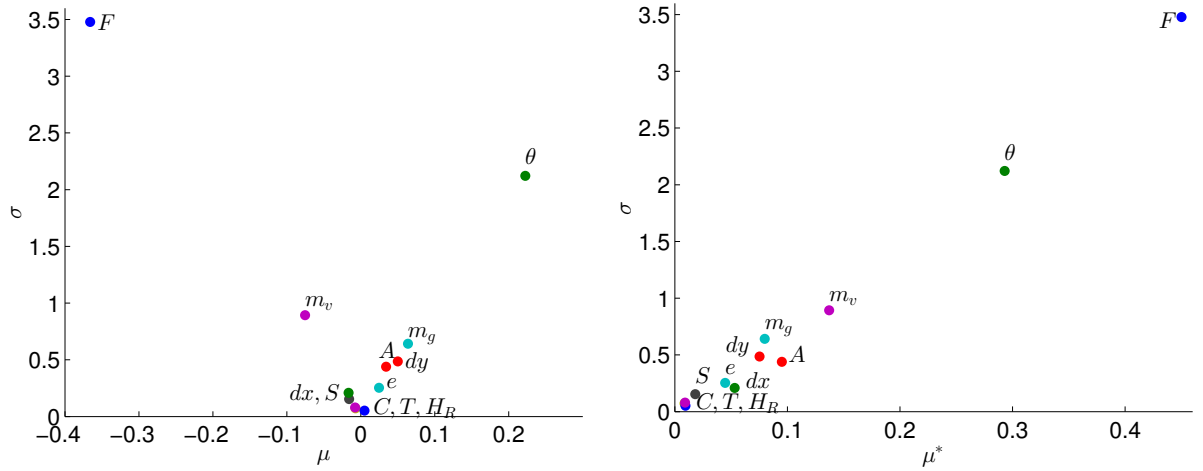
Figure 2.10 − The aggregate screening results for all normalized outputs, considered at the whole COSMO frequency band and angles from 20° *to* 70°*, in the* $\mu\sigma$*-plane (left) and the* $\mu^*\sigma$*-plane (right). A forest of trunks and branches was examined. Frequency and angle are the most important factors, with weaker effects than in the trunks only case.*

In that case, the radar frequency was again by far the most important model input followed by the incidence angle. The effects though, seem much weaker than in the trunks only case. This can be due to the much stronger forest backscatter in high frequencies when branches are added, compared to the fast decay observed when just trunks were considered. This difference was observed during the investigation of the forest elements effect on the backscatter and is presented in details in Chapter 3. A characteristic example of this branches effect can be seen in Fig. 2.11, where σ^0_{HH} decays much slower when branches exist. The effect is apparent even in a forest where just 10 branches per tree were considered. The rest of the COSMO factors treated are of rather small importance, with the vegetation moisture being the most influential among them and the height of the radar, the temperature and the ground content the negligible ones. In Fig. 2.12 the screening results for all three backscatter coefficients and the phase difference are also presented. As expected, for the σ^0_{pq} the results are very similar to the aggregate ones, while $\phi_{HH} - \phi_{VV}$ is affected a lot by the positioning factors. Nevertheless, the existence of branches raised the significance of frequency making it the most important parameter together with e for the phase difference also. Branches increased in addition the vegetation moisture effects, probably because of the large increase of the single bounce scattering observed via the second Pauli vector component $S_{HH} - S_{VV}$ (see Fig. 2.13).
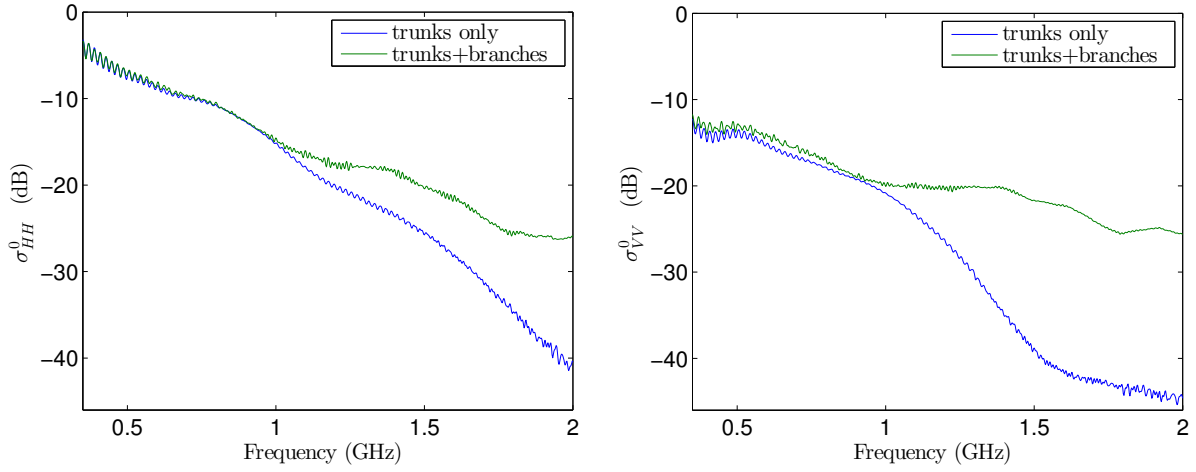
Figure 2.11 – The backscattering coefficients of the received signal in HH polarization (left), in VV (right) for the cases of a forest with trunks only and the same trunks with 10 branches added to each one. The incidence angle of the emitted wave was $40°$. The decay of the backscattering for frequencies higher than $1\,\mathrm{GHz}$ is faster when just trunks are considered, something that explains the stronger and non-linear parameter effects observed in that case.
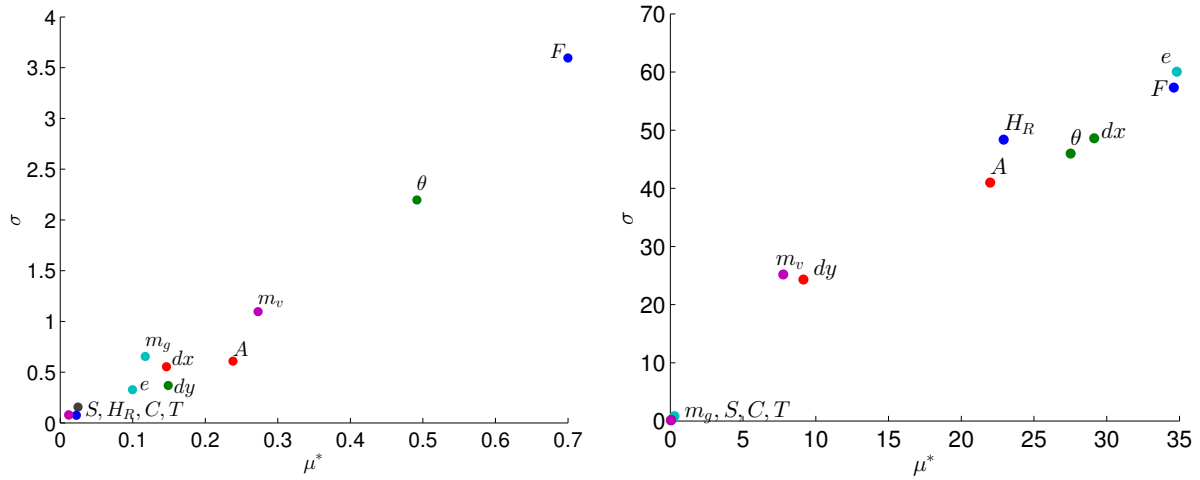
Figure 2.12 – The screening results in the $\mu^*\sigma$-plane, for the backscattering coefficients of the received signal in all polarizations (left) and the phase difference $\phi_{HH} - \phi_{VV}$ (right), considered at the whole COSMO frequency band and angles from $20°$ to $70°$. A forest of trunks and branches was examined. There is a much weaker age effect on the σ^0_{pq}, but stronger F and e effects on the phase difference.

2.5.4 Study of a forest of trunks and branches - All angles

If the angle domain is extended to the $[5°, 85°]$ one, during the branches case study, a notable change is observed with respect to the previous example. The incidence angle was for the first time the most important model parameter followed by the frequency, in both the aggregate results and the results concerning the backscattering coefficients, as seen in Fig. 2.14 and 2.15. It was probably due to the weaker backscattering decay with respect to the frequency, observed when branches exist. For the phase difference, e and θ were still the most important factors.
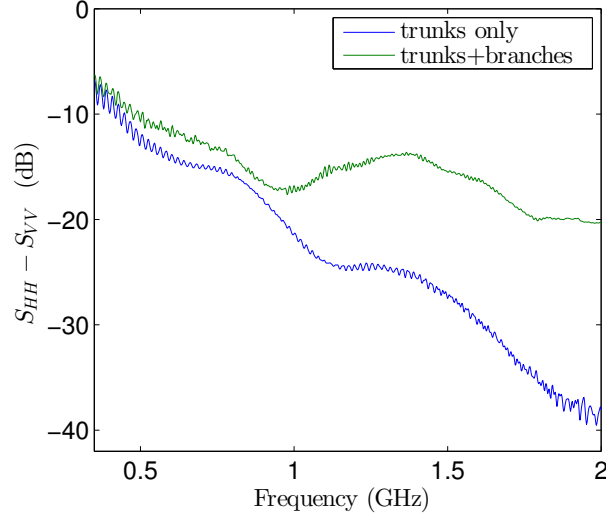
Figure 2.13 – The comparison of the $S_{HH} - S_{VV}$ values obtained from a forest of trunks only and the same trunks with 10 branches added on each one. The big difference observed for frequencies higher than 1 GHz, can be attributed to the branches significant single bounce scattering.

Nonetheless, if we compare the results from the two angle cases, as depicted in the right plots of Fig. 2.12 and 2.15, it is implied by the higher μ^* and σ values that the angle showed much stronger effects in the present case. The rest of the parameters did not appear to change behaviors, apart from the higher moment values observed and attributed to the interactions with the angle.
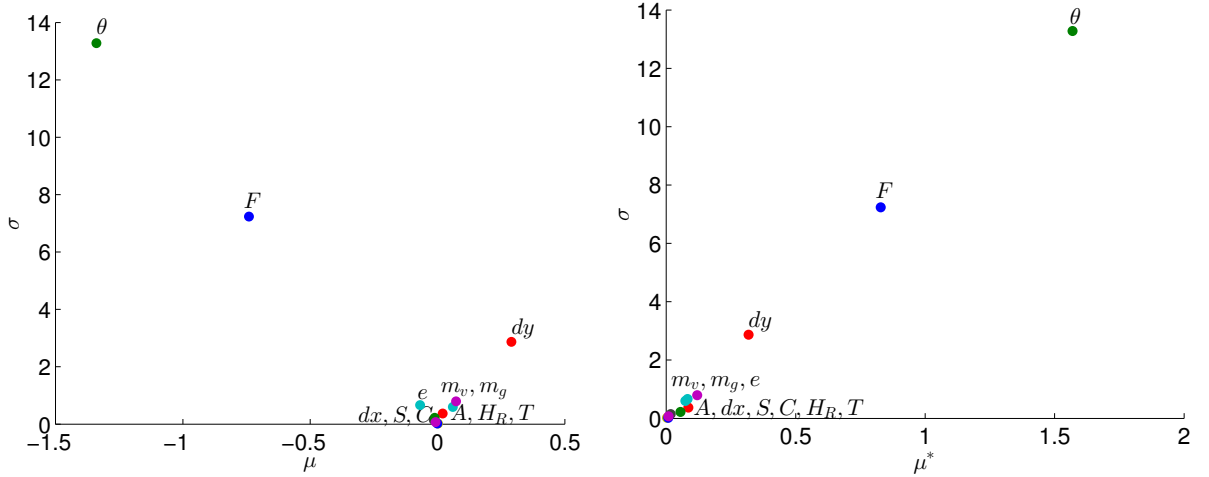
Figure 2.14 – The aggregate screening results for all normalized outputs, considered at the whole COSMO frequency band and angles from 5° to 85°, in the $\mu\sigma$-plane (left) and the $\mu^*\sigma$-plane (right). A forest of trunks and branches was examined. It is the first example where the angle becomes the most important model factor.
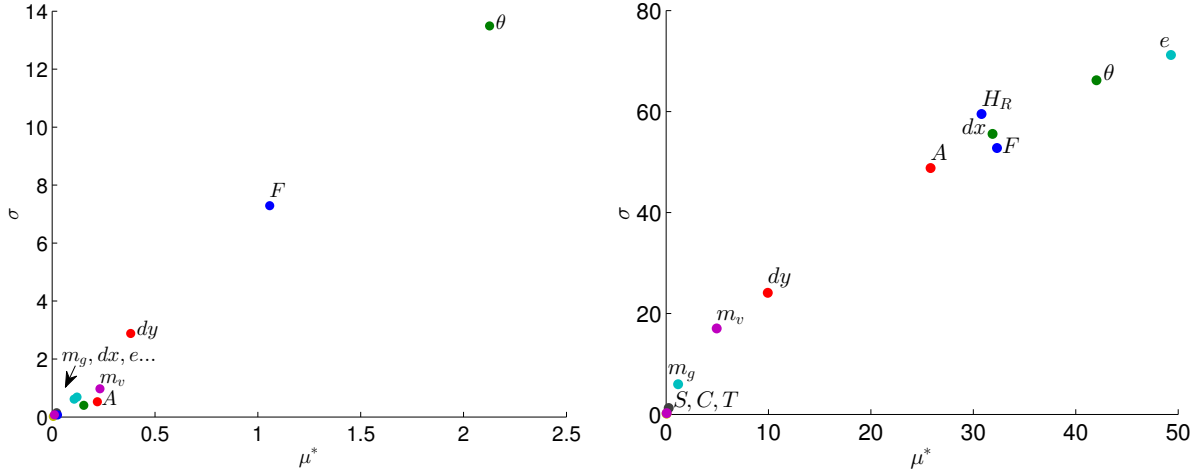
Figure 2.15 – The screening results in the $\mu^*\sigma$-plane, for the backscattering coefficients in all polarizations (left) and the phase difference $\phi_{HH} - \phi_{VV}$ (right), considered at the whole COSMO frequency band and angles from 5° to 85°. A forest of trunks and branches was examined. e remains the most important parameter for the phase difference, followed by θ after the expansion of the angle domain of study.

2.6   Conclusions

In the previous pages, we quickly reviewed SA and its main methods, with more emphasis given to the Morris screening method. This method, in its particular version implemented by Camplolongo et al., was at a next step adjusted to fit our purposes and applied to COSMO. It was the first time, to the best of our knowledge, that a mathematical technique from DASE was applied to radar studies of forests. Different cases concerning fully or quasi-periodical forests of trunks only and of trunks and branches were examined. A wide domain was investigated for each of the inputs under consideration. Finally, by performing this SA on COSMO, we succeeded in assessing the importance of its main input factors, via their effects on the several different outputs. The frequency and the incidence angle of the emitted signal were identified as the most important COSMO parameters, followed by the age of the forest and the permittivity of the vegetation. On the contrary, the radar height, the temperature and the ground synthesis parameters showed negligible effects and can in most of the experiments be set at constant values to lighten COSMO, without largely affecting its performances.

The case of the phase difference where the positioning parameters were of great importance was highlighted also. In addition, we discovered the fact that the angle can sometimes be the most important factor of the model, showing highly non-linear behavior and interactions with the frequency mostly. This has to be further examined and considered during the angle normalization methods for the backscatter comparison, which are mainly based on cosine models as seen in [Huang et al., 2015]. These new information on COSMO and forest radar studies that the SA came with, need to be further verified. In saying so, distinct COSMO simulation studies for each important factor are necessary, in order to confirm its high importance and examine the extent of the effect. These studies will be carried out in the upcoming chapter.

3

Analysis of the forest backscattering with COSMO

Contents

3.1 Introduction

After presenting the Screening SA method and testing it on COSMO in the previous chapter, we will now proceed to the validation of its conclusions, while analyzing the COSMO simulation results. The purpose of this chapter is not to exploit COSMO and go deeply into the physics of the forest scattering, but rather to justify and study on the one hand the results of the SA concerning the model's most important parameters (the frequency, the angle of incidence, the age and the humidity of the vegetation), and on the other hand to verify our proposed strategy. In saying so:

(i) to check and analyze the effects of these important parameters, as well as the effects of the different forest elements and arrangements,

(ii) to interpret and explain these effects in terms of the physics of the phenomenon, whenever possible

(iii) and to suggest optimal radar configurations (frequency and polarization) for the detection of these effects, during radar investigations.

In the next chapter, we will complement this analysis by checking the applicability and the utility of the metamodel in step (i), while using the configurations suggested in step (iii). So that the use of the metamodel would provide a fast and real-time analysis, to be carried out during our future adaptive radar observations.

The analysis done in this chapter, consisted of the examination of the forest response in both frequency and time domains. As far as the frequency domain is concerned, the analysis was performed on the polarimetric quantities introduced in Chapter 1, i.e. the σ^0_{pq} and the components $\mathbf{k}_{P_i}$ of the Pauli feature vector, as presented in Eq. 1.20. From the three components of $\mathbf{k}_P$, representing the double bounces, the single bounces and the volume scattering respectively, the first two were mainly examined. The conclusions concerning the breaking of the symmetry and thus the volume scattering provided by the third component, could be also derived by the σ^0_{VH}. During the time domain analysis, only the amplitude of the received signal was investigated. An IFFT was employed to transform the received signal from the frequency domain to the time domain, using all the emitted bandwidth each time. An analysis like this took place for the first time in the a radar study of forests. As a consequence, the extraction of supplementary information on the forest geometrical structure was possible.

3.2 Frequency domain analysis

In this first part of the analysis, we will examine the received signals simulated by COSMO in the frequency domain, which is the model's original domain. The identification of the most important factors by the SA, will be now validated and the factors specific effects will be checked. Then, the investigation of the effects regarding the branches presence, their density, the addition of a spherical target and the forest arrangement will follow. The whole COSMO frequency spectrum $(350\,\mathrm{MHz} - 2\,\mathrm{GHz})$ will be used under all linear polarizations. In the first subsection, the angles examined will vary within the $[20°, 70°]$ interval. For the rest of the analysis though, the results obtained under a constant angle of $40°$ will be presented only, for the sake of brevity and the results relevance. An angle like this, is commonly used to normalize backscatter datasets acquired for different incidence angle values as e.g. in [Mladenova et al., 2013].

As far as the scene is concerned, it was a maritime pine forest, as described in Section 1.3.3, distributed within a scene of about $40\,\mathrm{m} \times 50\,\mathrm{m}$. There were 63 trees generated, having their trunks inclined up to $10°$ from the vertical position and the branches uniformly distributed around them. In the generic case there were no branches, in order to focus on trunks which mainly backscatter in the frequencies we use. Whenever branches were added, it will be explicitly stated. The distribution of the trees was periodical, when not mentioned otherwise, having a $6\,\mathrm{m}$ mutual distance between them in both directions. The age of the forest was 30 years in all experiments, apart from these where the age effect on the forest scattering was studied, in Paragraphs 3.2.2 and 3.3.2. The rest of the scene parameters concerning the trunks, the branches when added, the ground etc. are gathered in the Table 3.1. The choice of the parameters was arbitrary,

respecting though the real data, the allometric equations concerning this type of forests - taken from [Saleh et al., 2005] and presented in Section 1.3.3 - and the physical constraints. However, there were various cases examined which could be regarded as far from being real, since for instance forests with naked trunks do not exist in general. These theoretical examples were selected on purpose, in order to serve in the isolation and identification of certain scattering effects.

Parameters	Values
Trunk height	18.6 m
Trunk radius	15.9 cm
Ambient temperature	15 °C
Gravimetric humidity of the ground m_g	40%
Sand content	50%
Clay content	30%
Silt content	20%
$\mathrm{Re}\,(\varepsilon_g)$	$[33.57, 38.47]$
$\mathrm{Im}\,(\varepsilon_g)$	$[-5.81, -2.53]$
Branch length	93 cm
Branch radius	3.13 cm
Volumetric / gravimetric vegetation humidity	40% / 35.7%
$\mathrm{Re}\,(\varepsilon_v)$	$[9.92, 13.1]$
$\mathrm{Im}\,(\varepsilon_v)$	$[-5.87, -3.28]$
RMS height of ground roughness	5 cm
Correlation length of ground roughness	1 m

Table 3.1 – The ground and the vegetation parameters concerning the COSMO simulations analyzed in this chapter. The values of the humidity of the vegetation and the corresponding permittivity stand for all experiments, apart from the ones where these quantities were the subject of the study.

Before starting the analysis of the most critical model parameters, let us first present the effects on the model outputs of two of the non-important parameters, the moisture of the ground and the ambient temperature. During the SA in the previous chapter, these factors were not among the essential ones, especially for the radar angles as seen in Fig. 2.5. By examining different values for these quantities and testing the change on the backscattering, we finally arrived in confirming the SA conclusions. As presented in Fig. 3.1, the temperature shows almost no effect on σ^0_{HH}. At the same time, the ground humidity shows a very small and linear influence on σ^0_{HH} and a negligible one on σ^0_{VH}. To highlight these conclusions, we provided both results for the ground moisture, because σ^0_{VH} was the most varying quantity in the other forest parameters cases, as we will see later on. Similar results were discovered for the other polarimetric quantities under study, but they will not be presented as these tests served rather as a verification of our SA results and they are not part of the upcoming analysis.

3.2.1 Effects of the frequency and the angle

The analysis of the received signal generated by COSMO, will focus firstly to the effect of the two most important parameters of the model identified by the SA, i.e. the frequency and the
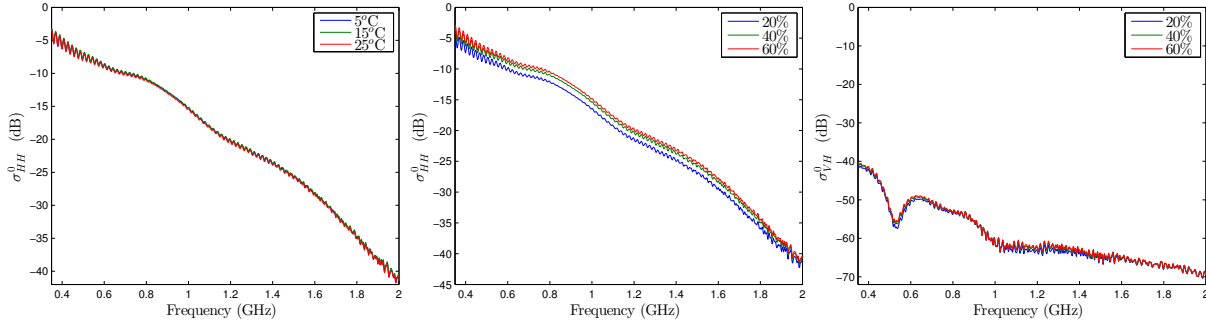
Figure 3.1 − The HH backscattering coefficient for the same forest of trunks having three different ambient temperature values (left) the same quantity for three different values of the ground humidity (middle) and the VH backscattering coefficient for the same three values of the ground humidity (right). The effects present on the signals, confirm the SA conclusions which stated that temperature is among the negligible COSMO factors, while the humidity of the ground - with its weak and linear modification - is among the non-important ones.

angle of incidence of the emitted EM wave. As already mentioned, COSMO operates in P- and L-bands within the $[350\,\mathrm{MHz}, 2\,\mathrm{GHz}]$ frequency range and it can "emit" under all possible angles of incidence from $1°$ to $89°$. Nevertheless, in this analysis we will examine only angles within the $[20°, 70°]$ interval, which are the most commonly used in radar observations, and the whole frequency band. The effects on the backscattered signal of six different angles of incidence will be presented, those of $20°, 30°, 40°, 50°, 60°$ and $70°$. Variations of $\sim 10°$ or less are usually assumed to produce negligible variability effects (see [Mladenova et al., 2013]) and they were not examined. In this stage of the study, a forest of trunks only will be examined in order to isolate and focus on the desired effects. The branches effect on the forest scattering will be the subject of Subsection 3.2.3 later on.

Proceeding to the discussion of the results obtained, the corresponding plots for the backscattering coefficients and the Pauli vector elements are presented in Fig. 3.2 and 3.3. It is obvious from these graphs, that the backscattered energy tends to decrease with the frequency for small angles. When the angle gets steeper, this effect weakens and the signal fluctuates more around the same values and even increases slightly for the $70°$. For the cross-polarization, the strong decrease gets stabilized after $1\,\mathrm{GHz}$. There is also a threshold around $1\,\mathrm{GHz}$, after which the scattering is stronger for angles $\geq 50°$ in the co-polarizations and in the two first Pauli vector components.

Physical interpretation   As far as the physical interpretation is concerned, because of the existence of the almost vertical trunks only, σ_{HH}^0 is superior to σ_{VV}^0. In addition, the cross-polarized received signal is very low, within the whole emitted bandwidth, since the scene is highly symmetric. Concerning the scattering mechanisms, the graphs of Fig. 3.3 and 3.4 show that the double bounces, as represented by $S_{HH} + S_{VV}$, decrease with the frequency for all angles $< 70°$. The single bounces decrease strongly for angles up to $50°$ and then they mainly fluctuate. The double bounces stay almost always the dominant scattering mechanism, apart from the case of the $20°$ where the trunks scatter equally in single and double bounces. This was rather expected, since in our examination only trunks were present, which favor the double bounces in general.
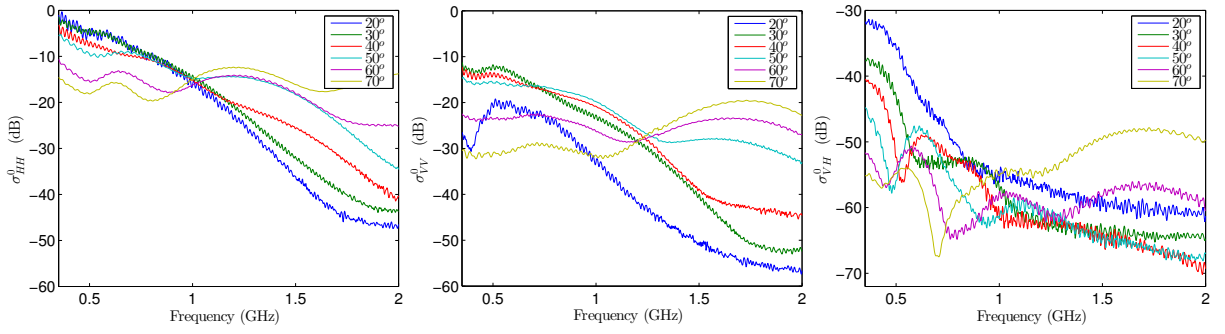
Figure 3.2 – The three backscattering coefficients for the whole COSMO frequency range and 6 different angles of incidence, ranging from 20° to 70°.
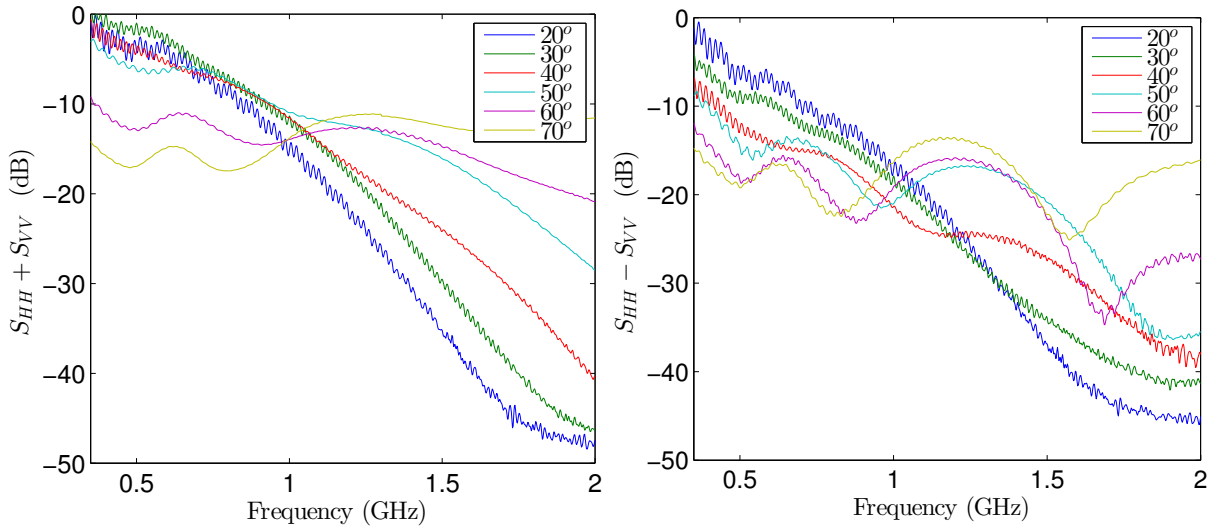
Figure 3.3 – The two first Pauli vector elements for the whole COSMO frequency range and 6 different angles of incidence, ranging from 20° to 70°.
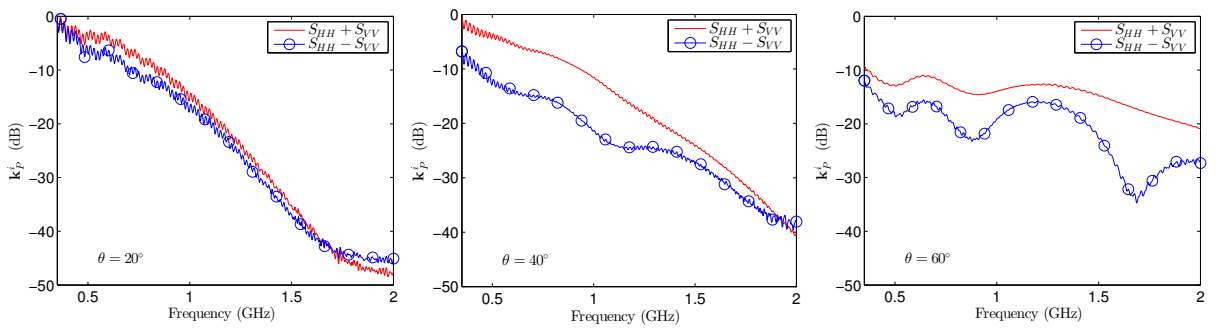
Figure 3.4 – The comparison of the two first Pauli vector components corresponding to the double and single bounces mechanisms respectively, for an incidence angle of 20° (left), 40° (middle) and 60° (right). For the small angles the single backscattering is almost as strong as the double one, while for bigger angles it is the double bounces mechanism that dominates the backscattering.

Another interesting effect observed was the low VV backscattering compared to the HH, for an incidence angle of 20° principally and of 70° secondarily. It was observed directly from the

σ_{VV}^0 values in Fig. 3.2 and indirectly from the nearly equal values of $S_{HH} + S_{VV}$ and $S_{HH} - S_{VV}$ in Fig. 3.4 which imply that $S_{VV} \to 0$. Taking a closer look and comparing the HH and VV values in Fig. 3.5, we see that for large angles the VV and the HH polarizations show similar behaviors, with a constant difference of at most $10 - 15\,\mathrm{dB}$ between their values. Nevertheless, when the incidence angle is $20°$ this difference reaches up to almost $30\,\mathrm{dB}$ for low frequencies, showing a steep drop of the VV values.

Physical interpretation This huge difference could be explained by the Brewster angle effect due to the vegetation and it was actually the fact that triggered a more profound analysis of this effect. However, we will not go further for the moment, as a specific part of this chapter, Section 3.4, is attributed to the analysis and the results of the Brewster angle effect.

To close this section, we could say that the significant alterations of the model behavior with respect to both the frequency and the angle of the wave emission, confirm the SA conclusions. The non-linearities, the fluctuations and the steep drops of the studied values, imply factors with a very strong overall influence on the model, as discovered in the previous chapter and depicted in Fig. 2.5 and 2.8.
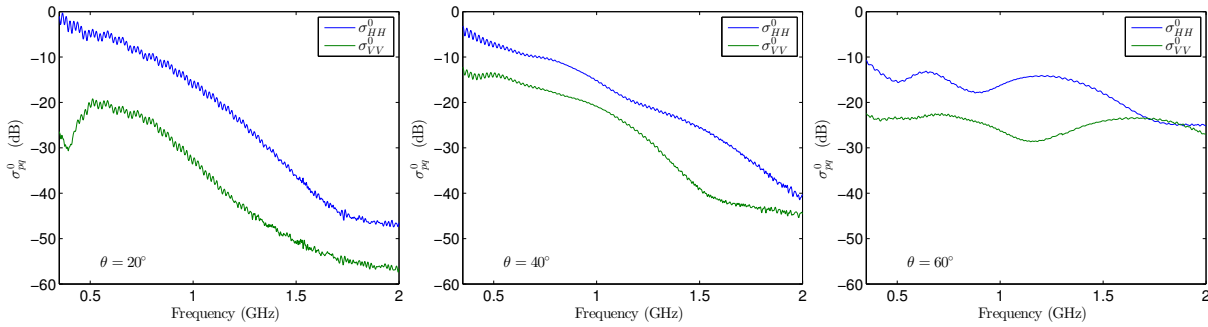
Figure 3.5 − The comparison of the co-polarized backscattering coefficients for an incidence angle of $20°$ (left), $40°$ (middle) and $60°$ (right). A difference between the co-polarized values is almost everywhere existing and takes the highest values for the case of an angle of incidence of $20°$. The latter can be attributed to the Brewster angle effect because of the vegetation scattering.

3.2.2 Study of the age and the humidity effect

After investigating the effect of the most important radar parameters, the frequency and the incidence angle of the emitted signal, we will now continue with the study of the effect of the two most essential forest parameters, the age and the humidity of the vegetation. These factors do not affect the forest backscattering directly, but indirectly via other physical quantities. The age controls the dimensions of the forest elements by the allometric equations (see Section 1.3.3) and the humidity of the vegetation affects directly the dielectric property (see Section 1.3.4) and therefore the reflectivity of the trees. As mentioned before, all the effects will be examined along the whole COSMO frequency band and under a constant incidence angle of $40°$. The effects of the two parameters under study were investigated in a forest of trunks only, so that their effects could be more isolated and identified.

The age effect

As far as the frequency domain analysis of the age effect is concerned, three different forest stands will be presented here. These forests had the same tree arrangement and an age of 10, 30 and 50 years respectively. The dimensions of the trunks corresponding to the three differently aged stands and their ratio with respect to the wavelength are presented in Table 3.2. The results for the σ_{pq}^0 values and the first two components of $\mathbf{k}_P$ are presented in Fig. 3.6 and 3.7. The first conclusion that can be drawn is that the older the trunks were, the more they backscattered and the less "noisy" the signal was. A more interesting result, that can be used for discerning forests of different ages, is the characteristic drops observed in the VH backscattering coefficient for different frequency values (see right plot of Fig. 3.6). The older the forest was, the lower the frequency where the first drop occurred and the more steep the drops were. The age seemed to affect the signal a lot, showing weaker non-linear effects than the frequency and the angle though.

Physical interpretation   The older the trunks, the largest their dimensions are and thus the forest backscattering. Concerning the scattering mechanisms, since just trunks exist, the double bounces dominate the whole COSMO operating band, apart from a few high frequencies close to 2 GHz, for all forest ages (see Fig. 3.8).

Age	Trunk height	height/λ	Trunk radius	radius/λ
10 y.o.	8.13 m	9.5–54	6.6 cm	0.07–0.44
30 y.o.	18.64 m	21.7–124.3	15.9 cm	0.185–1.06
50 y.o.	23.53 m	27.45–156.8	20.2 cm	0.236–1.35

Table 3.2 – The trunk dimensions corresponding to the forest age for the three virtual stands considered in this section. The ratios of these dimensions with respect to the wavelength, are also presented next to the column of each dimension.
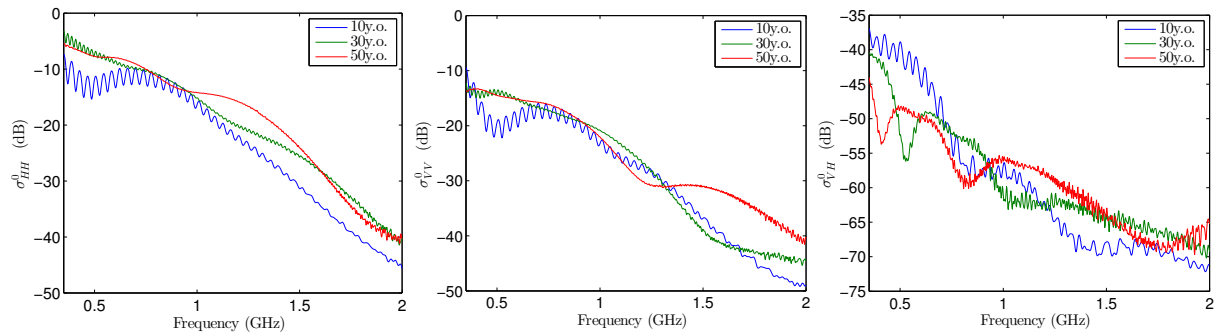
Figure 3.6 – The backscattering coefficients in HH (left), in VV (middle) and in VH (right) for the whole COSMO frequency range and for three different forest ages. The older stands were backscattering more energy in general.
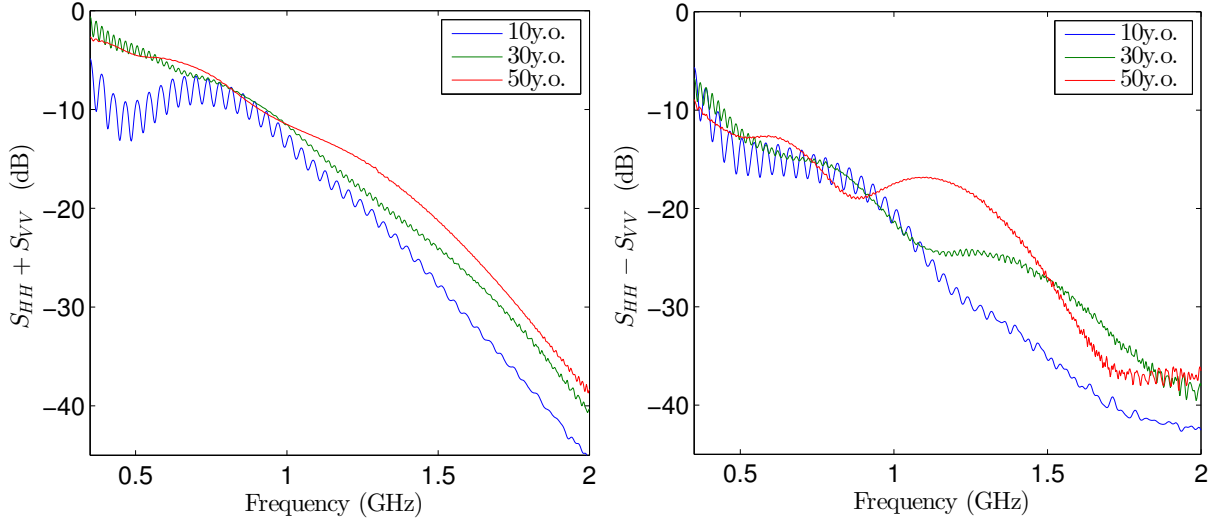
Figure 3.7 – The two first Pauli vector elements for the whole COSMO frequency range and for the three different forest ages of 10, 30 and 50 years.
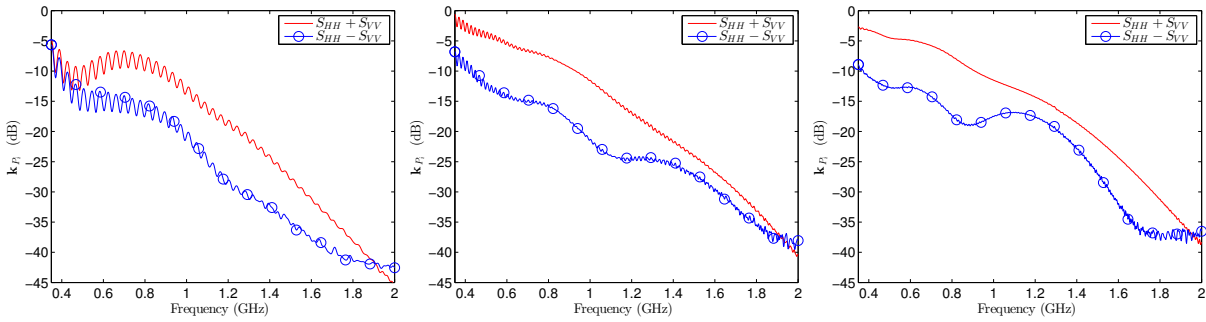
Figure 3.8 – The comparison of the first and second Pauli vector components for three forest of trunks having 10 (left), 30 (middle) and 50 (right) years of age. The first component corresponding to the double bounces mechanism is dominant along almost the whole frequency range for all three cases.

The humidity effect

The volumetric moisture of the vegetation was identified as the fourth most important COSMO parameter during the SA. It was showing in general less non-linear effects than the three more important factors, the frequency, the angle and the age, as deduced by the low variance (σ) values for its elementary effects (see for example Fig.2.8). These SA conclusions and the physical intuition were both reflected in the analysis of the humidity effect presented here. The forest studied was a 30 years old one, with a volumetric percentage of the vegetation humidity varying from 10% to 60%. From the test cases generated and simulated, only three will be presented here, the ones assuming volumetric humidity values of 20%, 40% and 60% respectively. A percentage of 60% for the humidity of the trunks could be regarded as a non realistic one[16], it was chosen though as an extreme case for a more integrated study of the effect. The gravimetric humidities and the real and imaginary parts of the relative permittivities, corresponding to the cases presented here, are contained in the Table 3.3.

---

[16]In [El-Rayes and Ulaby, 1987] the gravimetric content examined reached up to 50% in the centre of the trunk while higher values were considered, but only as far as the leaves were concerning.

m_v^{vol}	m_v^{grav}	$\mathrm{Re}\,(\varepsilon_v)$	$\mathrm{Im}\,(\varepsilon_v)$
20%	17.2%	$[3.59, 4.86]$	$[-1.47, -0.94]$
40%	35.7%	$[9.92, 13.4]$	$[-6.25, -3.28]$
60%	55.6%	$[19.54, 24.64]$	$[-13.4, -6.14]$

Table 3.3 – The gravimetric moisture (m_v^{grav}) and the real and imaginary parts of the relative permittivity corresponding to the volumetric moisture (m_v^{vol}) values examined in this section.

Concerning the results of the humidity effect now, let us start with the backscattering coefficients as done before. It is obvious from Fig. 3.9, that the m_v^{vol} values affected in a more or less linear way the σ_{HH}^0 values and the σ_{VV}^0 values for the wetter vegetation cases. As the moisture was increasing, so did the backscattered energy along the whole frequency band, with the gap being more important between 20% and 40% than between 40% and 60%. The existing non-linear and non-monotonic effects of m_v^{vol} were mostly shown in the dry case and the cross-polarized response. It is mostly the trunks having a $m_v^{vol} = 20\%$ that showed unexpected oscillations for the VV and VH backscattering. These results can be extended to the Pauli vector elements also. As seen in Fig. 3.10, between 40% and 60% the effect for both $S_{HH} + S_{VV}$ and $S_{HH} - S_{VV}$ was almost linear, while the dry vegetation showed a more strange behavior especially in high frequencies.
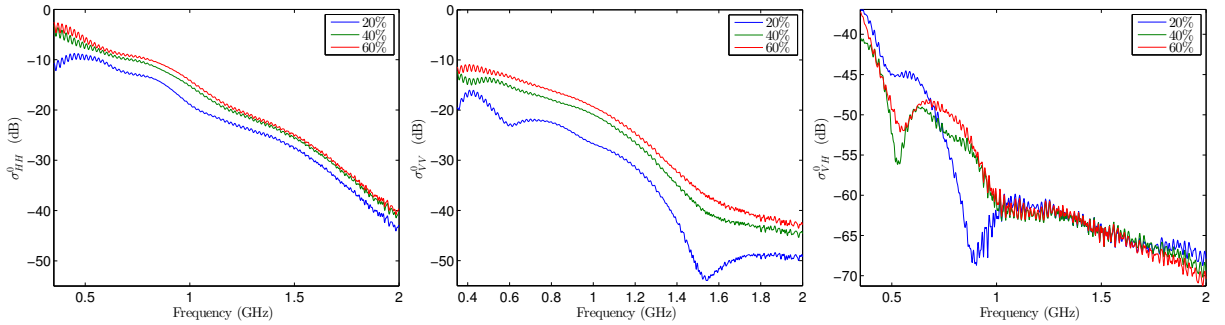
Figure 3.9 – The three backscattering coefficients with respect to the frequency and for 3 different volumetric vegetation humidity values for the forest of trunks. The wetter the vegetation was, the more it backscattered.

Physical interpretation The linear effect of the moisture increase in HH was expected, as well as the same effect on the VV backscattering for the higher moisture values. As the vegetation gets wetter, its permittivity and thus its reflectivity increases, resulting in a stronger signal received by the radar. On the contrary, the dry trunks tend to be more transparent to the incident radiation. As far as the non-linear effect on the σ_{VV}^0 is concerned, it takes place for low moisture values and could be attributed to the Brewster angle effect, since it does not exist in HH. The equal single and double bounces values, as seen in the left plot of Fig. 3.10 for frequencies from $1.4\,\mathrm{GHz}$ and more, verify this conclusion as they imply that $S_{VV} \to 0$. More comments and an integrated analysis on that effect will be provided in Section 3.4. Apart from the case and the sub-band showing this effect, the double bounces mechanism is always dominant as expected since trunks only exist.
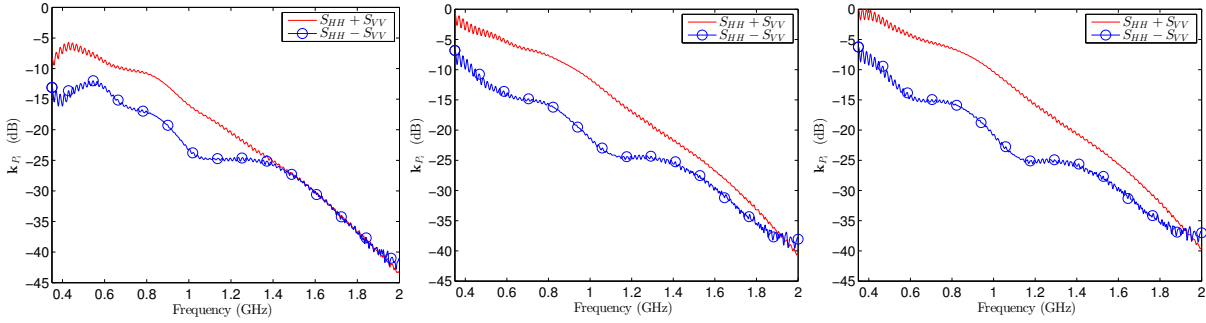
Figure 3.10 − The comparison of the first and second Pauli vector components for three forests of trunks having $m_v = 20\%$ (left), $m_v = 40\%$ (middle) and $m_v = 60\%$ (right) respectively. The first component corresponding to the double bounces mechanism is dominant almost everywhere, especially when the humidity increases.

The examination of the vegetation humidity effect confirmed the SA conclusions. The factor shows relatively average effects on the COSMO outputs, which are more or less monotonic. The few non-linearities provide us the possibility to distinguish the different moisture values for the vegetation. In the case of the dry forests, the VV or the VH backscattering coefficients or the two first Pauli vector elements have to be examined together so that the non-linear drops are detected or the similar co-polarized values. Humidity values of 40% and 60% showed very similar behaviors, despite the difference in the backscattered energy, for all quantities treated. Thus, when the arrangement was the same as in our case, they could be hardly differentiated.

3.2.3   The branches effect

After focusing on the most important COSMO factor effects for a forest of trunks only, in the present section, the examination of the scattering behavior of the branches will be presented. Several different aspects of the branches effect were considered, but those who will be presented here are the most significant and discernible ones. The forest taken under consideration was a periodical one, since the examined effects when the tree positions were semi-periodic with a certain displacement from the periodical positions, were very similar to the ones corresponding to the periodical forest and thus they will not be presented. This periodical forest had 30 years of age and the same parameters values as those given in Table 3.1. The number of the added branches was 10 per tree, corresponding to a density of 0.0422 branches/m^3 for the upper layer of the forest containing them. An incidence angle of 40° was selected as previously. In order to better understand the branches scattering with respect to the emitted frequency, their dimensions and the corresponding ratios with the wavelength are presented in Table 3.4. The very small length/wavelength ratio for all frequencies (ratio < 10), led COSMO to simulate the branches response via the Physical Optics Approximation, instead of the Infinite Cylinder one.

The effect of the branches in the frequency domain, as far as the backscattering coefficients are concerned, is presented in Fig. 3.11. It is apparent from these three plots, that the branches addition affected significantly the received signal in all polarizations. In the co-polarizations the contribution took place in frequencies higher than 1 GHz. This effect was stronger for VV, changing therefore the HH-VV ratio of the trunks. For frequencies close to 2 GHz, the difference

Branch length l$_{\mathbf{br}}$	l$_{\mathbf{br}}$/$\boldsymbol{\lambda}$	Branch radius r$_{\mathbf{br}}$	r$_{\mathbf{br}}$/$\boldsymbol{\lambda}$
93 cm	1.085–6.2	3.13 cm	0.037–0.21

Table 3.4 – The branches dimensions and their ratios with respect to the wavelength. We can see that all ratios are <10.
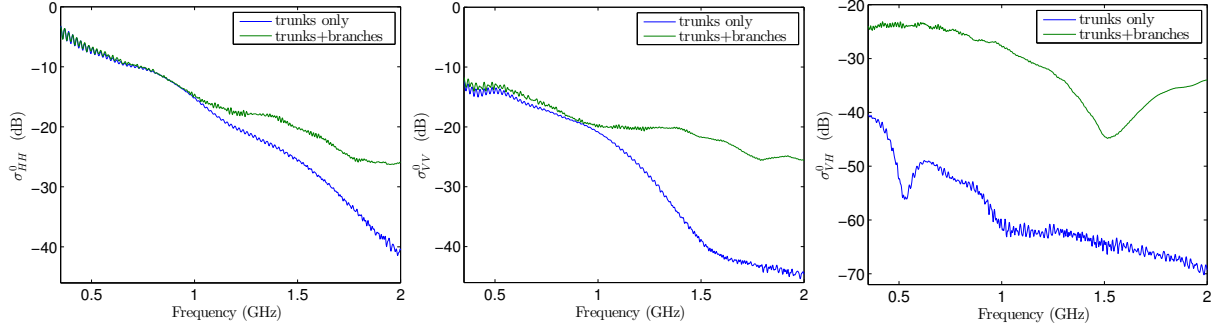
Figure 3.11 – The backscattering coefficients of the received signal in HH polarization (left), in VV (middle) and in VH (right) for the cases of a forest with trunks only and the same trunks with branches added. The branches contribute to the co-polarized signal after 1 GHz and to the cross-polarized one within the whole spectrum. The incidence angle of the emitted wave was 40°.

between the two signals with and without branches took its largest value, which reached 15 dB for the HH polarization and 20 dB for VV. Concerning the cross-polarization now, the branches addition resulted in an increase of the backscattered energy along the whole frequency band, by 16 dB at least. The difference of the two signals took its highest value close to 2 GHz, where it exceeded 35 dB. Another characteristic effect of the branches existence on the VH backscattering, was also the 10 dB drop observed around 1.5 GHz. The Pauli vector coefficients on the other hand, were also enhanced by the branches scattering, in a different way though. As seen in Fig. 3.12 and 3.13, $S_{HH} + S_{VV}$ increased only after 1.6 GHz, while $S_{HH} - S_{VV}$ and $2S_{VH}$ were affected along the whole spectrum used. This was due to the different way branches scatter in the various scattering mechanisms, as we will see in the next paragraph.

Physical interpretation   As expected from the frequencies emitted, the branches contribute mostly on the upper half of the selected spectrum, i.e. the L-band. In low frequencies, the waves penetrate the canopy and the trunks dominate the co-polarized backscattering. The branches response is so low that it is almost invisible up to 1 GHz - where their radius $r_{br} \leq 0.1\lambda$. It is only when the trunks co-polarized scattering becomes inferior to 15 dB, that the branches' contribution is visible. In cross-polarization on the contrary, the effect is very strong for all frequencies. There is always a $15-35$ dB difference between the scattering from the trunks only and the one from the whole trees, as seen in the right plot of Fig. 3.11. Because of their uniform arrangement around the trunks and their various entry angles, the branches "break" the symmetry of the trunks and contribute significantly in the volume scattering of the forest, represented by σ^0_{VH} and $2S_{VH}$ in our plots (Fig 3.11 and 3.12). Apart from the volume scattering, branches contribute also in both double and single scattering mechanisms, as obvious from Fig. 3.13. This contribution is much stronger for the single bounces, than for the double ones. This effect can be attributed to the fact that the branches apart from scattering back the emitted signal, they also attenuate the scattering from the lower level. As a consequence, their effect on the single bounces is strictly
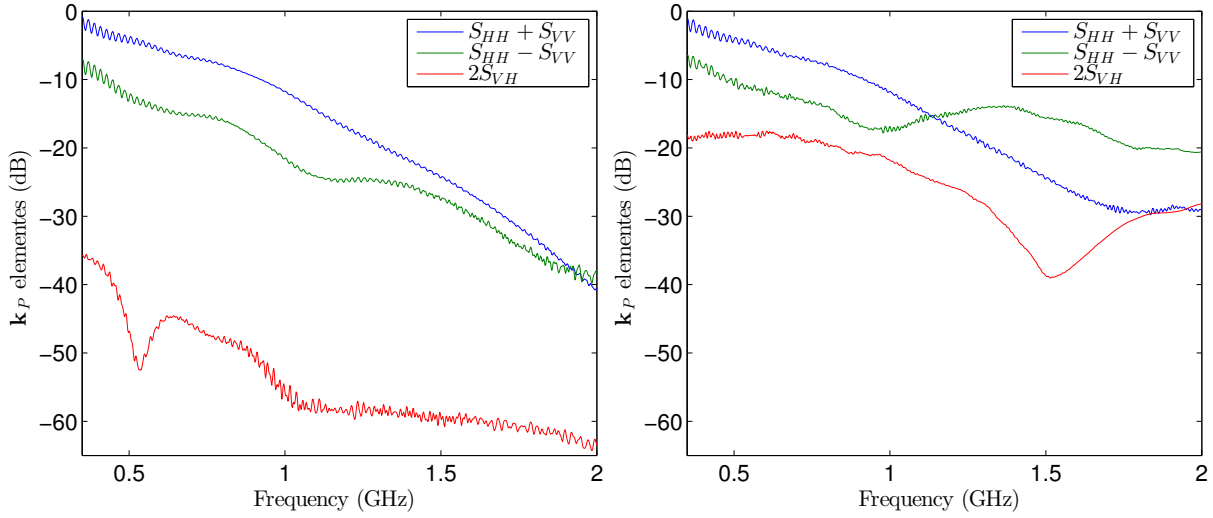
Figure 3.12 – The three Pauli vector elements $S_{HH} + S_{VV}$, $S_{HH} - S_{VV}$ and $2S_{VH}$ for a forest of trunks only (left) and the same forest with the trunks having 10 branches each one. The branches affect mostly $2S_{VH}$ and $S_{HH} - S_{VV}$, while $S_{HH} + S_{VV}$ is modified after 1.6 GHz only.

additive, while in double bounces they both enhance and attenuate the trunks scattering. This is why branches contribute to the $S_{HH} + S_{VV}$ values, i.e. the double bounces scattering, after 1.6 GHz and to the $S_{HH} - S_{VV}$ values, i.e. the single bounces scattering, in almost the whole frequency range. The branches effect on $S_{HH} - S_{VV}$ can reach up to 20 dB where the trunks contribution decays fast, at frequencies higher than 1 GHz. And it is after this threshold - around 1.15 GHz - that the single bounces become the dominant scattering mechanism, as observed in Fig. 3.14. Whereas for the trunks, the double bounces is everywhere dominant. In both cases the scattering decays for double and single scattering, but the change of the dominant mechanism is due to the different decay rates. The volume scattering, as previously mentioned, is much stronger when branches are added, but it is always at least 7.5 dB weaker than the dominant mechanism as seen in Fig. 3.12.

Increasing the number of the branches

The previous results correspond to a forest of trees having 10 primary branches each one. If the number of the branches is increased up to 20 or 30 per tree, with corresponding densities of 0.0845 and 0.1267 branches/m^3 respectively, the results for the backscattering coefficients are presented in Fig. 3.15. As far as the co-polarizations are concerned, there was more energy backscattered (up to 5 dB) in frequencies higher than 1 GHz, where the branches mainly contribute. In lower frequencies, where the trunk scattering was dominant and the branches scattered very weakly, there was almost no difference among the three cases. On the other hand, the cross-polarized backscattering was stronger along the whole frequency range whenever the number of the branches was getting larger. Regarding the Pauli vector now, the increasing number of branches resulted always in an increase of the first component values above 1.6 GHz and of the single bounces along the whole spectrum, especially above 900 MHz (see Fig. 3.16).

Physical interpretation   As expected from the theory, the main conclusion drawn from Fig. 3.15 and 3.16 is that the more scatterers exist, the stronger the backscattered signal is. This was also the case previously, when branches were added to the trunks (see Fig. 3.11),
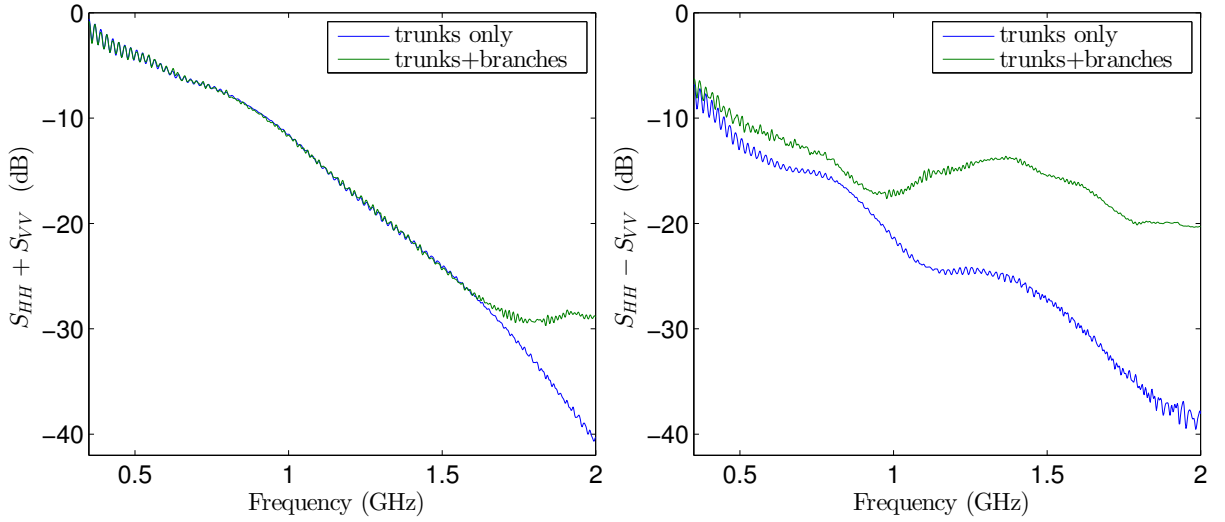
Figure 3.13 – The first Pauli vector element, $S_{HH} + S_{VV}$ (left) and the second $S_{HH} - S_{VV}$ (right), for the cases of a forest with trunks only and the same trunks with branches added. The incidence angle of the emitted wave is 40°. The trunks dominate the double bounces scattering till 1.7 GHz, even when branches exist, whereas the branches contribute to the single bounces scattering along the whole frequency spectrum.
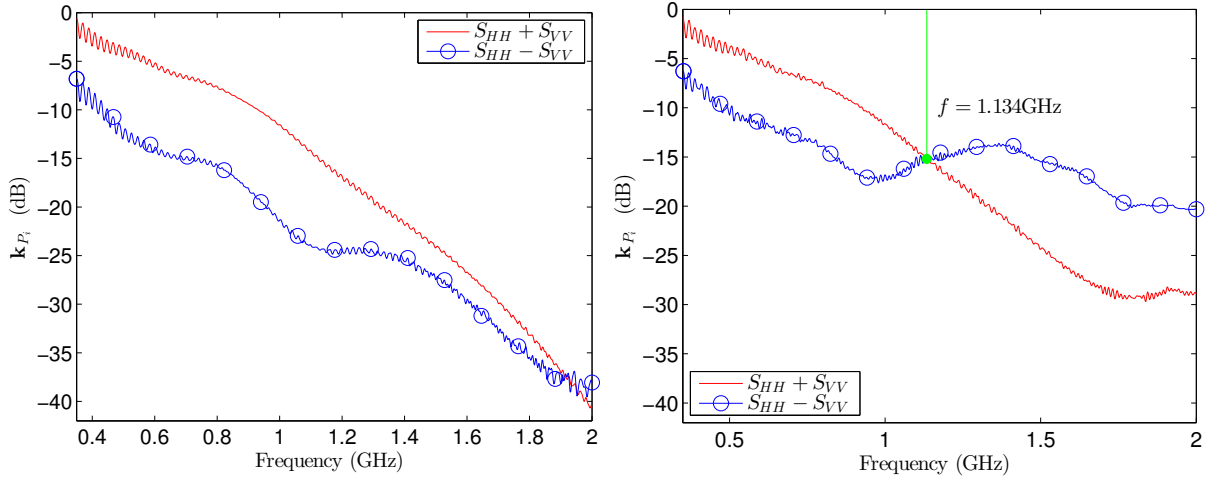
Figure 3.14 – The comparison of the first and second Pauli vector components for a forest of trunks only (left) and the same forest with 10 primary branches per tree (right). The existence of branches change the rate of decay in both quantities causing a change of the dominant scattering mechanism from the double bounces to the single ones, at a frequency of 1.134 GHz.

despite their relatively small dimensions with respect to these of the trunks. Another important conclusion was extracted, when extra focus was put on the single and double bounces mechanisms values. As seen in Fig. 3.17, the decrease with respect to the frequency decays when more branches are added and the frequency where the change of the dominant scattering mechanism from double to single bounces takes place, gets lower with the increase of the branches number. This can be explained by the fact that dense forests act as high frequency, i.e. whatever the situation is, the canopy scattering dominates, as if high frequencies were used.
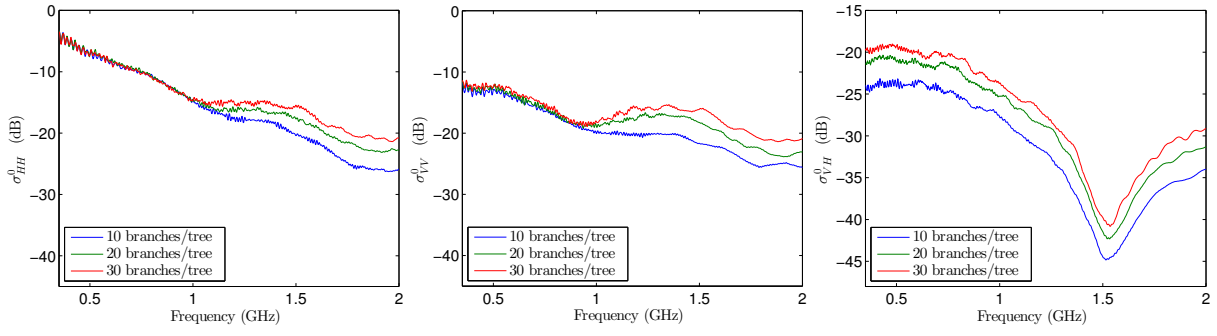
Figure 3.15 – The backscattering coefficients of the received signal in HH polarization (left), in VV (middle) and in VH (left) for the cases of a forest with trunks having 10, 20 and 30 primary branches per tree. The incidence angle of the emitted wave is 40°.
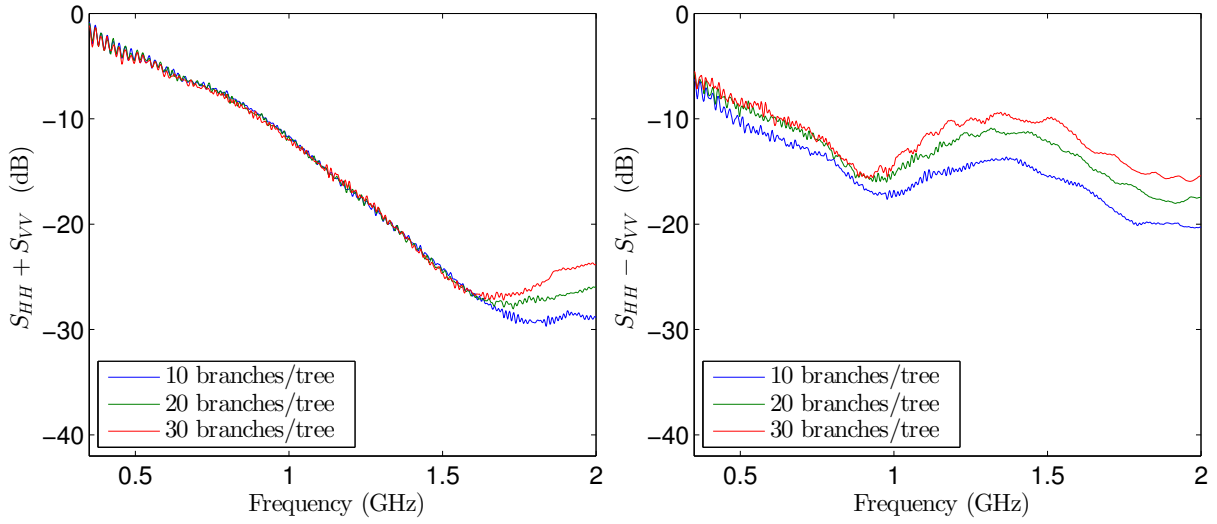
Figure 3.16 – The first Pauli vector element, $S_{HH} + S_{VV}$ (left) and the second $S_{HH} - S_{VV}$ (right), for the cases of a forest with trunks having 10, 20 and 30 primary branches per tree. The incidence angle of the emitted wave is 40°.
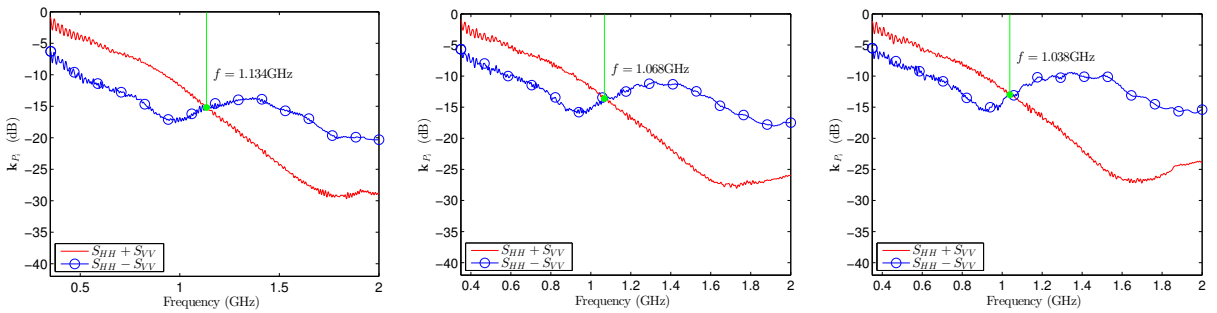
Figure 3.17 – The comparison of the first and second Pauli vector components for a forest with 10 branches per tree (left) 20 branches per tree (middle) and 30 branches per tree (right). As branches are increasing, the frequency where the change of the dominant scattering mechanism takes place was decreasing.

Concluding the aforementioned comments, the existence of branches in a forest is definitely obvious in cross-polarization and in the co-polarizations for frequencies above 1 GHz. So if

the objective of a radar observation is to identify the existence of branches and study their density and arrangement, it is probably better to exploit our results and focus on L-band, no matter the polarization, or just use the cross-polarization in a single polarization system. If the change of the dominant scattering mechanism needs to be studied, intermediate frequencies (0.8-1.3 GHz) have to be selected. These recommendations will be validated in Chapter 5, during the realizations of our proposed sequential strategy.

3.2.4   The target effect

One of the main objectives of the radar campaigns over forested areas, is the so-called FOPEN (Foliage Penetration) detection of targets hidden in a forest concealment. So, this section is devoted to the examination of the effect, caused by placing a target among the trees of a periodical forest. The target was supposed to be a perfectly electric conducting sphere (PEC), with a radius $r_t = 2\,\mathrm{m}$. The radius was chosen to be sufficiently larger than the wavelength ($r_t/\lambda \in [2.33, 13.33]$), so that COSMO could easily estimate its backscattering contribution. This sphere was positioned on the ground, in the empty space between the fourth and fifth trunk lines along the site dimension, while generating the forest (see Fig. 3.18). Two cases were again considered, a forest of naked trunks and one where 10 uniformly distributed branches were added to each trunk.
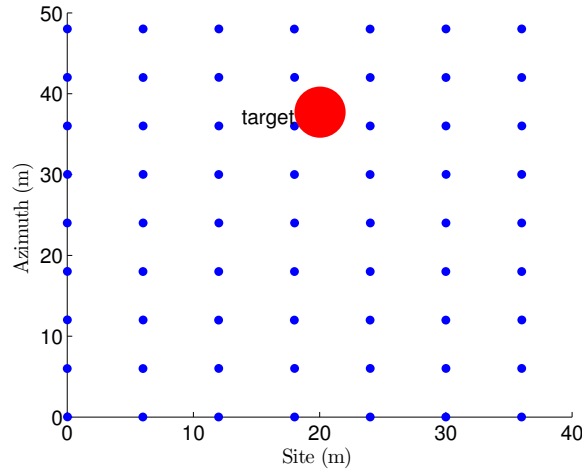
Figure 3.18 − The position and the size of the target hidden within a periodical forest. The target is generated by COSMO between the fourth and the fifth trunk lines in the site dimension.

At first, let us examine the target effect on the COSMO simulation results, when just trunks were considered. The addition of the target among the trees caused a significant difference - more than $20\,\mathrm{dB}$ - in the power backscattered in both co-polarizations, after $1\,\mathrm{GHz}$ (see Fig. 3.19). For the VV polarization in addition, the signal was much more noisy when the target was present and almost equal in power to the HH one for frequencies higher than $1.2\,\mathrm{GHz}$. On the contrary, the difference observed in the cross-polarized signal, as seen in the right plot of Fig. 3.19, was almost negligible along the whole frequency range. As far as the Pauli vector components are concerned, $S_{HH} + S_{VV}$ was slightly inferior when the target was present, while the $S_{HH} - S_{VV}$ was significantly enhanced and almost stabilized around $-15\,\mathrm{dB}$ after $1\,\mathrm{GHz}$

(see Fig. 3.20). When branches existed in the scene the target effect was much weaker, as expected. It was again negligible for the co-polarizations in low frequencies and it became stronger ($\sim 5\,\mathrm{dB}$) in high frequencies, as seen in Fig.3.21. In cross-polarization, the target positioning in the forest resulted in a slight power decrease. Lastly, as seen in Fig. 3.22 the $S_{HH} + S_{VV}$ values were almost not affected at all, whereas the $S_{HH} - S_{VV}$ ones were a little enhanced for $f \geq 500\,\mathrm{MHz}$. In all cases, the stronger target contribution was observed in $2\,\mathrm{GHz}$.
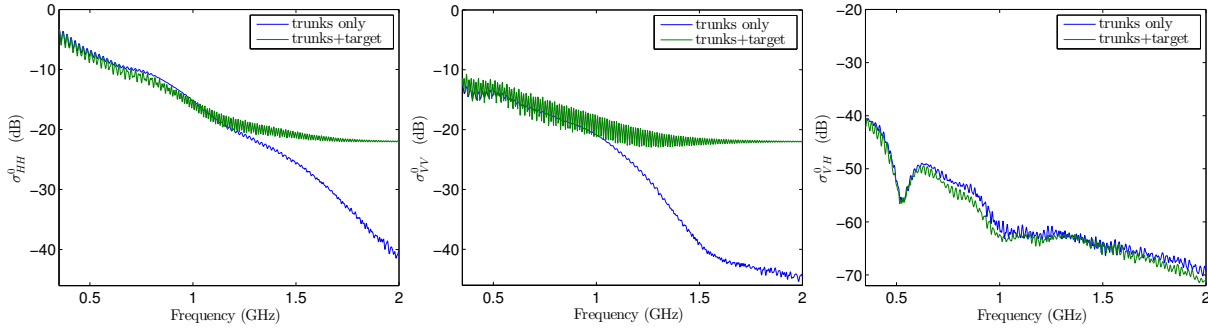
Figure 3.19 – The backscattering coefficients of the received signal in HH polarization (left), in VV (middle) and in VH (left), for the cases of a forest with trunks only and the same forest with a spherical target hidden in it. The effect of the target is clearly visible in the co-polarizations for frequencies $> 1\,\mathrm{GHz}$. The incidence angle of the emitted wave was $40°$.
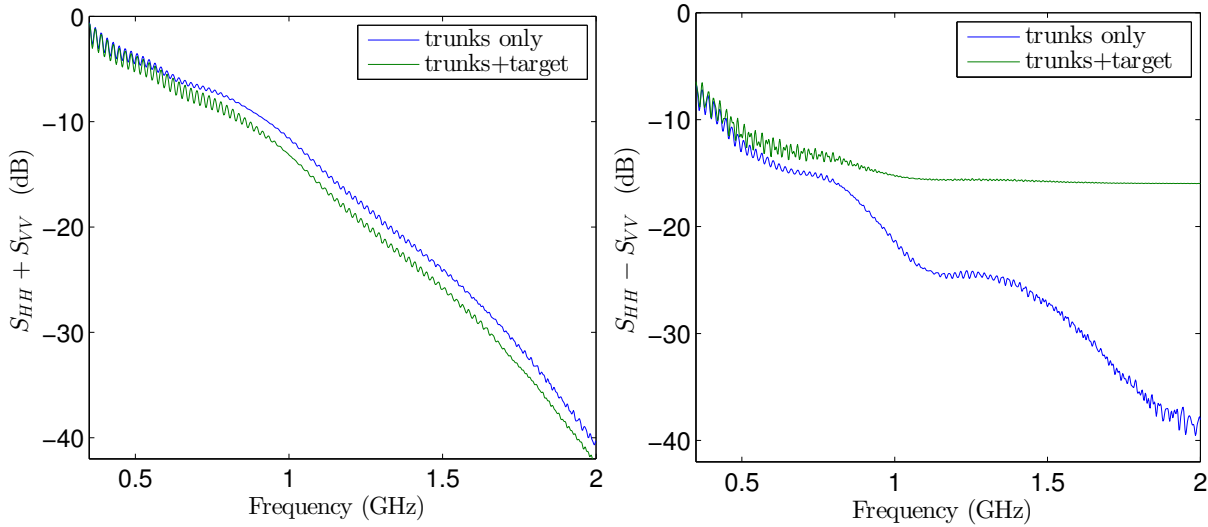
Figure 3.20 – The first Pauli vector element $S_{HH} + S_{VV}$, (left) and the second $S_{HH} - S_{VV}$ (right), for the cases of a forest with trunks only and the same forest with a target hidden among the trees. The target response is far more obvious in $S_{HH} - S_{VV}$, i.e. the single bounces mechanism. The incidence angle of the emitted wave was $40°$.

Physical interpretation   The target, because of its spherical shape, "increases" the symmetry of the scene in all cases. This explains the strong contribution in the co-polarizations and the decrease in VH even when branches exist. The co-polarized scattering was not increasing in any case, but rather decaying much slower, hardly falling under $-20\,\mathrm{dB}$. The noisy variations
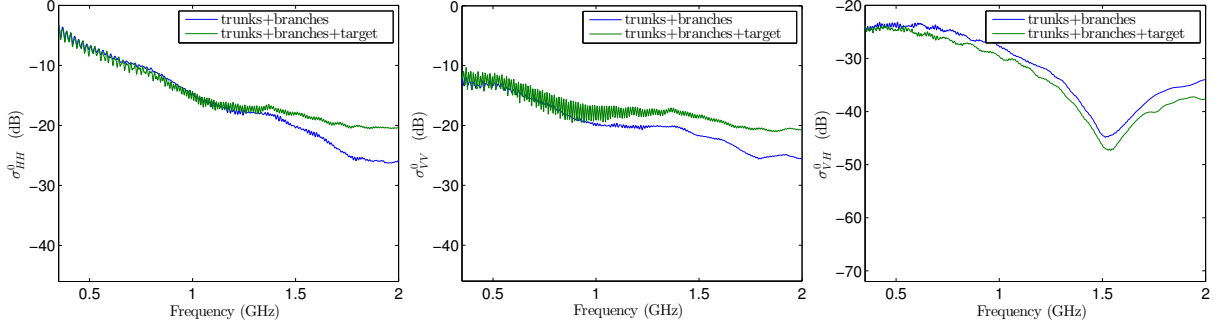
Figure 3.21 – The backscattering coefficients of the received signal in HH polarization (left), in VV (middle) and in VH (left), for the cases of a forest with trunks and 10 primary branches per trunk and the same forest with a target hidden among the trees. The incidence angle of the emitted wave was $40°$. The effect of the target is much weaker when branches exist and it is visible in high frequencies only.
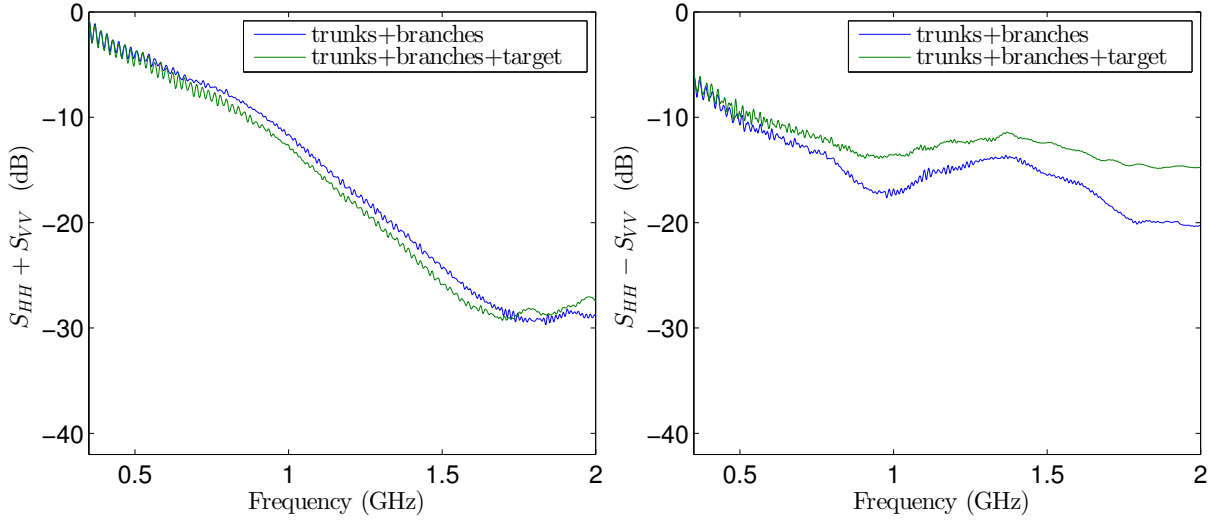
Figure 3.22 – The first Pauli vector element $S_{HH} + S_{VV}$, (left) and the second $S_{HH} - S_{VV}$ (right), for the cases of a forest with trunks and branches (10 branches/tree) and the same forest with a target hidden among the trees. The incidence angle of the emitted wave is $40°$. The target contributes only in the single bounces scattering of the scene.

observed in the VV response are linked to the radius of the sphere. Regarding the scattering mechanisms, the target backscatters via the single bounces mechanism only and stabilizes it around $-15\,\mathrm{dB}$ in high frequencies. This fact corresponds to the polarimetric signature of a sphere. In double bounces, the target slightly "blocks" the ground-trunk contributions and causes an average small reduction to them along the whole frequency range. When trunks exist only, the target is responsible for the change of the dominant scattering mechanism (see Fig. 3.23). The single bounces become the dominant mechanism after $\approx 1.1\,\mathrm{GHz}$. When branches are added, the change of the dominant mechanism takes place in a lower frequency. As seen in Fig. 3.24, in this case the single bounces dominate the scattering in the whole L-band. Another important target effect is the σ_{HH}^0 and σ_{VV}^0 convergence observed for frequencies after $1.2\,\mathrm{GHz}$ (see Fig. 3.25). This convergence neutralizes the Brewster angle effect in high frequencies, as we will see in an upcoming paragraph.
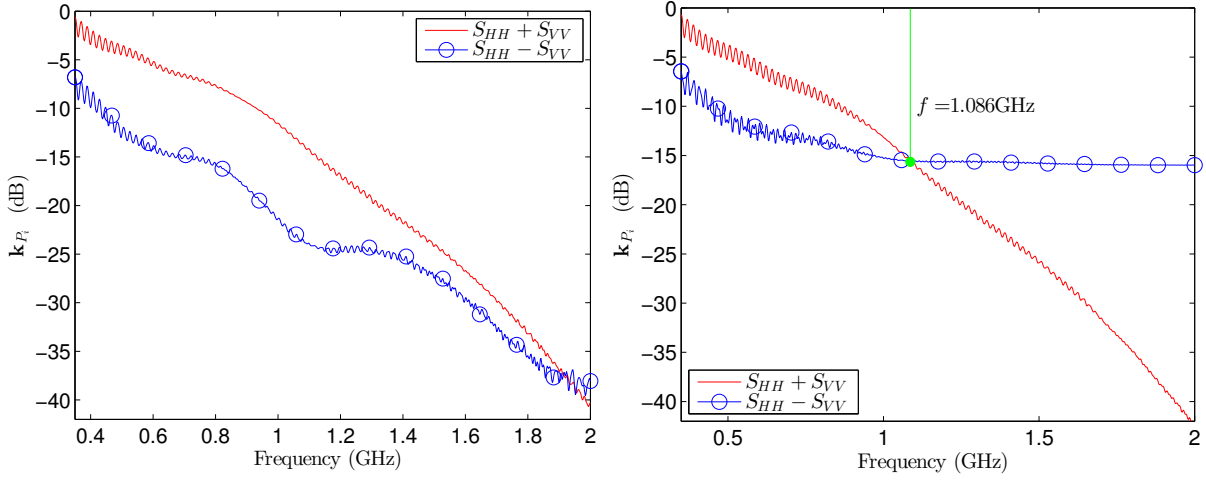
Figure 3.23 – The comparison of the first and second Pauli vector components for a forest of trunks only (left) and the same forest with a target hidden in it (right). The target contributes in the single bounces along almost the whole COSMO frequency band, making them the dominant mechanism in more than half of it.
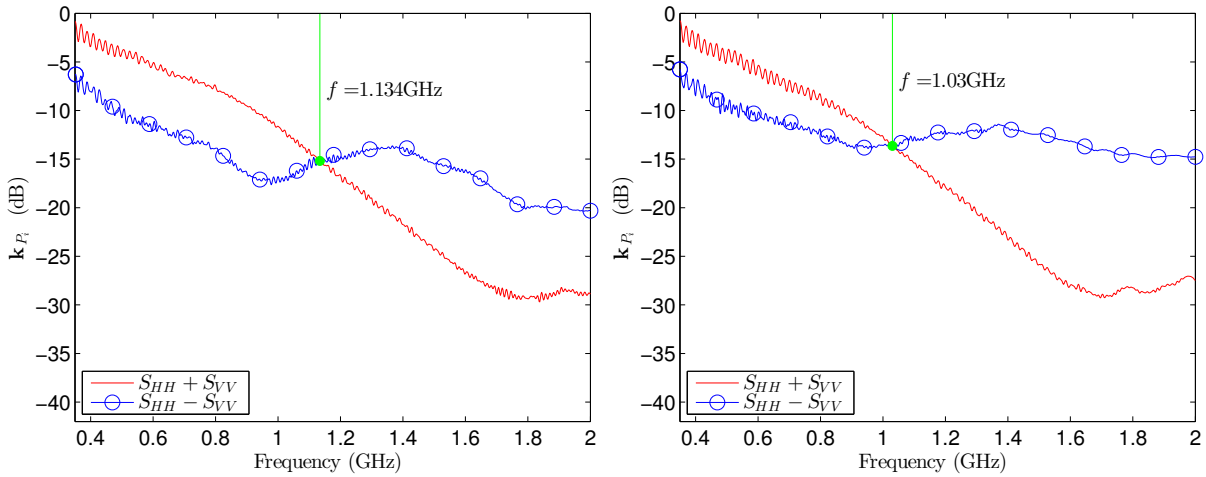
Figure 3.24 – The comparison of the first and the second Pauli vector components for a forest of trunks having 10 branches/trunk (left) and the same forest with a target concealed in it (right). The target contributes mostly to the single bounces, smoothing their decrease and making them the dominant mechanism in a frequency slightly lower than that of the branches or the target alone.

Summarizing the points above, we can say that the target effect on the scattering of a forest of naked trunks is a very strong one and can be easily identified. The situation becomes more difficult when branches exist. Since branches share some common scattering properties with the target, as for example the favor to single bounces or the strong co-polarized backscatter after $1\,\mathrm{GHz}$, the target effect is not very distinguishable. It could be easily attributed to an increase of the branches density. However there exist more specific characteristics which are representative of the target. These are mainly the noisy response in VV and the convergence of the co-polarized backscattering coefficients for frequencies $\geq 1.2\,\mathrm{GHz}$. Among the two, since the VV oscillations are closely related to the sphere, the HH, VV convergence is preferred. So, in order to discover if a target is hidden in a forest during a future radar observation, emissions in
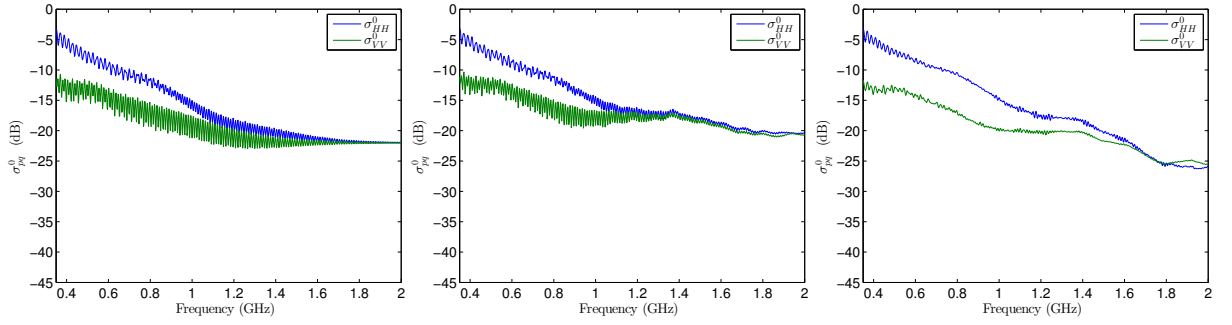
Figure 3.25 – The co-polarized backscattering coefficients of the received signal for a forest of trunks alone having a target hidden in it (left), the same forest with 10 branches added on each trunk and the target present (middle) and the forest with the trunks and branches without the target (right). Whenever the target is added, the co-polarized σ^0_{pp} are comparable in the $1.2 - 2$ GHz frequency band. The incidence angle of the emitted wave was $40°$.

high frequencies using both co-polarizations are recommended.

3.2.5 Effect of the forest arrangement

In radar observations of forests, the effect of the forest arrangement on the backscattered signal, cannot be fully examined. The natural forests have in general a random tree distribution, while the man-made ones tend to be more periodical. However, even for the periodically distributed ones, we cannot fully control the exact positioning of the trees, their mutual distance and their orientations. On the other side, our numerical model COSMO provides us the freedom to construct the forest and choose several of its spatial distribution parameters. In that way, we can examine various different forest arrangements and identify what differences each one causes to the backscattered signal. In the present study, four different arrangements were examined. One totally periodical, two semi-periodicals having $1\,$m and $2\,$m of displacement from the periodical positions respectively and a totally random one. The forest under consideration was 30 years old and it consisted of 63 trees distributed within an area of around $40\,$m $\times 50\,$m[17]. The exact positions of the 63 trees of the forest for each distribution are presented in Fig. 3.26 and 3.27, whereas the simulation parameters are these of the Table 3.1. The chosen angle of incidence was the reference one of $40°$.

The effect of the positioning of the trees within the forests described above, was examined in two distinct cases. Forests of trunks alone and forests of trunks and branches - 10 branches per trunk - were investigated separately. The outputs analyzed were, as in the previous cases, the backscattering coefficients and the Pauli vector elements. Let us start with the cases of the forests having the trunks only. As seen in Fig. 3.28 and 3.29, the four arrangements shared very similar scattering behaviors, especially the periodical and the semi-periodical ones, despite the sometimes significant difference in the tree positions with respect to the wavelength - up to almost 7λ for the $2\,$m displacement when $f = 1\,$GHz. The random forest was backscattering more energy than the others in general and the periodical one less. The

---

[17]Because of the displacement of the trees in the semi-periodical and random arrangements, the "active" scene is a bit longer in these cases, than in the periodical one. And so a periodical forest distributed within a scene of approximately $40\,$m $\times 50\,$m, when having a $6\,$m mutual distance between the trees it extends in an area of $36\,$m $\times 48\,$m, while when having a $2\,$m of displacement it covers an area of $40\,$m $\times 52\,$m.
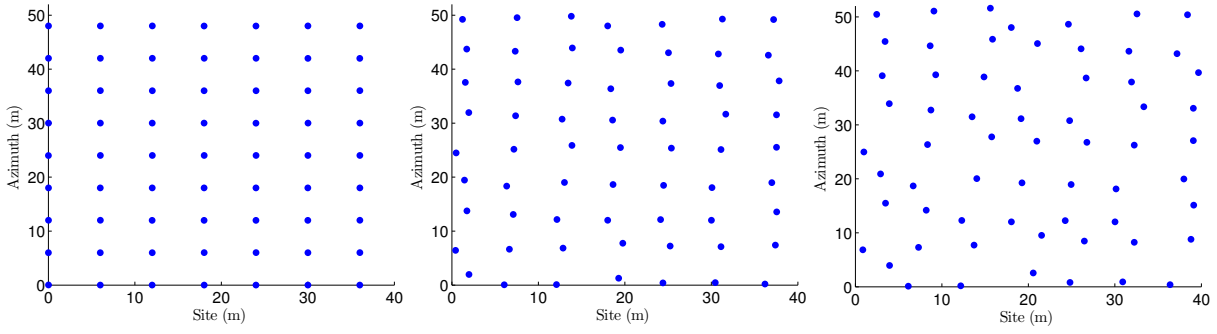
Figure 3.26 – Three periodical and semi-periodical forest arrangements. The totally periodical forest with a 6 m mutual distance between the trees in both directions (left), the same arrangement with a 1 m displacement from the original tree positions (middle) and the same arrangement with a 2 m displacement from the original tree positions (right). Each of the three forests consisted of 63 trees.
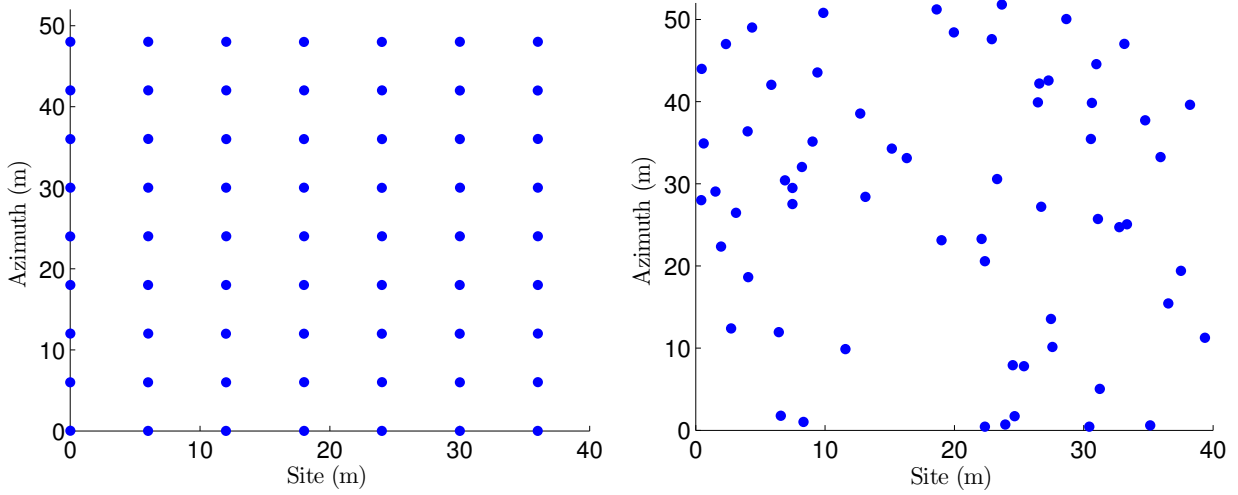
Figure 3.27 – The totally periodical arrangement of 63 trees in the scene (left) and a random distribution of the same trees (right).

most significant effect was the much stronger co-polarized backscattering of the random forest in high frequencies. When the branches were added, this effect was normalized, as seen in Fig. 3.30 and 3.31. The four responses were even more complicated and hard to distinguish and only in the VH backscattering there was a characteristic lower response from the random forest. It is obvious from these results, that it is a hard task to try to discern forest having different tree arrangements. If the differences are very small, as for periodical and semi-periodical ones, this is almost impossible. The only thing that seem feasible to be done, is the differentiation between an organized artificial forest and a natural, randomly distributed one.

Physical interpretation The periodical and semi-periodical forests show very similar scattering behavior, due to their similar tree arrangements. On the other hand, the random forest was backscattering more ($\sim 5\,$dB) under the co-polarizations in high frequencies, because of its stronger single bounces. When the branches are added, this difference is normalized and all four responses variations are found within a range of $2-2.5\,$dB. The only exception is in

VH, where the random trunk arrangement seem not to favor the volume scattering as the more organized ones do.
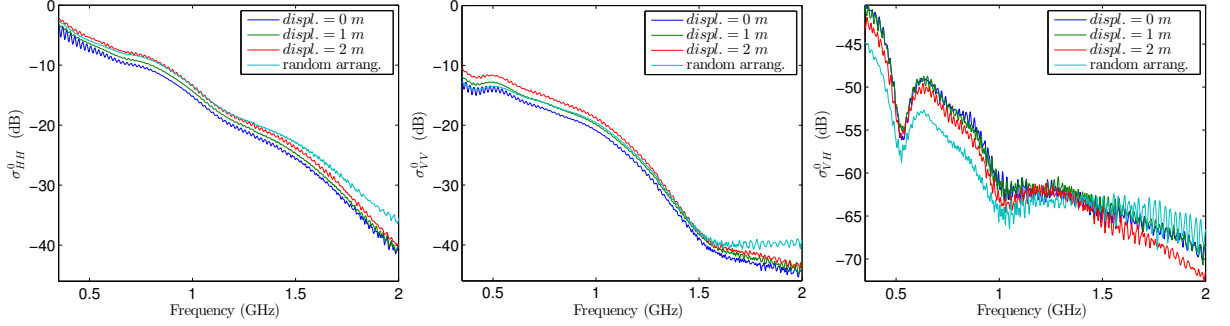
Figure 3.28 – The backscatter coefficients for the HH polarization (left), the VV polarization (center) and the VH polarization (right) for four different forest arrangements. The three first arrangements were periodical and semi-periodical with a displacement from the periodical position of 1 m and 2 m and the last arrangement was a random one. The forests were consisting of 63 trees, represented by their trunks only. In all cases the forest response was similar, especially for the periodical and semi-periodical cases.
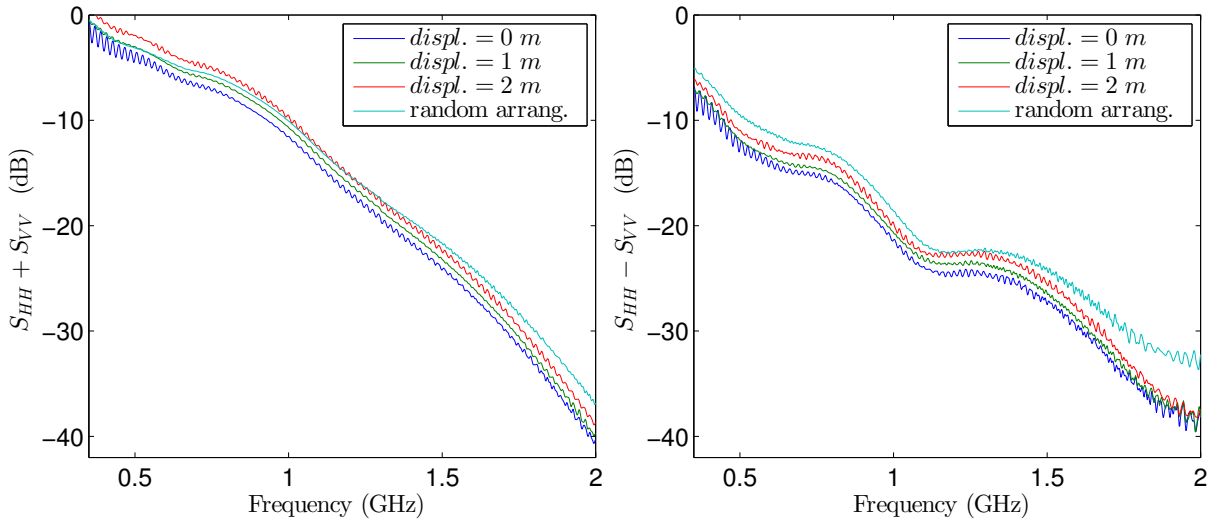
Figure 3.29 – The Pauli vector elements $S_{HH} + S_{VV}$ (left) and $S_{HH} - S_{VV}$ (right) for four different forest arrangements. The three first arrangements were periodical and semi-periodical with a displacement from the periodical position of 1 m and 2 m and the last arrangement was a random one. The forests were consisting of 63 trees, represented by their trunks only. As for the backscattering coefficients, in all cases the Pauli vector elements were similar, especially for the periodical and semi-periodical cases.

3.3   Time domain analysis

After investigating the forest effect on the simulated received signal in the frequency domain, it was now the turn of the time domain analysis. It was the first time an analysis like this was performed on the COSMO results and in radar studies of forests in general. Since COSMO operates in the frequency domain, an Inverse Fast Fourier Transform (IFFT) was applied to
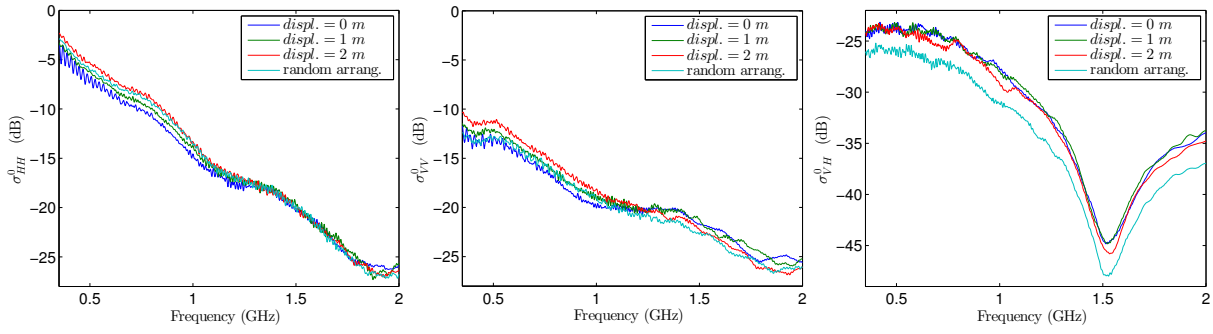
Figure 3.30 – The backscatter coefficients for the HH polarization (left), the VV polarization (center) and the VH polarization (right) for four different forest arrangements. The three first arrangements were periodical and semi-periodical with a displacement from the periodical position of $1\,\text{m}$ and $2\,\text{m}$ and the last arrangement was a random one. The forests were consisting of 63 trees with trunks and branches. In all cases the forest response was similar, especially for the periodical and semi-periodical cases.
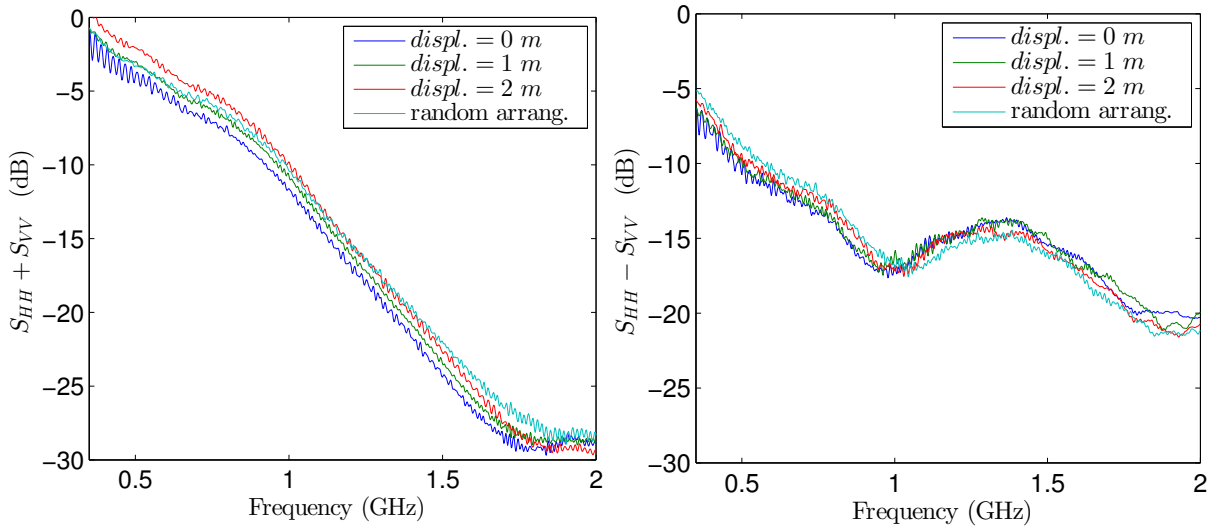
Figure 3.31 – The Pauli vector elements $S_{HH}+S_{VV}$ (left) and $S_{HH}-S_{VV}$ (right) for four different forest arrangements. The three first arrangements were periodical and semi-periodical with a displacement from the periodical position of $1\,\text{m}$ and $2\,\text{m}$ and the last arrangement was a random one. The forests were consisting of 63 trees with trunks and branches. As for the backscattering coefficients, in all cases the Pauli vector elements were similar, especially for the periodical and semi-periodical cases.

extract the time signal. The whole frequency spectrum $[350\,\text{MHz}, 2\,\text{GHz}]$ and the frequency step $df = 2\,\text{MHz}$ between the emitted frequencies were used for this transform. The only quantity analyzed and presented here was the amplitude of the received time signal, in all polarizations. This quantity was apparently affected by the input parameter variations and the forest elements. The way it was affected each time, provided supplementary information about the scene under study. The time domain analyses will start with the study of the four most important parameters effects, to continue with the forest elements ones and finish with the forest arrangements.

3.3.1 Effects of the frequency and the angle

In this first analysis, the effects of the frequency and the angle on the time signal will be investigated. Since it is the first attempt to analyze the signal in time domain, other comments concerning the polarization effect and the signal structure are going to be mentioned also. As the time signal is extracted from the frequency one, all simulation parameters were the same as in Paragraph 3.2.1. A periodical forest of trunks only was examined and the results concerning the amplitude of the received time signal in all three polarizations are presented in Fig. 3.32. As seen in these plots, the co-polarized signals show a certain and similar structure which is directly connected to the geometrical characteristics of the scene. In saying so, the pulses have seven (7) distinct peaks, corresponding to the tree lines in the site dimension (see Fig. 3.33). Since the forest was totally periodical, each tree line was backscattering as a single object resulting in these signal peaks. Since no other scatterers were existing, there is no signal between each pair of peaks and the peaks mutual distance was reflecting the mutual distance between the trunk lines. The whole length of the pulse was also proportional to the site dimension of the scene.
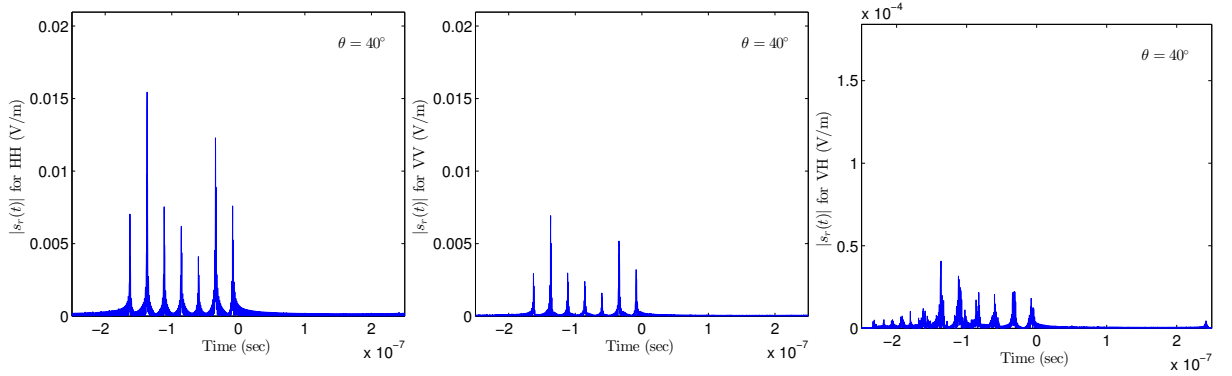
Figure 3.32 – The amplitude of the received time signal from a forest of periodically positioned trunks in HH polarization(left), in VV (middle) and in VH (right). The energy backscattered was more in HH than in VV and it was really low in VH, because of the symmetry of the scene.

The wide frequency band was responsible for the very good resolution achieved in all polarizations. We remind the the whole COSMO frequency band $[350\,\mathrm{MHz}, 2\,\mathrm{GHz}]$ results in a very fine range resolution of $\delta_r \approx 10\,\mathrm{cm}$. As far as the cross-polarization is concerned, the signal was more noisy and it seemed less useful for information extraction with respect to the co-polarized ones. As in the frequency domain, the power backscattered in HH was more than in VV and the VH backscattering was very low, due to the symmetry of the scene. The peaks of each signal had different intensities, probably due to the fact that during the separation of the scene, not the same number of trunks were put in each resolution cell (see Fig. 3.34). And that is why the relative intensities of the peaks in the co-polarized signals were the same, despite the different total energy backscattered.

If we narrow the frequency bandwidth, the time signals obtained after the IFFT correspond to different frequency bands and are suitable for comparisons. Signals like these are presented in Fig. 3.35. It is obvious from this figure, that when using low frequencies, the structure of the received signal in time domain was still highly correlated with the geometry of the scene and similar enough to the full bandwidth one. The energy backscattered was less and the signal was also a little noisy. However, the capability to extract the geometrical scene information was not
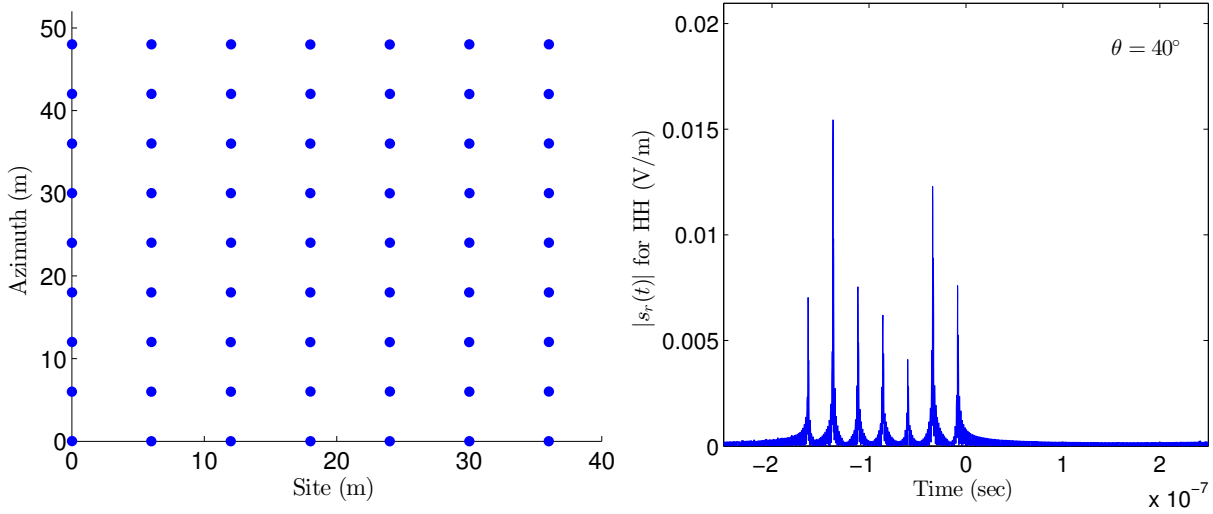
Figure 3.33 – The amplitude of the received time signal from a fully periodical forest in HH had seven peaks (right), corresponding to the trunk lines along the site dimension of the forest arrangement (left). The length of the whole pulse corresponded to the site dimension of the scene and the space between the peaks to the distance between the trunk lines.
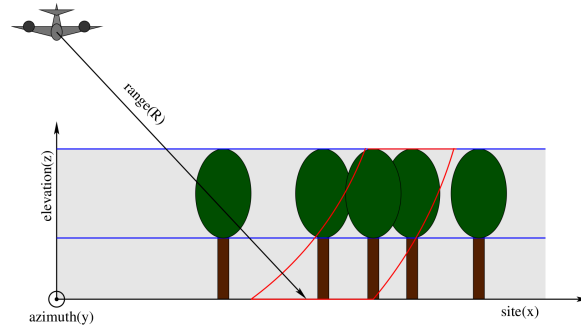
Figure 3.34 – The separation of the scene into layers and resolution cells in COSMO. The intersection of a layer and a pixel, bounded with the red line, is a cell of the scene. As the incidence angle increases the cells tend to become parallelepiped.

affected. If for the responce of a less periodical or a totally random scene this capability will be more affected, we will see it in Section 3.3.5. When a narrow band in the upper part of the frequency domain is selected, the energy backscattered is around 100 times less than in the low frequency case. This was expected, since for the infinite cylinder approximation an increase in frequency is translated in a decrease of the scattering amplitude (see [Ulaby and Elachi, 1990]). As also seen in the right plot of the Fig. 3.35, the signal is much more noisy and extended with respect to the full band one. The distinct peaks are less than the trunk lines and no certain and valuable information on the geometry of the scene can be subsequently obtained.

As far as the incidence angle is concerned, the effect of the angle increase on the time signal in HH polarization, is presented in Fig. 3.36. When the angle was increasing, the range of the distributed target was increasing also and so the length of the received pulse in time domain. The main structural properties of the received pulses were the same under all angles of incidence, since they were strongly related to the geometrical characteristics of the scene. Only
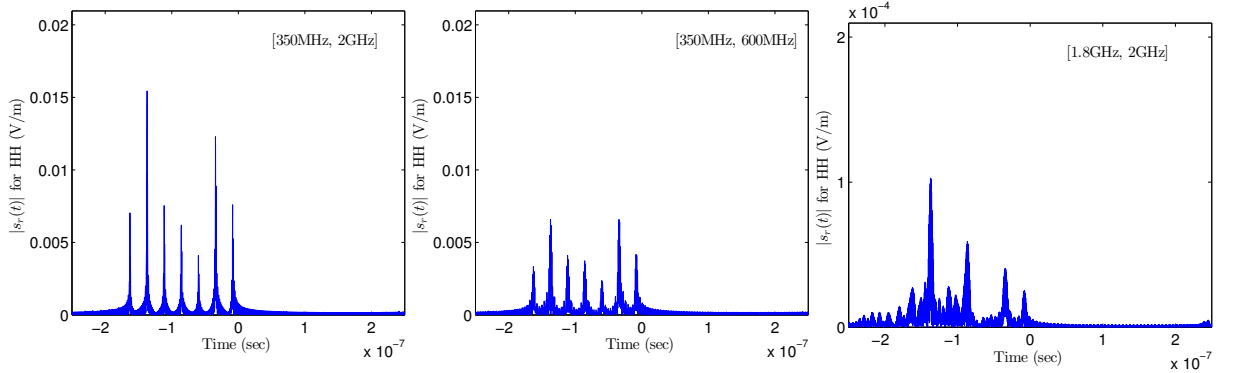
Figure 3.35 – The amplitude of the received time signal from a periodical forest in HH polarization, when used the whole COSMO band (left), a narrow low frequency band (middle) and a high frequency narrow band (right). The signal corresponding to the high frequency narrow bandwidth is much weaker and more noisy than the others. No geometrical information of the scene can be extracted from it.

the relative peaks intensities were different for the different angles, as a change in the angle causes a change in the resolution cell shape and to the number of the elements contained in it (see Fig. 3.34). As observed in the frequency domain also, the backscattered energy in HH was decreasing with the angle and so did the amplitude of the signal peaks.
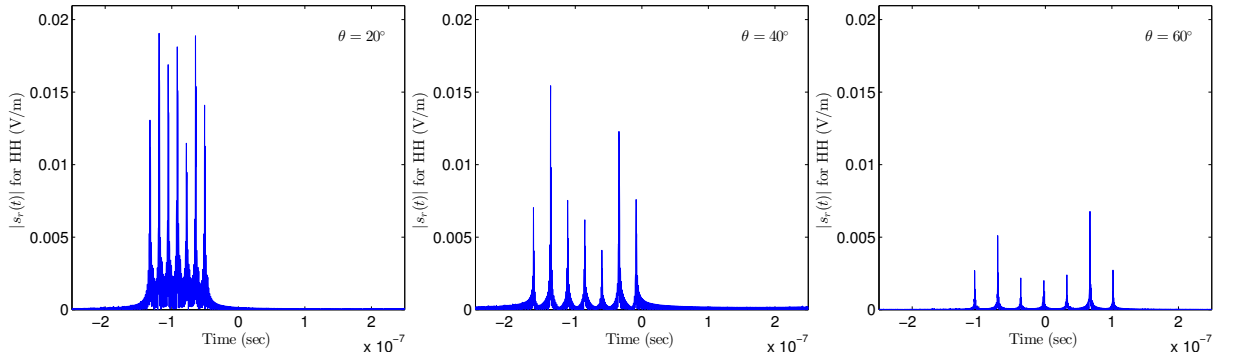
Figure 3.36 – The amplitude of the received time signal from a periodical forest of trunks in HH polar-ization for an incidence angle of 20° (left), 40° (middle) and 60° (right). The number of the peaks (7) is the same under all angles with less intensity for the steeper ones. The length of the pulse and the space between the peaks, which correspond to the size of the scene and the distance between the trunk lines, were expanding as the incidence angle was increasing.

3.3.2 Study of the age and the humidity effects

As already seen in the previous section, the time domain analysis of the received signal, comes with results on the geometric characteristics of the scene. It is the distribution of the trunks within the forest that is reflected in the signal transformed by the IFFT. Subsequently, in this case where just the age and the volumetric humidity of the trunks were varying among the forest parameters, no big differences were expected to be observed in the different time signals. Indeed, as seen in Fig. 3.37, only the amplitude of the received pulse peaks and their relative intensities were changing. The older the stand was, the stronger it backscattered in general.

For some of the weaker peaks, the energy seemed to decrease with the age, something that contradicted common sense and the results in frequency domain (see Fig. 3.6). However, this could be explained by the fact that the change of the age caused a change in the dimension of the elements and probably a change in the number of elements contained in each resolution cell. The length of the pulse, the number of the peaks and their mutual distances were identical for all ages. Similar results were observed for the different humidity values also. Since the forest arrangement was not changed, the signal was just showing stronger peaks as the vegetation was getting wetter and reflected more energy back to the radar (see Fig. 3.38).
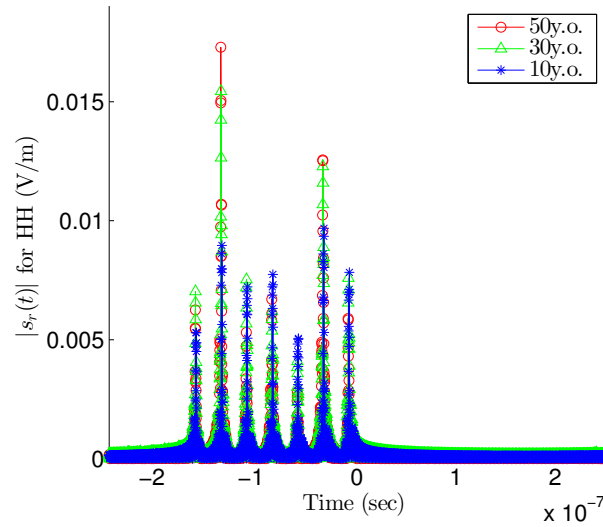
Figure 3.37 − The amplitude of the received signal in the HH polarization for 3 different ages of the forest. The position of the peaks was exactly the same, as the trunk positions in all three forests. The only difference observed was in the backscattered energy, which was rising in general as the forest age was increasing and so the dimensions of the trunks.

3.3.3 The branches effect

In the time domain analyses of the previous sections, we saw that the amplitude of the received time signal contained some information about the geometry of the illuminated scene. In all cases the tree (just trunks) arrangement was the same and so were the basic characteristics of the received pulse. Let us now examine what kind of differences the addition of 10 branches per tree caused on the geometry of the forest and on the received signal. If we go through Fig. 3.39 we can see that in the case of a totally periodical forest the addition of the branches did not have a very significant influence on the amplitude of the received signal. Most of the backscattered energy was still concentrated on the seven peaks representing the scattering of the site trunk lines. The branches effect was that of extending the signal and making it more noisy, as in the case of the high frequency observations (see Fig.3.35). In addition, when the number of the branches per tree was doubled or tripled, the signal was becoming more noisy, and the peaks amplitudes were slightly decreasing (see Fig. 3.40. These conclusions could be attributed to the fact that in P- and L-bands trunks dominate the backscattering because of their large dimensions.
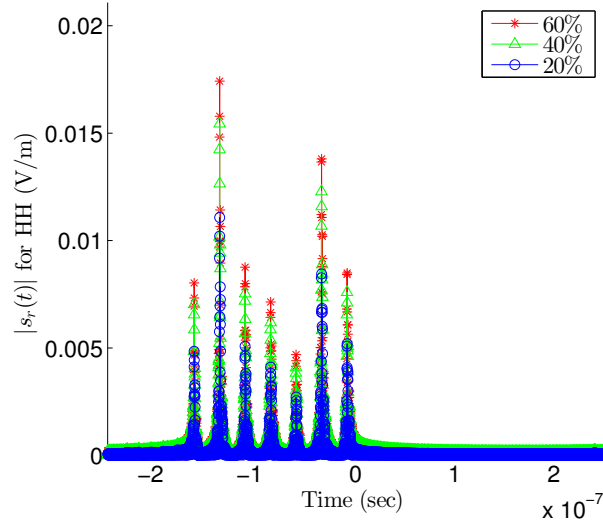
Figure 3.38 − The amplitude of the time signal in the HH polarization for 3 different forest of trunks having $m_v = 20\%$, $m_v = 40\%$ and $m_v = 60\%$ respectively. The position of the peaks was exactly the same, as the trunk positions in all three forests. The only difference observed was the backscattered energy, which was rising as the vegetation was getting wetter and the vegetation reflectivity was increasing.
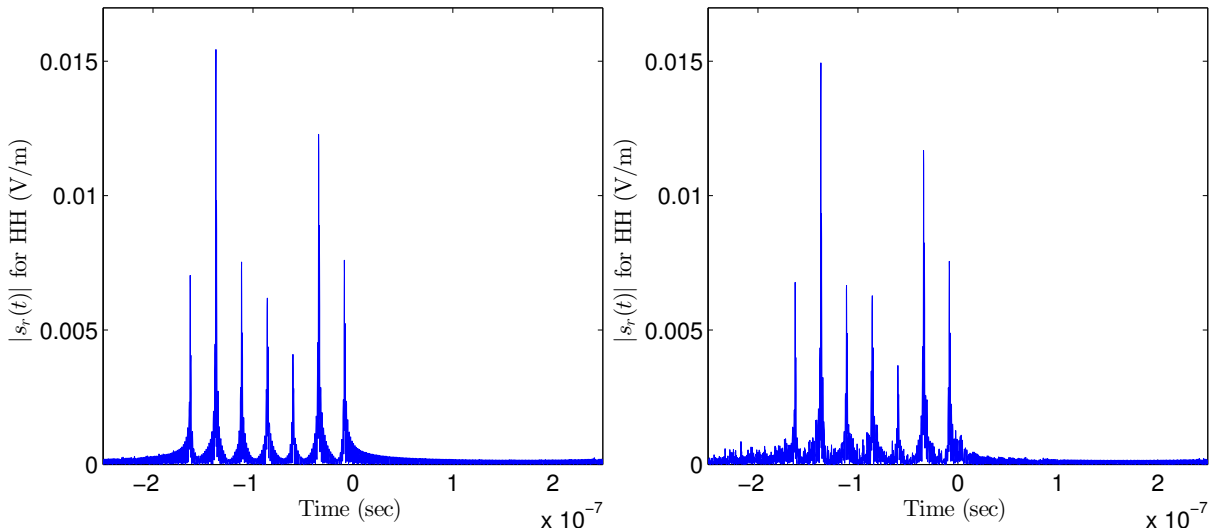
Figure 3.39 − The amplitude of the received time signal in HH for the periodical forest of trunks only (left) and for the same forest with 10 branches per trunk (right). The positions of the peaks were exactly the same, as the trunk positions were the same in both forests. The only difference observed was that the right signal was more noisy and the amplitude of the peaks was slightly smaller with respect to the left one.

3.3.4 The target effect

The positioning of the target within a forested area, could be regarded as a significant change in the geometry of the scene. Apart from the seven distinct tree lines along the site dimension, there was also a spherical target with a 2 m radius placed between the fourth and the fifth tree lines (see Fig.3.18). Consequently, we expected a distortion on the received time signals of Fig. 3.39 concerning both cases of a forest with trunks only and with the branches added.

87
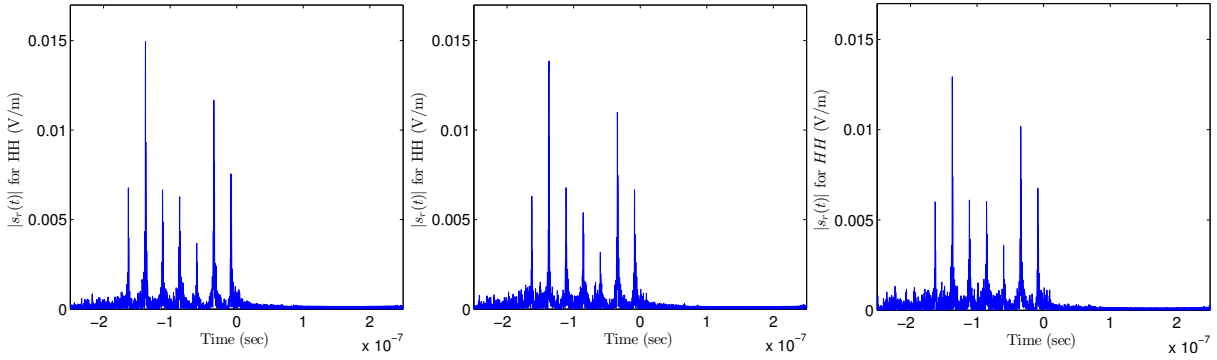
Figure 3.40 – The amplitude of the time signal in the HH polarization for the same periodical forest of trunks having 10 branches/tree (left), 20 branches/tree (middle) and 30 branches/tree (right). The position of the peaks was the same, as the trunk positions also, in all three forests. The more branches were added to the trees, the more noisy the signal became and the less the amplitudes of the peaks were in general.

Indeed, as evidenced by Fig. 3.41, the target backscattering resulted in an extra peak in the amplitude of the time signal in the HH polarization. This peak was found between the fourth and the fifth peak of the pulse, as the target was placed between the corresponding tree lines in the site dimension. Even when branches existed, which were rather hiding the target effect in frequency domain, the target peak in time domain was still quite obvious. The time signal could be therefore considered as a potential valuable tool for the target detection.
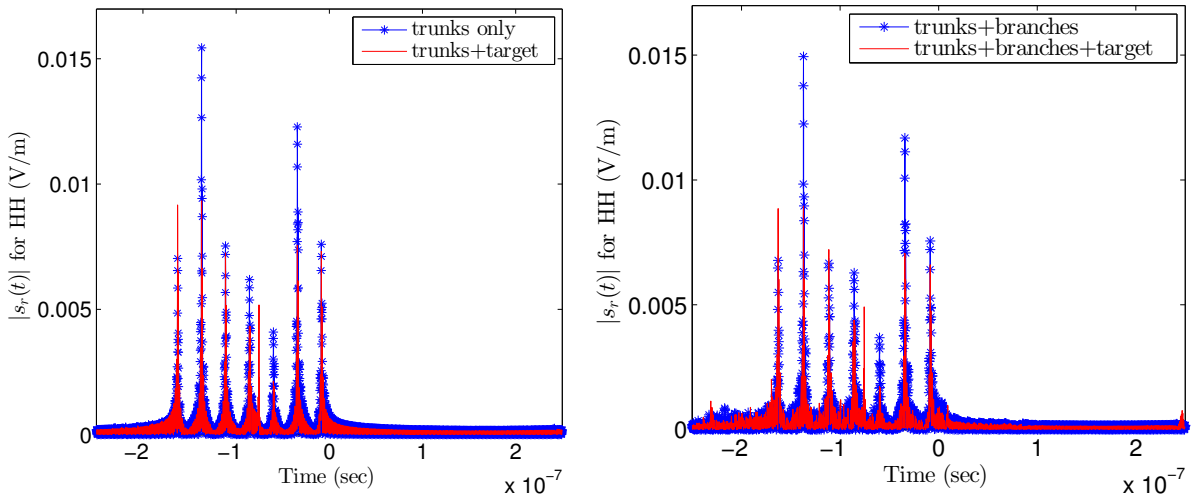
Figure 3.41 – The effect of the target addition on the amplitude of the received time signal in HH when trunks only exist (left) and when trunks and 10 branches/trunk exist (right). In both cases an extra peak was observed between the fourth and the fifth peak of the signal, in a position corresponding to the position of the target in the scene (see Fig. 3.18).

3.3.5 Effect of the forest arrangement

As we saw in Paragraph 3.2.5, the exact positioning of the trunks within the forest affected little the backscattering coefficients and the Pauli vector elements in the frequency domain. It is mostly the tree density that governed the signal modifications in that case. In the time domain case however, it is the tree positioning that is directly reflected on the time signal structure. So the investigation of the forest arrangement effect on the time signal is of major importance. We remind that the four different arrangements examined were varying from a totally periodical one, to semi-periodicals having a displacement of 1 m and 2 m, and finally to a totally random one. The four time signals in HH polarization, corresponding to the four different forest arrangements, are presented in Fig. 3.42. As we can see, the pulse duration was more or less the same in all cases, around 1.7 ms, corresponding to the scene size. The little variations were due to the small extension of the scene in the non-periodical forests (see Fig. 3.26 and 3.27).

The pulses themselves were becoming more noisy as the trunks were displaced from the periodical site lines. In particular, if we observe the signal corresponding to the semi-periodical forest with the 2 m displacement, we can see that it showed more similarities with the random forest signal than with the other ones. This was expected, as the 2 m displacement could be translated into several wavelengths in the upper part of the frequency domain (e.g. $f = 1\,\text{GHz} \Leftrightarrow \lambda = 30\,\text{cm}$ and $e = 2\,\text{m} \approx 7\lambda$). As far as the signal peaks were concerned, there were appearing stronger and more clear in the periodical forest (due to the coherent addition) than in the other arrangements. Whenever the trunks were displaced from a site trunk line, the dominant peaks were losing intensity and shorter peaks were appearing between them, making the energy to be more uniformly distributed along the pulse length. In such cases, little geometrical information could be extracted from the signal. To conclude, despite the weak influence of the forest arrangement on the signal in the frequency domain, in the time domain its effect is a very significant one. Therefore, we could use the time signal to distinguish natural forests from man-made ones.

3.4 The Brewster angle effect

Definition of the Brewster angle

In this last section of the chapter, the "marginal" conclusions concerning the Brewster angle effect will be treated. Marginal, because they were beyond the scope of this dissertation initially. However, the significant results discovered in the meantime, led us to dedicate a whole separate section on this effect. The *Brewster angle* is defined in Electromagnetics as the angle of incidence at which the reflection of the vertically polarized waves from a planar interface, between two loseless materials with different permittivities, vanishes [Balanis, 1989]. This angle depends only on the permittivities of the two materials and assuming a sufficiently smooth medium it is given by:

$$\theta_B = \tan^{-1}\left(\sqrt{\frac{\varepsilon_t}{\varepsilon_i}}\right) \tag{3.1}$$

where ε_i and ε_t are the relative permittivities of the material in which the wave travels and in which it is transmitted respectively. Furthermore, in radar observations the incident wave is often in free space and so $\varepsilon_i = 1$ [Cloude, 2009] and equation (3.1) becomes:

$$\theta_B = \tan^{-1}\sqrt{\varepsilon_t} \tag{3.2}$$
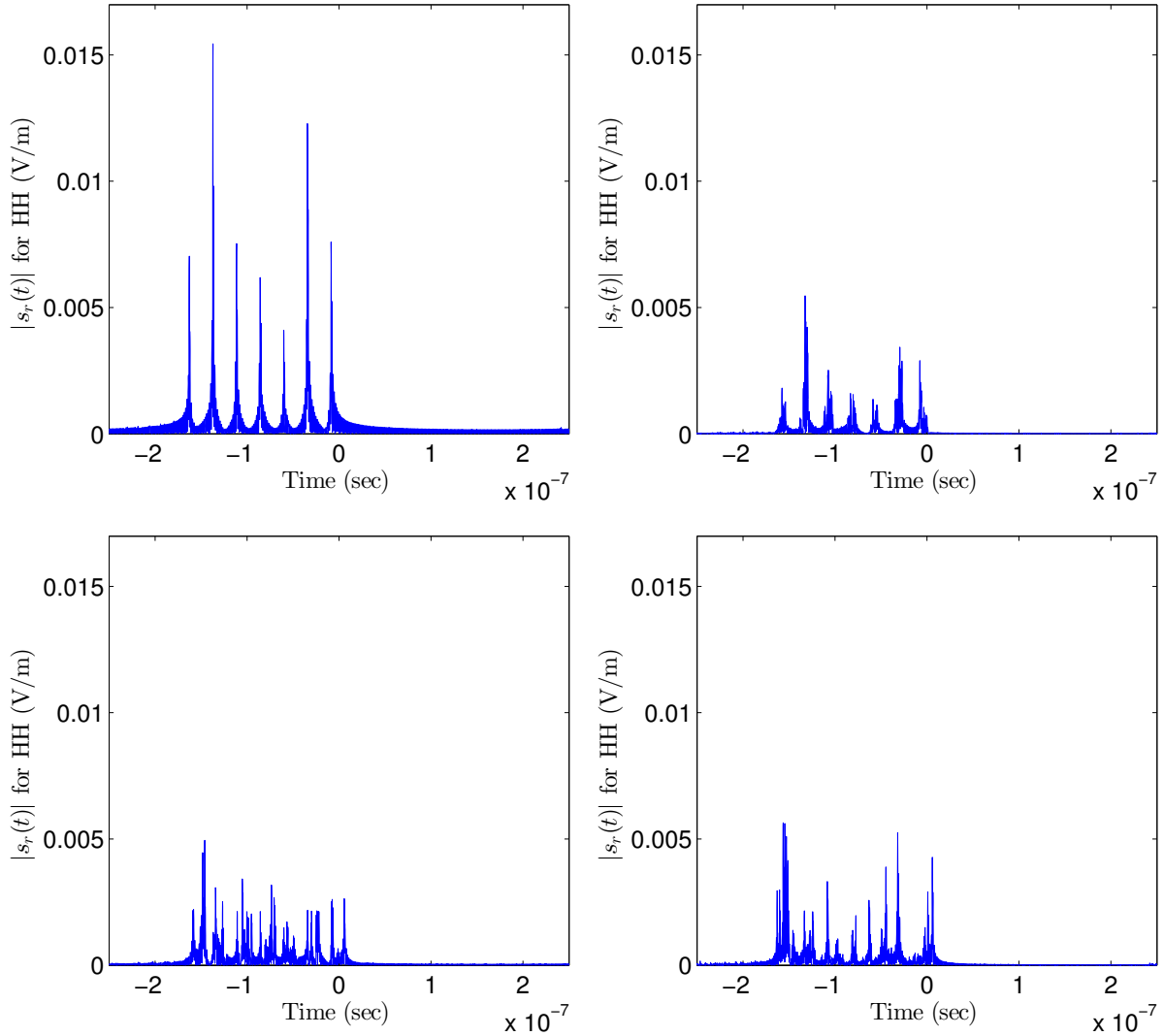
Figure 3.42 – The amplitude of the received signal in HH polarization for the periodical forest (top left), the semi-periodical with the 1 m displacement from the exact periodical positions (top right), the semi-periodical with the 2 m displacement (bottom left) and the randomly distributed one (bottom right).

In the particular case of a monostatic configuration, the Brewster angle effect is present in both reflections of the double bounce scattering mechanisms. For example, in the case of double bounce scattering with the ground and the trunk, assuming they are both lossless, there are two VV backscattering drops present because of the geometry of the interface depicted in Fig. 3.43. The two distinct angles related to these effects are θ_B^g for the scattering on the ground and θ_B^v for the scattering on the trunks/vegetation. The latter stands for the complementary angle of the real Brewster angle because of the geometry of the scene. As previously mentioned, these angles depend only on the surfaces characteristics as described by their dielectric constants, ε_g for the ground and ε_v for the vegetation:

$$\theta_B^g = \tan^{-1} \sqrt{\varepsilon_g}, \qquad \theta_B^v = \frac{\pi}{2} - \tan^{-1} \sqrt{\varepsilon_v} \qquad (3.3)$$

Whenever the permittivity of the ground or the vegetation is increasing (e.g. because of the

humidity), the Brewster angle θ_B^g is increasing also, whereas the complementary angle θ_B^v is decreasing.
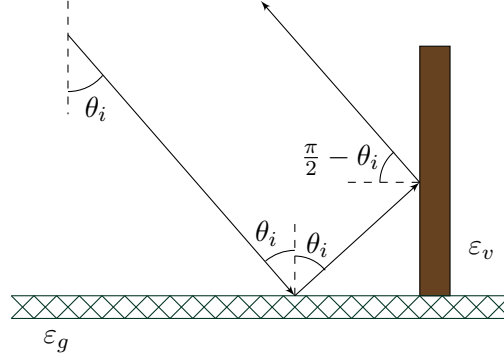
Figure 3.43 – The double bounce mechanism representing the ground-trunk scattering of a wave, under a θ_i angle of incidence. Each surface is characterized by its relative permittivity, ε_g for the ground and ε_v for the trunk.

For the previous ground-trunk double bounce scattering problem, we assumed that the materials are loseless, so that the Brewster angle definition could apply. However, the Brewster angle effect can be observed also when the materials of the interface are lossy and not lossless. Examples can be found even in real radar data, as seen in[Freeman, 2007]. In that case, as the relative permittivities of the lossy materials are complex, the Brewster angle evaluated from Eq. (3.1) will be complex also. It means that there is no real angle for which the reflectance of the vertically polarized waves becomes zero, as it does for a lossless material. Instead, there is always an angle for which the energy reflected reaches to a minimum and it is called the *pseudo Brewster angle θ_B'*. This pseudo Brewster angle is in the cases of lossy media directly related to the real part of the permittivity (see [Freeman, 2007]). This angle will be mentioned as the Brewster angle from now on, since no lossless materials exist neither in radar forest investigations nor in our COSMO simulations.

As already mentioned, the Brewster angle effect can be observed in real life experiments concerning either forest observations ([Freeman, 2007]) or even urban areas ones (see [Thirion-Lefevre et al., 2015]). In our forest simulation studies, where the ground and the tree elements are assumed to be lossy dielectric, the Brewster angle effect can be also observed in certain cases. For instance, during the illumination of a forest of vertical aligned trunks by a wave of 400 MHz under all possible angles of incidence within the $[5°, 85°]$ domain, two sharp drops in the $HH - VV$ difference in backscattering were observed, as seen in the right plot of Fig. 3.44. The first one corresponded to the reflection of the wave on the cylindrical trunks and the second to the reflection on the ground. These results are comparable to the theoretical ones concerning a lossy dielectric cylinder, as presented in the left plot of the same figure. The two drops in the VV backscattering, which is the primary Brewster angle effects, are usually outside the bounds of the angles selected for radar observations. However, apart from these two energy drops, there is a big difference between σ_{HH}^0 and σ_{VV}^0 along the whole frequency spectrum emitted. In particular, there are two distinct frequency intervals, the $[13°, 30°]$ and the $[55°, 85°]$, where $\sigma_{HH}^0 - \sigma_{VV}^0 \geq 10$ dB. This difference can be regarded as a secondary Brewster angle effect and because of its extent it is expected to be observed both during COSMO simulations

and real radar experiments.
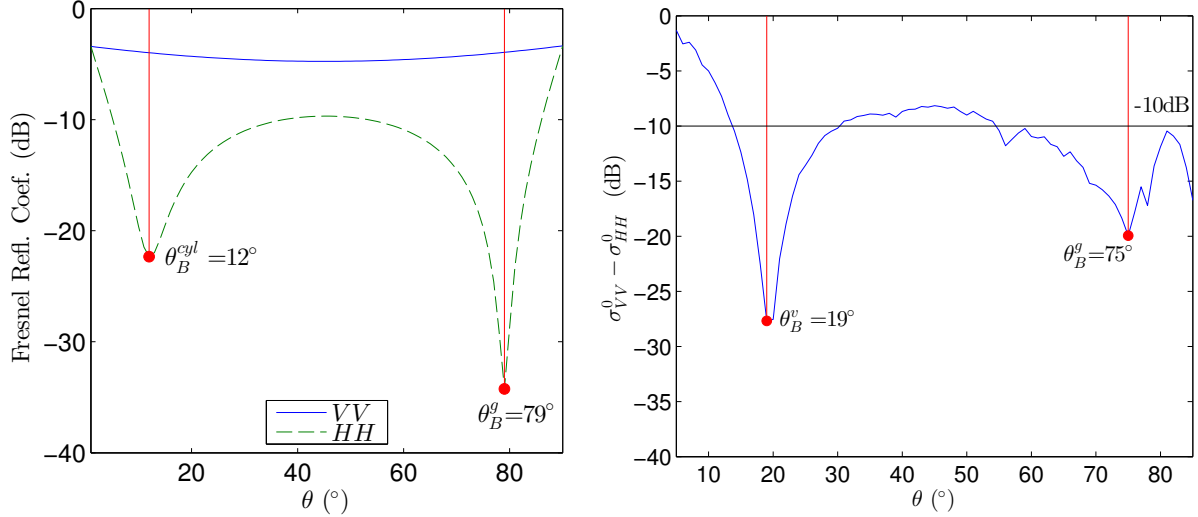
Figure 3.44 – The Fresnel reflection coefficients for the theoretical test case of a circular cylinder over the ground (left) and the difference in the co-polarized backscattering coefficients concerning the COSMO simulated observation, of a forest of cylindrical trunks (right). In both cases, there are two drops in the backscattered power due to the Brewster angle effect. The first drop corresponds to the scattering with the cylinders and the second to the ground reflection. The frequency of the emitted wave was $400\,\mathrm{MHz}$ in both experiments. For the theoretical case we had $\varepsilon_g = 26.39 - 3.17i$ for the ground and $\varepsilon_{cyl} = 23.01 - 11.71i$ for the cylinder, whereas for the forest of trunks we had $\varepsilon_g = 38.4 - 5.8i$ and $\varepsilon_v = 13.1 - 5.87i$. The analogies between the results of the two cases are evident.

The Brewster angle effect in COSMO simulations

It was already highlighted in Section 3.2.1, that a significant loss in the energy backscattered in VV occurred when a signal under an incidence angle of 20° was emitted to a periodical forest of trunks (see the middle plot of Fig. 3.2). After examining more thoroughly several similar and not only cases, this fact was finally attributed to the Brewster angle effect. In what follows, we will exploit COSMO in order to check the occurrence of this effect, for several forest arrangements. In the aforementioned figure, the effect was observed in a periodical forest, when it was illuminated under a small incidence angle with a low frequency wave, close to $400\,\mathrm{MHz}$. As a first attempt to investigate the phenomenon, we will extend the angle domain of interest and make our survey finer. In saying so, the whole $[5°, 85°]$ will be simulated with a step of 1°. The results following below, will be focused on the two sub-bands showing the most interesting effects, the $[400\,\mathrm{MHz}, 700\,\mathrm{MHz}]$ for the low frequencies and the $[1.7\,\mathrm{GHz}, 2\,\mathrm{GHz}]$ for the high ones. The forest examined was the same as previously, having $m_v^{vol} = m_g = 40\%$. The effect of the humidities on the $\sigma_{HH}^0 - \sigma_{VV}^0$ difference will not be thoroughly examined, as it was the expected one. It means that a drop in the m_g values was causing a decrease in θ_B^g, because of the permittivity values decrease and a decrease in m_v^{vol} was causing an increase in the complementary angle θ_B^v. This means that the drier the ground and the vegetation, the closer the two Brewster angles were and the widest the range of the angles where VV-HH$\leq -10\,\mathrm{dB}$ was. The two extreme cases will be highlighted only, one where both the ground and the vegetation were dry and one where both were wet. The results from these cases will be used for

confirming some recent discoveries in the Brewster angle study.

Starting with a totally periodical forest with the trunks alone, we can see in Fig. 3.45 that there were existing two distinct areas of low VV backscattering, one around $19° − 20°$ and one around $75°$. In particular, the lowest values of the backscattered energy were observed for an incidence angle of $20°$ and a frequency of $400\,\mathrm{MHz}$, the exact case where we first identified that effect during our analysis. As a consequential outcome of these two drops, the HH-VV difference was remaining high for a wide range of angles, even for these commonly used during real radar forest investigations. If we move towards the upper part of the COSMO frequency band, our remarks do not stand exactly. On the one hand, the first sharp drop was smoothened and extended forming a "valley" of low difference values, centered around $25°$. The lowest values did not exceed $−10\,\mathrm{dB}$ a lot. On the other hand, the second drop maintained its lowest values which were observed for angles closer to $80°$ and for $f = 2\,\mathrm{GHz}$.
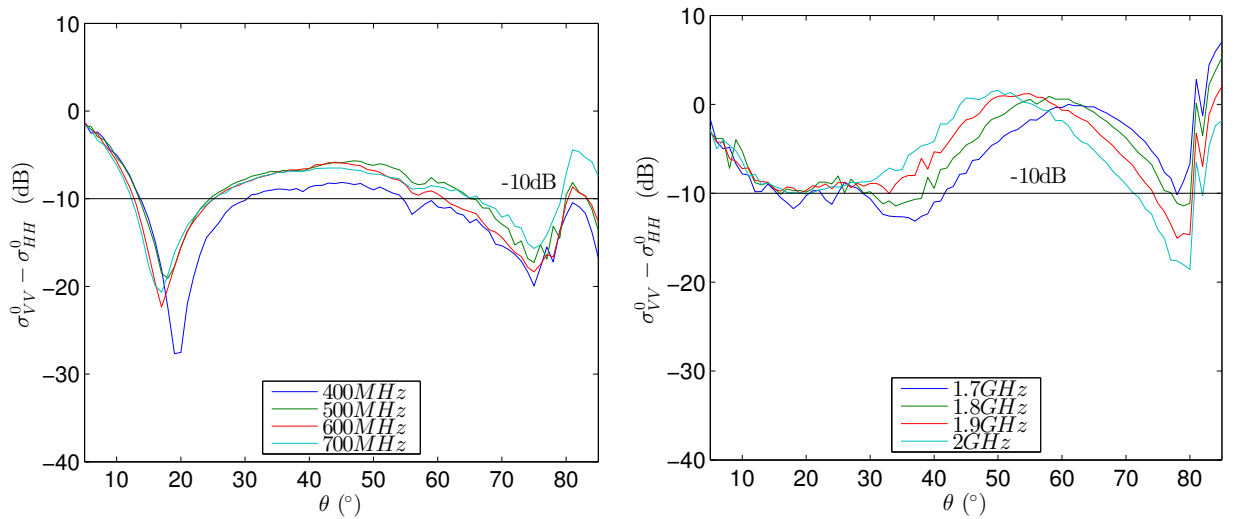
Figure 3.45 − The co-polarized backscattering coefficients difference for a totally periodical forest of 63 trunks, as a function of the incidence angle. For the low frequencies (left) a big difference due to the Brewster angle effect is present for all incidence angles, with the two minima having values way lower than −10 dB. For the high frequencies (right) the difference is much smaller, the two drops are translated with the first one - attributed to the vegetation scattering - being smoothened a lot.

The addition of branches to the trunks and the concealment of a potential target in the forest, can change dramatically the scattering behavior of the trunks concerning the VV-HH difference. We have already seen that when branches were existing, the co-polarized backscattering coefficients were comparable in several cases, especially for high frequencies (see Section 3.2.3). Indeed, as seen in Fig. 3.46, when 10 branches were added per trunk, the two simultaneous characteristic drops of the previous cases disappeared. There existed just one drop around $20°$ for the low frequency observations, which was sharper the lower the frequency was, and a moderate decrease around $75°$, which was evident over $1.8\,\mathrm{GHz}$ but it was hardly approaching $−10\,\mathrm{dB}$. For the intermediate frequencies, the co-polarizations difference was very low and no effect was observed. When the number of the branches was doubled, the Brewster effects were smoothened even more, as observed in Fig. 3.47, and there was actually just the low frequency drop due to the vegetation remaining, quite weak though. The positioning of a target in the

scene had a similar effect to the one of the branches, almost neutralizing the Brewster effect in high frequencies (see Fig. 3.48). Last, the change of the tree arrangement to a semi-periodical or even a random one did not affect the Brewster angle effect almost at all (see Fig. 3.49).
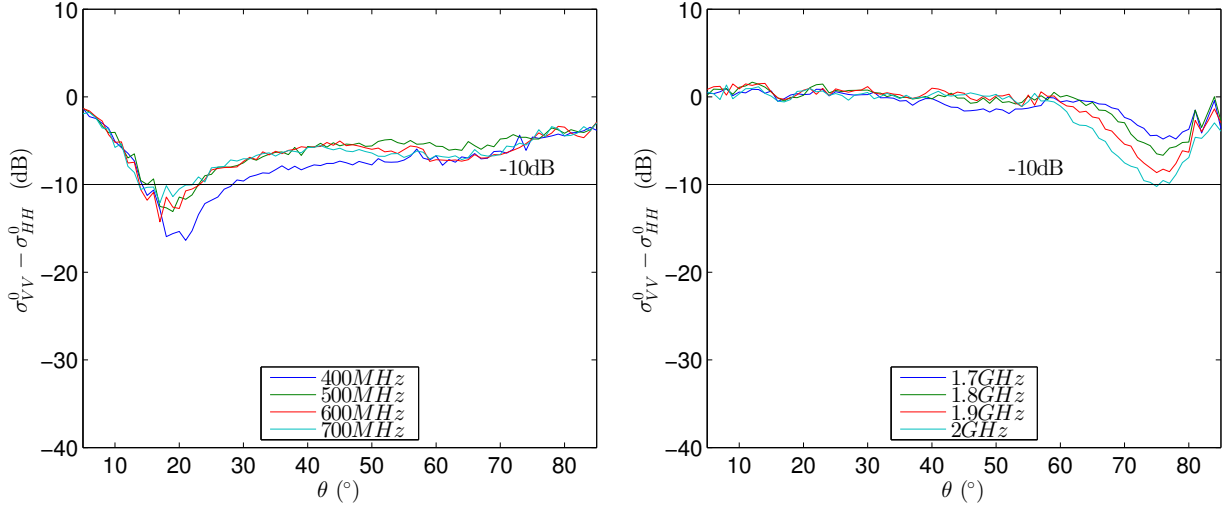
Figure 3.46 – The co-polarized backscattering coefficients difference for a totally periodical forest having 63 trunks with 10 branches each one, as a function of the incident angle. The Brewster angle effect is now disturbed, since there is just one drop corresponding to each frequency sub-band. For low frequencies (left) the drop is centered around 20° and take values much close to −15 dB, whereas for the high frequencies (right) it hardly approaches −10 dB and only for steep incidence angles.
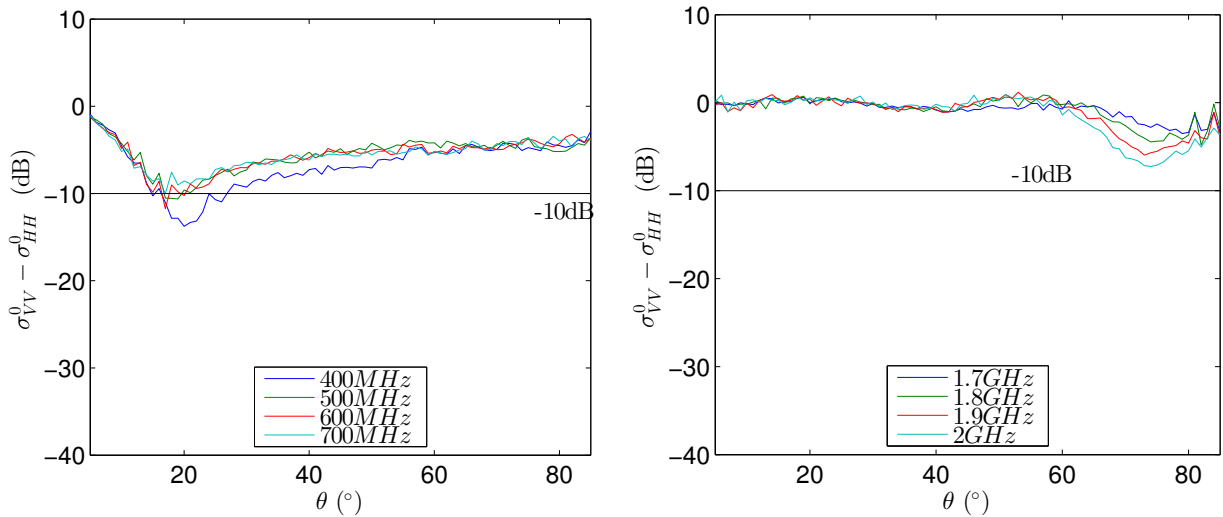
Figure 3.47 – The co-polarized backscattering coefficients difference for a totally periodical forest having 63 trunks with 20 branches each one, as a function of the incidence angle. The extra branches added smoothened the Brewster angle effect more, letting actually just one drop existing for low frequencies only (left). For the highest frequencies (right) the difference is always much lower than −10 dB and the Brewster angle effect due to the ground scattering is barely observable.
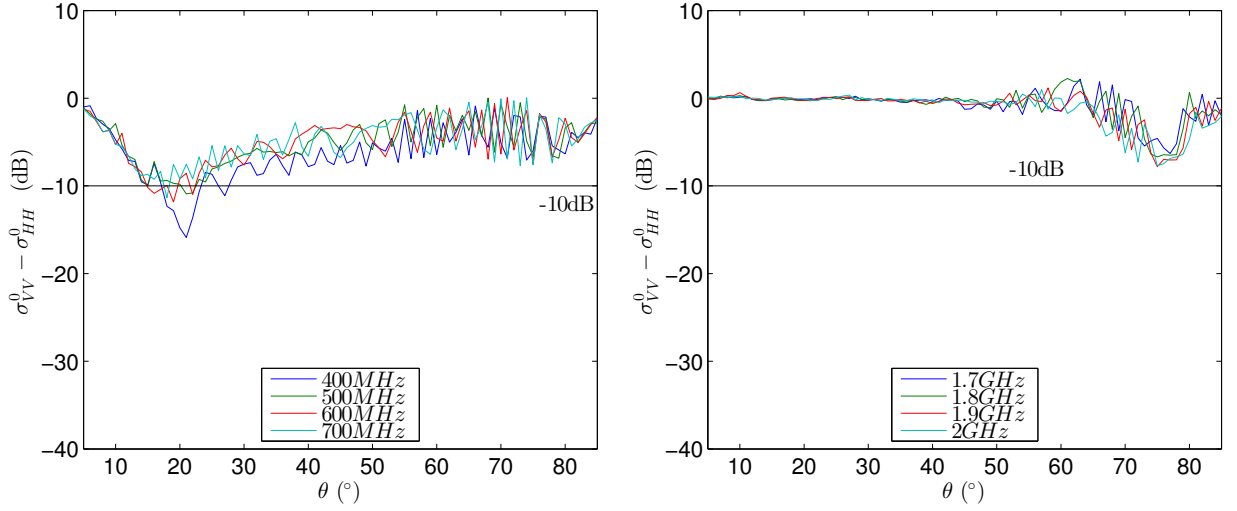
Figure 3.48 – The co-polarized backscattering coefficients difference for a totally periodical forest having 63 trunks, 10 branches per trunk and a target concealed in it, with respect to the incidence angle. The target slightly enhanced the branches distortion of the Brewster angle effect in low frequencies (left) and especially in high frequencies (right). It also made the signal and the co-polarizations difference much more noisy than before.
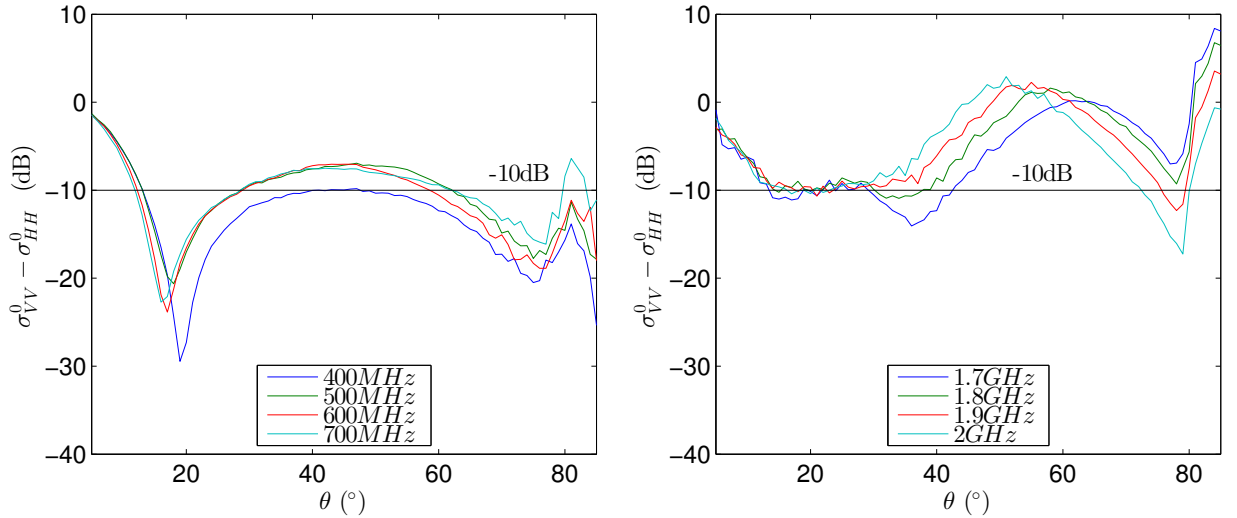
Figure 3.49 – The co-polarized backscattering coefficients difference for a random forest of trunks alone, as a function of the incident angle for low frequencies (left) and high frequencies (right). The change in the forest arrangement did not influence the Brewster angle effect significantly, as compared with the results in Fig. 3.45.

From the above-mentioned results, we can conclude that the Brewster angle effect, when present in radar forest investigations, is caused by the trunks-ground double scattering only. It is the geometry of the this configuration that governs this effect, which appears mainly whenever the signal manages to reach to the trunks, i.e. when few branches exist or low frequencies are emitted. The branches, when existing, they normalize the Brewster effect probably by attenuating a part of the energy backscattered via the double bounces mechanism. The effect

95

is mostly visible under certain angles of incidence, depending on the scene under study and its permittivity characteristics. However, it has to be kept always in mind and taken into consideration, since it can significantly distort the forest response and complicate radar studies. For example, the Brewster angle effect could lead to erroneous conclusions when results from different incidence angles are to be compared, as done in [Mladenova et al., 2013].

We will close this section by adding some comments on a recent work presented in [Thirion-Lefevre et al., 2015]. In this study, a wide range of cases was examined not for the primary Brewster effect, but for the secondary one. In the left plot of Fig. 3.50, the width of the angle range where VV-HH≤ -10 dB is presented. We can see that for the case of very low permittivity values, this angle range could reach $50°$ thus containing many of the angles used in radar studies. For large permittivity values, that width decreases a lot. Two corresponding cases, one of a very dry forest of trunks ($m_v^{vol} = m_g^{grav} = 10\%$) and one of a wetter one ($m_v^{vol} = m_g^{grav} = 40\%$) are presented in the right plot of Fig. 3.50. The emitted wave had a frequency of 400 MHz and the permittivities of the scene were $\varepsilon_v = 2.24 - 0.2i$ and $\varepsilon_g = 11.4 - 2.83i$ for the dry case and $\varepsilon_v = 13.1 - 5.9i$ and $\varepsilon_g = 52.3 - 6.53i$ for the wet case. The accord with the results from [Thirion-Lefevre et al., 2015] is total. For the case of the dry forest, a very strong and combined double Brewster effect is present, causing the VV-HH difference values to be inferior to -10 dB for all angles in the $[30°, 80°]$ interval. On the contrary, in the case of the wetter forest the two Brewster effects are distinct and only for angles around the characteristic drops it is VV-HH≤ -10 dB.
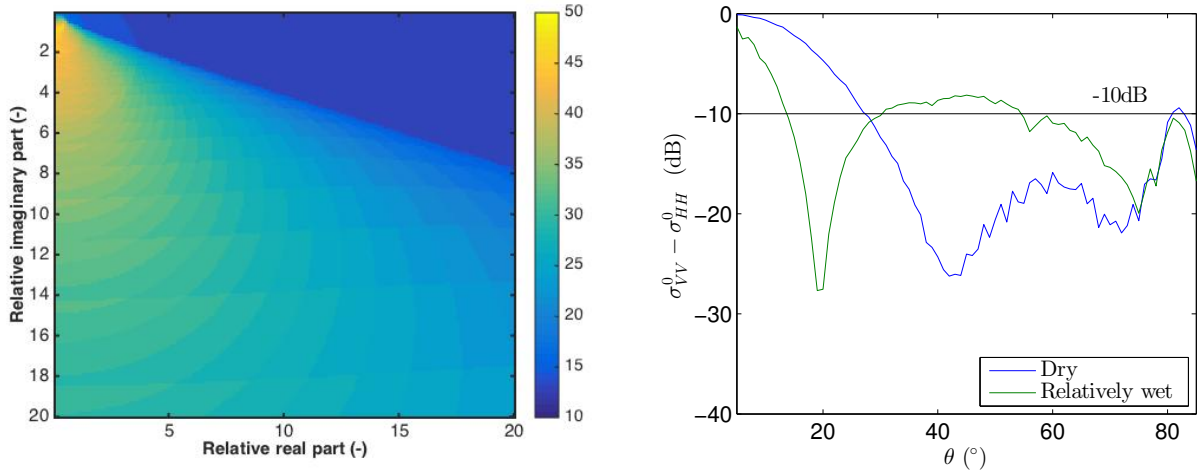
Figure 3.50 − The width of the angle domain where HH-VV≤ -10 dB with respect to the permittivity (left) and the HH-VV values for the cases of a dry and a relatively wet forest illuminated by a wave of 400 MHz (right).

3.5   Conclusions

We will close this chapter by summarizing what was presented in the previous pages and what can be done to complement these results. In Chapter 2 we evaluated, during the SA, the input parameters importances and identified the most critical among them for the model operation.

After that, it was time to proceed to the verification of these results and the examination and analysis of the parameter specific effects. An analysis having three objectives was performed. The first objective was to confirm the SA results and examine the influence on the output that the variation of the most important parameter (frequency, angle, age and vegetation humidity) had. The effects of the branches addition and density, as well as that of the target existence were also studied. Not a full physical analysis was performed, but a rather fast one, focused on the main effects only. Second objective was to assess the physical interpretation of these effects, whenever possible, in terms of scattering mechanisms or the geometry of the scene. The last objective was to suggest proper radar configurations for an easier identification of the discovered effects.

What was achieved during this 3-step analysis was the discovery of certain effects which could be undoubtedly assigned to their corresponding sources. Some of these effects were evident in the frequency domain, while others were stronger in the time domain. The "cause and effect" matchings thus attained, could be subsequently used in the planning of more focused radar campaigns. Specific frequencies or polarizations could be favored in each observation, with respect to the effect under study. It is of great interest to check in a future project the extent and the validity of the conclusions drawn here, for different angles (since just the 40° one was treated), different combinations of the inputs, forest having branches of different sizes and leaves in all experiments, different forest types supported by COSMO (e.g. tropical forests) and on data from real forest radar observations also. Lastly, the Brewster angle effect during COSMO simulations was examined and the cases when it can be significant were highlighted. The conclusions derived here will be in a later step used for the design of more focused and adaptive radar observation strategies.

4

Surrogate modeling and approximation of COSMO

Contents

4.1 Introduction

In the present chapter, the second statistical method which will be employed in our radar simulation studies, that of surrogate modeling, will be presented. As we saw in the previous chapters, the first statistical method applied on COSMO provided valuable information on the model factors importances. These informations were subsequently verified in Chapter 3, in order to discover the exact parameters and forest elements effects, attribute their physical interpretations and recommend the optimal configurations for their identification during radar studies. The latter aims to be integrated in the radar observation practice in a later step, in

order to supplement it. Unfortunately, the necessary fast real-time analysis of the radar data, is almost impossible, even when using numerical codes like COSMO. It is the use of a metamodel that can help us surpass this difficulty. A model like this, can approximate the numerical code values in very low computational time, based on a few simulation results only. Therefore it could substitute COSMO in the design of an adaptive, in real-time, radar observation strategy for forests.

In the upcoming sections, we will quickly review surrogate modeling and its most widely applied methods. Continuing, the kriging interpolation method which will be applied to the COSMO approximation will be treated. This method provides a measure of the approximation's uncertainty, which can be used to construct more efficient adaptive metamodels. A metamodel like this will be tested on appropriate toy functions, before qualified to be used on COSMO. Concerning the COSMO approximation, the metamodel will be used in the approximation of the COSMO outputs corresponding exactly to the cases studied in Chapter 3. The possibility to detect the effects of the important inputs and the forest elements on the outputs, will be examined. The chapter will close with the conclusions derived and a discussion on the limitations and constraints of the metamodel applicability.

4.2   Surrogate modeling

Surrogate Modeling (or metamodeling) emerged during the last decades of the previous century, from the need to optimally design and perform the simulation experiments. The latter gradually substitute physical experiments in many scientific domains. The simulation experiments are used to study problems concerning physical phenomena that cannot be solved directly with mathematical calculus. They can consider scenarios for many different input values and study what happens to the output. Nevertheless, the huge amount of data obtained from these experiments and their heavy - often - computational load, impose the necessity to organize the way these experiments are conducted. The methods to do that are grouped under the name of *Design of Experiments* (DoE) - or *Design and Analysis of Simulation Experiments* (DASE) as suggested in [Kleijnen, 2008] - and they aim to optimally design the experiments and to exploit their results.

One of the major issues of numerical modeling and DoE is the heavy computational load. In several simulation experiments we deal with expensive-to-evaluate functions, where even one single simulation can last several days or weeks. In cases like these, many different input configurations for the model, are hard to be examined. It is when the use of approximation methods based on probabilistic surrogate models (also called metamodels) comes up with some significant advantages. These methods are faster and they also require fewer function evaluations/simulations, since they take into account less inputs factors than the original model does. A complex computer code can be replaced by a surrogate model which has to be as representative as possible of this code and with good prediction capabilities. In addition, it must require a negligible calculation time. These metamodels can help us explain the underlying simulation behavior of a model and predict the expected output $f(\mathbf{x})$ of its I/O function f, for combinations of input values $\mathbf{x}$ that have not yet been simulated [Kleijnen, 2009]. Rendering that way a view of the entire design space. Apart from prediction, the surrogate models can be additionally used for validation of the simulation model, sensitivity analysis (SA) and optimization [Kleijnen, 2007].

4.3 Surrogate modeling methods

There exist several metamodeling techniques currently in use. In general, they consider the system of the simulation experiment as a "black-box", since usually no closed-form formulation or gradient information of the objective function are available. The only information that we have are the measurements of the system performance, which can be updated only by running new simulations. The black-box assumption within a probabilistic frame can make up for the lack of knowledge and the information shortage on the I/O function. Until recently, the majority of the scientific publications on metamodels was focused on low-order *Polynomial Regression* [Kleijnen, 2009]. These metamodels are fitted to data obtained from local or global experiments of the simulation model and they are used for explanation of the model's behaviour and prediction. The polynomial models can have any power for any factor and interactions of powers of factors, but in practice mostly first and second order polynomials are used. If $y = f(\mathbf{x}) + \varepsilon$ is the model response assuming an error ε, the polynomial prediction for the first and second order are given by the following formulae [Simpson et al., 2001]:

$$\hat{y} = \beta_0 + \sum_{i=1}^{k} \beta_i x_i, \quad \hat{y} = \beta_0 + \sum_{i=1}^{k} \beta_i x_i + \sum_{i=1}^{k} \beta_{ii} x_i^2 + \sum_{i=1}^{k} \sum_{\substack{j=1 \\ i<j}}^{k} \beta_{ij} x_i x_j \qquad (4.1)$$

where x_i are the factors-components of $\mathbf{x}$ and β_i, β_{ij} are the polynomial coefficients usually determined by Least Squares Regression [Kleijnen, 2007] using the existing data.

A more recent metamodeling method which flourishes since the beginning of the century and can approximate functional data also, is the so-called *kriging interpolation*. Kriging is based on Gaussian Random Processes (GRP) or Gaussian Random Fields (GRF)[18] and it can be fitted to data obtained from larger experimental areas, than the areas used in low-order polynomial regression [Kleijnen, 2007]. If $\{f(\mathbf{x}_i)\}_{i=1}^{n}$ is the set of the already obtained simulations results, then the kriging predictor for an unsimulated point $\mathbf{x}$ is given by:

$$\hat{f}(\mathbf{x}) = \sum_{i=1}^{n} \lambda_i f(\mathbf{x}_i) \qquad (4.2)$$

where λ_i are the so-called kriging coefficients or weights. These weights are selected using the *Best Linear Unbiased Predictor (BLUP)* which minimizes by definition the *Mean Square Error (MSE)* of the prediction. The kriging weights are not constants as the β_i and β_{ij} ones, but they decrease with the distance between the point under prediction $\mathbf{x}$ and the already simulated ones $\mathbf{x}_i, i = 1, \ldots, n$ [Kleijnen, 2007]. Moreover, kriging provides an estimation of the prediction uncertainty, which can be used in adaptive strategies as we will see later on.

If the objective is to approximate scattered multivariate data, the *Radial Basis Function (RBF)* method can be applied [Queipo et al., 2005]. The general form of a radial basis interpolator is [Baxter, 1992]:

$$s(\mathbf{x}) = \sum_{i \in I} y_i \varphi\left(\|\mathbf{x} - i\|\right), \quad \mathbf{x} \in \mathbb{R}^d \qquad (4.3)$$

---

[18]Random Processes are used when the model is a function of one variable (usually time) and Random Fields when it is a function of more variables (usually spatial ones).

where $\varphi : [0, \infty) \to \mathbb{R}$ is a fixed univariate function, I is the set of the so-called centers of the radial basis function intepolant and the coefficients y_i are real numbers evaluated using the simulation responses. There is no restriction on the norm $\| \cdot \|$ but the Euclidean norm is the most commonly used. For the radial basis functions φ some of the most common choices are the multiquadric, the thin plate splines, the inverse multiquadric and the Gaussian functions [Baxter, 1992].

Other methods used for metamodeling are the *Artificial Neural Networks*, which are composed by multiple linear regression models with a nonlinear transformation on the output y (e.g. the sigmoid) [Simpson et al., 2001], [Rumelhart et al., 1994], and a quite recent one providing also the first statistical moments of the output, as kriging does, is the *Polynomial Chaos Expansion (PCE)* [Blatman, 2009]. Apart from these single surrogate methods, using multiple surrogates can improve the global search capability in cases where sparse data exist, but in the price of a much higher computational load.

So far, there is no conclusion about which metamodel is definitely superior to the others [Wang and Shan, 2006]. Depending on the problem under consideration, a particular modeling scheme may outperform the others and in general it is not known a priori which one should be selected [Queipo et al., 2005]. However, kriging and low-order polynomials are the most widely used. In the present dissertation, we will use the kriging interpolation. Firstly, because of its ability to approximate data from large experimental areas and secondly because it can provide a measure of the approximation uncertainty. The stepwise reduction of this uncertainty can be a valuable tool for designing more sophisticated adaptive sampling techniques, which result in more effective metamodels.

4.4 Kriging interpolation

Kriging, also known as spatial correlation modeling, is a probabilistic method which originated from Geostatistics. It was designed for interpolating functions that show certain spatial correlation. Its name was coined by G.Matheron in honor of D.Krige, who first applied the empirical version of this method to estimate the most likely distribution of gold in an area, based on a few samples only. Matheron himself established later the theoretical basis of the method (see [Matheron, 1963] and [Matheron, 1969]). Kriging is based on GRF[19] and its metamodels can be fitted to data that are obtained from large experimental areas. These metamodels can provide a cheap and accurate approximation of the objective function under study, together with an estimation of the potential error of this approximation. The latter is the main advantage of the method and together with the method's flexibility contributed to its quick expansion during the last years. Nowadays kriging is used in several different scientific fields, both for deterministic[20] and stochastic simulations experiments, even in high dimensional cases.

---

[19]A GRF can be viewed as a function whose values are random variables that have a Gaussian (or normal) distribution.

[20]It seems odd that a random metamodel can be applied to a deterministic simulation model. J.P.C. Kleijnen's interpretation is that the deviations of the simulation output f from its mean μ form a random process, with the characteristics of a *stationary covariance process* (with zero mean). f is assumed to be a sample path of a second-order Gaussian random process F. If we denote as $(\Omega, \mathcal{A}, \mathcal{P})$ the underlying probability space, this amounts to assuming that $\exists \, \omega \in \Omega$, such that $F(\omega, \cdot) = f(\cdot)$ [Villemonteix et al., 2009].

The main idea of the method is to model the I/O function by a GRF. This provides a probabilistic framework which accounts for the uncertainty stemming from the lack of information on the system [Villemonteix et al., 2009]. The GRF is fully characterized by its mean and covariance, which are both derived from the existing data. The covariance is strongly dependent on the observation points and reflects the correlation among them, which is usually assumed stationary. Stationarity implies that only the distance between two points is important and the covariance is invariant under translation. This assumption is being done for computational reasons and not because it is always compatible with the physics of the problem.

Three steps are important while building a kriging metamodel:

1. the choice of the input variables,

2. the design of the input (sample) space and

3. the choice of the covariance function of the predictor.

There are many different kriging methods, most of them concerning interpolation of scalar values. Recently, some new implementations in approximating curves via the so-called *functional kriging*, were carried out (see [Giraldo et al., 2007], [Delicado et al., 2009] and [Bilicz, 2011]). However, scalar kriging methods still cover the needs of most applications, while keeping the computational load sufficiently low. In our case, scalar kriging was finally preferred to the functional one, not only because of its simpler form and the much lower computational load, but also because in our adaptive-cognitive strategy which will be presented in Chapter 5, the data will be so sparse that no functional kriging method can be employed. For a review of the various scalar kriging techniques that exist, the interested reader can refer to [Chilès and Delfiner, 1999]. In this study, the most common ones called *Universal Kriging* (UK) and *Ordinary Kriging* (OK) will be employed. OK assumes a constant mean[21] for the entire domain and a known stationary covariance model. UK keeps the known stationary covariance model but it considers a general polynomial trend model for the mean. Despite the existence of more complicated kriging versions, these two are still the most widely applied in practice.

Kriging interpolation has the advantage of providing an estimation of the prediction uncertainty via the variance of the prediction error, also called *kriging variance*. Apart from assessing the overall quality of the approximation, this variance can be a powerful tool for designing adaptive metamodeling strategies. In fact, adaptive sampling methods gain ground recently against the traditional prefixed sampling ones for two reasons. Firstly, because the computer experiments proceed sequentially and so adaptive methods seem more "natural" for them [Jin et al., 2002] and secondly because they are known to be more efficient - they require fewer observations - than fixed-sample procedures[22] [Kleijnen and van Beers, 2004]. Various ways to implement an adaptive design have already been tested, using different measures of the prediction uncertainty and reducing it sequentially. For example, the kriging variance was used in [Bect et al., 2012] to estimate the probability of failure and in [Chevalier et al., 2014] for a parallel stepwise uncertainty reduction schema. However, the cross-validation and jackknifing estimation methods show superior performance than the kriging variance based sequential designs in several cases [Kleijnen and van Beers, 2004]. So, a combination of kriging variance and

---

[21] As shown in [Chilès and Delfiner, 1999] the case of the known constant mean is equivalent to the case of zero mean.

[22] Procedures with an a priori designed sample space which does not change during the prediction.

the Leave-One-Out Cross-Validation error to sequentially expand the sample space by adding one or several points at-a-time was adopted in [Le Gratiet and Cannamela, 2012], the kriging variance with the probability density function (PDF) of the input parameter uncertainties and the gradients of the kriging predictor were also used and compared in [Shimoyama et al., 2013] and a "normalized" jackknife variance multiplied with the maximal minimum distance between the observation points and the new point to be added in a functional kriging procedure were selected in [Bilicz, 2011] and [Vaskó, 2011]. In this work, the latter one, already successfully applied to COSMO approximations in [Vaskó, 2011], was qualified together with the product of the jackknife variance with the original kriging one, to improve the prediction and define its confidence intervals. This adaptive kriging method will be described in details in the upcoming section.

4.5 Adaptive kriging

We have already mentioned that the kriging method is based on a GRF and its predictor is a linear combination of the simulated values. As a consequence, kriging performance depends on both the choice of the input values, where the observations are to be done, and the choice of the covariance and mean of the GRF. For the input sample, a sequential design will be generated, based on a small initial pre-fixed sample of observations. Concerning the mean of the predictor, UK assumes a polynomial trend model, based on l linear independent monomials of the components of $\mathbf{x}$:

$$m\left(\mathbf{x}\right) = \sum_{0}^{l} \alpha_i g_i\left(\mathbf{x}\right) \tag{4.4}$$

where α_i are unknown coefficients which will be estimated from the data. In case all g_is are constant, $m\left(\mathbf{x}\right) = \mu$ is also constant and we have OK. About the covariance, since it is unknown but has to "reflect" somehow the spatial correlation of the observation points, a flexible function has to be chosen. So that we can "tune" it to best fit our data via the covariance parameters estimation. The Matérn covariance function is a good choice, since it offers the possibility to adjust its regularity - and thus the prediction's smoothness - with just a single parameter[23]. Other commonly used covariance models are the exponential, the spherical and the Gaussian ones, which do not provide any control on the flexibility of the random field though. The covariance is assumed stationary - only the distance between two points is of interest - and anisotropic. Stationary because the non-stationary ones are seldom in practice (an example of their use can be found in [Xiong et al., 2007]) and require a particularly difficult parameter estimation. Anisotropic because the model factors are of different nature and their domains can potentially vary a lot. The distance function that will reflect the spatial correlation and also introduce the anisotropy is defined as:

$$h\left(\mathbf{x}_i, \mathbf{x}_j\right) = \sqrt{\sum_{k=1}^{d} \left(\frac{x_{i,k} - x_{j,k}}{\rho_k}\right)^2} \tag{4.5}$$

---

[23]As Michael Stein mentions, the Matérn covariance includes a parameter that allows any degree of differentiability for the random field. It also includes the exponential covariance model as a special case and the Gaussian model as a limiting case [Stein, 1999], two models that are also frequently used in metamodeling construction. For more information see Appendix A.1 and [Stein, 1999].

where $x_{i,k}, x_{j,k}$ are the k-th components of the $\mathbf{x}_i$ and $\mathbf{x}_j$ vectors respectively, ρ_k is the scaling factor for the k-th component of the input vectors and d is the dimension of the metamodel input space. The scaling factors stand for the sensitivity of the model to the different inputs - anisotropy. High ρ_k implies low sensitivity of the model to the corresponding input [Bilicz, 2011] as seen also in Fig. 4.1. Using the distance in Eq. (4.5) the Matérn covariance model is given by the formula:

$$k\left(\mathbf{x}_i, \mathbf{x}_j\right) \equiv k\left(h\left(\mathbf{x}_i, \mathbf{x}_j\right)\right) = \frac{2^{1-\nu} \cdot \sigma^2}{\Gamma\left(\nu\right)} \cdot \left(2\sqrt{\nu}h\left(\mathbf{x}_i, \mathbf{x}_j\right)\right)^{\nu} \mathcal{K}_{\nu}\left(2\sqrt{\nu}h\left(\mathbf{x}_i, \mathbf{x}_j\right)\right) \qquad (4.6)$$

where ν is the parameter that controls the regularity of the covariance function and $\sigma^2 = k\left(0\right)$. In Fig. 4.1, the effect of the different values of ν on the Matérn covariance function is also shown. Since the covariance is unknown, we have to estimate its parameters so that they will better fit our model i.e. our observations. These covariance parameters (also called hyper-parameters) are ν, σ^2 and the scaling factors $\{\rho_k\}_{k=1}^{d}$ and their estimation will be done by the REstricted Maximum Likelihood estimation (REML) method (see Appendix A.2). For the hyper-parameter estimation, the Leave-One-Out Cross-Validation (LOOCV) method can be employed also[24]. In our case, the LOOCV was giving similar or worse estimations for the hyper-parameters than REML did and since REML is lighter from a computational point of view, it was finally preferred for our metamodel.
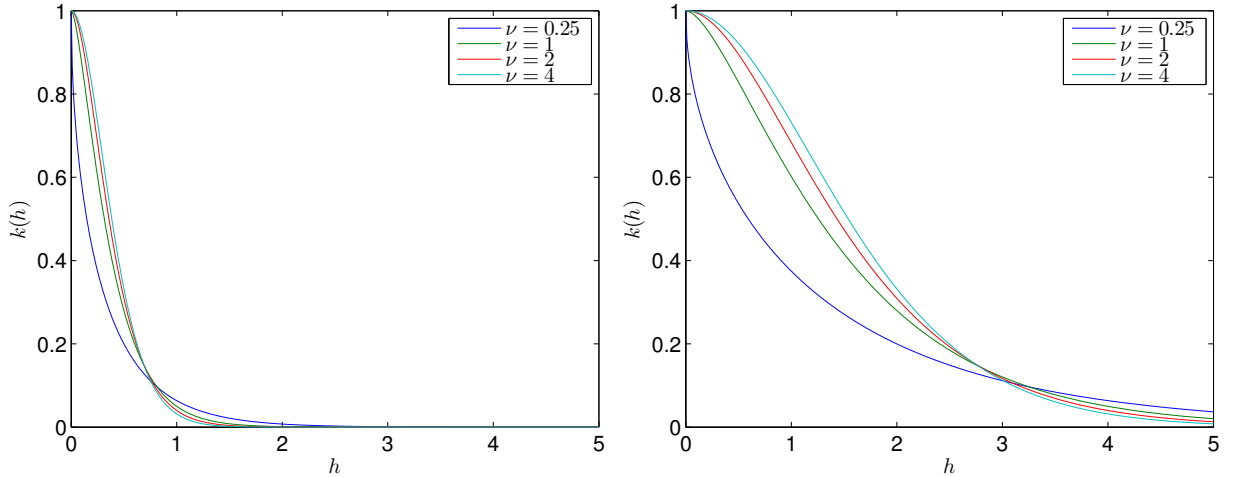
Figure 4.1 – The Matérn covariance plot with respect to the distance h for different values of the smoothing parameter ν for $\rho_k = 0.5$ (left) and $\rho_k = 2$ (right). The variance was set $\sigma^2 = 1$. It is obvious that the highest the value for ρ_k, the less sensitive the covariance is to the distance, for the k-th input.

After defining the mean and the covariance of the model, kriging calculates the prediction via the equation (4.2), using the data from the initial sample. The λ_i weights are selected so that the interpolator is the BLUP of the forward function in the vector space generated by the observations. This predictor[25] is *linear* because it evaluates the forward function approximation as a linear combination of the observations (equation (4.2)). It is also *best* because it minimizes

---

[24]Information about the Cross Validation method and a direct comparison with the Maximum Likelihood Estimation can be found in [Bachoc, 2013].

[25]Predictors estimate random effects while estimators estimate fixed effects [Robinson, 1991].

the Mean Squared Error (MSE) of the prediction:

$$\min_{\substack{\lambda_i \in [-1,1] \\ i=1,\dots,n}} MSE\left[\hat{f}\left(\mathbf{x}\right)\right] = \min_{\substack{\lambda_i \in [-1,1] \\ i=1,\dots,n}} MSE\left[\sum_{i=1}^{n} \lambda_i f\left(\mathbf{x}_i\right)\right] = \min_{\substack{\lambda_i \in [-1,1] \\ i=1,\dots,n}} \left[\mathbb{E}\left(\sum_{i=1}^{n} \lambda_i f\left(\mathbf{x}_i\right) - f\left(\mathbf{x}\right)\right)^2\right]$$
(4.7)

where $\mathbf{x}$ may be any input point in the experimental area. Moreover, this minimization must account for the condition that the predictor is *unbiased*:

$$\mathbb{E}\left(\hat{f}(\mathbf{x})\right) = \mathbb{E}\left(f(\mathbf{x})\right)$$
(4.8)

where in deterministic simulation, as in our case, we can replace $\mathbb{E}\left(f(\mathbf{x})\right)$ with $f(\mathbf{x})$, as every simulation at $\mathbf{x}$ gives the same value $f\left(\mathbf{x}\right)$. It can be proved that the solution of the constrained minimization problem defined by Eq. (4.7) and (4.8), given the mean in Eq. (4.4), implies that the weights of the kriging linear predictor must satisfy the so-called *universality condition* (see [Chilès and Delfiner, 1999] for more details):

$$\sum_{i=1}^{n} \lambda_i = 1 \quad \text{or} \quad \mathbf{1}^T \boldsymbol{\lambda} = 1$$
(4.9)

After specifying the kriging model to be used for the prediction, it is time to sketch out the sequential procedure to be performed. In Fig. 4.2 its general flowchart is presented. The loop opens with the generation of the initial sample. Then the simulations are run on the sample points and the initial prediction is calculated via the simulations results. The estimation of the initial prediction's uncertainty follows and if the terminal criterion of the loop is not met, a new simulation point is added to the sample and the loops starts over again. If the criterion is met, the prediction is the optimal one, with respect to our needs, and the loop closes. The following paragraphs contain a thorough description of each step of this sequential procedure.

4.5.1 Initial prediction

Kriging is an exact interpolation method, so it needs the results of several simulation runs of the model, in order to predict the function under study. The adaptive procedure requires as a first step an initial prediction, based on the results of a sample adequately spread in the input space. Despite the fact that the initial prediction will be improved later on, a good initial prediction is never superfluous, as long as it does not require much computational time. Since the most natural choice of a rectangular grid of points (also known as full factorial design) requires many points to cover the input space, especially when the dimensions are increasing, a *Latin Hypercube Sample (LHS)* is preferred. LHS consists in dividing the domain of each input variable in N equiprobable strata, and in sampling once from each stratum. These samples are proven able to cover the input space in a better way than the factorial designs do, i.e. using less points [McKay et al., 1979]. Nevertheless, LHS alone does not ensure the proper filling, so a *maximin* criterion will be used. This criterion maximizes the minimum distance between each new point with the already existing design [Fang et al., 2006] and it is available even as a Matlab built-in function. The LHS generated is always within the unit hypercube as seen in Fig. 4.3 for the 2-dimensional case, so in order to evaluate the appropriate forward function values it is necessary to expand it to the original input space $\mathbb{X}$. As mentioned before, kriging is an exact interpolator and extrapolation is not recommended [Bachoc et al., 2014]. It is thus
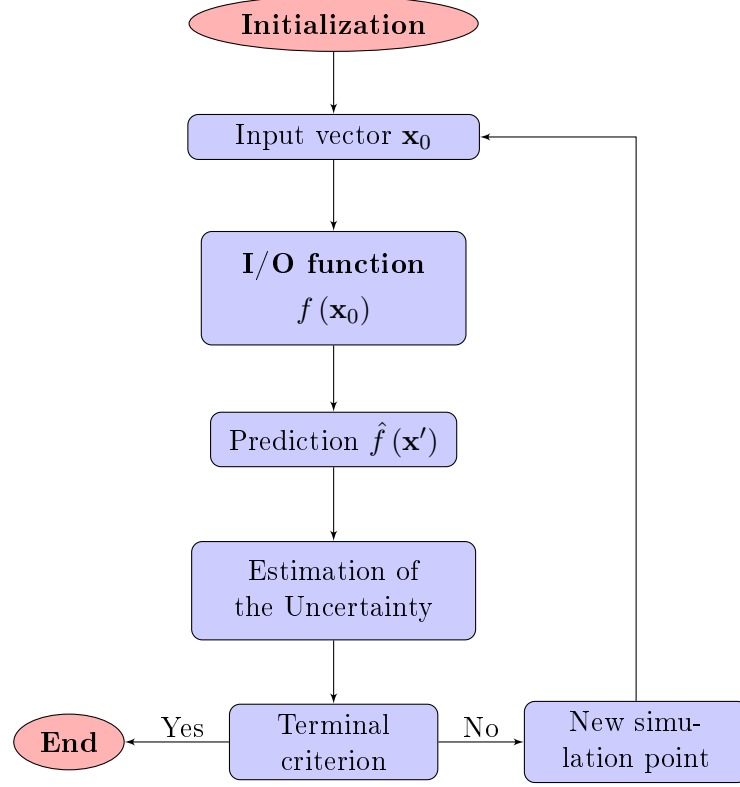
Figure 4.2 − The general flowchart of an adaptive metamodel.

necessary to supplement the sample with border points of the input space to achieve trustworthy results. The resulting set contains n vectors $\mathbb{X}_n = \{\mathbf{x}_i\}_{i=1}^n$ which gives us the vector of the n observations $\mathbf{f}_{\mathbb{X}_n} = (f(\mathbf{x}_1), \dots, f(\mathbf{x}_n))^T$. The mean for the universal kriging is given by Eq. 4.4.

After constructing the initial observation sample, in order to proceed to the prediction of the I/O function at a point $\mathbf{x} \in \mathbb{X}\backslash\mathbb{X}_n$, we need to compute the $n \times n$ covariance matrix of this sample space:

$$\mathbf{K} = [k(\mathbf{x}_i, \mathbf{x}_j)], \ i,j = 1, \dots, n$$

the covariance vector of the prediction point $\mathbf{x}$:

$$\mathbf{k}(\mathbf{x}) = (k(\mathbf{x}, \mathbf{x}_1), \dots, k(\mathbf{x}, \mathbf{x}_n))^T$$

the matrix of the g_i coefficients of the observation points:

$$\mathbf{G} = \left(\mathbf{g}(\mathbf{x}_1)^T, \mathbf{g}(\mathbf{x}_2)^T, \dots, \mathbf{g}(\mathbf{x}_n)^T\right)^T \tag{4.10}$$

where $\mathbf{g}(\mathbf{x}_i) = \left(g_0^i, g_1^i, \dots, g_l^i\right)^T$ for the observation points $\mathbf{x}_i, i = 1, \dots, n$ and the corresponding vector $\mathbf{g}(\mathbf{x}) = (g_0, g_1, \dots, g_l)^T$ for the prediction point $\mathbf{x}$. After these we are ready to compute the kriging coefficients $\lambda_i(\mathbf{x})$ and the Lagrange multipliers $\boldsymbol{\mu}(\mathbf{x})$ for the prediction point $\mathbf{x}$, by solving the following linear system (in Lagrangian form):

$$\begin{pmatrix} \mathbf{K} & \mathbf{G} \\ \mathbf{G}^T & \mathbf{0} \end{pmatrix} \cdot \begin{pmatrix} \boldsymbol{\lambda}(\mathbf{x}) \\ \boldsymbol{\mu}(\mathbf{x}) \end{pmatrix} = \begin{pmatrix} \mathbf{k}(\mathbf{x}) \\ \mathbf{g}(\mathbf{x}) \end{pmatrix} \tag{4.11}$$
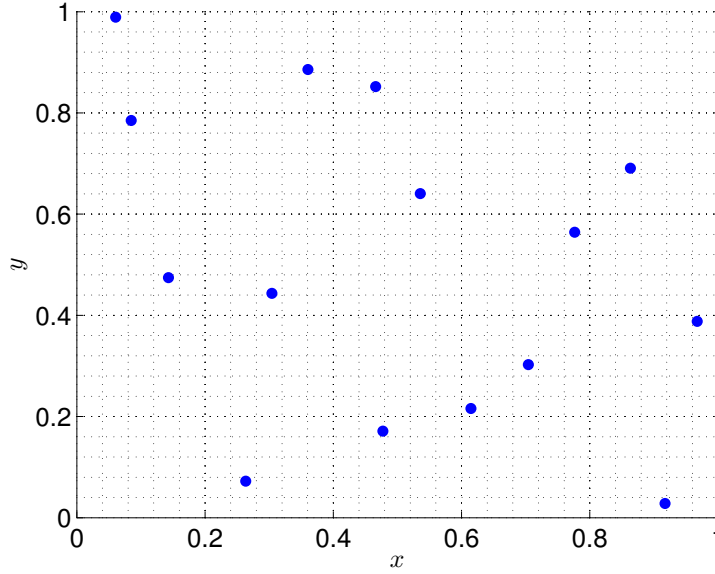
Figure 4.3 – A 15-point maximin LHS in a 2-D unit cube, as generated by the Matlab built-in function.

where $\mathbf{0}$ is a matrix of zeros. For OK, since the mean is constant we have $\mathbf{G} = (1, \ldots, 1)^T$, $\mathbf{g}(\mathbf{x}) = 1$, $\mu(\mathbf{x})$ scalar and so the system in Eq.(4.11) becomes:

$$\begin{pmatrix} \mathbf{K} & \mathbf{1} \\ \mathbf{1}^T & 0 \end{pmatrix} \cdot \begin{pmatrix} \boldsymbol{\lambda}(\mathbf{x}) \\ \mu(\mathbf{x}) \end{pmatrix} = \begin{pmatrix} \mathbf{k}(\mathbf{x}) \\ 1 \end{pmatrix} \tag{4.12}$$

The initial prediction for the I/O function is subsequently given by the formula [Villemonteix et al., 2009]:

$$\hat{f}(\mathbf{x}) = \boldsymbol{\lambda}(\mathbf{x})^T \mathbf{f}_{\mathbb{X}_n} \tag{4.13}$$

The kriging property of exact interpolation results that $\forall \mathbf{x}_i \in \mathbb{X}_n$, it is $\hat{f}(\mathbf{x}_i) = f(\mathbf{x}_i)$ while for all the other $\mathbf{x} \in \mathbb{X}$, it is $\hat{f}(\mathbf{x}) \simeq f(\mathbf{x})$.

4.5.2 Estimation of the uncertainty

A major advantage of the kriging metamodeling procedure is that it provides the prediction together with an estimation of the its uncertainty. This quantity is not directly connected with the prediction error:

$$\varepsilon(\mathbf{x}) = \left\| \hat{f}(\mathbf{x}) - f(\mathbf{x}) \right\| \tag{4.14}$$

which cannot be evaluated without running a simulation at $\mathbf{x}$. However, this uncertainty can indicate whether a prediction is good or not. The prediction unertainty is given by the variance of the prediction error called also *kriging variance* which is defined as [Villemonteix et al., 2009]:

$$\hat{\sigma}^2(\mathbf{x}) := \mathbb{E}\left[\left(\hat{f}(\mathbf{x}) - f(\mathbf{x}) \right)^2 \right] = k(0) + \boldsymbol{\lambda}(\mathbf{x})^T \mathbf{K} \boldsymbol{\lambda}(\mathbf{x}) - 2\boldsymbol{\lambda}(\mathbf{x})^T \mathbf{k}(\mathbf{x}) \tag{4.15}$$

From the system in (4.11), we have:

$$\mathbf{K}\boldsymbol{\lambda}(\mathbf{x}) + \mathbf{G}\boldsymbol{\mu}(\mathbf{x}) = \mathbf{k}(\mathbf{x}) \Leftrightarrow \mathbf{K}\boldsymbol{\lambda}(\mathbf{x}) = \mathbf{k}(\mathbf{x}) - \mathbf{G}\boldsymbol{\mu}(\mathbf{x}) \tag{4.16}$$

and:
$$\mathbf{G}^T \boldsymbol{\lambda}(\mathbf{x}) = \mathbf{g}(\mathbf{x}) \Leftrightarrow \boldsymbol{\lambda}(\mathbf{x})^T \mathbf{G} = \mathbf{g}(\mathbf{x})^T \tag{4.17}$$

and thus Eq. (4.15) takes the form:

$$
\begin{aligned}
\hat{\sigma}^2(\mathbf{x}) &= k(0) + \boldsymbol{\lambda}(\mathbf{x})^T \mathbf{K}\boldsymbol{\lambda}(\mathbf{x}) - 2\boldsymbol{\lambda}(\mathbf{x})^T \mathbf{k}(\mathbf{x}) \\
&\overset{(4.16)}{=} k(0) + \boldsymbol{\lambda}(\mathbf{x})^T \mathbf{k}(\mathbf{x}) - \boldsymbol{\lambda}(\mathbf{x})^T \mathbf{G}\boldsymbol{\mu}(\mathbf{x}) - 2\boldsymbol{\lambda}(\mathbf{x})^T \mathbf{k}(\mathbf{x}) \\
&\overset{(4.17)}{=} k(0) - \boldsymbol{\lambda}(\mathbf{x})^T \mathbf{k}(\mathbf{x}) - \mathbf{g}(\mathbf{x})^T \boldsymbol{\mu}(\mathbf{x})
\end{aligned}
\tag{4.18}
$$

and for the case of OK:
$$\hat{\sigma}^2(\mathbf{x}) = k(0) + \boldsymbol{\lambda}(\mathbf{x})^T \mathbf{k}(\mathbf{x}) - \mu(\mathbf{x}) \tag{4.19}$$

If the kriging variance is high for a certain prediction, the variance of this prediction's error is high, and thus the prediction is a non satisfying one.

Despite the fact that the kriging variance $\hat{\sigma}^2$ can indicate whether a prediction is poor or not, it is not the best choice for designing adaptive schemas. Its main drawback is that in a stationary case as ours, both the kriging weights and the kriging variance are shift invariant. So there is no direct relation between the kriging variance and the location of input samples. It is the mutual distance between two points that affects $\hat{\sigma}^2$ and the covariance function that links it indirectly with the sample points, via the hyper-parameter estimation. In addition, it is also proven in [den Hertog et al., 2004] that the kriging variance formula (4.15) underestimates the true variance of the prediction error. Thus, in order to use the prediction uncertainty to locate the new observation points during the adaptive sampling procedure in an optimal way, another measure has to be introduced. Resampling methods, such as jackknifing or bootstrapping, can be used instead and give better estimates as shown in [den Hertog et al., 2004], [Kleijnen, 2011] and [Bilicz, 2011]. However, since these methods are based in resampling the original sample, extra attention should be paid on the possibility to highly overestimate the error at an observation point. In this work, the jackknife method which is an approximation of bootstrapping[26] will be used, because it is simpler than bootstrapping and computationally cheaper.

The jackknife variance

Jackknife is a technique for estimating the bias and the standard error of an estimate [Efron and Tibshirani, 1994]. It is based on the evaluation of the so called *reduced predictions* for every prediction point, by leaving out one observation at a time. Jackknife consists of the following four steps :

1. Evaluating the i-th reduced prediction, by leaving out of the sample the i-th point:

$$\hat{f}^{(-i)}(\mathbf{x}) = \boldsymbol{\lambda}^{(-i)}(\mathbf{x})^T \mathbf{f}_{\mathbb{X}_n}^{(-i)} \tag{4.20}$$

2. Defining and calculating the *pseudovalues*, which are the differences between the prediction based on the whole sample and those based on the reduced ones:

$$\tilde{f}^{(-i)}(\mathbf{x}) = n\hat{f}(\mathbf{x}) - (n-1)\hat{f}^{(-i)}(\mathbf{x}), \quad i = 1, \dots, n \tag{4.21}$$

---

[26]The interested reader can refer to [Shao and Tu, 2012] and [Efron and Tibshirani, 1994] for a thorough presentation of both jackknife and bootstrap, which are the most popular data-resampling methods used in statistical analysis.

The pseudovalues can be treated as though they were n independent and identically distributed (i.i.d.) data values.

3. Calculating the *modified prediction*, which is the mean of the pseudovalues:

$$\hat{f}_{jack}\left(\mathbf{x}\right) = \frac{1}{n} \sum_{i=1}^{n} \tilde{f}^{(-i)}\left(\mathbf{x}\right) \tag{4.22}$$

4. Estimating the jackknife variance, by the standard error of the mean and using the variance of the pseudovalues:

$$\hat{\sigma}_{jack}^{2}\left(\mathbf{x}\right) = \frac{1}{n\left(n-1\right)} \sum_{i=1}^{n} \left(\tilde{f}^{(-i)}\left(\mathbf{x}\right) - \hat{f}_{jack}\left(\mathbf{x}\right)\right)^{2} \tag{4.23}$$

The index $(-i)$ in the equations above, implies that the i-th observation is being ignored during the calculations[27]. Jackknife, as a resampling method, can be sometimes misleading about the real variance values around the observation point left out during each reduced prediction. Nevertheless, the latter defect can be easily surpassed, as we will see in the next paragraph, and jackknife can be a powerful tool to assist in improving the initial prediction during the adaptive sampling.

4.5.3 Stepwise uncertainty reduction

When constructing a metamodel, the goal is to generate an input database which will be a kind of a discrete representation of the I/O function. This can significantly contribute in a better prediction accuracy, but it cannot take place with the traditional fixed sampling designs. The best way to design a representative input sample, is to start from a small but sufficiently spread initial set and adaptively implement it using an appropriate criterion. The basic idea behind this adaptive sampling is to locate where should the evaluation of the model be carried out optimally, to improve our knowledge on the forward function, based on the previous observations and predictions. The location of the new points to be simulated, can be discovered by the uncertainty of the prediction. Each new sample point has to be a point where the prediction is poor. When this point is added in the input sample and the new prediction is done, the prediction will be improved and the uncertainty will be lower. Continuing like that, we reach to a stepwise uncertainty reduction scheme. The last to be defined in this scheme is the terminal criterion of this adaptive procedure, i.e. when no more points are needed. This terminal criterion could be either a maximum number N_0 of extra points to be added, or a desired value M for the prediction uncertainty.

The main tool for the uncertainty reduction, is the uncertainty itself. In the previous section we explained why the jackknife estimation of the variance is the appropriate measure of this uncertainty. Thus, we will find the new sample points in our adaptive procedure, where the estimated jackknife variance is high. To surpass the problem of the possible large values around the observation points, that can cause singularity to the matrices in Eq. (4.11) and (4.12), two different methods are proposed. The first uses the minimum Euclidean distance between the new point and the sampled ones and the second the kriging variance as presented in Eq. (4.18)

---

[27]We take care not to ignore the observations done on the border of the input space, because they are indispensable for the kriging predictor, since it is only an interpolator and not an extrapolator.

or Eq. (4.19), depending on the kriging method. In both methods, the jackknife variance is multiplied by either the minimum distance or the kriging variance which are both eliminated at the already observed points of the input space. The new point to be added to the database is subsequently selected as follows:

$$\mathbf{x}_{n+1} = \arg\max_{\mathbf{x}\in\mathbb{X}} \left[\left(\min_{i=1,...,n} \|\mathbf{x} - \mathbf{x}_i\| \right) \cdot \hat{\sigma}_{jack}\left(\mathbf{x}\right) \right] \tag{4.24}$$

or

$$\mathbf{x}_{n+1} = \arg\max_{\mathbf{x}\in\mathbb{X}} \left(\hat{\sigma}\left(\mathbf{x}\right) \cdot \hat{\sigma}_{jack}\left(\mathbf{x}\right) \right) \tag{4.25}$$

The difference between the two criteria is that while in the Eq. (4.24) the exact euclidean distance is used, in the Eq. (4.25) the distance corresponding to the hyper-parameter values of both Eq. (4.5) and (4.6) estimated from the data is used via the kriging variance. This measure is supposed to represent better the data and the I/O function properties than the euclidean distance does. While testing these criteria on toy functions, we observed that they were giving comparable results in terms of time and prediction quality. None of the two was generally superior to the other, although in the examples of this dissertation the latter was selected since it could provide satisfying confidence intervals for the predictions.

By maximizing the products of Eq. (4.24) or (4.25), we ensure that both a high jackknife variance and a high minimum distance from the already observed points or that both the variances are high. We continue the aforementioned procedure of selecting new points and reducing the prediction uncertainty, until a terminal criterion is met. This terminal criterion can be set as the total number of the points in the input sample, or the level of prediction accuracy to be achieved. For each new point added to the sample, we have to re-evaluate both the kriging prediction by Eq. (4.13) and the jackknife variance by Eq. (4.23). As soon as the optimal input sample $\mathbb{X}$ is complete, the same formulae will give us the final prediction and its level of uncertainty. If the uncertainty is the product of the kriging and jackknife variances, it can be also used to determine the confidence intervals of the prediction. Otherwise, the square root of the kriging variance (kriging standard deviation (std)) can be used. As already mentioned, we preferred the square root of the product used in Eq. (4.25), to have the same units as the quantity of interest. So the std $\tilde{\sigma}$ used was:

$$\tilde{\sigma}\left(\mathbf{x}\right) = \sqrt{\hat{\sigma}\left(\mathbf{x}\right) \cdot \hat{\sigma}_{jack}\left(\mathbf{x}\right)} \tag{4.26}$$

and the confidence intervals $\pm\tilde{\sigma}$ for each prediction point $\mathbf{x}$ are $\left(\hat{f}\left(\mathbf{x}\right) - \tilde{\sigma}\left(\mathbf{x}\right), \hat{f}\left(\mathbf{x}\right) + \tilde{\sigma}\left(\mathbf{x}\right) \right)$. Finally, our adaptive metamodeling method is complete and its detailed flowchart is presented in Fig. 4.4.

4.6   Validation of the metamodel

The quality of a metamodel can be estimated using real simulation results either over the set of all prediction points, or over a test sample of it. If the real values of all N prediction points are known, the overall approximation error can be calculated using the *Mean Squared Error* (MSE) or the *Root Mean Squared Error* (RMSE) given by the following formulae [Wackerly et al., 2002],
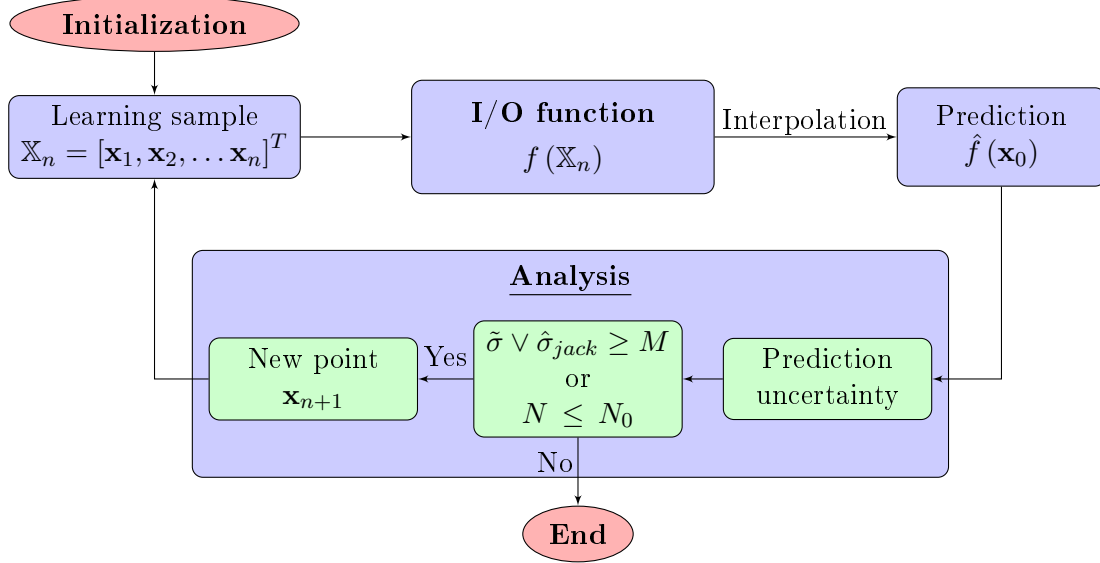
Figure 4.4 – The flowchart representing the closed loop operation of our adaptive metamodel.

[Jin et al., 2002]:

$$\text{MSE} = \frac{1}{N} \sum_{i=1}^{N} \left(\hat{f}(\mathbf{x}_i) - f(\mathbf{x}_i) \right)^2, \qquad \text{RMSE} = \sqrt{\frac{1}{N} \sum_{i=1}^{N} \left(\hat{f}(\mathbf{x}_i) - f(\mathbf{x}_i) \right)^2} \qquad (4.27)$$

Whenever an adaptive metamodel is employed, a way to quantify the improvement of the initial prediction after the stepwise uncertainty reduction procedure is necessary. This can be done by evaluating the *Absolute Improvement* (AI) of the prediction with respect to the RMSE. The AI is calculated, using the RMSE_{in} of the initial prediction and the RMSE_{fin} of the final one, by the formula:

$$\text{AI} = \frac{|\text{RMSE}_{fin} - \text{RMSE}_{in}|}{\text{RMSE}_{in}} \cdot 100\% \qquad (4.28)$$

If simulation results are not available for all prediction points, test samples are usually generated to estimate the quality of the metamodel. This quality can be measured by the *predictivity coefficient* Q_2, which gives the percentage of the output variance explained by the metamodel and is defined as [Iooss et al., 2010]:

$$Q_2 = 1 - \frac{\sum_{j=1}^{n_{test}} \left[\hat{f}(\mathbf{x}_i) - f(\mathbf{x}_i) \right]^2}{\sum_{j=1}^{n_{test}} \left[f(\mathbf{x}_i) - \frac{1}{n} \sum_{j=1}^{n} f(\mathbf{x}_j) \right]^2} \qquad (4.29)$$

where $\{\mathbf{x}_i\}_{j=1}^{n_{test}}$ is a test sample independent from the input sample $\{\mathbf{x}_i\}_{j=1}^{n}$. The aforementioned measures can be also used to compare the quality of different metamodel predictions, of the same I/O function and input sample, but based on different variances for the uncertainty reduction or different g_i monomials for the mean of the UK. In our work, the MSE, the RMSE and the AI will be employed, since all prediction points will be simulated to check the absolute error values for the verification of the results. However, in potential applications of our method, the predictivity coefficient could also be used as few data are usually available in practice.

4.7 Test of the adaptive metamodel on toy functions

After presenting in details our metamodeling method, we will test its effectiveness on toy functions, as done for the SA method also. Two toy functions were selected, one having an 1-dimensional input and the other a 2-dimensional one. Both functions show non-linear and non-monotonic effects, which impose difficulties during the metamodel prediction and they are commonly used for similar purposes. Despite the fact that in the present study 2-dimensional metamodel predictions will not be tried on our numerical model, a 2-dimensional test was performed. This was done in order to both check the metamodel capabilities and to open the ground for high-dimensional COSMO applications in the future.

4.7.1 Approximating a 1-D non-linear test function

In the first test of our adaptive kriging method, we will try to approximate the 1D toy function f plotted in Fig. 4.5 and defined as:

$$f(x) = x(1-x)\sin(2\pi x), \qquad x \in [0, 3]$$

The increasing oscillating nature of this function is a challenge for the fixed design prediction models. Indeed, as seen in the left plot of Fig. 4.6, the initial kriging prediction based on 7 simulation points failed in approximating well the function values, despite the fact that they were contained in the confidence intervals. After adding the 10 adaptively chosen points via the stepwise uncertainty reduction procedure, the kriging prediction achieved a very good accuracy and almost coincided with the real function.
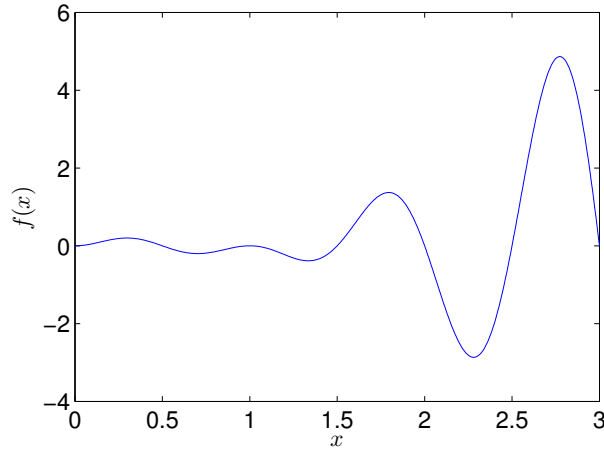
Figure 4.5 − The plot of the 1-D non-linear test function.

Both ways to reduce the uncertainty presented in Eq. (4.24) and (4.25) were tested during the adaptive sampling, providing similar results and comparable computational loads. For the predictions presented in Fig. 4.6 and 4.7, the standard deviation $\tilde{\sigma}$ of Eq. (4.26) was used to locate the new point to be added to the sample and its square root (std) was used to estimate the confidence intervals of the prediction. Fig. 4.7 shows that there was a general, not absolute though, accordance between the oscillations of the absolute error and those of $\tilde{\sigma}$. This accordance assisted in identifying the points where the error was high and considerably improve the prediction. The MSE and the RMSE of the final prediction were MSE = 0.02762 and
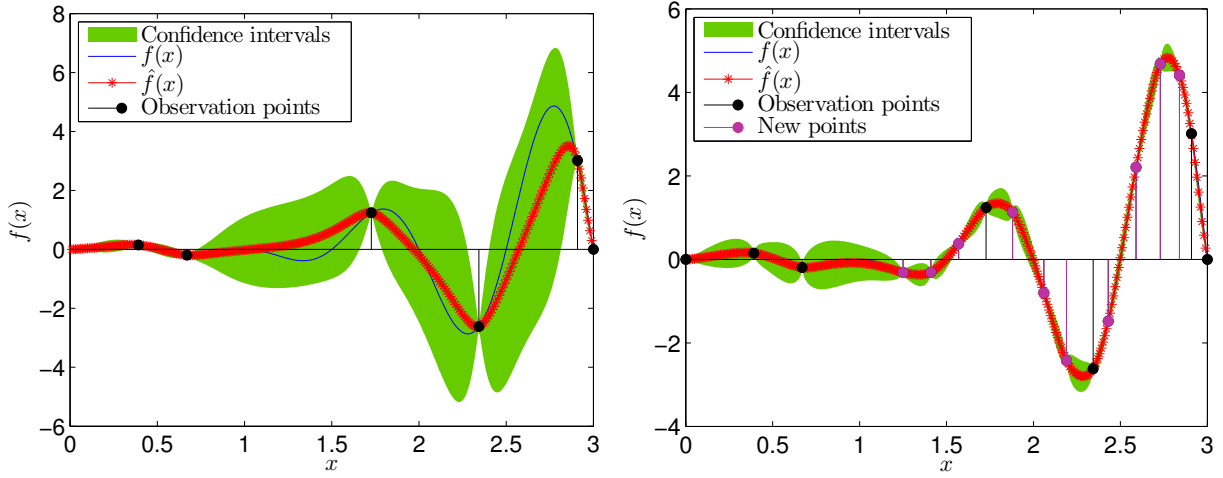
Figure 4.6 – The initial prediction with its confidence intervals for the 1-D test function based on 7 simulation points (left) and the final prediction with its confidence intervals, after adding 10 points using adaptive sampling (right). The final prediction improved significantly the initial one and succeeded in almost coinciding with the real function.

RMSE = 0.0395 respectively, with the latter showing an absolute improvement of 99.88%. The absolute error presented in the plots was calculated in all prediction points by the Eq. (4.14) and it reached negligible levels after the final prediction. Lastly, in Fig. 4.8, a comparison of the three std, the kriging $\hat{\sigma}$, the normalized jackknife $\hat{\sigma}_{jack}^{norm}$ and the product $\tilde{\sigma}$ of the jackknife and the kriging ones is presented. It is obvious that the one approximating worse the absolute error is the kriging variance. The other two approximated well the absolute error fluctuations and gave comparable final predictions, as mentioned already.
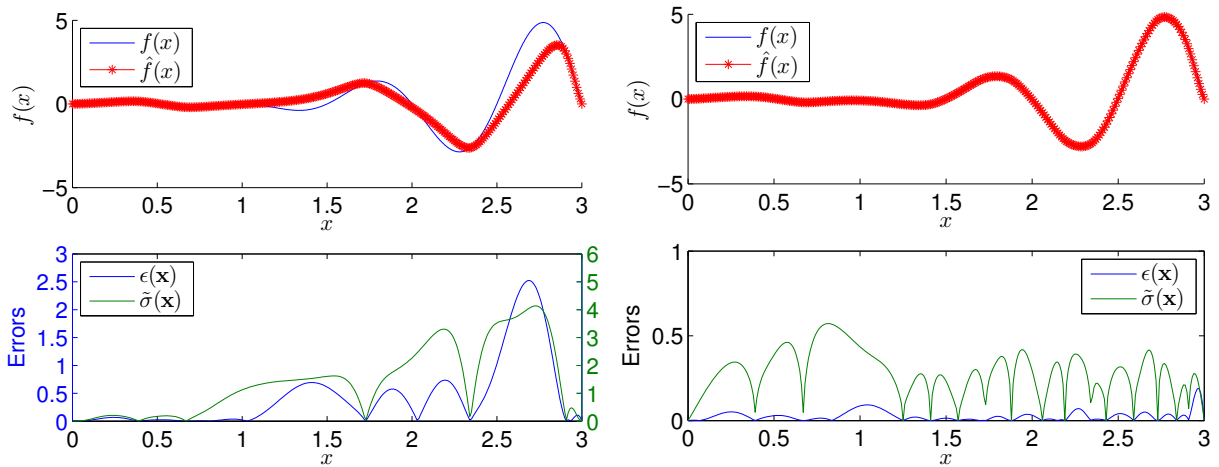
Figure 4.7 – The initial prediction for the 1-D test function based on 7 simulation points (left) and the final prediction with the adaptively chosen extra points (right). Their absolute errors and $\tilde{\sigma}$ standard deviations are presented below. The oscillations of the absolute error are well represented by $\tilde{\sigma}$ in general. Therefore, the final absolute error after the adaptive sampling reached negligible levels.
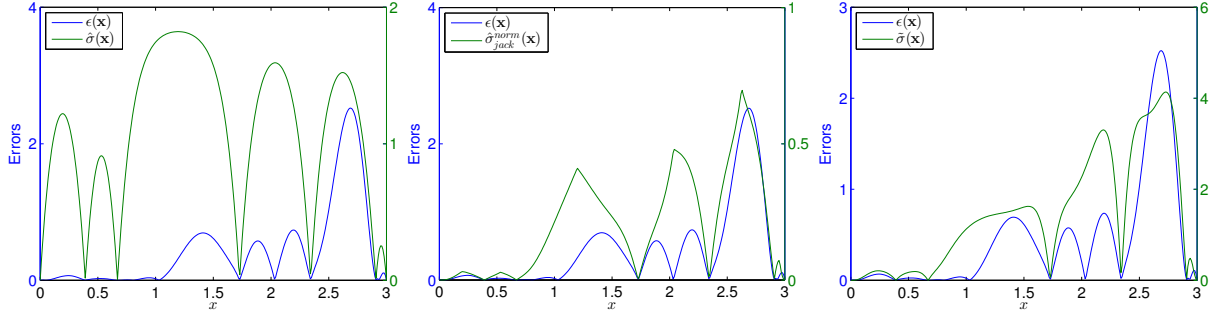
Figure 4.8 – The three uncertainties of the prediction together with the real absolute error. The kriging variance (left) depends on the points distance only, while the normalized jackknife one (middle) and the jackknife-kriging product (right) take into account the quality of the prediction also. Their oscillations thus imitate better the absolute error's behavior and so they are more appropriate for the stepwise uncertainty reduction procedure.

4.7.2 Approximating the irregular 2-D test function

After successfully testing our metamodel on the 1-D toy function, we will attempt now to approximate a common 2-dimensional test function, the so-called irregular test function which is defined as [Iooss et al., 2010]:

$$f_{irr}(x,y) = \frac{e^x}{5} - \frac{y}{5} + \frac{y^6}{3} + 4y^4 - 4y^2 + \frac{7x^2}{10} + x^4 + \frac{3}{4x^2 + 4y^2 + 1}$$

with $(x,y) \in [-1,1]^2$. In Fig. 4.9 we can see the 3D plot of this function together with the contour lines. The oscillating and non-linear nature of this function could challenge our adaptive metamodel. The kriging approximation was attempted in order to predict the function values on 1000 points spread all over its domain. The initial sample contained 15 points only and another 35 were added adaptively. In Fig. 4.10 we can see and compare the contour plot of the poor initial prediction with the real contour plot of f. After adding the adaptively chosen points, in such a way that $\tilde{\sigma}^2$ was reducing sequentially, a very good approximation was achieved. The final prediction showed a MSE = 0.0405, a RMSE = 0.045 and it is presented in Fig. 4.11. The AI with respect to the initial RMSE was almost 89% and the maximum final absolute error was less than 0.17 (see Fig. 4.11).

4.8 Applicability of the metamodel on COSMO results analysis

The metamodel proposed in the previous sections, was proven capable in approximating both the 1-D and the 2-D non-linear toy functions. It is now time to go on and verify the applicability of this metamodel on COSMO and especially on the COSMO analyses carried out and presented in Chapter 3. In saying so, we will check whether the metamodel is able to substitute COSMO in the analysis procedure, while providing the same or comparable conclusions with it. If the answer is positive, the ground opens for new faster, adaptive and objective-driven analyses. In what follows the most characteristic and information providing quantities were approximated. The surrogate model was based on the model values calculated on 20 simulation points, 7 initially generated by LHS and the rest selected in such a way that the uncertainty of the prediction was reduced gradually. The calculation of
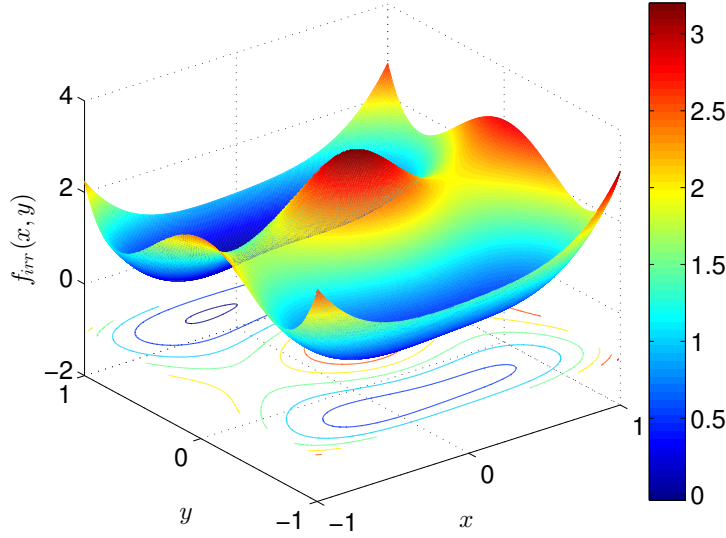
Figure 4.9 – The 3D plot and the contour lines of the irregular test function. Its oscillating nature in both dimensions, imposes difficulties to the approximation methods.
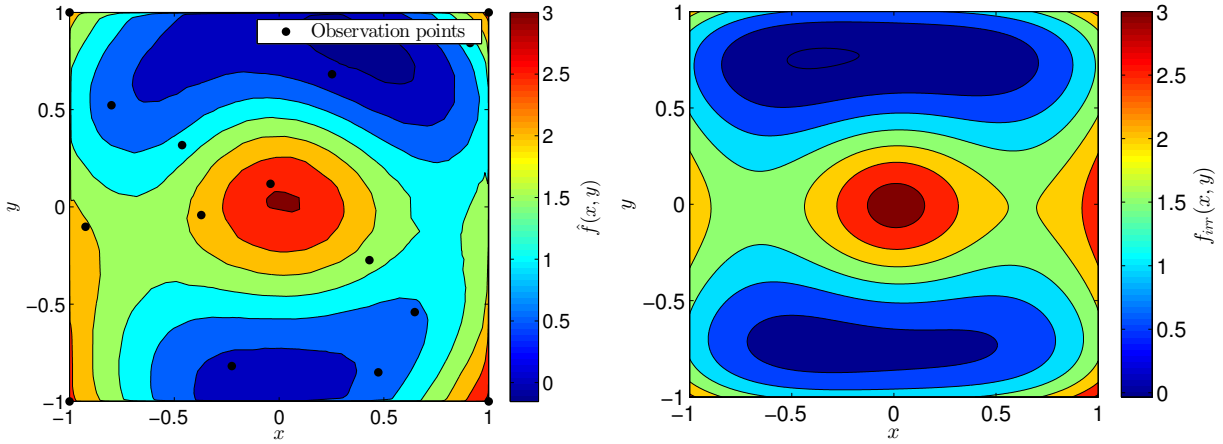
Figure 4.10 – The contour plot of the initial prediction for the 2-D irregular test function based on 15 simulation points (left) and the real contour plot of the irregular function (right). The initial fixed sample failed to well approximate the fluctuations of the irregular function.

this uncertainty was each time connected with the quantity under approximation, so that a quicker reduction could be achieved. The scenes under study were the ones analyzed in the corresponding cases in Chapter 3. The mean simulation time of a metamodel approximation was about $210\,\text{sec}$, less than $1/40$ of the simulation time required for COSMO to obtain the real results. In what follows, only 1-dimensional COSMO approximations, with respect to the frequency of the emitted wave, will be presented. The frequency is the easier radar parameter to be changed in real-time. And since the long-term objective of the metamodel is its incorporation in an adaptive radar strategy, these examples were selected to be presented only.
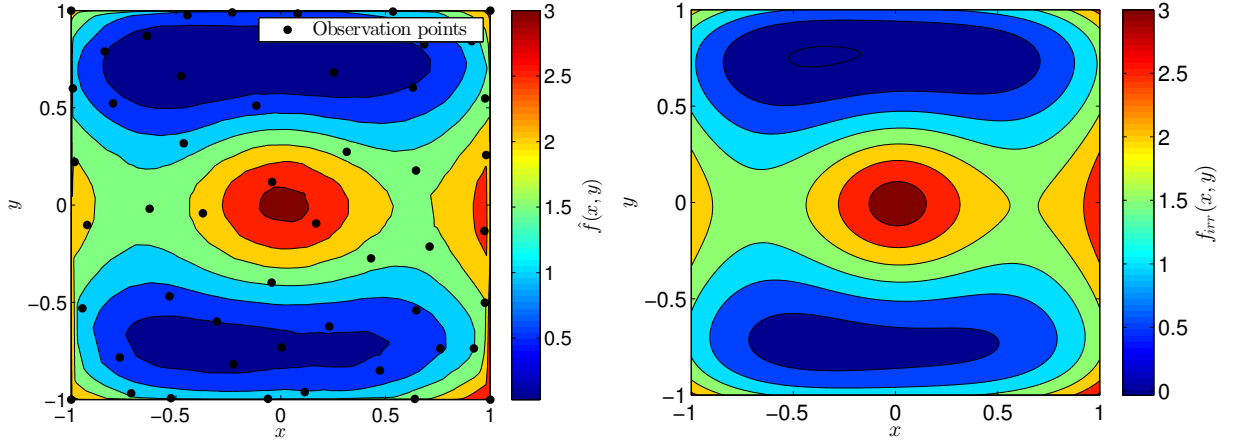
Figure 4.11 – The contour plot of the final prediction for the 2-D irregular test function used 35 extra, adaptively chosen, simulation points (left) and the real contour plot of the irregular function (right). After the adaptive sampling procedure, the final prediction showed an AI of 89% and approximated well the real function.

4.8.1 Detection of the model parameters effects

Let us start justifying the proposal of the metamodel utilization in the received signal analysis, by the four model factors examined. Considering the whole frequency bandwidth for several incidence angles, we can see in Fig. 4.12 that for the VV backscattering coefficient, the metamodel was able to predict the overall model behavior, albeit without being able to provide all the local noisy oscillations. However, it could be successfully used to distinguish the angle effect on this backscattering coefficient and the global fluctuations with respect to the frequency, with just a few of their simulated values. What is also obvious from this figure, is that the metamodel succeeded also in identifying the Brewster angle effect on σ_{VV}^0, present in the response of a forest of trunks alone. The very weak energy returned to the radar in low frequencies under an incidence angle of 20°, is clearly observed even with this 20 frequency points based metamodel prediction.

Similar results were obtained in the cases of the effects of the age and the moisture on the received signal also. The overall behavior of the VH and VV backscattering coefficients could be clearly predicted, as seen in Fig. 4.13 and 4.14 respectively. Concerning the age effect, once the appropriate quantity is selected to be approximated, namely σ_{VH}^0, even the age of the forest could be roughly guessed. Since the huge drop in the backscattered energy changes with respect to the age, as concluded in Section 3.2.2, and the metamodel is able to provide information on the frequency of that drop (see Fig. 4.13), it can assist in estimating the forest age. Considering vegetation humidity now, comparable conclusions could be derived. As seen in Fig. 4.14, the driest forest stands can be easily identified by the σ_{VV}^0 different oscillations in the $[0.4\,\mathrm{GHz}, 0.7\,\mathrm{GHz}]$ and $[1.4\,\mathrm{GHz}, 1.7\,\mathrm{GHz}]$ frequency intervals.

4.8.2 Detection of the forest elements effect

The metamodel succeeded in approximating sufficiently COSMO, in order to detect the most characteristic effects of the model parameters on the received signal. In this section, it will

117
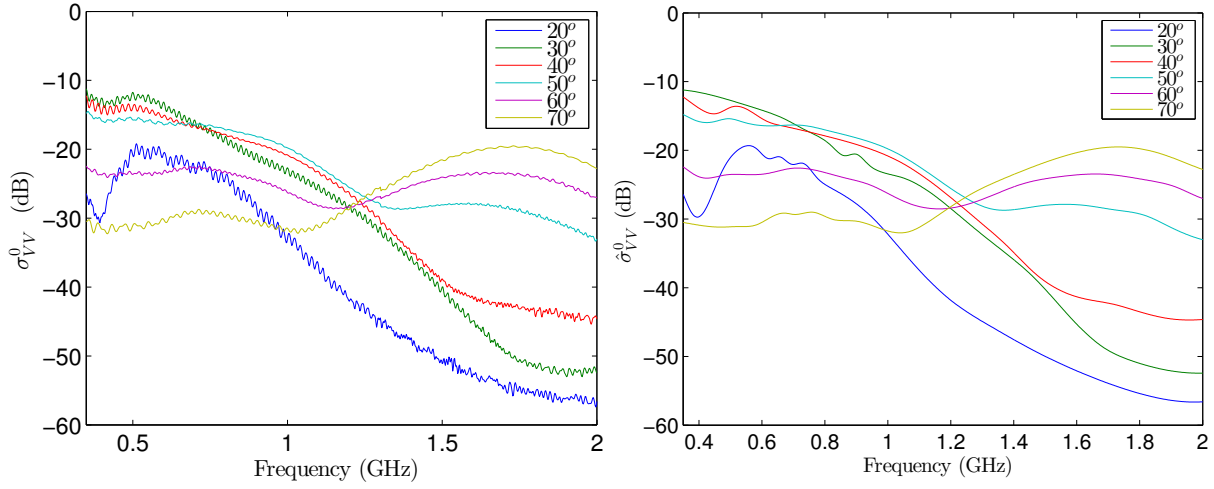
Figure 4.12 – The VV backscattering coefficients for the whole COSMO frequency range and for 6 different angles of incidence ranging from 20° to 70° (left) and their kriging predictions based on 20 adaptively chosen frequency points (right). The metamodel can provide an approximation showing the overall behavior of the signals, in less than 1/40 of the time required for the simulations.
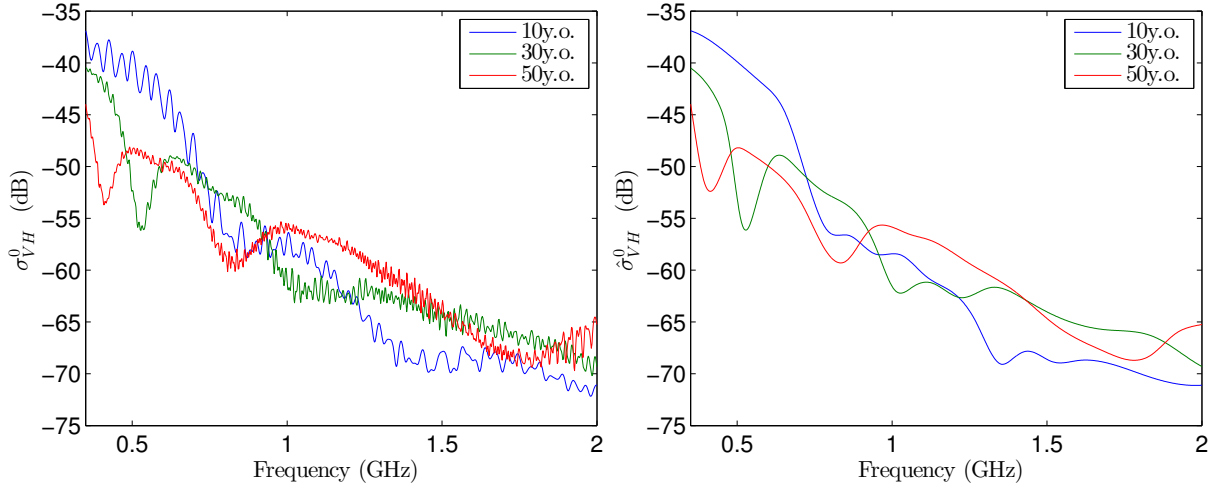
Figure 4.13 – The cross-polarized backscattering coefficients for the three stands having 10, 30 and 50 years of age respectively (left) and their kriging predictions based on 20 adaptively chosen frequency points (right). The metamodel can provide an approximation showing the overall behavior of the signals and their characteristic drops, in less than 1/40 of the time required for the simulations.

be tested on the approximation of the branches and target effects respectively. Firstly, the effect of the branches existence was examined. The metamodel showed promising results both in approximating the general behavior of the backscattering coefficients and recognizing the branches effect, as well as in the identification of the dominant scattering mechanism of the scene under study. In Fig. 4.15 we can see the estimation of the global fluctuations of σ_{VV}^0. The branches effect on it, i.e. the slower decay for frequencies $\geq 1\,\mathrm{GHz}$ is clearly visible. Additionally, in Fig. 4.16, the ability of the metamodel to predict the frequency where the change of the dominant mechanism occurs, is depicted. This fact could be useful in cases where the assumption of a dominant scattering mechanism is imposed for the decomposition of
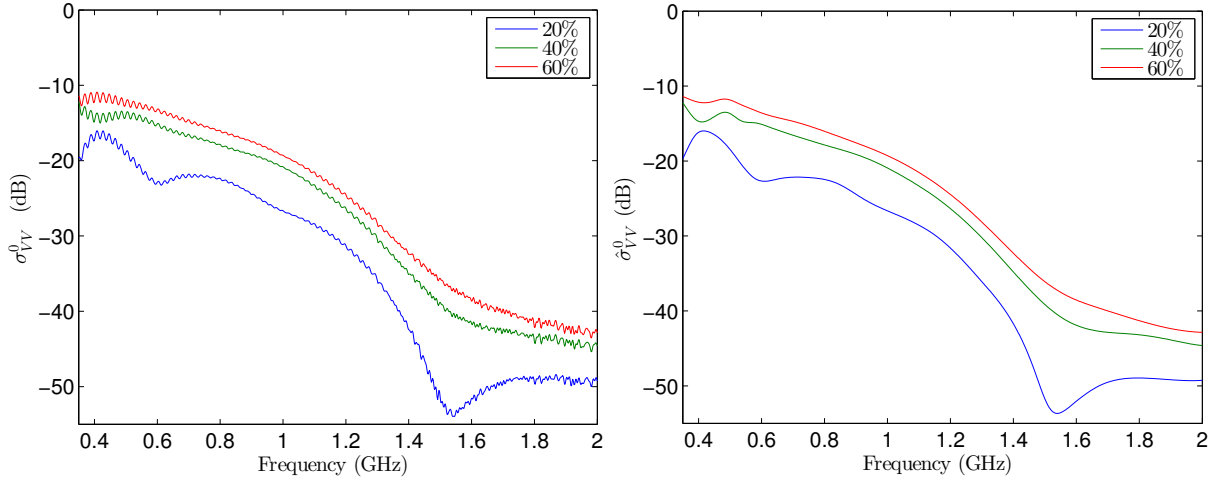
Figure 4.14 – The VV backscattering coefficients for the three stands having $m_v = 20\%$, $m_v = 40\%$ and $m_v = 60\%$ respectively (left) and their kriging predictions based on 20 adaptively chosen frequency points (right). The metamodel can provide an approximation showing the overall behavior of the signals and distinguishing them, in less than 1/40 of the time required for the simulations.

the scattering matrix, as for instance in the Freeman–Durden decomposition (see [Cloude, 2009]).
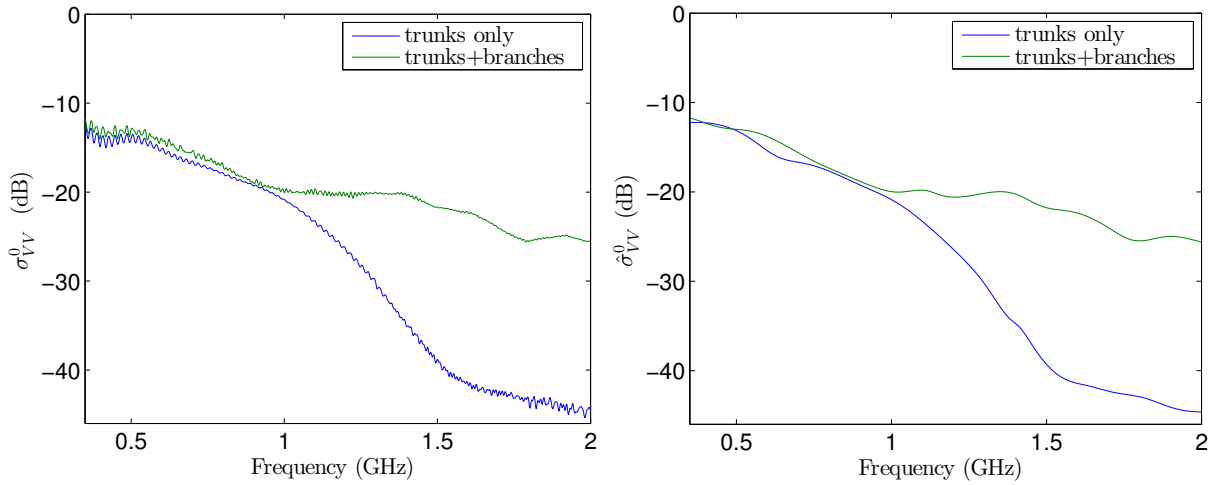
Figure 4.15 – The backscattering coefficients in VV for the two forest arrangements having trunks only and trunks with 10 branches each (left) and their kriging predictions based on 20 adaptively chosen frequency points (right). The metamodel can provide a satisfactory approximation showing the overall behavior of the σ_{VV}^0 values and the branches effect on it after $1\,\mathrm{GHz}$, in less than 1/40 of the time required for the full simulation.

For the case of the target effect investigation, the 20 frequency point metamodel succeeded again in approximating sufficiently the backscattering coefficient values under study, as seen in Fig. 4.17 for the HH polarization. Despite the fact that branches existed, and the target effect identification was difficult as explained in Section 3.2.4, the convergence of the co-polarized backscattering coefficients for high frequencies is clearly predicted and visible in Fig. 4.18. In the next figure, Fig. 4.19, we can see that the metamodel did also well in approximating the
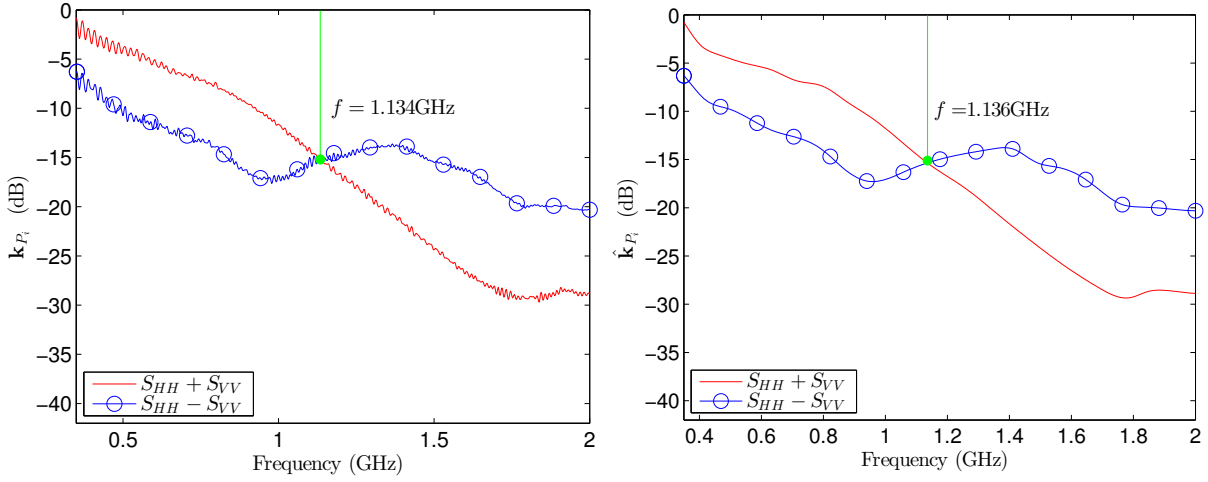
Figure 4.16 – The singe and double bounces as represented by the first two Pauli components values (left) and their kriging predictions based on 20 adaptively chosen simulation points (right). The metamodel approximation provides the overall behavior of the two first Pauli vector components and also the frequency where the dominant scattering mechanism changes from double to single bounces, with a certain but very small error.

smooth, close to constant, single bounces scattering in L-band. As stated in Section 3.2.4, the ensemble of these two latter effects could most probably assure us about the existence of the target and that was achieved with the metamodel, using just a few simulated values.
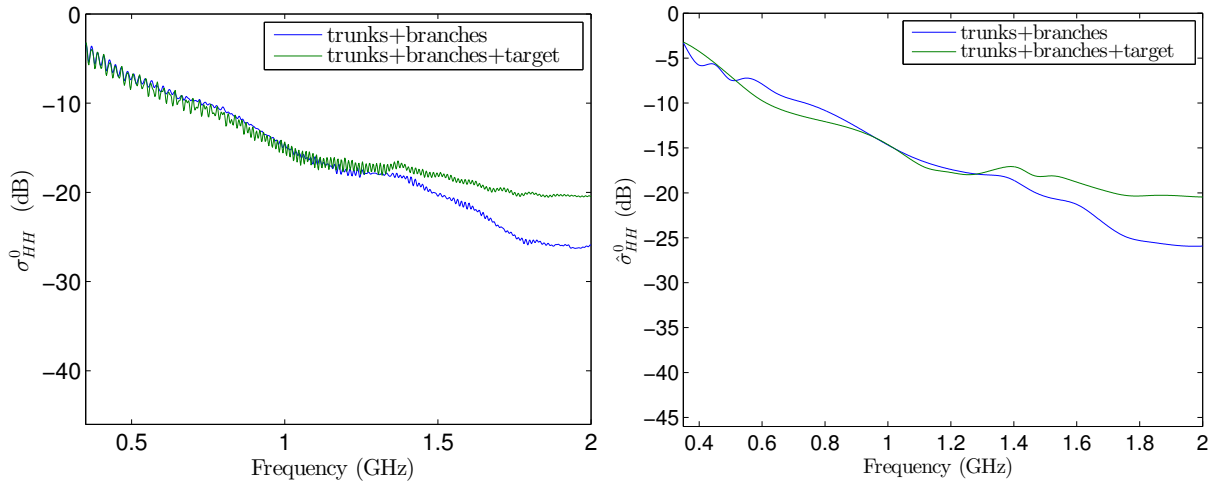
Figure 4.17 – The HH backscattering coefficients for a periodical forest of 63 trunks having 10 branches each with and without a target hidden in it (left) and their kriging predictions based on 20 adaptively chosen frequency points (right). The kriging metamodel succeeded in identifying the overall σ^0_{HH} behavior, especially the different values fluctuations for the two forests in the $1.6 - 2$ GHz sub-band, where the target effect can be recognized.
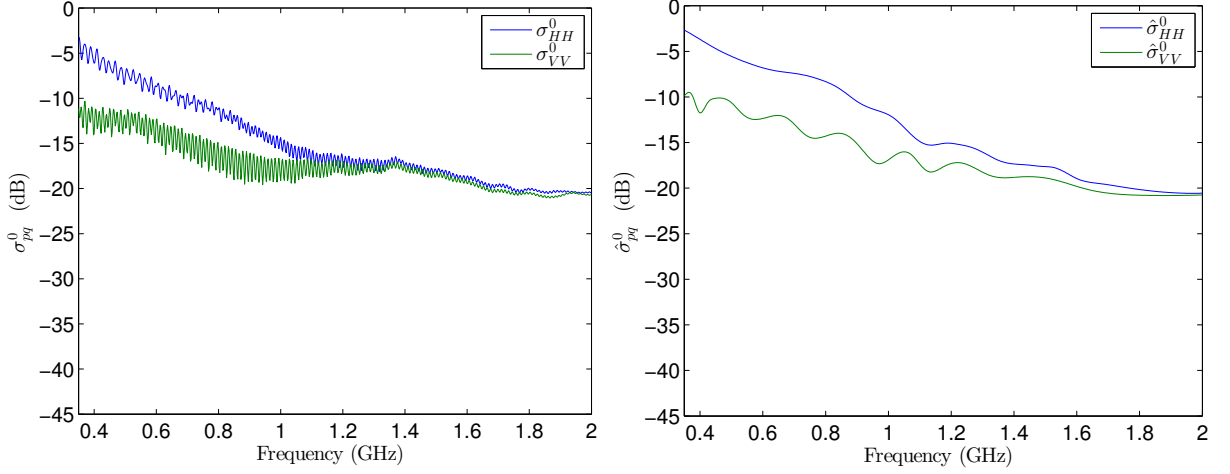
Figure 4.18 – The co-polarized backscattering coefficients for a periodical forest of 63 trunks having 10 branches each with and without a target hidden in it (left) and their kriging predictions based on 20 adaptively chosen frequency points (right). The kriging metamodel succeeded in discovering the convergence of the energy scattered in the co-polarizations, in high frequencies.
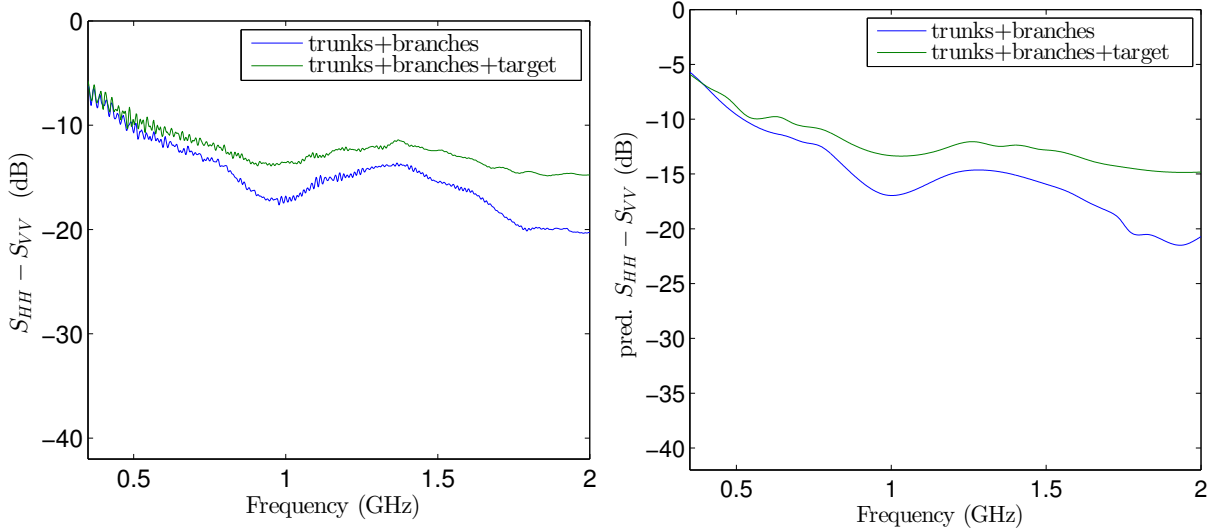
Figure 4.19 – The $S_{HH} - S_{VV}$ real values for a periodical forest of 63 trunks having 10 branches each with and without a target hidden in it (left) and their kriging predictions based on 20 adaptively chosen frequency points (right). The kriging metamodel approximating sufficiently the very smooth and close to constant single bounces behavior in L-band.

4.8.3 Forest arrangement

In this last test of the metamodel's applicability, we will attempt to approximate the responses of the four different forest arrangements examined. These arrangements shared many common scattering characteristics, especially the periodical and semi-periodical ones, who showed differences very close or inferior to the radar measurements error. On the contrary, there are some characteristics of the random forests scattering which could be potentially used for a more focused radar observation of this kind of forests. In saying so, the increasing VV backscattering in high frequencies and the low VH backscattering when branches exist. From

Fig. 4.20 and 4.21 it is obvious that the 20-point kriging metamodel was able to detect the random arrangements effects, with its approximations. Indeed, the slightly increasing VV backscattering for frequencies of 1.5 GHz and higher is clearly visible in the right plot of Fig. 4.20. Equally visible is the weaker VH backscattering of the random forest within the whole COSMO frequency band, as seen in Fig. 4.21.
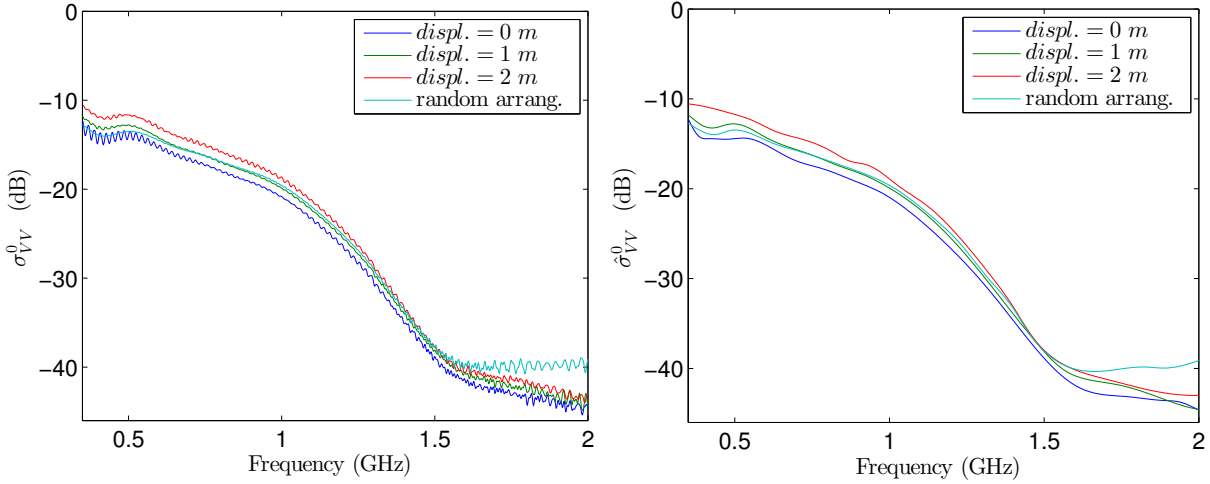
Figure 4.20 – The VV backscattering coefficients for the four different forest arrangements (left) and their kriging predictions based on 20 adaptively chosen frequency points (right). The three first arrangements were periodical and semi-periodical with a displacement from the periodical position of 1 m *and* 2 m *and the last arrangement was a random one. All forests had 63 trunks and 10 branches per trunk. The metamodel can provide an approximation showing the overall behavior of the signals, in less than* 1/40 *of the time required for the simulations. In addition, it succeeded in predicting the slightly increasing VV backscattering of the random forest in high frequencies.*
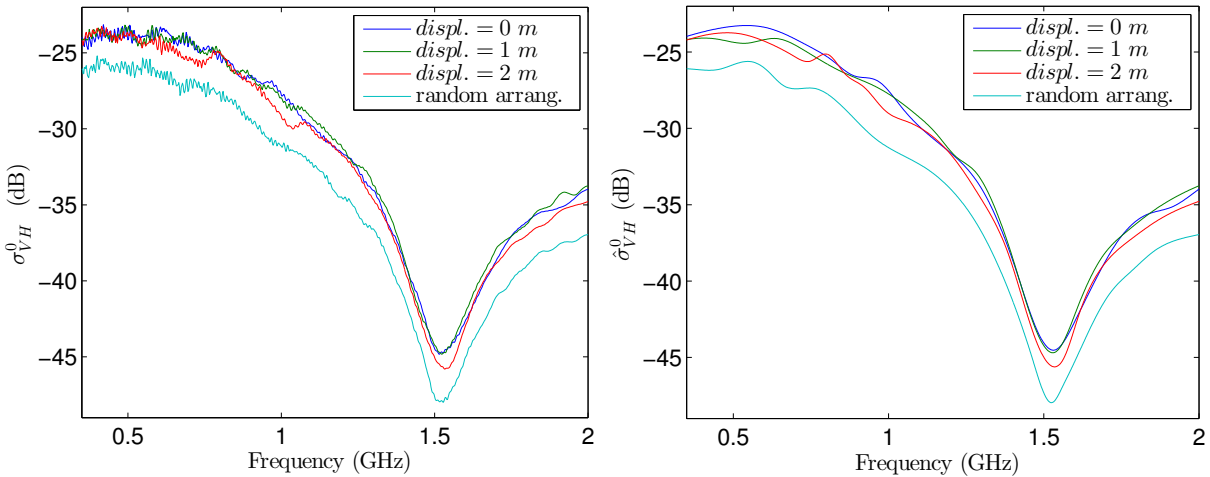
Figure 4.21 – The cross-polarized backscattering coefficients for the four different forest arrangements (left) and their kriging predictions based on 20 adaptively chosen frequency points (right). The three first arrangements were periodical and semi-periodical with a displacement from the periodical position of 1 m *and* 2 m *and the last arrangement was a random one. The weaker scattering of the random forest for all frequencies is clearly predicted by the metamodel.*

4.9 Discussion

All statistical methods that attempt to approximate the behavior of a function with just a few of its values, show certain limitations. This is due to the generalizations and assumptions done, because of the lack of information. Kriging is not an exception. Despite the fact that it is widely used and validated, even in cases where the data do not follow Gaussian distributions, there are many cases where it fails. In addition, there exist several open questions concerning its construction and performance, which cannot be answered before applying the method. In certain cases, these cannot be fully answered even after the method application. Some of these open questions already date several years ago (see [Kleijnen, 2008]):

- Asymptotic proofs of sequential designs performances are missing; Do these designs approximate an optimal design?

- Is there a rule of thumbs for the size of the initial sample?

- Are there any optimal stopping rules for the sequential designs, based on measures of accuracy?

Some other questions can complete this list:

- Is there an optimal uncertainty to be used in the sequential procedures and in the confidence intervals?

- Can we conclude in advance if a function can be approximated well by kriging or not?

The latter question especially is one of the most important ones in surrogate modeling practice. In our case, we had to check if our adaptive kriging metamodel was able to approximate the amplitude of the received electric field. This was the main tool necessary for the thorough analysis of the forest backscattering and the design of our adaptive-cognitive observation strategy. The answer however, as revealed in practice, was unfortunately negative. The amplitude evaluated by COSMO under all polarizations, is varying too fast as seen in Fig. 1.15. All interpolations attempted, failed in predicting the quantity oscillations in a much lower computational time than that of the real simulations. In Fig. 4.22 we can see the approximation of the response in VV coming from a very elementary scene generated by COSMO, by an 100-point based adaptive metamodel. It is obvious, that despite the large number of the observation points used, the amplitude is not sufficiently predicted. Neither a SAR image can be constructed based on these values, nor a correct time signal can be extracted. This fact was more or less expected, since kriging assumes a spatial correlation between the points in the input space, which is not the case for $\left| E_{pq}^r (f) \right|$. Indeed, even very close frequency points can have very different backscattering, which the metamodel cannot predict. The same conclusions were derived for the phase of the received signal also. This failure led us eventually to apply the metamodel to the "smoother" backscattering coefficients and Pauli vector components only.

4.10 Conclusions

An adaptive metamodeling method for approximating a numerical model, was presented in the previous pages. It was based on kriging interpolation and it was designed to provide a stepwise uncertainty reduction for the prediction. The jackknife and the kriging estimations of the
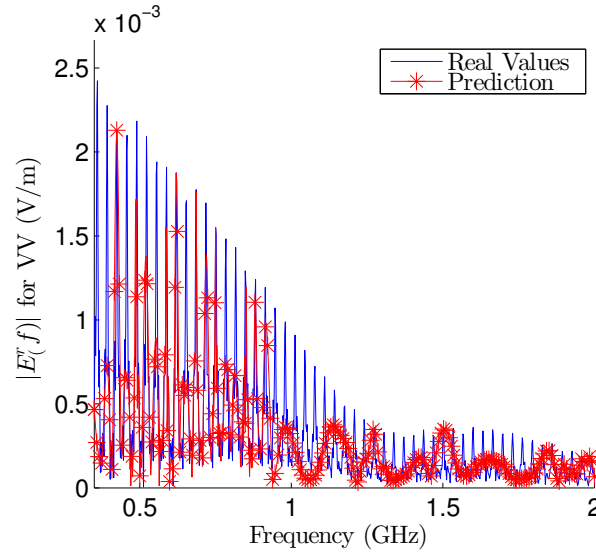
Figure 4.22 – The kriging prediction of the electric field amplitude in VV, done by an adaptive kriging metamodel based on 100 observation points. The metamodel cannot approximate well the function oscillations, despite the large input sample.

prediction uncertainty were used, to optimally choose the new simulation points to be added to the sample. The adaptive metamodel thus constructed, was validated in approximating some common toy functions. Subsequently its applicability in the COSMO results analysis was checked and verified. The metamodel managed to predict the global behavior of the backscattering coefficients and the Pauli vector components in all cases, losing though the local noisy variations of these quantities. These predictions were achieved in a very low computational time, using 20 frequency points only. The metamodel also succeeded in extracting physical information from the predicted signal values, while following the suggestions for the radar configuration from the previous chapter. It identified the characteristic effects on the signal caused by the existence of the branches and the target, as well as these due to the variations of the most important parameters. As a consequence, we can now proceed to the next step of our project which is the design of an innovative radar observation strategy which will be based on the metamodel operating frame and prediction capabilities and on the cognitive radar principle.

<center>5</center>

Cognitive radar principle in forest investigation

Contents

5.1 Introduction

In this chapter, an innovative adaptive strategy to carry out radar observations of forests will be proposed. This strategy takes advantage of the fact discovered in the previous chapter, that the metamodel can identify fast some of the scene characteristic effects. The knowledge acquired on these effects can be subsequently used to the design of a new, more focused signal to be emitted in real-time. In order to optimally use the previous acquired knowledge on the forest under study for the new signal design, the cognitive radar principle will be employed. This principle, which has not been neither realized nor materialized yet, is going to be used here for the first time, to our knowledge. The analogies between the metamodel and the cognitive radar general principles, leads us to fit the cognitive radar idea to the global metamodel operating frame. Thus, the metamodel will finally assist in both aspects, as a global frame for our strategy and as a tool which can accelerate the analysis done in the homonymous step of the strategy.

In the following paragraphs, a detailed presentation of the cognitive radar principle and our radar observation strategy will be provided. The way S. Haykin envisaged his innovative cognitive radar is explained together with the main operating principles. These principles are corresponding to the adaptive metamodel operating principles and so they were both associated within the metamodel operating frame. This frame served as the operating frame of our adaptive-cognitive

<center>125</center>

strategy, which was tested on some characteristic examples-applications on simulated radar observations of forests. These examples referred to certain objectives of the forest studies, as the forest signature acquisition, the focus on the forest canopy or on the trunks and the detection of a hidden target. They succeeded in justifying our proposed method which could hopefully open the ground for reconsidering and improving the way radar observations are carried out nowadays.

5.2 Principles of cognitive radar

Radar campaigns up to now, are usually designed without taking into account the effect of the environment under study. This is due to the fact that in many applications, little *a priori* information of the scene exist. Thus, a certain waveform corresponding to the radar technical requirements and the predefined objectives of the study is generated and emitted. During an observation, several pulses are sent towards the scene, all of the same initial configuration. The radar return and the knowledge extracted, are not involved in the emission procedure. It is as each new wave emission is the initial one and the object of interest is treated as a black-box during the whole process.

The concept of the *cognitive radar*, as envisaged by S. Haykin in [Haykin, 2006], aspires to correct this omission. This is a new framework for radar systems, which aims to adjust their emitted signals with respect to the environment. The main idea of this innovative type of radar is that the waveform emitted at time $t+1$, will be dependent on the radar returns at times $t, t-1, \ldots$ and the analysis that has been done on these returns. In particular, S. Haykin suggested that a cognitive radar should consist of [Haykin, 2006]:

1. intelligent signal processing,

2. feedback from the receiver to the transmitter and

3. preservation of the information content of radar returns.

So far, no system like the one described by Haykin has been materialized, despite the author's optimism at that time. Several technical limitations are still to be surpassed, concerning both the real-time analysis of the backscattered signal and the change of the radar configuration. Concerning the signal processing in real-time especially, the time needed for the interpretation of the obtained data is prohibitive for the venture. It is exactly where the metamodel can come up with its fast prediction capabilities and accelarate this procedure. Additionally, the main idea of the sequentials designs like the one we adopted in Chapter 4, is that "the observations are analyzed - so the data generating process is better understood - before the next input combination is selected" [Kleijnen, 2008]. This idea corresponds exactly to the main idea of the cognitive radar. So the steps of the cognitive radar operation can be directly associated with the main steps of the adaptive metamodeling procedure (see Fig. 4.4), as depicted in Fig. 5.1. The outcome is a conjunction of the two methods, for the design of an adaptive-cognitive radar observation strategy, which can be realized using the COSMO simulation capabilities. In the following section, the exact way in which these methods were combined will be presented in more details.
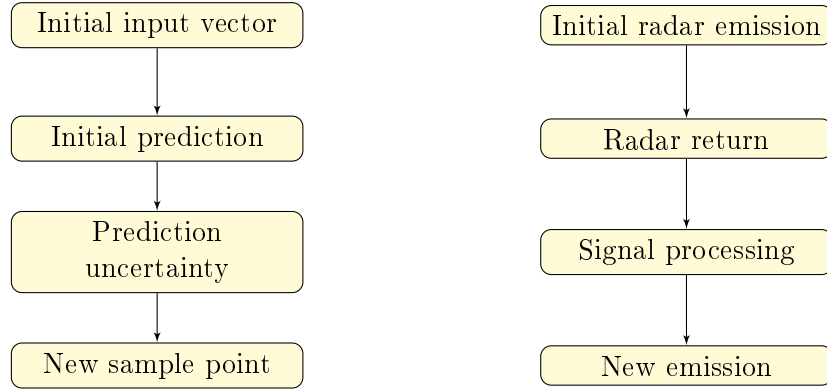
Figure 5.1 – The rough flowcharts of an adaptive metamodel (left column) and a cognitive radar (right column). The correspondences and the resemblance of the general idea between the two methods are obvious, letting us combine them in an integrated adaptive-cognitive radar observation strategy.

5.3 Cognitive radar principle within the metamodel frame

As described before, a radar system observing an unknown distributed target like a forest, treats its object of study as a black-box. No prior information is usually available and it is after the end of the campaign, when all responses will be treated and analyzed together. On the contrary, a cognitive radar could potentially start from a black-box and exploit any return, in order to use the obtained knowledge to adaptively change the new emission configuration. The correspondence between the operation of this radar type and our proposed metamodeling technique in Chapter 4 is obvious and depicted in Fig. 5.1. The initial predefined waveform to be sent, would correspond to the initial fixed sample of the metamodel. Then the radar return corresponding to the initial prediction would follow, full of information to be extracted during the signal processing. This processing is analogous to the prediction analysis when estimating the uncertainty. Finally, the discoveries of the analysis will be taken into account in the design of the new signal, as the uncertainty is used for the detection of the new sample point. Both loops can be continued iteratively till a terminal criterion is fulfilled. A cognitive radar can be therefore incorporated directly within the adaptive metamodel operation frame. A general flowchart representing this incorporation is sketched in 5.2.

The main constraints in the realization of a cognitive radar, are the time limitation for the analysis of the backscattered signal, before emitting the new one, and the difficulty to obey the changes of the radar configuration imposed by the analysis, e.g. change of the frequency or the polarization. A numerical model like COSMO, as more flexible and less expensive, seems an appropriate tool for surpassing the difficulties in changing the radar configuration. Furthermore, as already presented, it is able to provide measurements concerning the different mechanisms of the forest backscattering, thus contributing to a deeper knowledge of the forest structure and a more focused adaptation of the new waveform to our needs. As far as the time limitation is concerned, the metamodel, apart from the provision of its adaptive frame, can assist in accelerating the analysis of the received signal. It is able to provide fast predictions for the quantities of interest, by interpolating in non-emitted frequencies. It can additionally point out a proper configuration for the new signal, so that the current predictions uncertainty is reduced. However, the metamodel has to be explicitly connected with the initial objective
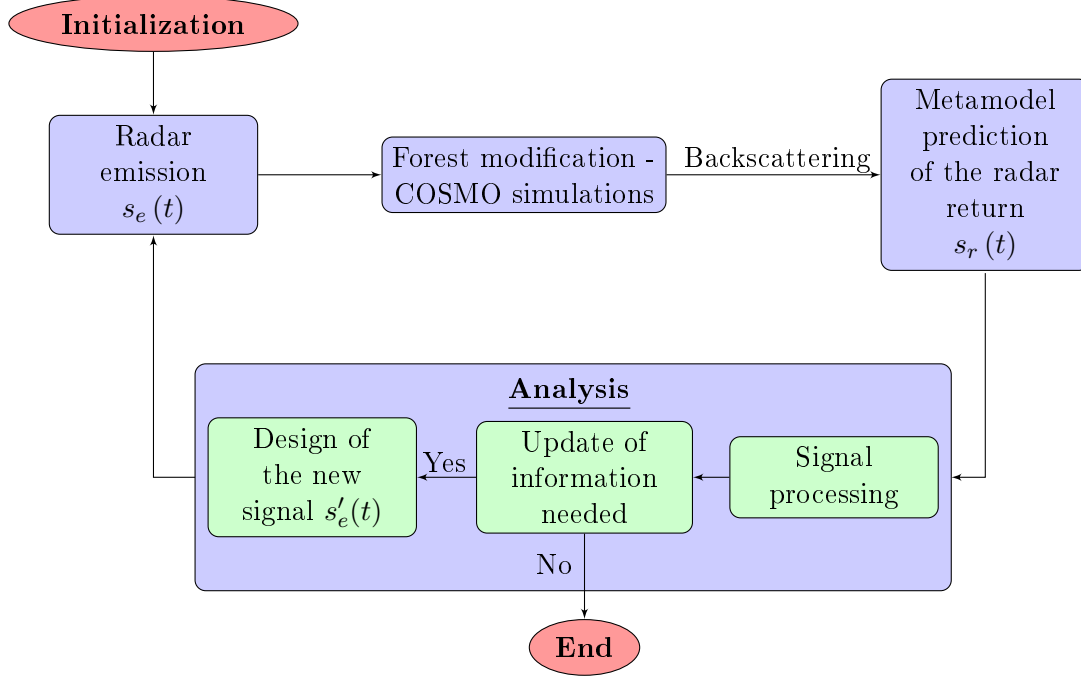
Figure 5.2 – The flowchart representing a realization of the cognitive radar based on the metamodel closed loop operation.

and the possible intermediate ones, which will result from the update of the scene information. Since it is able to predict several quantities concerning the backscattering, we have to define the ideal ones for approximation and uncertainty reduction, corresponding to each goal. To do so, the information about the signal effects obtained during the analysis in Chapter 3, will be taken into account and the suggested observation strategies will be adopted. The outcome is presented in Fig. 5.3.

In the descriptive flowchart of our adaptive-cognitive observation strategy, only the frequency and the polarization is changing before the new emission. This assumption is done, as these are the easiest parameters to be changed in real-time radar investigations. In addition, most of the forest effects on the received signal examined in Chapter 3, were considered under a constant incidence angle of 40°. In a more detailed future study, where more angles will be considered, a 2-dimensional metamodel can be employed and then the angle could be varying also for the new emission. A fast real-time change of the incidence angle is not possible in real radar systems, but if a numerical code is used this capability could be exploited. It is then the turn of the radar engineers to make the seemingly impossible possible, as already done in certain cases before.

The four intermediate objectives defined in Fig. 5.3 after the initial radar return, are corresponding to the examples presented in the upcoming section. The latter served in verifying the applicability of our strategy, while exploiting the tools constructed and the conclusions extracted during the whole project. In these examples the four possibilities examined were the following:

- to derive a fast forest signature,

- to study the branches effect and the change of the dominant scattering mechanism,
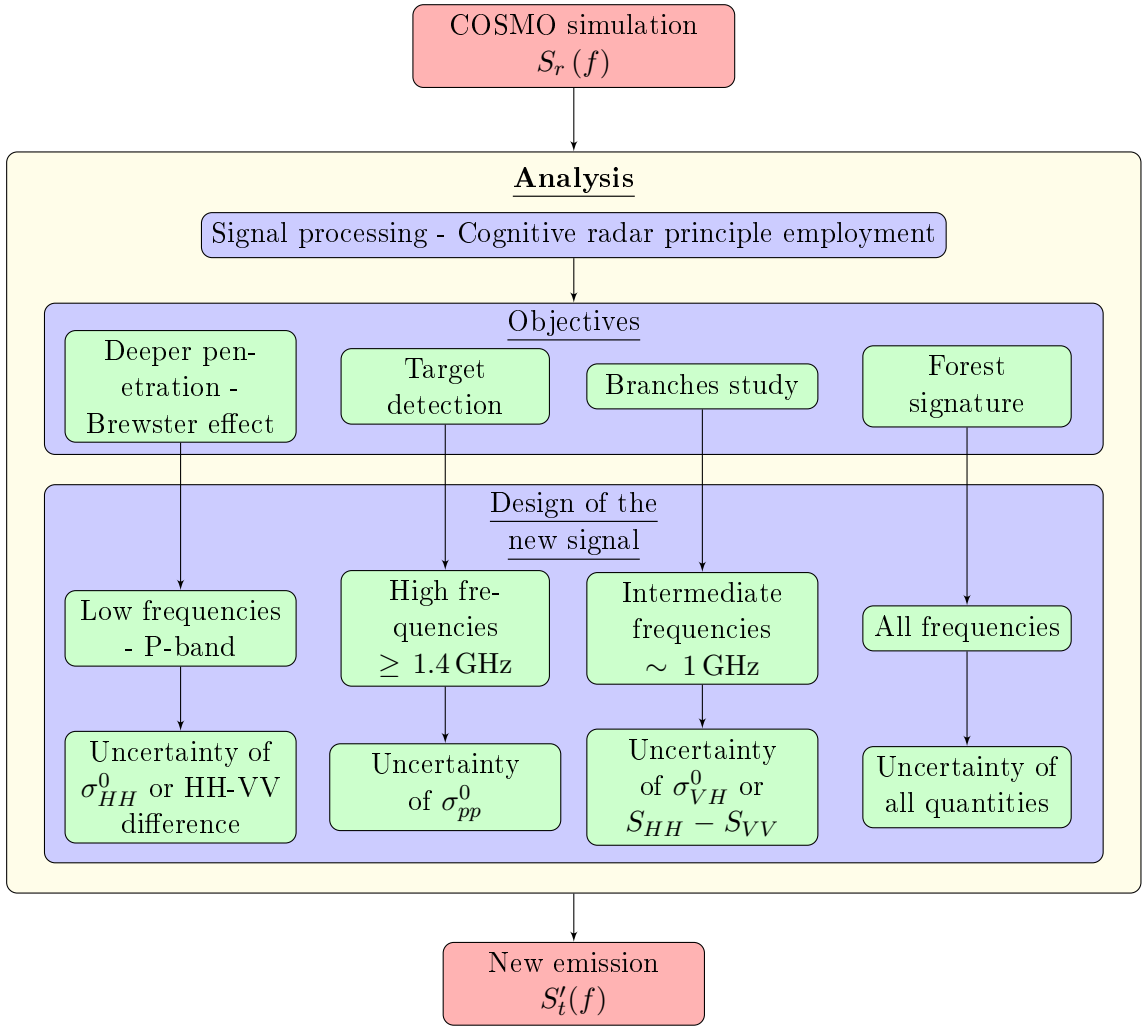
Figure 5.3 – The detailed flowchart representing the analysis part of an adaptive radar observation, which makes use of the cognitive radar principle. Four different intermediate objectives lead to different observation strategies and thus designs of the new signal to be emitted.

- to detect a hidden target and

- to study the trunks and the extent of the Brewster angle effect.

For each objective, a different frequency band was selected for the design of the new signal and a different measure of uncertainty. Whenever 2 or more uncertainties are to be employed in one case, a combination of all could be preferred to be reduced, or the one showing the highest values. After explaining the main principles of our strategy, we will now proceed to the presentation of the examples.

5.4 Examples

In this section, the four different examples of our adaptive and cognitive strategy for radar observations of forests, will be presented. These examples were based on the scheme presented in

Fig. 5.3 and they were conducted in such a way that the computational load was kept sufficiently low. In saying so, the least simulation points (least frequencies possible) providing a satisfactory prediction and the special effects recognition, were used. In all these examples, the quantities studied were those who can be approximated by our metamodel, namely the backscattering coefficients and the Pauli vector components. The most important quantities, the amplitude and the phase of the received signal, could not be part of the quickly predicted magnitudes, because of their fast oscillating nature (as seen in Section 4.9).

5.4.1 Acquisition of a fast forest signature

For the first example demonstrating the utility of our proposed observation strategy, we attempted a fast acquisition of the forest signature in the frequency domain. This signature includes the way the forest scatters in all polarization combinations and scattering mechanisms. The initial predictions were based in 5 initial frequency points - selected via LHS - and even if they did not approximate well the studied quantities, they provided some rough information about them. In saying so, what kind of general signal characteristics exist, what are the levels of the predicted quantities values and in which frequency intervals there is the highest uncertainty. These predictions, together with their $\pm\tilde{\sigma}$ confidence intervals are presented in Fig. 5.4 and their uncertainties in Fig. 5.5. The uncertainties $\tilde{\sigma}^2$ were normalized by the mean absolute value of their corresponding quantities, in order to be comparable. They came up with some meta-information concerning the scene, by indicating that the new frequencies to be emitted should be mostly contained in two distinct intervals. The first around $1\,\mathrm{GHz}$, where the change of the scattering mechanism occurs if branches exist and the other in high frequencies $\geq 1.5\,\mathrm{GHz}$, in order to study more the forest canopy. This kind of information could be taken into account in real-time and focus the new emissions into a smaller frequency sub-band, as we will see in the next paragraph.
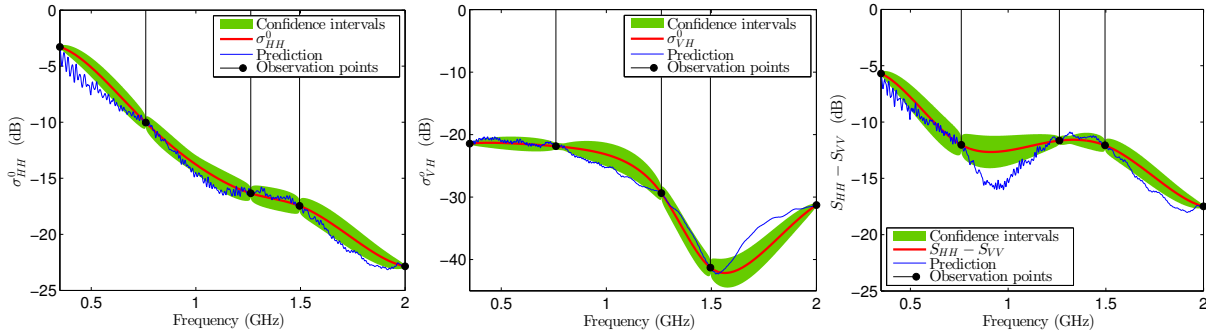
Figure 5.4 – The initial predictions for σ^0_{HH} (left), σ^0_{VH} (middle) and $S_{HH} - S_{VV}$ (right) with their confidence intervals $\pm\tilde{\sigma}$, based on 5 simulation points. The prediction is not a satisfactory one, since there are real function values even out of the confidence intervals.

During the sequential sampling procedure, 10 frequency points adaptively chosen were added to the initial 5-point sample. The uncertainty used was the $\tilde{\sigma}^2$ corresponding to the σ^0_{VH} prediction, which showed the highest normalized values, as seen in Fig. 5.5. After the 10 extra points were added, the sample was ready to be used for the final prediction on 826 frequency points. All quantities were satisfactorily approximated, in less than $1/50$ of the time necessary for the simulation on all the prediction points. The $\hat{\sigma}^0_{VH}$ prediction especially, showed an absolute error much less than $1\,\mathrm{dB}$ within the whole frequency spectrum, as seen in Fig. 5.6.
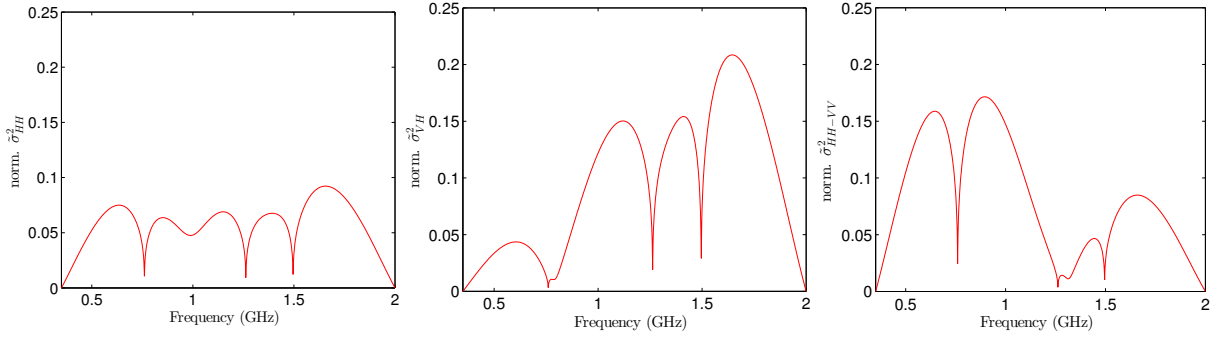
Figure 5.5 – The initial normalized uncertainties corresponding to $\tilde{\sigma}$ for σ^0_{HH} (left), σ^0_{VH} (middle) and $S_{HH} - S_{VV}$ (right), based on 5 simulation points. The frequency intervals where the uncertainty is high, can provide some meta-information on the scene and suggest the configuration of the new signal to be emitted.

Limiting the frequency spectrum to a certain band, during the adaptive sampling procedure, was also attempted. Let us assume that information concerning the L-band for example, are needed. We can then keep the initial sample points contained in this band and construct the final sample by adding the necessary border point $(1\,\text{GHz})^{28}$ and the rest of the extra points adaptively chosen within this narrower band. Such a case is presented in Fig. 5.7, where the single bounces scattering is approximated. The final absolute error was again lower than 1 dB. It worths mentioning again, that in the final predictions presented, the adaptively chosen points were not the same. Despite the fact that most of the extra points in the first case were in L-band, they were almost all of them around 1.5 GHz, whereas in the second case the majority of the points was around 1.2 GHz. This difference can be attributed to the different information necessary to be extracted in each case and is characteristic of the cognitive way of conducting the extra simulations. Before proceeding to the next example, we have to say that this one was corresponding to a 30 years old periodical forest 40 m × 50 m, containing 63 trunks having 20 branches each and illuminated under an incidence angle of 40°. The rest of the scene parameters were the same as in Table 3.1.

5.4.2 Focusing on the branches effect

In this second example of our adaptive-cognitive strategy, the object of interest was the same forest as in the previous case, having 10 branches per tree this time. Here we will focus on the upper level of this forest, which was containing the branches. An initial waveform was emitted, so that we could have enough information to assume the existence of branches or not. Then a second more focused observation was performed, to identify the exact influence of the branches on the forest response and especially on the scattering mechanisms. The initial signal consisted of 10 frequency points and it was sent under a 40° angle of incidence. The simulated values obtained, were used for the initial kriging predictions of the backscattering coefficients and the Pauli vector elements values, along the whole COSMO band. These predictions, presented in Fig. 5.8, showed a relatively strong cross-polarized signal, together with a change of the dominant scattering mechanism from the double bounces to the single ones, around 1.1 GHz. Considering the conclusions extracted in Section 3.2.3, we can state

---

[28]As explained in Chapter 4, kriging needs border points because it fails in extrapolating.
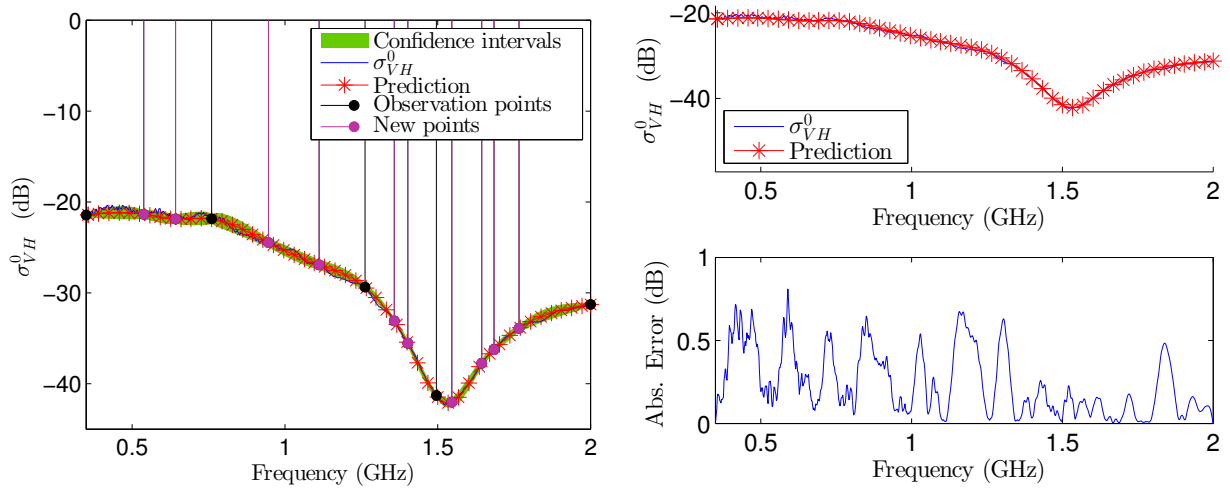
Figure 5.6 – The final prediction for σ_{VH}^0 with its confidence intervals $\pm\tilde{\sigma}$ (left) and the same prediction with the corresponding absolute error (right). The prediction was based on 5 initial simulation points and 10 adaptively chosen, so that the corresponding uncertainty was sequentially reduced. This prediction achieved a satisfactory accuracy, since the absolute error was always inferior to $1\,\mathrm{dB}$.
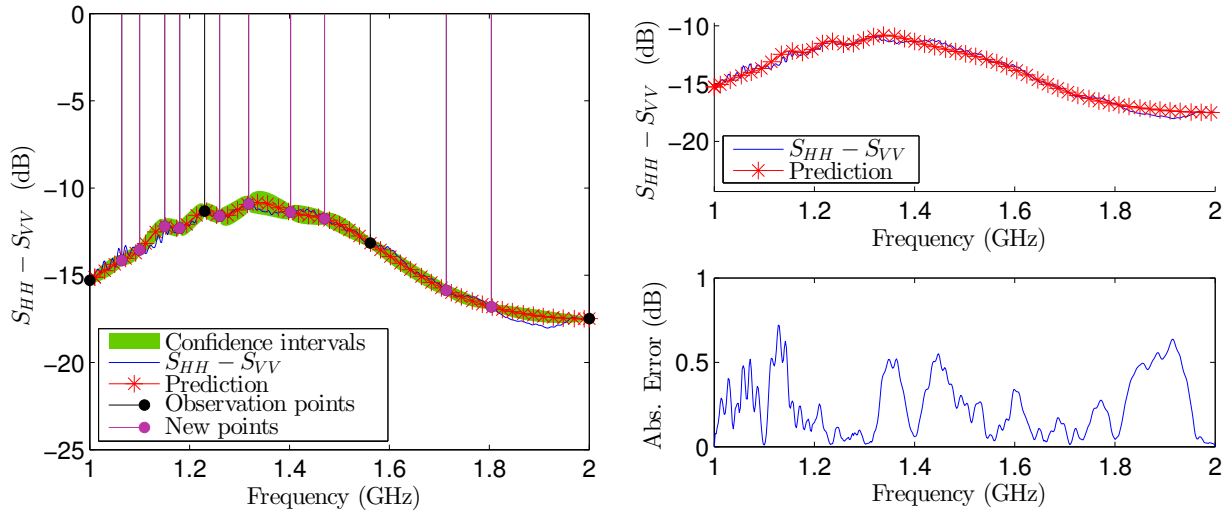
Figure 5.7 – The final prediction for $S_{HH} - S_{VV}$ in L-band together with its confidence intervals $\pm\tilde{\sigma}$ (left) and the same prediction with the corresponding absolute error (right). The prediction was based on the 3 initial simulation points contained in L-band and 10 adaptively chosen, so that the lower border point is also simulated and the corresponding uncertainty was sequentially reduced. The final prediction showed an absolute error always inferior to $1\,\mathrm{dB}$.

that these information lead to the conclusion that branches were existing in the forest observed. As a consequence, taking into account the knowledge just obtained that branches exist, a new signal to be emitted was designed so that it was best fitted to our updated objective, that of the branches study. The adaptive sampling which pointed out the new frequencies that should be emitted, took place along the $0.8 - 1.3\,\mathrm{GHz}$ frequency interval. It provided 5 extra points, which completed the 3 points of the initial sample space contained

in this sub-band. The uncertainty had to correspond to one of the two first Pauli vector components, since the dominant scattering mechanisms were the subject of the study. Here the one of the $S_{HH} - S_{VV}$ prediction was preferred, because of the $S_{HH} - S_{VV}$ non-monotonic nature.
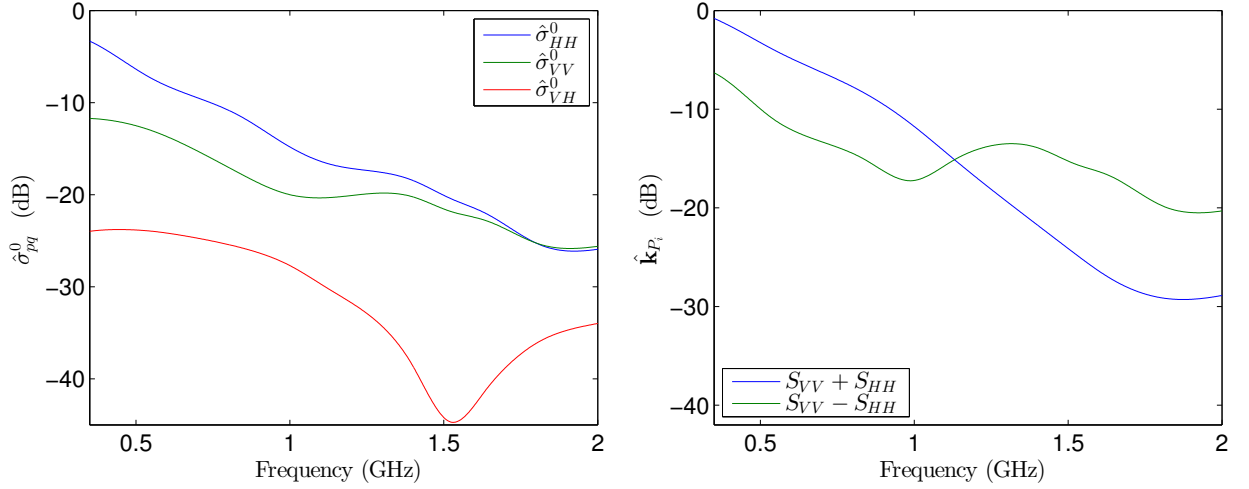
Figure 5.8 − The initial predictions for the backscattering coefficients (left) and the first two Pauli vector components (right). These predictions were based on 10 simulated points.

The final prediction for the Pauli vector components, which was based on 8 simulation points only, is presented together with the real values in Fig. 5.9. Despite the small number of the simulation results used, the final predictions were more than satisfying compared to the real values. The quantities variation ranges were provided and the point where the change of the dominant scattering mechanism - from the double bounces to the single ones - takes place was predicted with an accuracy of 99.82% (see Fig. 5.9). For an even better accuracy, since not always such a strong accuracy is achieved, we could have narrowed more the frequency band to $1 - 1.2\,\mathrm{GHz}$, during the adaptive sampling strategy. The absolute errors of the final approximations for both $S_{HH} + S_{VV}$ and $S_{HH} - S_{VV}$, as calculated over more than 800 points, were not exceeding $0.4\,\mathrm{dB}$ (see Fig. 5.10), being much lower that the $1\,\mathrm{dB}$ minimum radar error.

5.4.3 Strategy for target detection

One of the main objectives of forest observations by radars, is the detection of a target concealed in a forest environment. As we have already seen in Section 3.2.4, this task could be a rather challenging one, even when just trunks and branches exist to cover the target. Based on the conclusions of the above-mentioned section, we will define an adaptive strategy which will enable the possibility to confirm the existence of a hidden target with just a few frequencies emitted. In a later step, a more thorough and focused observation can follow, to discover the exact location of the target if possible. The scene was the same as in the previous example, having now a spherical target of a $2\,\mathrm{m}$ radius placed between the fourth and fifth trunks lines in the site dimension (see Fig. 3.18). As a first step of our strategy, an initial 10 frequencies observation was performed. The data from this observation were subsequently used for the metamodel predictions of all outputs. Since the target effect is not very distinguishable when branches exist, all these quantities needed to be studied, in order to exploit any possible clue of the target existence. As seen in Fig. 5.11, the metamodel predicted
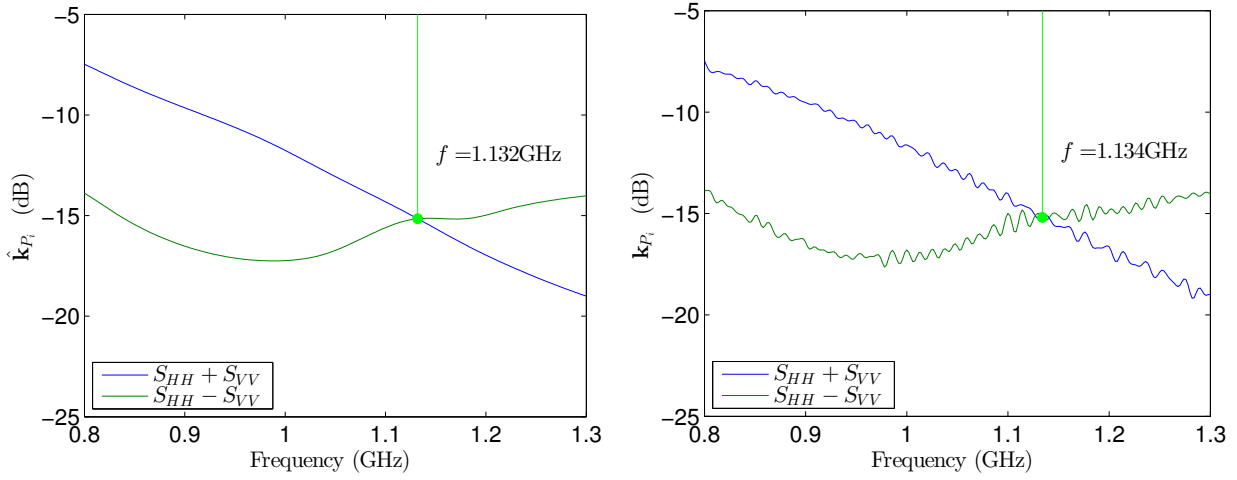
Figure 5.9 − The predicted values for the double and single bounces within the $0.8 − 1.3$ GHz frequency interval (left) and the corresponding real values (right). The point where the change of the dominant scattering mechanism happens, is predicted with an accuracy of about 99.8%, even if just 8 simulation results were used.
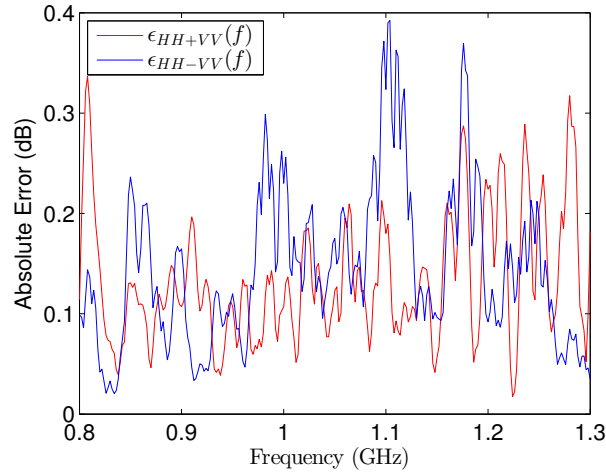
Figure 5.10 − The errors of the final 8-point prediction for the two first Pauli vector components. Along the desired band, where the 5-point sequential sampling was conducted, the error is not exceeding 0.4 dB for both quantities. The depicted results are these obtained after passing a moving average filter of span 5, over the data.

similar HH and VV backscattering above 1.5 GHz, as well as a more or less constant single bounce scattering ($S_{HH} − S_{VV}$) after 1 GHz. These effects are closely related with the existence of a spherical target in the forest, as explained in Section 3.2.4 and depicted in Fig. 3.21 and 3.22.

In order to proceed with our investigation, the radar configuration proposed in Section 3.2.4 for the target effect recognition will be selected. In saying so, we are going to focus to the $1.4 − 2$ GHz sub-band and improve the initial prediction for both co-polarized backscattering coefficients. To the 4 points from the initial sample found in the $1.4−2$ GHz, we will add 5 extra ones adaptively chosen, so that both uncertainties of the σ_{pp}^0 predictions will be sequentially
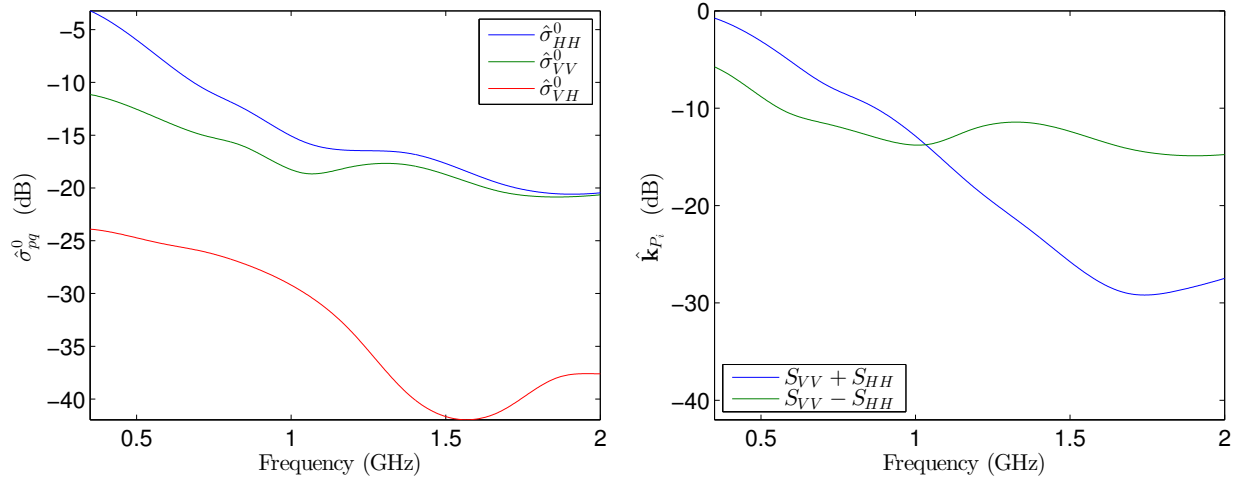
Figure 5.11 – The initial predictions for the backscattering coefficients (left) and the first two Pauli vector components (right). These predictions were based on 10 simulated points.

reduced. The results obtained after the final prediction are shown in Fig. 5.12, together with the real values. The final approximation was a very good one, as in both plots the quantities almost coincide. Both absolute errors were much lower that the radar measurements error, hardly reaching $0.5\,\mathrm{dB}$ (see Fig. 5.13). Therefore, the new information revealed by the final prediction confirm our initial suspicion that a target is found among the trees. After this cognitive observation, we can also continue the investigation of the scene, in order to attempt the localization of the target. However, to do so many simulation points will be needed in order to extract a time signal with a good resolution like the one in Fig. 3.41.
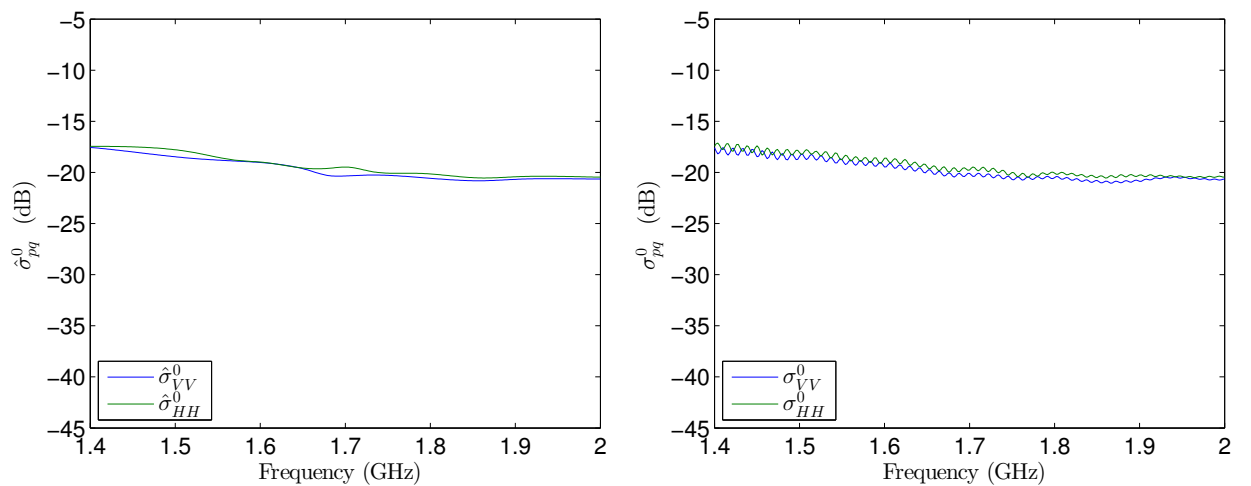
Figure 5.12 – The final prediction for the co-polarized backscattering coefficients in the limited band $1.4 - 2\,\mathrm{GHz}$, after adding 10 extra simulation points (left) and their real values (right).
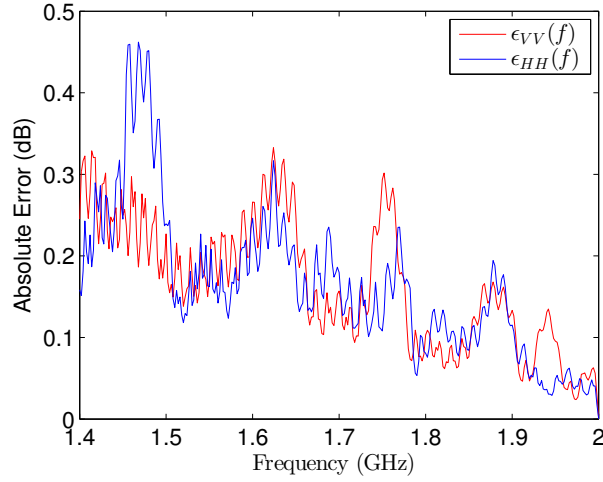
Figure 5.13 – The errors of the final prediction for the two co-polarized backscattering coefficients focused on the upper part of the COSMO frequency band. Along this desired sub-band, where the 10-point sequential sampling was conducted, the error hardly reaches $0.5\,$dB. The depicted results are these obtained after passing a moving average filter of span 5, over the data.

5.4.4   Low frequency strategy for penetration and Brewster effect study

The last example of our radar strategy is focused on the lower part of the forest. The part where the trunks dominate the backscatter and the Brewster angle effect is visible, due to the local trunk-ground dihedral configurations. The same scene as in the second example will be observed and the same initial approximation will be also used. If we take a look again at Fig. 5.8, we can see that the initial kriging approximation predicts a high difference between the co-polarized backscattering coefficients for low frequencies. This effect reminds as the results presented in Section 3.4 and it could be attributed to the Brewster angle effect. In particular, the Brewster effect due to the vegetation, since an angle of 40° could be mostly affected by the complementary $\theta_B^v = \frac{\pi}{2} - \tan^{-1}\sqrt{\varepsilon_v}$ angle of the Equation (3.3). In that case, it could be interesting to focus on the bottom layer of the forest containing the trunks and check how the co-polarized difference evolves.

In order to make the wave penetrate the canopy and reach the trunks, we will focus our study on P-band. It means that we will keep only the simulated points contained in it and we will run the adaptive sequential sampling in this band. We need again to pay attention that the border points are contained in the sample, so that kriging will not need to extrapolate the values. The approximated quantity was the $\sigma_{HH}^0 - \sigma_{VV}^0$ difference and its corresponding uncertainty was used for the 10-point adaptive sampling. The results of the focused study in P-band are presented in Fig. 5.14. As seen in the right plot, the final prediction based on 14 frequency points in total, approximated well the HH-VV backscattering difference, with an absolute error much less than $1\,$dB. Nonetheless, some of the real values local oscillations failed to be within the $\pm\tilde{\sigma}$ confidence intervals. The latter did not affect significantly the result, as the general behavior and the level of the co-polarized difference is obvious in the left plot. The highest difference values are observed for frequencies of $400\,$MHz and less, while the effect decays as we move towards the upper part of the frequency band. This difference is not significantly high, however at 40° we expect to see only the secondary Brewster effect as stated in Section 3.4. Moreover, branches exist in our scene and they "disturb" the dihedral trunk-ground geometry,

which favors the Brewster effect. Therefore, a constant $\sigma^0_{HH} - \sigma^0_{VV}$ difference of more than $7 - 8\,\mathrm{dB}$ along the $[350 - 450\,\mathrm{MHz}]$ interval, as predicted by our metamodel, could be reasonably attributed to the Brewster angle effect.
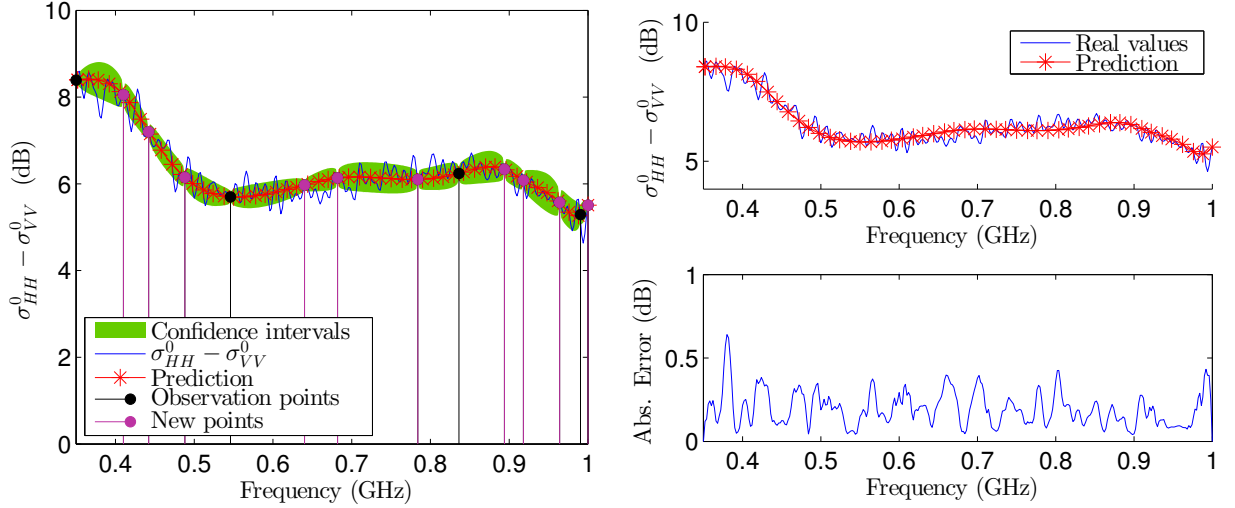
Figure 5.14 − The final prediction for $\sigma^0_{HH} - \sigma^0_{VV}$ within the P-band, together with its confidence intervals $\pm\tilde{\sigma}$ (left) and the same prediction with the corresponding absolute error (right). The prediction was based on the 4 initial simulation points contained in P-band and the 10 adaptively chosen ones. This prediction achieved a very good accuracy with an absolute error much lower than $1\,\mathrm{dB}$, although the confidence intervals could not contain all the local oscillations.

5.5   Conclusions

An innovative radar observation strategy was proposed in this chapter. It was based on the cognitive radar principle and the metamodeling techniques developed in this work. So we started with the presentation of the cognitive radar and the novelty it introduces, i.e. the sequential observations which take into account the effect of the environment. The main idea of this radar operation accords with the basic idea of our metamodel adaptive sampling. Therefore, a combination of these two methods was attempted. In saying so, the cognitive radar principle was incorporated in the metamodel frame, in order to realize an adaptive observation scheme. To complete this scheme, we used information from Chapter 3 to define certain strategies for the sequential observations. Each objective was connected with a forest effect and a certain radar configuration to be selected. To accelerate the analysis of the received signals and make the real-time operation feasible, we employed again the metamodel and its fast predictions. The metamodel uncertainty was connected with a different quantity each time. The choice of this quantity was depending on the scene information, reflecting thus the cognitive radar principle. The strategy finally defined, could stand as an elementary attempt towards a cognitive radar. This strategy was checked in four different examples. These examples were corresponding to forest effects already studied in this dissertation, such as the branches or the target effect on the forest response. Our innovative method succeeded in sequentially improving our knowledge on the scene under study, by identifying the forest effects, while taking into account the already obtained results.

6

Conclusions and perspectives

Contents

  In this last chapter of the dissertation, the work done and presented in the previous pages will be overviewed and concluded. The main points, contributions, results and inferences will be summarized, to provide a global view and highlight the "spine" of the project. The conclusions will be subsequently followed by a list of suggestions and ideas for future work. These perspectives aspire to complement the work carried out and presented here and, if possible, to bring it closer to the real radar investigation practice.

6.1 Conclusions

During this project, we introduced some mathematical tools and methods widely used in Design and Analysis of Simulation Experiments, to the radar observation practice. It was the first time, to the best of our knowledge, that similar statistical tools were used in analyzing radar data. In doing so, the aim was to initiate a discussion about reconsidering the way radar forest investigations take place nowadays. For that reason, a new strategy, based on the mathematical tools introduced, was suggested and tested in the previous pages. Instead of real datasets, the COSMO numerical model, which simulates forest microwave observations, was used in our strategy. COSMO is able to calculate the forest backscattering for numerous different input values, concerning both the radar and the forest parameters. Therefore, a big number of different forest arrangements was examined, under different radar configurations. The initial goal of obtaining these large datasets was to use SA techniques in order to identify the importance of each parameter effect on the forest backscattering.

  For computational reasons, a screening SA was selected to be performed on our model, namely the so-called Elementary Effects method. This qualitative method provides a list of the most important model factors, with a few simulations and a low computational cost. Indeed, in our case it succeeded in identifying the parameters affecting mostly the outputs and those showing certain non-linear and interaction effects. Based on the SA results, we discovered that the frequency and the incidence angle are the most important COSMO factors overall. As far as the scene is concerned, the age and the moisture of the vegetation showed the biggest influence

on the outputs. On the contrary, other factors such as the ambient temperature and the sand and clay content of the ground, showed an almost negligible influence.

Despite the wide verification of the EE method in SA applications, its results concerning COSMO were proceeded to be further analyzed. In saying so, the most important parameters had to be qualified as such and the extent of their effects had to be examined in different forest scenes. This examination concerned the influence on the backscattered signal in both frequency and time domains. In most cases, a certain effect was finally attributed to each parameter and the physical interpretation was provided. The same analysis was later performed on the effects of the forest elements, i.e. trunks, branches and target, and of the different forest arrangements, i.e. periodical, semi-periodical and random. The most important outcome of these analyses was the discovery of certain frequency sub-bands and polarizations which favor the identification and study of the important effects. For instance, if the goal is to study the change of the dominant scattering mechanism due to the branches effect, the interval $[0.9, 1.3]$GHz is recommended. If the existence of a spherical target is to be deduced, the upper part of the L-band is preferred, where the forest scatters the same in both HH and VV, due to the target. These discoveries would be valuable in the design of innovative adaptive radar strategies. However, a strategy like this could not be realized if a way to accelerate the signal analysis was not available.

Surrogate modeling was the second mathematical method from the Design and Analysis of Simulation Experiments, which was employed in this work. The kriging method we used is very popular in various scientific domains, for building statistical approximation metamodels of numerical codes. These metamodels can be used to understand and reconsider the numerical model, as well as to predict its non-simulated values. The most powerful and flexible metamodels are the adaptive ones, which are fitted to the numerical model by sequentially reducing the uncertainty of the prediction. In our case, a model like this was proven capable of approximating several of the COSMO outputs, such as the backscattering coefficients and the Pauli vector components in the frequency domain. In addition, its capability to assist the backscattered signal analysis and identify the major forest effects, using only a few simulation points, was verified.

Combining all the previous conclusions and results with the cognitive radar principle, we had all the necessary tools to design an innovative strategy for adaptive radar observations of forests. This strategy was based on the incorporation of the cognitive radar principle in the metamodel operational frame. All previous achievements were employed in the design and realization of this strategy. The suggestions for the radar configurations resulting from the signal analyses, were adopted with respect to the observation objectives. The metamodel was used again in a smaller scale, to predict the forest signature, to accelerate the real-time signal analysis and thus to assist in identifying the forest elements effects. Finally, its stepwise uncertainty reduction scheme together with the previous analyses information were responsible for the cognitive aspect of this strategy.

6.2   Perspectives

Since this work served as a first step towards an innovative way to consider, design and perform radar experiments, without always following the standard radar formalism, it leaves open ground for complementation. Problems and constraints faced during the realization of this project on

the one hand, and potential extensions on the other, set the new perspectives for the future research. The most straightforward extensions, would be the application of what has been done on more detailed forest scenes, i.e. branches existing in all cases and forests with more layers containing secondary branches and leaves also, even if the last are not expected to contribute significantly in the COSMO operating frequencies. Moreover, as COSMO can generate three different tree crown types, it would be interesting in examining their effect in high frequencies where not that much penetration occurs. The Brewster angle effect needs a more profound analysis also. The study of this effect in forested areas started to develop recently and so there is still enough "space" for new discoveries. As far as the target is concerned, since spherical targets are not common in FOPEN applications, differently shaped-targets have to be examined also, hidden under foliages of various densities. Other polarimetric and interferometric tools such as the covariance matrix, the entropy or the interferometric coherence could be also introduced, to integrate our method from a radar scientist point of view also.

In forest radar investigations, one of the main issues, apart from the target detection, is to estimate the forest ecological characteristics. Especially the aboveground biomass, which controls the global carbon emission. To do so, the estimation of several forest parameters, such as the age, density and humidity values is indispensable. Thus, the solution of the inverse problem using the metamodel for retrieval purposes in low computational time, is an interesting potentiality.

As far as the metamodel approximation of COSMO is concerned, the most important and also hard issue to be resolved is the prediction of the backscattered electric field. We explained in Chapter 4, that the amplitude and the phase of the received signal were oscillating too fast to be satisfactorily interpolated, in reasonable computational time, by our adaptive kriging metamodel. However, if this will could be successfully done in the future, it would open the ground for a fast improvement of the construction of a SAR image of the scene and the realization of a fully cognitive radar. A radar that will be able to provide all quantities necessary for a thorough analysis of the signal, even in time domain, with the low computational load guaranteed by the metamodel.

Another perspective could also be the redesign of COSMO to allow different functionalities. COSMO evaluates the received signal which have been modified twice by the forest, once while travelling within the scene towards the ground and then back to the radar. So throughout this work, the forest 2-way modification on the signal was examined. It would be really interesting to complement COSMO in such a way that the 1-way modification of the forest would be available. This could facilitate the investigation, in FOPEN studies, of the forest effect on the emitted signal, before the latter arrives to the target. That way, the target backscattering would be easier to be isolated and well identified. The information on the 1-way modification of the forest could open also the ground for designing special waveforms which would be able to "compensate" this forest effect during a cognitive observation.

All the aforementioned perspectives refer to simulation studies. These studies are of great importance but they cannot fully substitute real measurements. No matter how extensively validated a model is, it is of great importance to complement our knowledge and verify the usefulness of our methods on real data. It is true that certain limitations exist and pose difficulties to such an attempt. Firstly, not all cases considered in this dissertation were realistic. In addition, real forest data are in general sparse and hard to obtain. Nevertheless, it is necessary to verify the plausibility of our conclusions at least on the close to reality examples

considered. That could potentially serve as a preparatory step for the actualization of a real cognitive radar, provided that several technical issues would be solved in the meantime.

A

Statistical background

Contents

A.1 Matérn covariance function

For the complex random vectors $\mathbf{x}$ and $\mathbf{x}'$, the covariance function of a zero-mean process f is defined as:

$$k\left(\mathbf{x}, \mathbf{x}'\right) = \mathbb{E}\left[f\left(\mathbf{x}\right) f^*\left(\mathbf{x}'\right)\right] \tag{A.1}$$

where f^* denotes the complex conjugate of f. In surrogate modeling stationary covariances are mostly used. Stationarity stands for the property of the second-order or weak stationarity, which implies that both the first two moments of the joint bivariate distribution $\left(f\left(\mathbf{x}\right) f^*\left(\mathbf{x}'\right)\right)$ depend only on the spatial separation $\|\mathbf{x} - \mathbf{x}'\|$ i.e. the length of this vector. The covariance function is then a function of $h = \|\mathbf{x} - \mathbf{x}'\|$ and it can be written as a function of a single argument $k\left(h\right)$ ([Rasmussen and Williams, 2006]). If in addition the covariance function is supposed to be anisotropic, it means that it also depends on the direction of the $\|\mathbf{x} - \mathbf{x}'\|$ vector [Haskard, 2007], since the different inputs/coefficients of $\mathbf{x}$ are not of the same nature and thus the function does not behave in the same way along all the dimensions of the input space.

 The *Matérn* covariance function is an example of a stationary covariance function, which can be both isotropic and anisotropic, depending on the model under study. It was introduced during the 60's as the natural correlation for spatial processes. If $h = \|\mathbf{x} - \mathbf{x}'\| \geq 0$ is the distance between two observation points, the isotropic Matérn covariance function is given by ([Stein, 1999], [Villemonteix et al., 2009]):

$$k\left(h\right) = \frac{\sigma^2}{2^{\nu-1}\Gamma\left(\nu\right)} \left(\frac{2\sqrt{\nu}h}{\rho}\right)^\nu \mathcal{K}_\nu\left(\frac{2\sqrt{\nu}h}{\rho}\right) \tag{A.2}$$

where σ^2 is the variance of the model, $\sigma^2 = k\left(0\right)$, $\nu > 0$ is a parameter controlling the smoothness of the underlying process as $[\nu]$ [29] determines the number of times the underlying spatial process is mean-square differentiable (the larger the ν the smoother the process is), $\rho > 0$ is a distance

---

[29]With $[\nu]$ the integer part of ν is denoted.

parameter which measures the decay of the correlation with distance (which in our case, where anisotropicity is assumed, we will include within the distance function) and $\mathcal{K}_\nu$ is a modified Bessel function. The Matérn correlation family can give for different values of ν the exponential correlation function (if $\nu = \frac{1}{2}$), the Whittle's elementary correlation function (if $\nu = 1$) and it approaches the Gaussian one when (if $\nu \to \infty$) [Haskard, 2007].

A.2 REstricted Maximum Likelihood estimation (REML)

The REML is an extension of the more general Maximum Likelihood Estimation (MLE), which is a very common estimation method in Statistics (see [Stein, 1999] for more information). In ordinary kriging, as already mentioned, we assume that the vector of the observation has a Gaussian distribution with unknown mean, which is also a subject of maximization during the MLE. To suppress the unknown mean from the MLE, in order to decrease the unknown quantities under estimation, we transform the Gaussian distribution to a zero-mean one - main idea of the REML. This linear transformation is performed using the QR-decomposition of $\mathbf{p} = \mathbf{1}$ [30]

In order to estimate now the vector of the hyper-parameters $\boldsymbol{\theta} = \left(\sigma_0^2, \nu, \rho_1, \ldots, \rho_d\right)$ of our model, we need to assign to it an initial set of values and to evaluate the covariance matrix $\underline{\underline{\mathbf{K}}}$ for them. Using a rule of thumbs, we assume that $\nu = \frac{3}{2}d$ where d is the dimension of the input space, the σ_0^2 is the variance of the observations and each ρ_k is equal to the half of the interval diameter corresponding to x_k. The likelihood function for the REML method is then given by [Bilicz, 2011]:

$$\mathcal{L}\left(\boldsymbol{\theta}|\underline{\underline{\mathbf{W}}}\boldsymbol{f}_{\mathbb{X}}\right) = \frac{1}{\sqrt{(2\pi)^{(n-1)}\left|\underline{\underline{\mathbf{W}}}\,\underline{\underline{\mathbf{K}}}\,\underline{\underline{\mathbf{W}}}^T\right|}}\exp\left[-\frac{1}{2}\left(\underline{\underline{\mathbf{W}}}\boldsymbol{f}_{\mathbb{X}}\right)^T\left(\underline{\underline{\mathbf{W}}}\,\underline{\underline{\mathbf{K}}}\,\underline{\underline{\mathbf{W}}}^T\right)^{-1}\left(\underline{\underline{\mathbf{W}}}\boldsymbol{f}_{\mathbb{X}}\right)\right] \quad \text{(A.3)}$$

where $\underline{\underline{\mathbf{K}}}$ is actually $\underline{\underline{\mathbf{K}}}\left(\boldsymbol{\theta}\right)$. The REML method estimates the covariance parameters so that the probability density of the data is maximized. We will denote by $\hat{\boldsymbol{\theta}} = \left(\hat{\sigma}_0^2, \hat{\nu}, \hat{\rho}_1, \ldots, \hat{\rho}_d\right)$ the vector of these optimal covariance parameters values evaluated by:

$$\hat{\boldsymbol{\theta}} = \arg\max_{\boldsymbol{\theta}}\left[\pi\left(\boldsymbol{\theta}\right) \cdot \mathcal{L}\left(\boldsymbol{\theta}|\underline{\underline{\mathbf{W}}}\boldsymbol{f}_{\mathbb{X}}\right)\right] \quad \text{(A.4)}$$

where $\pi\left(\boldsymbol{\theta}\right)$ is a regularizing factor that uses the a priori knowledge of the hyper-parameters, in order to avoid the ill-conditionedness of the $\underline{\underline{\mathbf{K}}}$ matrix. Since we usually don't have any a priori knowledge of these parameters, we assume a multivariate Gaussian distribution for them. The initial value is the mean of this distribution and we choose a desired variance which controls the "freedom" of the estimator [31]. So:

$$\pi\left(\theta\right) = \prod_{i=1}^{N+2}\frac{1}{\sqrt{(2\pi)\,\sigma_{pr,j}^2}}\exp\left[-\frac{(\theta_i - \theta_{pr,i})^2}{2\sigma_{pr,j}^2}\right]$$

---

[30]In the more general case of *universal kriging* $\mathbf{p} = \mathbf{p}(\mathbf{x}) = (p_1(\mathbf{x}), \ldots, p_l(\mathbf{x}))$ a vector of l known low-order monomials of $\mathbf{x}$ that give the unknown mean of the quantity under study by the formula $m(\mathbf{x}) = \boldsymbol{\beta}^T\mathbf{p}(\mathbf{x})$, where $\boldsymbol{\beta}$ is a vector of unknown constants. The REML helps us suppress the coefficients of $\boldsymbol{\beta}$ that should be also estimated if the mean is not zero [Bilicz, 2011].

[31] In general, we choose an appropriate variance so that the hyper-parameters values will not be far from the "rational" region around the initial values.

where the *pr* index distinguishes the mean and the variance of the prior hyper-parameters distributions.

Index

Bibliography

[Arnaubec et al., 2014] Arnaubec, A., Roueff, A., Dubois-Fernandez, P., and Refregier, P. (2014). Vegetation Height Estimation Precision With Compact PolInSAR and Homogeneous Random Volume Over Ground Model. IEEE Transactions on Geoscience and Remote Sensing, 52(3):1879–1891. 31

[Bachoc, 2013] Bachoc, F. (2013). Cross Validation and Maximum Likelihood estimation of hyper-parameters of Gaussian processes with model misspecification. Computational Statistics and Data Analysis, (66):55–69. 105

[Bachoc et al., 2014] Bachoc, F., Bois, G., Garnier, J., and Martinez, J.-M. (2014). Calibration and Improved Prediction of Computer Models by Universal Kriging. Nuclear Science and Engineering, (176):81–97. 106

[Balanis, 1989] Balanis, C. (1989). Advanced Engineering Electromagnetics. Wiley. 89

[Baxter, 1992] Baxter, B. (1992). The Interpolation Theory of Radial Basis Functions. PhD thesis, Cambridge University. 101, 102

[Bect et al., 2012] Bect, J., Ginsbourger, D., Li, L., Picheny, V., and Vazquez, E. (2012). Sequential Design of Computer Experiments for the Estimation of a Probability of Failure. Statistics and Computing, 22(3):773–793. 103

[Behan and Woodhouse, 1999] Behan, A. and Woodhouse, I. (1999). Synthetic Aperture Radar Polarimetry for Forestry Applications. 15

[Bilicz, 2011] Bilicz, S. (2011). Application of Design-of-Experiment Methods and Surrogate Models in Electromagnetic Nondestructive Evaluation. PhD thesis, Université Paris Sud - Paris XI; Budapest University of Technology and Economics. 103, 104, 105, 109, 144

[Blatman, 2009] Blatman, G. (2009). Adaptive Sparse Polynomial Chaos Expansions for Uncertainty Propagation and Sensitivity Analysis. PhD thesis, Université Blaise Pascal - Clermont II. 102

[Brigui, 2010] Brigui, F. (2010). Algorithmes d'imagerie SAR polarimétrique basés sur des modèles à sous-espace. Application à la détection de cible sous couvert forestier. PhD thesis, Université Paris Ouest - Nanterre La Défense. 17

[Bucci and Isernia, 1997] Bucci, O. M. and Isernia, T. (1997). Electromagnetic Inverse Scattering: Retrievable Information and Measurement Strategies. Radio Science, 32(6):2123–2137. 16

[Campolongo and Cariboni, 2007] Campolongo, F. and Cariboni, J. (2007). Sensitivity Analysis: How to Detect Important Factors in Large Models. Technical Report EUR 22798 EN, European Commission, Doctorate-General Joint Research Centre, Institute for the Protection and Security of the Citizen. 45, 48, 50, 52

[Campolongo et al., 2007] Campolongo, F., Cariboni, J., and Saltelli, A. (2007). An Effective Screening Design for Sensitivity Analysis of Large Models. Environmental Modelling & Software, 22(10):1509 – 1518. 45, 46, 47

[Campolongo et al., 2005] Campolongo, F., Cariboni, J., Saltelli, A., and Schoutens, W. (2005). Enhancing the Morris Method. In Sensitivity Analysis of Model Output (SAMO), pages 11–pages. 48

[Campolongo et al., 2011] Campolongo, F., Saltelli, A., and Cariboni, J. (2011). From Screening to Quantitative Sensitivity Analysis. A Unified Approach. Computer Physics Communications, 182(4):978 – 988. 44, 45

[Castel et al., 2001] Castel, T., Beaudoin, A., Floury, N., Le Toan, T., Caraglio, Y., and Barczi, J. (2001). Deriving Forest Canopy Parameters for Backscatter Models Using the AMAP Architectural Plant Model. IEEE Transactions on Geoscience and Remote Sensing, 39(3):571–583. 28, 29

[Chauhan et al., 1991] Chauhan, N., Lang, R., and Ranson, K. (1991). Radar Modeling of a Boreal Forest. IEEE Transactions on Geoscience and Remote Sensing, 29(4):627–638. 32

[Chevalier et al., 2014] Chevalier, C., Bect, J., Ginsbourger, D., Vazquez, E., Picheny, V., and Richet, Y. (2014). Fast Parallel Kriging-Based Stepwise Uncertainty Reduction with Application to the Identification of an Excursion Set. Technometrics, 56(4):455–465. 103

[Chilès and Delfiner, 1999] Chilès, J. and Delfiner, P. (1999). Geostatistics: Modeling Spatial Uncertainty. Wiley Series in Probability and Statistics. Wiley. 103, 106

[Cloude, 2009] Cloude, S. (2009). Polarisation: Applications in Remote Sensing. OUP Oxford. 27, 89, 119

[Cloude and Papathanassiou, 1998] Cloude, S. and Papathanassiou, K. (1998). Polarimetric SAR interferometry. IEEE Transactions on Geoscience and Remote Sensing, 36(5):1551–1565. 31

[Curlander and McDonough, 1991] Curlander, J. and McDonough, R. (1991). Synthetic Aperture Radar: Systems and Signal Processing. Wiley Series in Remote Sensing and Image Processing. Wiley. 22

[Daniels, D.J and Institution of Electrical Engineers, 2004] Daniels, D.J and Institution of Electrical Engineers (2004). Ground Penetrating Radar. Number τ. 1 in IEE radar, sonar, navigation, and avionics series. Institution of Electrical Engineers. 33, 34

[Dechambre et al., 2003] Dechambre, M., Le Hegarat, S., Dreuillet, P., and Champion, I. (2003). Polarimetric Analysis of P-BAND SAR Data Acquired Over a Forested Area: "The PYLA 2001 Experiment". In IEEE International Geoscience and Remote Sensing Symposium (IGARSS), volume 4, pages 2550–2552 vol.4. 17, 20, 32, 36

[Delicado et al., 2009] Delicado, P., Giraldo, R., Comas, C., and Mateu, J. (2009). Statistics for spatial functional data: Some recent contributions. Environmetrics, 21:224–239. 103

[den Hertog et al., 2004] den Hertog, D., Kleijnen, J., and Siem, A. (2004). The Correct Kriging Variance Estimated by Bootstrapping. Discussion Paper 2004–46, Tilburg University, Center for Economic Research. 109

[Efron and Tibshirani, 1994] Efron, B. and Tibshirani, R. (1994). An Introduction to the Bootstrap. Chapman & Hall/CRC Monographs on Statistics & Applied Probability. Taylor & Francis. 109

[El-Rayes and Ulaby, 1987] El-Rayes, M. and Ulaby, F. (1987). Microwave Dielectric Spectrum of Vegetation-Part I: Experimental Observations. IEEE Transactions on Geoscience and Remote Sensing, GE-25(5):541–549. 68

[Fang et al., 2006] Fang, K.-T., Li, R., and Sudjianto, A. (2006). Design and Modeling for Computer Experiments. Chapman and Hall/CRC Computer Science and Data Analysis Series. Chapman & Hall/CRC, London. 106

[Ferrazzoli and Guerriero, 1995] Ferrazzoli, P. and Guerriero, L. (1995). Radar Sensitivity to Tree Geometry and Woody Volume: A Model Analysis. IEEE Transactions on Geoscience and Remote Sensing, 33(2):360–371. 15

[Ferrazzoli et al., 2002] Ferrazzoli, P., Guerriero, L., and Wigneron, J.-P. (2002). Simulating L-band Emission of Forests in View of Future Satellite Applications. IEEE Transactions on Geoscience and Remote Sensing, 40(12):2700–2708. 28

[Fournier et al., 1997] Fournier, R. A., Rich, P. M., and Landry, R. (1997). Hierarchical Characterization of Canopy Architecture for Boreal Forest. Journal of Geophysical Research: Atmospheres, 102(D24):29445–29454. 29

[Freeman, 2007] Freeman, A. (2007). Fitting a Two-Component Scattering Model to Polarimetric SAR Data From Forests. IEEE Transactions on Geoscience and Remote Sensing, 45(8):2583–2592. 91

[Giraldo et al., 2007] Giraldo, R., Delicado, P., and Mateu, J. (2007). Geostatistics for Functional Data: An Ordinary Kriging Approach. Technical report, Universitat Politècnica de Catalunya. 103

[Haskard, 2007] Haskard, K. (2007). An Anisotropic Matern Spatial Covariance Model: REML Estimation and Properties. PhD thesis, University of Adelaide, School of Agriculture, Food and Wine. 143, 144

[Haykin, 2006] Haykin, S. (2006). Cognitive Radar: A Way of the Future. IEEE Signal Processing Magazine, 23(1):30–40. 17, 126

[Huang et al., 2015] Huang, W., Sun, G., Ni, W., Zhang, Z., and Dubayah, R. (2015). Sensitivity of Multi-Source SAR Backscatter to Changes in Forest Aboveground Biomass. Remote Sensing, 7(8):9587. 44, 60

[Iooss et al., 2010] Iooss, B., Boussouf, L., Feuillard, V., and Marrel, A. (2010). Numerical Studies of the Metamodel Fitting and Validation Processes. International Journal on Advances in Systems and Measurements, 3(1 & 2):11–21. 112, 115

[Jakubowski et al., 2013] Jakubowski, M., Li, W., Guo, Q., and Kelly, M. (2013). Delineating Individual Trees from Lidar Data: A Comparison of Vector- and Raster-based Segmentation Approaches. Remote Sensing, 5(9):4163. 15

[Ji and Wu, 2015] Ji, K. and Wu, Y. (2015). Scattering Mechanism Extraction by a Modified Cloude-Pottier Decomposition for Dual Polarization SAR. Remote Sensing, 7(6):7447. 27

[Jin et al., 2002] Jin, R., Chen, W., and Sudjianto, A. (2002). On Sequential Sampling for Global Metamodeling in Engineering Design. In ASME 2002 International Design Engineering Technical Conferences and Computers and Information in Engineering Conference, pages 539–548. American Society of Mechanical Engineers. 103, 112

[Kleijnen, 2007] Kleijnen, J. (2007). Design and Analysis of Simulation Experiments. International Series in Operations Research & Management Science. Springer. 100, 101

[Kleijnen, 2008] Kleijnen, J. (2008). Design of Experiments: Overview. In Proceedings of the 40th Conference on Winter Simulation, WSC '08, pages 479–488. Winter Simulation Conference. 17, 45, 100, 123, 126

[Kleijnen, 2009] Kleijnen, J. (2009). Kriging Metamodeling in Simulation: A Review. European Journal of Operational Research, 192(3):707–716. 100, 101

[Kleijnen, 2011] Kleijnen, J. (2011). Simulation Optimization Via Bootstrapped Kriging: Tutorial. Discussion paper. Tilburg University. 109

[Kleijnen and van Beers, 2004] Kleijnen, J. and van Beers, W. (2004). Application-driven Sequential Designs for Simulation Experiments: Kriging Metamodelling. Journal of the Operational Research Society, 55:876–883. 103

[Le Gratiet and Cannamela, 2012] Le Gratiet, L. and Cannamela, C. (2012). Kriging-based Sequential Design Strategies Using Fast Cross-Validation Techniques with Extensions to Multi-fidelity Computer Codes. 104

[Le Toan et al., 1992] Le Toan, T., Beaudoin, A., Riom, J., and Guyon, D. (1992). Relating Forest Biomass to SAR Data. IEEE Transactions on Geoscience and Remote Sensing, 30(2):403–411. 16

[Le Toan et al., 2011] Le Toan, T., Quegan, S., Davidson, M., Balzter, H., Paillou, P., Papathanassiou, K., Plummer, S., Rocca, F., Saatchi, S., Shugart, H., and Ulander, L. (2011). The BIOMASS Mission: Mapping Global Forest Biomass to Better Understand the Terrestrial Carbon Cycle. Remote Sensing of Environment, 115(11):2850 – 2860. {DESDynI} VEG-3D Special Issue. 16

[Lee and Pottier, 2009] Lee, J. and Pottier, E. (2009). Polarimetric Radar Imaging: From Basics to Applications. Optical Science and Engineering. Taylor & Francis. 26, 27

[Lillesand et al., 2004] Lillesand, T., Kiefer, R., and Chipman, J. (2004). Remote Sensing and Image Interpretation. Wiley. 20

[Lin and Sarabandi, 1999] Lin, Y.-C. and Sarabandi, K. (1999). A Monte Carlo Coherent Scattering Model for Forest Canopies Using Fractal-generated Trees. IEEE Transactions on Geoscience and Remote Sensing, 37(1):440–451. 29

[López-Martínez et al., 2011] López-Martínez, C., Alonso, A., Fàbregas, X., and Papathanassiou, K. (2011). Underlying Topography Estimation and Separation of Scattering Contributions over Forests Based on PolInSAR Data. FRINGE Workshop, pages 518–522. 31

[Matheron, 1963] Matheron, G. (1963). Principles of Geostatistics. Economic Geology, 58(8):1246–1266. 102

[Matheron, 1969] Matheron, G. (1969). Le Krigeage Universel. Centre de Morphologie Mathématique Fontainebleau: Les cahiers du Centre de Morphologie Mathématique de Fontainebleau. École nationale supérieure des mines de Paris. 102

[McKay et al., 1979] McKay, M. D., Beckman, R. J., and Conover, W. J. (1979). A Comparison of Three Methods for Selecting Values of Input Variables in the Analysis of Output from a Computer Code. Technometrics, 21(2):pp. 239–245. 106

[Mladenova et al., 2013] Mladenova, I., Jackson, T., Bindlish, R., and Hensley, S. (2013). Incidence Angle Normalization of Radar Backscatter Data. IEEE Transactions on Geoscience and Remote Sensing, 51(3):1791–1804. 17, 62, 64, 96

[Morris, 1991] Morris, M. (1991). Factorial Sampling Plans for Preliminary Computational Experiments. Technometrics, 33(2):161–174. 44, 45, 46, 48

[Norton, 2009] Norton, J. (2009). Selection of Morris Trajectories for Initial Sensitivity Analysis. In 15th IFAC Symposium on System Identification, pages 670–674, Saint-Malo, France. IFAC. 44

[Papathanassiou, 1999] Papathanassiou, K. (1999). Polarimetric SAR Interferometry. PhD thesis, Technical University Graz. 27

[Patel et al., 2008] Patel, S., Golakiya, B., Savalia, S., and Gajera, H. (2008). Glossary Of Soil Sciences. International Book Distributing Company. 34

[Peebles, 1998] Peebles, P. (1998). Radar Principles. A Wiley-Interscience publication. Wiley. 19

[Peplinski et al., 1995a] Peplinski, N., Ulaby, F., and Dobson, M. (1995a). Corrections to "Dielectric Properties of Soils in the 0.3-1.3-GHz Range". IEEE Transactions on Geoscience and Remote Sensing, 33(6):1340–. 34

[Peplinski et al., 1995b] Peplinski, N., Ulaby, F., and Dobson, M. (1995b). Dielectric Properties of Soils in the 0.3-1.3-GHz Range. IEEE Transactions on Geoscience and Remote Sensing, 33(3):803–807. 34

[Porté et al., 2000] Porté, A., Bosc, A., Champion, I., and Loustau, D. (2000). Estimating the Foliage Area of Maritime Pine (Pinus pinaster Aït.) Branches and Crowns with Application to Modelling the Foliage Area Distribution in the Crown. Annals of Forest Science, 57(1):73–86. 15, 28

[Prusinkiewicz and Lindenmayer, 1990] Prusinkiewicz, P. and Lindenmayer, A. (1990). The Algorithmic Beauty of Plants. Springer-Verlag New York, Inc., New York, NY, USA. 29

[Queipo et al., 2005] Queipo, N., Haftka, R., Shyy, W., Goel, T., Vaidyanathan, R., and Kevin Tucker, P. (2005). Surrogate-Based Analysis and Optimization. Progress in Aerospace Sciences, 41(1):1–28. 101, 102

Bibliography

[Rasmussen and Williams, 2006] Rasmussen, C. and Williams, C. (2006). Gaussian Processes for Machine Learning. The MIT Press. 143

[Robinson, 1991] Robinson, G. (1991). That BLUP is a Good Thing: The Estimation of Random Effects. Statistical Science, 6(1):15–32. 105

[Rumelhart et al., 1994] Rumelhart, D., Widrow, B., and Lehr, M. (1994). The Basic Ideas in Neural Networks. Communications of the ACM, 37(3):87–92. 102

[Runions et al., 2007] Runions, A., Lane, B., and Prusinkiewicz, P. (2007). Modeling Trees with a Space Colonization Algorithm. In Eurographics Workshop on Natural Phenomena. 29

[Saleh et al., 2005] Saleh, K., Porté, A., Guyon, D., Ferrazzoli, P., and Wigneron, J.-P. (2005). A Forest Geometric Description of a Maritime Pine Forest Suitable for Discrete Microwave Models. IEEE Transactions on Geoscience and Remote Sensing, 43(9):2024–2035. 28, 32, 51, 63

[Saltelli et al., 2008] Saltelli, A., Ratto, M., Andres, T., Campolongo, F., Cariboni, J., Gatelli, D., Saisana, M., and Tarantola, S. (2008). Global Sensitivity Analysis: The Primer. Wiley. 44

[Saltelli et al., 2000] Saltelli, A., Tarantola, S., and Campolongo, F. (2000). Sensitivity Analysis as an Ingredient of Modeling. Statistical Science, 15(4):377–395. 44

[Saltelli et al., 2004] Saltelli, A., Tarantola, S., Campolongo, F., and Ratto, M. (2004). Sensitivity Analysis in Practice: A Guide to Assessing Scientific Models. Wiley. 43, 44

[Santner et al., 2003] Santner, T., Williams, B., and Notz, W. (2003). The Design and Analysis of Computer Experiments. Springer Series in Statistics. Springer. 46

[Shao and Tu, 2012] Shao, J. and Tu, D. (2012). The Jackknife and Bootstrap. Springer Series in Statistics. Springer New York. 109

[Shimoyama et al., 2013] Shimoyama, K., Kawai, S., and J.J., A. (2013). Dynamic Adaptive Sampling Based on Kriging Surrogate Models for Efficient Uncertainty Quantification. In 54th AIAA/ASME/ASCE/AHS/ASC Structures, Structural Dynamics, and Materials Conference. 104

[Simpson et al., 2001] Simpson, T., Poplinski, J., Koch, P. N., and Allen, J. (2001). Metamodels for Computer-based Engineering Design: Survey and recommendations. Engineering with Computers, 17(2):129–150. 101, 102

[Skolnik, 1980] Skolnik, M. (1980). Introduction to Radar Systems. McGraw Hill Book Co., New York, 2 edition. 19, 22

[Stein, 1999] Stein, M. (1999). Interpolation of Spatial Data: Some Theory for Kriging. Springer Series in Statistics. Springer New York. 104, 143, 144

[Stellingwerf and Hussin, 1997] Stellingwerf, D. and Hussin, Y. (1997). Measurements and Estimations of Forest Stand Parameters Using Remote Sensing. Taylor & Francis. 15

[Thirion, 2003] Thirion, L. (2003). Modélisation de l'interaction cohérente des ondes électromagnétiques avec des couverts forestiers. PhD thesis, Université Paul Sabatier - Toulouse III. 31, 38

[Thirion et al., 2006] Thirion, L., Colin, E., and Dahon, C. (2006). Capabilities of a Forest Coherent Scattering Model Applied to Radiometry, interferometry, and polarimetry at P- and L-band. IEEE Transactions on Geoscience and Remote Sensing, 44:849–862. 17, 28, 31, 32, 34, 36, 37, 38

[Thirion-Lefevre et al., 2015] Thirion-Lefevre, L., Guinvarc'H, R., Piteros, P., and Lambert, M. (2015). The Polarimetric Signature of Double Bounces in Cities and Forests. The Double Brewster Effect. In 10th ASAR Workshop, Longueuil, Canada. 91, 96

[Ulaby and El-Rayes, 1987] Ulaby, F. and El-Rayes, M. (1987). Microwave Dielectric Spectrum of Vegetation - Part II: Dual-Dispersion Model. IEEE Transactions on Geoscience and Remote Sensing, GE-25(5):550–557. 34

[Ulaby and Elachi, 1990] Ulaby, F. and Elachi, C. (1990). Radar Polarimetry for Geoscience Applications. Artech House remote sensing library. Artech House. 15, 20, 27, 84

[Vaskó, 2011] Vaskó, A. (2011). Kriging-based Surrogate Model Generation for the Retrieval of the Characteristics of Forested Areas Based on Radar Measurements. Master's thesis, Budapest University of Technology & Economics. 104

[Villemonteix et al., 2009] Villemonteix, J., Vazquez, E., and Walter, E. (2009). An Informational Approach to the Global Optimization of Expensive-to-Evaluate Functions. Journal of Global Optimization, 44(4):509–534. 102, 103, 108, 143

[Wackerly et al., 2002] Wackerly, D., Mendenhall, W., and Scheaffer, R. (2002). Mathematical Statistics with Applications. Duxbury advanced series. Duxbury. 111

[Wang and Shan, 2006] Wang, G. G. and Shan, S. (2006). Review of Metamodeling Techniques in Support of Engineering Design Optimization. Journal of Mechanical Design, 129(4):370–380. 102

[Woodhouse, 2005] Woodhouse, I. (2005). Introduction to Microwave Remote Sensing. CRC Press. 17, 20, 28, 32, 33, 34, 36

[Xiong et al., 2007] Xiong, Y., Chen, W., Apley, D., and Ding, X. (2007). A Non-stationary Covariance-based Kriging Method for Metamodelling in Engineering Design. International Journal for Numerical Methods in Engineering, 71(6):733–756. 104

Titre : De l'utilisation de la méta-modélisation pour la modélisation et l'analyse de la réponse radar des forêts

Mots-clés : signature radar de la forêt, caractérisation de la forêt, analyse de sensibilité, plans d'expériences numériques séquentiels, métamodèle, krigeage, observations séquentielles, radar cognitif

Résumé : Dans ce travail, une nouvelle approche de conduite des observations radar de la forêt est proposée. Elle combine des méthodes statistiques pour l'analyse de sensibilité et les plans d'expériences numériques séquentiels et un code de calcul simulant la rétrodiffusion d'une forêt en vue de l'élaboration d'un modèle approché (métamodèle) à moindre coût numérique. L'introduction de ces outils mathématiques a pour objectif d'aider à la planification et à l'exécution des simulations radar et à l'organisation et l'analyse de leurs résultats. D'une part, les techniques de l'analyse de sensibilité sont appliquées afin de classer par ordre d'importance les paramètres d'entrée du modèle et d'identifier les paramètres de la forêt les plus significatifs ainsi que leurs effets sur le signal radar. D'autre part, la construction d'un métamodèle adaptable accélère le code de calcul, en préservant la physique du phénomène. Le cadre opérationnel de ce modèle approché sert finalement à introduire le principe du radar cognitif dans notre stratégie. Dans ce cas, une analyse rapide du signal reçu est nécessaire pour concevoir, en temps réel, le nouveau signal à émettre. De cette façon, les observations du radar simulées incluent en temps réel l'effet de l'environnement illuminé grâce aux simulations plus rapides et ciblées.

Titre : On the use of metamodeling for modeling and analysis of the radar response of forests

Keywords: forest radar signature, forest characterization, sensitivity analysis, adaptive design of simulation experiments, metamodel, kriging, sequential observations, cognitive radar

Abstract: In this work, a new approach to conduct the radar observations of forests is proposed. It combines statistical methods for sensitivity analysis and adaptive design of simulation experiments and a numerical code simulating the forest backscattering for the use of an approximate model (metamodel) with less computational cost. The introduction of these mathematical tools has as an objective to assist the design and the execution of radar simulations and the organization and analysis of their results. On the one hand, the sensitivity analysis techniques are applied in order to classify the input parameters by means of their importance and to identify the most significant forest parameters as well as their effects on the radar signal. On the other hand, the construction of an adaptive metamodel accelerates the simulation model, while keeping the physics of the phenomenom. The operational frame of this approximate model serves finally in the introduction of the cognitive radar principle in our strategy. In that case, a fast analysis of the received signal is necessary to design, in real-time, the new signal to be emitted. That way, the simulated radar observations take into account in real-time the effect of the illuminated environment, thanks to the more focused and fast simulations.